CENTRO DE NEUROCIENCIAS DE CUBA

SUBDIRECCIÓN DE NEUROINFORMÁTICA

LABORATORIO DE NEUROIMÁGENES

CARACTERIZACIÓN DE LA CONECTIVIDAD ANATÓMICA CEREBRAL A PARTIR DE LAS NEUROIMÁGENES DE LA DIFUSIÓN Y LA TEORÍA DE GRAFOS

Trabajo de Tesis para optar por el grado
de **Doctor en Ciencias de la Salud**

Yasser Iturria Medina

Ciudad de la Habana

2012

CENTRO DE NEUROCIENCIAS DE CUBA

SUBDIRECCIÓN DE NEUROINFORMÁTICA

LABORATORIO DE NEUROIMÁGENES

CARACTERIZACIÓN DE LA CONECTIVIDAD ANATÓMICA CEREBRAL A PARTIR DE LAS NEUROIMÁGENES DE LA DIFUSIÓN Y LA TEORÍA DE GRAFOS

Trabajo de Tesis para optar por el grado
de **Doctor en Ciencias de la Salud**

Por

Autor: MSc. Yasser Iturria Medina

Tutor: DrC. Nelson Trujillo Barreto

Ciudad de La Habana
2012

AGRADECIMIENTOS

Empecé a trabajar en temas de tractografía con Pedro A. Valdés Hernández, hace unos ocho años, cuando este aspiraba a un método nuevo para dar peso a las conexiones entre diferentes regiones cerebrales. A este esfuerzo pronto se sumó Erick J. Canales, dedicado más a la caracterización de la anisotropía intravoxel, junto a Lester Melie García y Yasser Alemán Gómez, pero siempre dispuesto a aportar ideas valiosas al análisis de la conectividad anatómica. La caracterización de las redes de conectividad comenzó, no mucho después, con Roberto Carlos Sotero, quien también dio aplicación a los métodos que iban surgiendo en modelos de actividad neural que desarrolló junto a Nelson Trujillo. Esos fueron los principios: todos inspirados a la vez en la bibliografía que surgía. A todos agradezco.

Cuando intenté dar otras aplicaciones a los métodos creados, Alejandro Pérez Fernández contribuyó a mejorar mis preguntas, muchas de las ideas actuales y planes futuros, sobre todo aquellos relacionados al estudio de patologías específicas, provienen de esa colaboración. También le debo cierta valiosa intervención para revisar esta tesis, labor a la que se han sumado, para mi suerte, María Antonieta Bobes, Ramón Martínez Cansino, Marlis Ontivero Ortega, Lester Melie García, Nelson Trujillo Barreto, Calixto Machado Curbelo y José Miguel Bornot.

Espero haber aprovechado las sugerencias de todos, y más aún, que el texto final cumpla por fin con sus expectativas.

SÍNTESIS

Las neuroimágenes de la difusión permiten reconstruir las trayectorias que presentan las fibras nerviosas de la materia blanca. Sin embargo, las metodologías asociadas presentan limitaciones y carecen de una formulación directa para caracterizar las conexiones anatómicas entre estructuras de la materia gris. En la presente tesis se aborda el problema de la caracterización de las conexiones anatómicas cerebrales basándonos en la información contenida en las neuroimágenes de la difusión y en la capacidad de la teoría de grafos para modelar matemáticamente relaciones cualesquiera entre objetos. En un primer paso, se combinan elementos de la teoría de grafos y de las neuroimágenes de la difusión para reconstruir y caracterizar las trayectorias de las fibras nerviosas entre diferentes regiones de interés. En un segundo paso, la metodología anterior es utilizada para reconstruir las redes anatómicas cerebrales de un grupo de humanos saludables, y luego se caracterizan estas redes empleando un conjunto de medidas topológicas que evalúan sus capacidades para lidiar con el flujo de información neural. En un tercer paso, se comparan los dos hemisferios cerebrales (en humanos saludables y un primate no-humano) según las características topológicas de sus correspondientes subredes anatómicas. En el cuarto y último paso, se propone analizar la topología de la red anatómica cerebral para discriminar condiciones cerebrales anómalas, y se analiza el caso de un modelo animal relevante para el estudio de las enfermedades desmilienizantes. Todos los métodos que se proponen han sido validados en datos simulados y reales, y los resultados han sido publicados en varios artículos que aquí se presentan.

TABLA DE CONTENIDO

Pág.

1. INTRODUCCIÓN

El advenimiento de las modernas técnicas de neuroimágenes ha generado una verdadera revolución en la comprensión del complejo sistema nervioso humano. La Tomografía Axial Computadorizada (TAC), la Tomografía por Emisión de Positrones (PET) y la Resonancia Magnética Nuclear (RMN), son algunos ejemplos de técnicas de relativa reciente aparición, que permean incluso el vocabulario común y la vida cotidiana. Estas técnicas posibilitan como nunca antes el acceso en forma de imágenes a la estructura del cerebro. Y no sólo eso, permiten además observar su funcionamiento en el tiempo: la progresiva activación de diferentes áreas cerebrales en la medida que una persona realiza determinada actividad mental. En general, gracias a ellas el estudio y la comprensión del cerebro ha tenido un desarrollo vertiginoso, convirtiendo en obsoleta aquella visión de "caja negra" que antes teníamos sobre este. Un rol exclusivo en estos avances lo tiene la RMN, técnica que cuenta con la enorme ventaja de ser no-invasiva. Las imágenes así obtenidas se basan en la cuantificación de las propiedades magnéticas de los diferentes tejidos, guardando distancia del proceso físico de la radiación y sus indeseables consecuencias, algo que sí está presente en las técnicas de TAC y PET. En parte por eso, su uso es muy amplio, sea en la clínica o en la investigación. Pero también porque a través de ella podemos desde explorar la integridad tisular, hasta inferir las zonas que se activan ante determinado proceso cognitivo, pasando por la posibilidad que brindan para determinar cómo están conectadas anatómica/funcionalmente unas y otras zonas del cerebro. Se podría afirmar que la información que esta técnica nos ofrece es tan rica y variada, que por ahora las limitaciones a su uso no son otras que las que imponga nuestro ingenio en la definición de nuevas metodologías para el análisis e interpretación del enorme caudal de datos que nos ofrece la RMN.

En este sentido, las *neuroimágenes de la difusión* han resultado ser una de las modalidades de más sorprendente desarrollo entre las técnicas de RMN.

Básicamente, las neuroimágenes de la difusión, también llamadas imágenes de resonancia magnética nuclear ponderadas en difusión, reflejan cómo ocurre el movimiento caótico de las moléculas de agua embebidas entre los diferentes tejidos cerebrales (Basser y col., 1994; LeBihan D. y col., 2001; LeBihan, 1995). Como se ilustra en la Figura 1a, el proceso de difusión del agua en la materia blanca se encuentra relacionado a la organización estructural de las fibras nerviosas: las moléculas fluyen con mayor facilidad en la dirección paralela a las fibras (donde se considera que la difusión es libre, pues no existen barreras) que en la dirección perpendicular (donde la difusión es restringida, pues las moléculas chocan con las paredes de los axones). Si dividiéramos todo nuestro cerebro en pequeños volúmenes cúbicos iguales (a los que suele llamárseles voxeles), y adquiriéramos una imagen típica de difusión, obtendríamos para cada voxel un valor de intensidad en la imagen: cuando el valor es bajo (pixel oscuro en la imagen), puede decirse que en este voxel hay mucha difusión en una dirección dada, y cuando el valor de intensidad es alto (pixel brillante en la imagen), se dice que ocurre poca difusión en la dirección observada. Esto permite investigar en qué direcciones específicas, de cada voxel, se mueven más las moléculas de agua, que como ya sabemos están “obligadas” a moverse en sentido paralelo a las fibras, por lo que de manera indirecta finalmente se asume que las fibras nerviosas en cada voxel están orientadas en aquellas direcciones en que más se movieron las moléculas de agua (Basser y col., 1994; Basser y col., 2000; Basser, 2002). La Figura 1b ilustra este proceso: en cada uno de los pequeños volúmenes en que hemos dividido el cerebro se obtiene una posible direccionalidad de las fibras contenidas. Una aplicación básica es emplear esta información direccional para seguir, de punto en punto (voxel a xoxel), la trayectoria de las fibras nerviosas al conectar las diferentes estructuras cerebrales (Ito y col., 2002; Mori y col., 1999), tal como se ilustra en la Figura 1c.

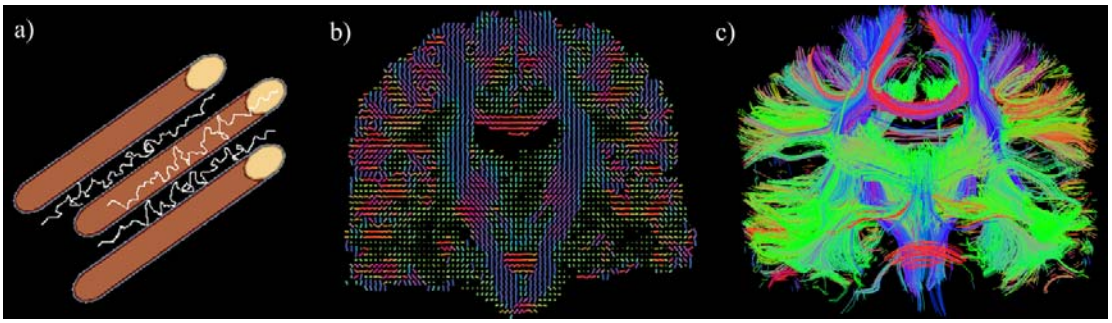

Figura 1. Del movimiento de las moléculas de agua a la reconstrucción de la trayectoria de las fibras nerviosas. a) Representación hipotética del movimiento de moléculas de agua (líneas blancas quebradas) alrededor de tres axones paralelos. b) Plano coronal del cerebro en el cual se presenta la dirección media de las fibras nerviosas en cada voxel. c) Trayectorias de fibras nerviosas estimadas a través de todo el cerebro luego de seguir de punto en punto la dirección media de las fibras obtenidas en cada voxel (Mori y col., 1999). En b) y c), el color de cada segmento o trayectoria se asignó de acuerdo al código RGB, según el cual cada vector toma un color que corresponde con su dirección. Por ejemplo, el color rojo indica que la orientación media de las fibras nerviosas es en la dirección medio-lateral, mientras el color verde corresponde a aquellas fibras orientadas en la dirección antero-posterior, y el color azul a las fibras orientadas en la dirección supero-inferior.

La obtención de las trayectorias que presentan las fibras nerviosas al conectar las diferentes estructuras que procesan la información neural, ha permitido profundizar por primera vez en la caracterización de la anatomía cerebral y en el entendimiento de la integración funcional del cerebro humano (Behrens y col., 2003a; Koch y col., 2002; LeBihan D. y col., 2001; Ramnani y col., 2004; Sotero y col., 2007; Sporns y col., 2005). Y todo esto es posible por primera vez *in vivo,* con el consiguiente impacto sobre el asesoramiento del estado de conectividad cerebral puntual de determinado ser vivo. Sin embargo, el punto álgido del tema lo constituyen aquellos algoritmos que permiten pasar de la estimación de la posible direccionalidad de las fibras en cada voxel (figura 1b) a la estimación de los tractos que conectan las regiones (figura 1c). Existe un consenso cada vez mayor sobre las múltiples limitaciones que poseen los algoritmos actuales de reconstrucción de trayectorias de fibras nerviosas. En particular los algoritmos

clásicos, guiados sólo por la dirección media de las fibras en cada voxel (Conturo y col., 1999; Mori y col., 1999), suelen fallar en aquellas regiones donde las fibras se cruzan, unen o divergen, siendo además muy sensibles al ruido intrínseco en la señal de RMN (Basser and Pajevic, 2000; Lori y col., 2002). Nuevos algoritmos, creados con el fin de superar las limitaciones anteriores, varían entre: i) versiones poco modificadas, que intentan emplear la información global del movimiento de las moléculas de agua en cada voxel, es decir, no sólo siguen la dirección media de las fibras sino que modifican esta dirección en dependencia del grado de difusión que hay en otros sentidos del voxel (Lazar y col., 2003; Weinstein y col., 1999); ii) algoritmos probabilistas basados, por ejemplo, en técnicas de Monte-Carlo, que proceden de manera similar, en cuanto a considerar la incertidumbre en la dirección estimada de las fibras, pero repiten el cálculo muchas veces para obtener un número elevado de trayectorias y dar al resultado final un sentido probabilista, el cual a su vez puede ser interpretado cuantitativamente como el grado de evidencia (o la *probabilidad frecuentista de conexión*) de que exista una unión anatómica de materia blanca entre dos puntos cualesquiera de interés (Behrens y col., 2003a; Behrens y col., 2003b; Parker and Alexander, 2003); y iii) algoritmos de propagación de frentes de ondas, los cuales expresan el trazado de la trayectoria de las fibras en términos de un frente de onda que emana del punto inicial y cuya velocidad de expansión depende de los datos de difusión (Parker y col., 2002; Staempfli y col., 2006; Tournier y col., 2003), en dependencia de la velocidad espacial del frente, a cada voxel cerebral es asignado un valor de tiempo, que puede interpretarse como el tiempo necesario que demora el frente para llegar desde el voxel fuente hasta cualquier voxel de interés, mientras que el camino de conexión queda establecido por aquella ruta que minimice el tiempo de arribo del frente de onda.

Pero aún cuando el trazado de la trayectoria de las fibras nerviosas permite hacer una evaluación de la integridad de las fibras pertenecientes a tractos específicos, e incluso, hacer comparaciones locales de medidas asociadas,

nuestra comprensión de la conectividad anatómica cerebral queda restringida a la comprensión de sus características anatómicas locales. Consideramos entonces que los estudios en el marco de las neuroimágenes de la difusión podrían ir mucho más allá y emplear las trayectorias estimadas de las fibras para caracterizar cuantitativamente las conexiones anatómicas entre diferentes regiones de materia gris, permitiendo no sólo describir conexiones específicas sino también evaluar las relaciones entre ellas y sus potencialidades para gestionar e integrar el flujo de información neural. Esto permitiría consecuentemente evaluar daños provocados por aquellos desórdenes o patologías cerebrales que alteran las conexiones nerviosas entre los diferentes centros de procesamiento de la actividad neural.

En particular, el uso de la teoría de grafos, cuyo surgimiento se inspira en las soluciones que en el siglo XVI Euler brindara al problema de encontrar el camino optimo para cruzar siete puentes de un río, permitiría la modelación de las conexiones cerebrales desde el punto de vista de nodos y arcos que representen todas las posibles conexiones entre las diferentes regiones anatómicas y funcionales. Este tipo de enfoque, intuitivamente muy simple pues condensa el complejo sistema de conexiones cerebrales a sólo un conjunto de puntos y líneas en el espacio, permitiría además caracterizar el patrón de las conexiones según un compendio de herramientas y medidas topológicas físicamente interpretables que han sido desarrolladas en las últimas décadas, bajo el albor de la teoría de grafos, para el análisis cuantitativo de las redes sociales y biológicas (Albert y col., 1999; Bassett and Bullmore, 2006a; Milos y col., 2002; Salvador y col., 2005a).

1.1. PROBLEMA CIENTÍFICO

Las metodologías actuales basadas en técnicas de las neuroimágenes de la difusión no permiten de forma directa: cuantificar las conexiones anatómicas entre regiones cerebrales de interés, caracterizar la red estructural asociada, según su capacidad para lidiar con el flujo de información neural, y evaluar las afectaciones estructurales provocadas por condiciones patológicas.

1.2. HIPÓTESIS

La combinación de las técnicas basadas en neuroimágenes de la difusión con elementos de la teoría de grafos permite la estimación de las conexiones anatómicas cerebrales, la caracterización de la red estructural asociada, según su capacidad para lidiar con el flujo de información neural, y la evaluación de las afectaciones provocadas por condiciones patológicas.

1.3. OBJETIVO GENERAL

Desarrollar una metodología, sobre el marco de las técnicas basadas en neuroimágenes de la difusión y la teoría de grafos, que permita estimar las conexiones anatómicas cerebrales, caracterizar la red estructural asociada, según su capacidad para lidiar con el flujo de información neural, y evaluar las afectaciones provocadas por condiciones patológicas.

1.3.1. OBJETIVOS ESPECÍFICOS

1. Evaluar la conectividad anatómica entre diferentes regiones cerebrales a partir de la reconstrucción de las trayectorias de las fibras nerviosas.
2. Caracterizar topológicamente la red anatómica cerebral de humanos típicos o sanos.
3. Estimar si existen diferencias interhemisféricas en las redes anatómicas en cuanto a la eficiencia y optimización estructural para lidiar con el flujo de información neural.
4. Evaluar la capacidad de las propiedades topológicas de la red anatómica cerebral para discriminar automáticamente una condición cerebral patológica.

1.3.2. TAREAS A CUMPLIR SEGÚN LOS OBJETIVOS ESPECÍFICOS

Relacionadas al objetivo 1:

1.1 Desarrollar un algoritmo que permita trazar la trayectoria de las fibras nerviosas entre diferentes estructuras cerebrales de interés.

1.2 Explorar en datos simulados y experimentales el comportamiento del algoritmo anterior, así como comparar su comportamiento con el de otros algoritmos propuestos anteriormente en la literatura.

1.3 Definir medidas geométricas para cuantificar las conexiones anatómicas entre diferentes estructuras de la materia gris, que pueden ser delimitadas de acuerdo a criterios histológicos, citoarquitectónicos o funcionales, a través de segmentaciones manuales, automáticas o semiautomáticas.

1.4 Explorar en datos simulados el comportamiento de las medidas definidas anteriormente para evaluar la conectividad entre estructuras de la materia gris, así como evaluar si son capaces de reflejar pérdidas hipotéticas de la integridad en la materia blanca.

1.5 Aplicar los métodos anteriores para calcular mapas de conectividad anatómica entre diferentes estructuras de la materia gris correspondientes a varios sujetos humanos sanos.

Relacionadas al objetivo 2:

2.1 Reconstruir la red estructural del cerebro humano sano a partir de los mapas de conectividad anatómica obtenidos entre las diferentes estructuras de la materia gris.

2.2 Evaluar medidas topológicas que describan las características intrínsecas de la red estructural del cerebro humano sano, teniendo en cuenta la disponibilidad local y global para el manejo e integración del flujo de información neural.

Relacionadas al objetivo 3:

3.1 Reconstruir la red estructural de los hemisferios izquierdo y derecho (para sujetos humanos y un primate no-humano) a partir de los mapas de conectividad anatómica obtenidos entre las diferentes estructuras de la materia gris, según diferentes métodos de trazado de las trayectorias de fibras nerviosas.

3.2 Evaluar e interpretar, para cada especie, medidas topológicas que describan las semejanzas y diferencias entre sus hemisferios cerebrales,

teniendo en cuenta la disponibilidad local y global para el manejo e integración del flujo de información neural.

Relacionadas al objetivo 4:

4.1 Reconstruir la red estructural del cerebro de ratones portadores de una mutación que provoca una sintomatología equivalente a la esclerosis múltiple en humanos (a los que nos referiremos como ratones temblorosos, del inglés *Shiverers*) y controles de igual rango de edad, a partir de los mapas de conectividad anatómica obtenidos entre las diferentes estructuras de la materia gris, según diferentes métodos de trazado de las trayectorias de fibras nerviosas.

4.2 Clasificar, según las características topológicas de las redes anatómicas individuales, a cada ratón de la muestra como sujeto patológico o sujeto control, obteniendo para ello un valor de probabilidad de pertenecer a un grupo u otro como índice individual de clasificación anatómica.

1.4. APORTE CIENTÍFICO

Los principales aportes científicos de esta tesis son:

- Empleo de elementos de la teoría de grafos para, a partir de neuroimágenes de la difusión, reconstruir las trayectorias de las fibras nerviosas entre diferentes regiones de interés y definir medidas cuantitativas para caracterizar las conexiones anatómicas en cuanto a: probabilidad, densidad y fuerza de conexión. Este enfoque no se ha utilizado con anterioridad para evaluar la conectividad anatómica.

- Reconstrucción de la red anatómica del cerebro humano (en 20 sujetos saludables) a partir de los mapas de conectividad anatómica obtenidos entre las diferentes estructuras de la materia gris, y evaluación de medidas topológicas sobre las redes pesadas obtenidas, teniendo en cuanta características instrínsecas como grado de clusterización, distancias característica entre regiones, eficiencia, optimización y motivos estructurales. Este tipo de análisis sólo se ha realizado antes para un sujeto saludable, reportándose sólo una medida de optimización de la red obtenida.

- Comparación de los dos hemisferios cerebrales (en humanos y primates no-humanos saludables) teniendo en cuenta las características topológicas de sus correspondientes redes anatómicas pesadas, en cuanto a semejanzas y diferencias en la disponibilidad local y global para el manejo e integración del flujo de información neural.

- Empleo de parámetros topológicos elementales de la red anatómica cerebral pesada para discriminar una condición cerebral anómala, específicamente el caso del ratón mutante Shiverer, o tembloroso, modelo animal empleado en el estudio de enfermedades desmilienizantes como la esclerosis múltiple y la encefalomielitis aguda diseminada.

2. DESCRIPCIÓN DE LOS ARTÍCULOS

2.1. EVALUACIÓN DE LA CONECTIVIDAD ANATÓMICA ENTRE DIFERENTES REGIONES CEREBRALES A PARTIR DE LA RECONSTRUCCIÓN DE LAS TRAYECTORIAS DE FIBRAS NERVIOSAS

Alrededor de un 60 % del volumen cerebral está compuesto por agua que difunde continuamente, debido al movimiento caótico de sus moléculas, entre los diferentes tejidos cerebrales. Pero la movilidad de estas moléculas de agua no siempre es la misma en todas las direcciones, depende de las características locales de los tejidos, que representan en sí mismos barreras estructurales y permiten en menor o mayor medida los procesos difusivos. Por ejemplo, el movimiento de las moléculas de agua en el líquido cefalorraquídeo[1] tiende a ser igual en todas las direcciones espaciales, o isotrópico, dado que no existen barreras que interfieran ante la movilidad de las moléculas; en cambio, el movimiento de las moléculas de agua alrededor de los axones de la materia blanca[2] tiende a ser mucho mayor en una sola dirección, o anisotrópico, pues las moléculas chocan contra las paredes de los axones y prácticamente pueden moverse sólo en la dirección paralela a ellos.

---

[1] Líquido de color transparente que baña el cerebro y la médula espinal, y sirve de vehículo para transportar nutrientes o desechos mientras compensa los cambios en el volumen de sangre intracraneal.

[2] Los axones conducen la información nerviosa de un grupo de neuronas a otro organizados en arreglos paralelos de entre 50 y 100 axones, a los que se les llama tractos de fibras nerviosas.

En 1994, Basser y colaboradores propusieron describir los procesos de difusión entre los diferentes tejidos cerebrales empleando un ente matemático conocido como *tensor de difusión* (Basser y col., 1994), que podría ser estimado a partir de las neuroimágenes de la difusión. El tensor de difusión es, básicamente, una matriz de 3 x 3 elementos, donde cada elemento refleja el grado de difusión en alguna dirección espacial, digamos por ejemplo, en los ejes coordenados *x*, *y, z,* o en direcciones intermedias a estos. El tensor de difusión suele ser representado geométricamente como un elipsoide, de forma tal que cuando el medio donde difunde el agua es aproximadamente isotrópico, como es el caso del líquido cefalorraquídeo, la forma geométrica del tensor de difusión es cercana a una esfera, donde sus tres semiejes principales son aproximadamente iguales (Figura 2.1a), indicando que la difusión molecular es similar en todas las direcciones. En cambio, cuando el medio es altamente anisotrópico, el caso de los axones de materia blanca, la forma del tensor es achatada, con un semieje notablemente mayor que los otros dos (Figura 2.1b), lo que refleja que la difusión ocurre con mayor facilidad en una dirección, aquella paralela a los axones de materia blanca.

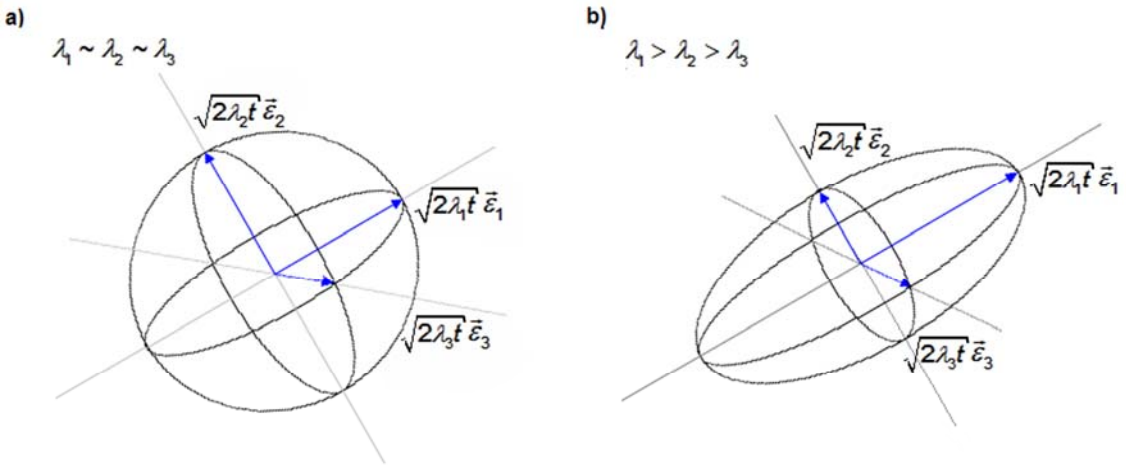

Figura 2.1. Se muestran los elipsoides correspondientes a tensores de difusión en medios a) aproximadamente isotrópicos, b) altamente anisotrópicos. Note como en el caso isotrópico, los tres semiejes del tensor (las líneas con saetas azules, orientadas en el sentido de los vectores $\vec{\varepsilon}_1$, $\vec{\varepsilon}_2$ y $\vec{\varepsilon}_3$, de longitudes $\sqrt{2\lambda_1 t}$, $\sqrt{2\lambda_2 t}$ y $\sqrt{2\lambda_3 t}$, respectivamente) son de similar longitud, reflejando que los procesos difusivos ocurren por igual en todas las direcciones; mientras, en el

caso anisotrópico, uno de los semiejes (aquel orientado en el sentido del vector $\vec{\varepsilon}_1$, y de longitud $\sqrt{2\lambda_1 t}$) es de considerable mayor longitud que los otros dos, indicando que la difusión ocurre con preferencia en esa dirección, pues en las otras (orientadas según $\vec{\varepsilon}_2$ y $\vec{\varepsilon}_3$, de longitudes $\sqrt{2\lambda_2 t}$ y $\sqrt{2\lambda_3 t}$, respectivamente) existen barreras que restringen el movimiento de las moléculas de agua. En esta figura, las longitudes de los semiejes de cada tensor ($\sqrt{2\lambda_1 t}$, $\sqrt{2\lambda_2 t}$ y $\sqrt{2\lambda_3 t}$, respectivamente) representan los desplazamientos cuadráticos medios de las moléculas de agua en un tiempo t.

A partir de los años 90 del siglo pasado las neuroimágenes de la difusión comenzaron a ser muy utilizadas para estimar los tensores de difusión en cada voxel del volumen cerebral. En el Anexo A se describe matemáticamente cómo estimar los tensores de difusión, tal como propusieron Basser y colaboradores (Basser y col., 1994), a partir de una secuencia de neuroimágenes de la difusión. El interés creciente que se ha despertado por esta modalidad de las neuroimágenes, radica en que al obtenerse los tensores de difusión no sólo es posible conocer cómo son los procesos difusivos en cada voxel, permitiendo inferir ante qué tipo de tejido nos encontramos (materia blanca, líquido cefalorraquídeo, materia gris), sino también, y más importante aún, deducir características geométricas y estructurales de los tejidos, en dependencia de la forma que poseen los tensores correspondientes. Por ejemplo, cuando se analiza un voxel perteneciente a la materia blanca, el elipsoide que representa al tensor de difusión asociado suele ser achatado, tal como se muestra en la Figura 2.1b. Como se recordará, el semieje mayor de este elipsoide se orienta en la dirección en que ocurre la mayor difusión, que a su vez puede coincidir con la dirección paralela a los axones de materia blanca. Entonces suele considerarse que el semieje mayor del tensor de difusión, en un voxel ubicado en la materia blanca, indica la dirección media de las fibras nerviosas en este voxel. Esta información pronto comenzó a ser utilizada, al seguirse como si fueran las huellas que dejan las rutas de los axones, para trazar las trayectorias

que presentan las fibras nerviosas al conectar las diferentes regiones de materia gris.

Al procedimiento de reconstruir o poner de manifiesto la trayectoria que presentan las fibras nerviosas a partir de la información que brindan las neuroimágenes de la difusión, se le conoce como tractografía, y ha representado un paso de avance en la descripción *in vivo* de la anatomía cerebral, contribuyendo significativamente a la comprensión de los procesos de integración anatomo-funcional (Koch y col., 2002; LeBihan D. y col., 2001; Ramnani y col., 2004; Sotero y col., 2007; Sporns y col., 2005). Sin embargo, desde la propuesta del primer algoritmo de tractografía hasta hoy, han surgido muchas variantes que tratan de superar las limitaciones propias de cada algoritmo anterior, así como de aprovechar mejor la información contenida en las neuroimágenes de la difusión para alcanzar una representación anatómica más realista. En el Anexo B de esta tesis se describen algunos de los algoritmos más empleados en el trazado de la trayectoria de las fibras nerviosas. Sin dudas, las múltiples formas en que estos han sido diseñados reflejan aspectos elementales a tenerse en cuenta al implementar la tractografía. Pero tal vez el más significativo de dichos aspectos, y que a su vez marca la diferencia esencial entre todos los algoritmos, lo constituye la selección adecuada, en cada voxel, de una dirección de avance que se aproxime lo más posible a la orientación real de las fibras nerviosas, siendo determinante la función o estrategia que se utilice. De esto depende la solución que se le dé a configuraciones complejas en la estructura local de la materia blanca, como pueden ser los cruces, dobleces o abanicamientos de fibras.

En este sentido, los datos de difusión presentan importantes limitaciones intrínsecas, dos de las más importantes son: (i) no permiten dilucidar el sentido de aferencia o eferencia de las fibras, debido a que aunque permiten saber en qué direcciones difunden las moléculas de agua, no brindan información sobre el sentido en que ocurre esta difusión para una dirección dada, por lo tanto al trazar la trayectoria de una fibra no sabemos si lo hacemos a favor o en contra

del sentido en que esta fibra conduce los impulsos nerviosos; (ii) existen múltiples configuraciones para las que puede obtenerse una misma señal de RMN ponderada en difusión. En la Figura 2.2 se presentan tres configuraciones distintas en las que se involucran varios tractos de materia blanca, y para los tres puede obtenerse similar señal de RMN, siendo hasta el momento imposible dilucidar en qué forma estos tractos se cruzan, doblan o abanican, sea cual sea el modelo de descripción intravoxel de orientación de las fibras que se utilice.

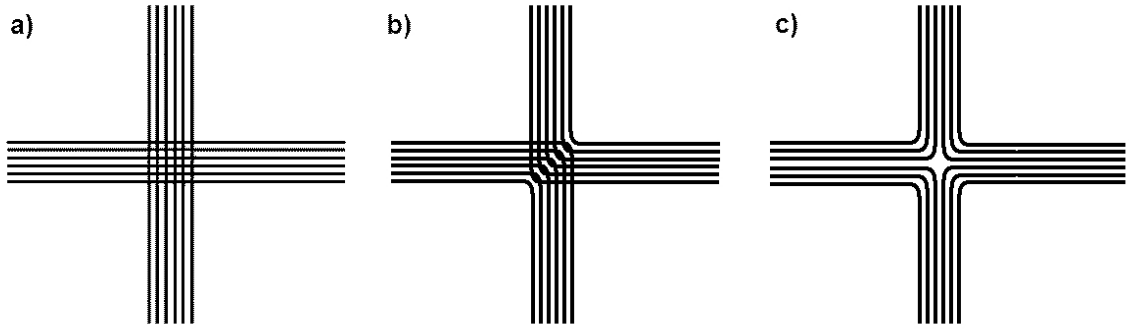

Figura 2.2. Posibles configuraciones de fibras nerviosas: a) cruce perpendicular de dos conjuntos de fibras paralelas; b) dobles en una misma región de dos tractos; c) dobles en una misma región de cuatro tractos. Otras múltiples configuraciones pueden corresponder a los mismos datos de difusión que se obtienen ante estos tres casos.

Una alternativa que pudiera ser idónea para lidiar con la situación de incertidumbre anterior, o con otras más complejas que pueden llegar a existir, es descartar el menor número de configuraciones posibles, es decir, diseñar métodos de tractografía que por su flexibilidad permitan considerar y evaluar la mayor cantidad de trayectorias anatómicas posibles. En tal caso, tiene más sentido tratar los métodos de tractografía con un enfoque probabilista, en el cual se considere numéricamente la incertidumbre que se tiene sobre la configuración real de las fibras en cada punto del cerebro y se utilice dicha incertidumbre para evaluar y decidir sobre una ruta de conexión dada según su validez ante el universo de todas las rutas posibles de fibras nerviosas. Más

concretamente, ¿cómo se podría hacer esto?: supongamos que primero pudiéramos computar un índice que exprese la concordancia de cada camino de fibra hipotético con la información que ofrecen los datos de difusión, o, en otras palabras, qué se pudiera cuantificar qué tanta incertidumbre o seguridad hay sobre las direcciones de las fibras nerviosas a lo largo de un camino de fibra considerado; luego, si pudiéramos evaluar este índice para todos los caminos de fibras posibles en el cerebro, entonces podríamos escoger aquel que resulta más válido, o de menor incertidumbre asociada, metodología que nos permitiría además considerar esa incertidumbre asociada como una medida de conectividad anatómica "optimizada" entre dos voxeles cualesquiera del cerebro.

En el Artículo 1, se introduce un método de tractografía diseñado para descartar el menor número de configuraciones de fibras posibles a la vez que exprese de forma cuantitativa la conectividad anatómica entre dos puntos cerebrales de interés. En este, para encontrar la ruta de conexión entre dos voxeles a través de la materia blanca, se propone analizar el espacio de todas las trayectorias discretas posibles entre ellos, arribando finalmente al camino que maximice la conectividad anatómica según el modelo planteado, basándonos en las facilidades que presenta la teoría de grafos para realizar tal tipo de definiciones. Otro punto que se tiene en cuenta, según la metodología presentada en el Artículo 1, y que permite formular directamente la teoría de grafos, es la caracterización de las conexiones anatómicas entre diferentes estructuras de materia gris. Aunque en estudios anteriores (Behrens y col., 2003a; Koch y col., 2002; Parker y col., 2002; Parker y col., 2003; Staempfli y col., 2006; Tuch D.S, 2002), se ha empleado la probabilidad frecuentista de conexión o una métrica de conectividad anatómica entre sólo dos voxeles, la generalización de esos conceptos entre regiones anatómicas que poseen cientos de voxeles no es inmediata. Un trabajo nuestro anterior, que no forma parte de estas tesis (Iturria-Medina y col., 2005b), propuso cuantificar la fuerza de conexión entre dos estructuras anatómicas a partir de la información geométrica de los caminos probabilísticos obtenidos entre estas estructuras. En este se definía la fuerza de conexión de manera proporcional al área que sobre la superficie de las

estructuras ocupan los caminos de fibras nerviosas calculados. Una matriz de conectividad estimada empleando dicha formulación fue utilizada para acoplar varias áreas cerebrales en un modelo de masa para la generación del EEG, obteniéndose resultados fisiológicamente correctos (Sotero y col., 2007).

Específicamente, en el Artículo 1 se emplea la teoría de grafos al introducir, por primera vez, un modelo grafo de conectividad anatómica cerebral. En un primer paso, (i) los voxeles del volumen cerebral son considerados nodos de un grafo pesado no-direccional, en el cual el peso de cada arco que conecta dos nodos contiguos se asigna según la probabilidad de que ambos nodos se encuentren conectados por fibras nerviosas. Dicha probabilidad se estima considerando tanto las segmentaciones probabilistas de tejidos de una imagen anatómica de resonancia magnética (por ejemplo, de una imagen ponderada en T1) como una función, denominada *función orientacional de las fibras nerviosas* (ODF, del inglés *Orientational Distribuction Function*), que expresa en cada voxel la probabilidad de encontrar un fibra nerviosa en cualquier dirección del espacio y que es estimada a partir de las señales de RMN ponderadas en difusión. Se propone entonces un nuevo algoritmo de tractografía, el cual resuelve el problema del camino más probable entre dos puntos de interés sobre el grafo definido, y además permite obtener mapas probabilísticos de conectividad anatómica entre los diferentes voxeles del volumen cerebral. En un segundo paso, con el objetivo de estimar las conexiones anatómicas entre K estructuras de materia gris, (ii) el grafo cerebral inicial es tratado como un grafo K+1 partito, para ello se particiona el conjunto de nodos inicial en K subconjuntos no solapados de materia gris y un subconjunto que reúne a los nodos restantes (aquellos que pertenecen a la materia blanca o al líquido cefalorraquídeo). Basado en dicho grafo multipartito, se definen tres medidas de conectividad entre estructuras: Fuerza de Conexión Anatómica (ACS), Densidad de Conexión Anatómica (ACD) y Probabilidad de Conexión Anatómica (ACP). ACS es una medida del flujo potencial de información entre cualquier par de regiones, considerando que dicho flujo es proporcional a la cantidad de fibras nerviosas conectoras. DCA es una medida de la fracción del área externa de las regiones

que se encuentra conectada con respecto al área externa total de ambas, es, por ende, una medida que intenta corregir ACS según el tamaño de las regiones involucradas en la conexión. Por último, ACP es una medida de la probabilidad de conexión, al menos por una fibra nerviosa, entre cada par de regiones. Esta refleja, por tanto, si dos regiones de interés se pueden encontrar vinculadas funcionalmente de forma directa, sin tener en cuenta las características geométricas (fuerza, densidad) de la conexión.

La metodología propuesta es evaluada en datos artificiales y reales. En ambos casos, los resultados muestran que las trayectorias de las fibras fueron correctamente reconstruidas entre las regiones de interés. Además, son presentados los mapas medios de ACS, ACD y ACP entre 71 estructuras de la materia gris, para 5 sujetos saludables. Un análisis de correlaciones entre los mapas individuales de conectividad muestra similaridades significativas entre los diferentes sujetos, lo que apoya la hipótesis de que individuos sanos deben presentar patrones similares de conectividad.

2.2. CARACTERIZACIÓN TOPOLÓGICA DE LA RED ANATÓMICA CEREBRAL DE HUMANOS SANOS

Casi de forma paralela al interés creciente en las técnicas basadas en neuroimágenes de la difusión, ocurrió en la comunidad científica el nacimiento de una nueva rama de las neurociencias que no tardó en esparcirse: el análisis topológico de las *redes complejas cerebrales*. En este tipo de análisis, el cerebro es modelado como una red compleja compuesta por *nodos* (puntos en el espacio) que representan regiones anatómicas o funcionales, y *arcos* (líneas que unen a los nodos) que representan las correspondientes conexiones anatómicas o funcionales. Luego se evalúan un conjunto de medidas topológicas que pueden ser interpretadas en términos de la disposición cerebral intrínseca, local o global, para el manejo e integración de la información neural.

Los primeros estudios en el campo de las redes complejas cerebrales (Hilgetag and Kaiser, 2004; Sporns and Zwi, 2004), se enfocaron básicamente en describir los atributos de *mundo-pequeño* (o *small-world*, en inglés) que presenta la red de las conexiones anatómicas en algunas especies de mamíferos como gatos y monos. El concepto de *mundo-pequeño*, surgió del análisis de las redes sociales y se asocia a una alta capacidad para intercambiar y procesar información a la vez que se mantiene un bajo costo de conexiones necesarias (Albert y col., 1999; Watts, 1999; Watts and Strogatz, 1998). Traducido al ámbito de la estructura cerebral a nivel macroscópico, aquel correspondiente al de las conexiones entre áreas anatómica o funcionalmente segregadas, estaría revelando una alta capacidad para el procesamiento local y global de la información a expensas de un costo anatómico relativamente bajo (Bassett and Bullmore, 2006b).

Para realizar los estudios anteriores, donde se revelaría la alta optimización estructural de las redes definidas por las conexiones anatómicas cerebrales de

determinados mamíferos (Hilgetag and Kaiser, 2004; Sporns and Zwi, 2004), se había empleado sólo información de conectividad anatómica adquirida *post mortem* a través de técnicas invasivas (básicamente trazadores radiactivos). Dichas técnicas invasivas no han sido aplicadas a igual escala en humanos, debido principalmente a las implicaciones éticas de tales procedimientos, y a las limitaciones intrínsecas de las metodologías basadas en trazadores radiactivos para estudiar un cerebro de mayor tamaño y complejidad que el de las otras especies mencionadas. Luego, la insuficiente información de conectividad anatómica cerebral reportada para humanos no permitía la caracterización de la red compleja definida por sus conexiones cerebrales. Sin embargo, ya en el año 2006 se emplearon técnicas basadas en neuroimágenes de la difusión para crear el primer mapa de conexiones anatómicas posibles entre pequeñas regiones que cubrían toda la materia gris de un humano sano (Hagmann y col., 2006). Para ello se trazaron las trayectorias de fibras que unían a las regiones de materia gris, y se consideró que cada región era representada por un nodo y que dos nodos cualesquiera (o regiones) estaban unidos por un arco si existía entre ellos una conexión de materia blanca, según las trayectorias de fibras reconstruidas. Los resultados de dicho estudio, basados principalmente en el análisis de algunas propiedades básicas de la red compleja obtenida, apoyaron el punto de vista de que el cerebro humano, a semejanza del de otras especies de mamíferos, está optimizado estructuralmente para lograr un elevado procesamiento local y global de la información, con un bajo costo de conexiones necesarias, cumpliendo con el principio de *mundo-pequeño*. Pero, a pesar de su originalidad y relevancia científica, este estudio presentó algunas limitaciones metodológicas notables, como el empleo de un solo sujeto, el análisis de sólo algunas pocas propiedades topológicas de la red, y la aproximación de esta red a un formato binario en el que se desprecia el peso o la evidencia numérica sobre la existencia de las conexiones estimadas (asumiendo que todas tienen igual valor).

A continuación, He y colaboradores (2007) propusieron estudiar patrones de conectividad reflejados en los cambios concurrentes en el grosor cortical de diferentes estructuras corticales (He y col., 2007). Dicho estudio se basó en la hipótesis de que dos regiones conectadas anatómicamente presentan características similares en cuanto al tipo de tejido que poseen, pues deben procesar información similar, y por ello debe esperarse que algunas de sus características geométricas se modifiquen de forma concurrente (por ejemplo el grosor cortical, que se asocia al ancho de las capas que componen las columnas corticales y subsecuentemente a la cantidad de neuronas contenidas en estas). Las cortezas cerebrales de 124 sujetos saludables fueron divididas en 54 estructuras típicas, definidas antes de acuerdo a criterios anatómicos y funcionales, y entonces dos estructuras cualesquiera fueron consideradas conectadas si existía una correlación significativa en la manera en que variaban sus grosores corticales a lo largo de todos los sujetos. Los resultados que se obtuvieron apoyaron también la hipótesis de que el cerebro humano está organizado estructuralmente siguiendo los principios de *mundo-pequeño*, así como también siguiendo otros atributos que implican una alta optimización, pero no podrían ser resultados concluyentes al respecto porque, entre otras causas, la metodología empleada no permitió incluir estructuras subcorticales internas, como los tálamos o las amígdalas, las cuales mantienen conexiones elementales con la corteza cerebral. No fue posible además obtener la red correspondiente a cada sujeto sino sólo una red global representando a toda la muestra, que a su vez, como en el estudio de Hagmann y colaboradores, fue analizada también sin considerar el peso o la evidencia numérica sobre la existencia de las conexiones estimadas.

En el Artículo 2, se continúa la caracterización de la red compleja constituida por las conexiones anatómicas en el cerebro humano. Para ello se extienden los trabajos pioneros de Hagmann y He anteriormente mencionados en varios puntos: 1) en lugar de crear una red binaria, se construye y analiza una versión pesada, donde el peso de cada conexión es asignado según la Probabilidad de

Conexión Anatómica (ACP) entre los pares de regiones consideradas, medida definida con anterioridad en el Artículo 1, que expresa la probabilidad de que dos regiones cualesquiera estén conectadas por al menos una fibra nerviosa; 2) se mapean las conexiones entre 90 estructuras corticales y subcorticales, cubriendo toda la materia gris de 20 humanos saludables, seleccionadas de acuerdo a criterios anatómicos y funcionales (Tzourio-Mazoyer y col., 2002); 3) además de evaluar atributos de *mundo-pequeño* y *grado de la distribución*, reportadas en los dos estudios anteriores, otras medidas topológicas de las redes son evaluadas, como *eficiencia*, *vulnerabilidad*, *centralidad nodal* y *composición de motivos estructurales*. En la Figura 2.3 se ilustra de forma general el procedimiento empleado para la reconstrucción de las redes anatómicas.

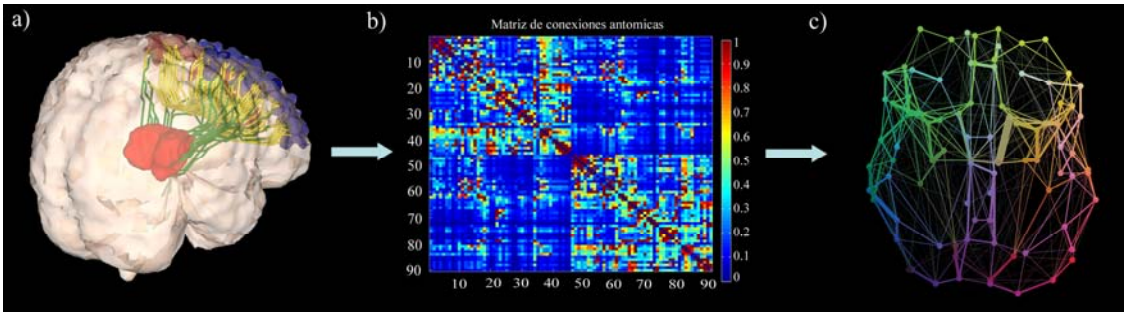

Figura 2.3. Reconstrucción de la red anatómica cerebral. a) Primeramente se estiman las trayectorias de las fibras nerviosas que conectan las diferentes regiones anatómicas (de acuerdo al algoritmo presentado en el Artículo 1), en este caso se muestran las trayectorias obtenidas entre los tálamos y los giros frontales superiores. b) Se crea una matriz donde el elemento correspondiente a la fila *i* y a la columna *j* expresa la probabilidad de que exista conexión entre las regiones *i* y *j* (según la medida PCA definida también en el Artículo 1), en este caso se muestra una matriz de conectividad entre 90 estructuras anatómicas. c) Finalmente la red pesada se crea definiendo un punto (nodo) en el espacio por cada región anatómica considerada y enlazando este a través de líneas (arcos) a aquellas regiones con las que se encuentra conectado por trayectorias de fibras nerviosas, siendo el grosor de cada línea proporcional al peso (probabilidad o densidad) de la conexión que representa.

Los resultados mostraron que la red anatómica obtenida para cada sujeto presenta los atributos de *mundo-pequeño*, con poca variabilidad entre los sujetos. Esto apoya el punto de vista de que el atributo de *mundo-pequeño* es una propiedad común de las redes anatómicas cerebrales correspondientes a los seres humanos sanos. También se comprobó, a través de la medida *grado de la distribución,* que la posibilidad de que una región específica esté conectada con un número creciente de otras regiones disminuye a medida que aumenta el número de regiones, comportamiento conocido como de *escala-amplia* (o *broad-scale*, en inglés). El comportamiento de *escala-amplia* encontrado sugiere un límite relativamente bajo en la cantidad de conexiones anatómicas que puede mantener cualquier región cerebral. Este resultado presenta cierta analogía con la conducta descrita para las redes de amigos, en las que si una persona tratara de incrementar constantemente su número de amigos tendería también a descuidar la calidad de las relaciones con ellos, por lo que de forma intuitiva prefiere mantener un número limitado de amistades iniciales o de restablecer prioridades entre estas y quienes va conociendo.

El análisis de *eficiencia* reveló que las redes obtenidas presentan menor eficiencia global y mayor eficiencia local que sus redes aleatorias equivalentes (aquellas que presentan igual cantidad de conexiones pero distribuidas aleatoriamente). Este hallazgo coincidió con lo observado, en el mismo estudio, para las redes cerebrales de gatos y macacos, así como con lo reportado previamente para redes funcionales en humanos creadas a partir de imágenes funcionales de RMN (Achard and Bullmore, 2007). Aunque no existe un consenso sobre su significado, pudiera estar indicando que el cerebro ha evolucionado tratando de mantener una eficiencia local alta, lo que es equivalente a priorizar el intercambio entre regiones que procesan similar información neural, mientras que a la vez optimiza el costo de los procesos de integración al garantizar sólo una eficiencia global intermedia, pues no es necesario el intercambio de información entre todas las regiones cerebrales.

Por otro lado, a partir del análisis de *vulnerabilidad* se identificaron aquellas regiones que hacen más frágil a la red anatómica cerebral (putamens, precuneus, ínsulas, parietales y frontales superiores), las cuales al ser eliminadas o afectadas causarían mayor pérdida en la capacidad general para el intercambio de información, análisis este de singular importancia para llegar a comprender cómo actúan determinadas enfermedades asociadas a cambios estructurales específicos. Curiosamente, también se encontraron unas pocas regiones (temporales superiores, supramarginales, pallidiums, helchs, cerebelos) que de ser eliminadas no provocarían una disminución en la capacidad general para intercambiar información, sino lo contrario, es decir, de no existir estas regiones las condiciones arquitectónicas cerebrales serían más óptimas para el intercambio de información. Pero, ¿implica esto que tenemos regiones neuronales de más?, ¿no va en contra de la arraigada idea de que la naturaleza se organiza siempre según el principio de mínima energía? Recordemos que hasta ahora sólo hablamos de la red estructural básica y no de las funciones que en sí cada región anatómica-funcional desempeña. Por tanto, dichas regiones de vulnerabilidad negativa pudieran estar siendo conservadas a lo largo de los procesos evolutivos porque desempeñan funciones específicas insustituibles, justificándose su presencia pese al alto costo anatómico que implican.

2.3. COMPARACIÓN, EN HUMANOS Y UN PRIMATE NO-HUMANO, DE LAS REDES ANATÓMICAS DEL HEMISFERIO DERECHO E IZQUIERDO EN CUANTO A EFICIENCIA Y OPTIMIZACIÓN ESTRUCTURAL PARA LIDEAR CON EL FLUJO DE INFORMACIÓN NEURAL

La *simetría* es considerada una de las componentes indispensables de perfección y belleza. Sin embargo, tal vez para reafirmarnos lo vano de aspirar a lo perfecto, ninguna de las formas presentes en la naturaleza es en realidad simétrica. Por el contrario, los conceptos de *simetría* y *asimetría*, complementarios entre sí, parecen estar siempre en pugna continua por un escalón dominante. Incluso nuestro cerebro, cuyo mayor atributo es la complejidad, y es constituido por dos hemisferios aparentemente iguales, no pudo escapar a esta lucha y revela cada vez más su carácter asimétrico. En 1861, el investigador francés Paul Broca realizó la primera descripción detallada de asimetría funcional en el cerebro humano. Este encontró una lesión post-mortem en el hemisferio izquierdo de un paciente que había presentado serias dificultades para hablar y consecuentemente Broca infirió que las habilidades para el lenguaje estaban lateralizadas (Broca, 1861). Alrededor de una década después Carl Wernicke, de origen polaco, reportó que el daño a una zona específica del hemisferio izquierdo podría causar también una seria afectación en la comprensión del lenguaje (Wernicke, 1874). Estos fueron los hechos iniciales que comenzarían la fascinante e inconclusa historia por revelar los misterios de la asimetría cerebral.

En el capítulo anterior de esta tesis hemos validado la propuesta realizada en el capítulo 1 de caracterizar la red de conexiones anatómicas cerebrales mediante la combinación de neuroimágenes de la difusión con elementos de la teoría de grafos. El próximo paso investigativo que nos ocupa y se presenta en el Artículo

3, tal y como sucede en la ciencia que discurre desde la ciencia básica hacia la aplicada, va entonces en el sentido de su utilización práctica. En un primer intento de abordaje de un problema práctico, se aplica la metodología descrita al tema de las asimetrías cerebrales comentado anteriormente. Resulta atractivo este tópico ya que con antelación, desde Broca y Wernicke hasta nuestros días, sólo se han explorado las asimetrías estructurales entre aquellas regiones que soportan funciones conocidas como muy lateralizadas (por ejemplo el lenguaje). Es decir, la investigación precedente se ha limitado a parear las conocidas lateralizaciones funcionales con su correspondiente asimetría en las conexiones de sustancia blanca entre las regiones que soportan esa función. Sin embargo, nosotros tenemos la posibilidad de caracterizar las asimetrías considerando no sólo regiones específicas, sino incluyendo a todo el hemisferio cerebral y su compleja red de conexiones. Además, la caracterización en términos de la teoría de grafo nos brindaría información no sólo en términos anatómicos, sino también en el sentido más general y fisiológico del manejo e integración del flujo de información neural.

Para lograr ese objetivo, se construyeron las redes cerebrales de cada hemisferio cerebral por separado. Se desprecian por lo tanto aquellas regiones comunes como el cuerpo calloso, el cual no está lateralizado ya que en sí su estructura consiste en el cruce de los axones desde un hemisferio cerebral a otro. La comparación numérica de las propiedades globales de estas redes hemisféricas muestran, tanto para un grupo de humanos sanos como para un primate-no humano, a un hemisferio derecho más interconectado y eficiente que el izquierdo. Además, en términos de la indispensabilidad de cada región cerebral en específico para el funcionamiento de la red global, se muestra a través de un índice de lateralización que el hemisferio izquierdo cuenta con más regiones consideradas como muy indispensables para el funcionamiento de la red como un todo. Estos dos resultados están en correspondencia con los conocidos hechos de que el hemisferio derecho tiene un rol principal en aquellos procesos más generales como las tareas de integración, mientras que el

hemisferio izquierdo tiene un rol principal en aquellos procesos específicos altamente demandantes como el lenguaje o las tareas motoras, que puedan requerir redes especializadas dedicadas a ellos. Resumiendo, el empleo de nuestra metodología basada en neuroimágenes de la difusión y teoría de grafos ha contribuido a proponer una posible explicación sobre el hecho de cuáles pueden ser las posibles ventajas evolutivas que confiere un cerebro lateralizado, algo en lo que hasta ahora no existe consenso. Por último vale destacar que, entre las salidas prácticas, en este artículo por primera vez se expone una explicación al por qué de la ocurrencia de fenómenos neuropsicológicos luego de lesión en determinadas regiones cerebrales en un hemisferio cerebral sí y en otro no.

2.4. DISCRIMINACIÓN AUTOMÁTICA DE UNA CONDICIÓN CEREBRAL PATOLÓGICA TENIENDO EN CUENTA LAS PROPIEDADES TOPOLÓGICAS DE LA RED ANATÓMICA CEREBRAL

Para un diagnóstico clínico se requiere por lo general de la intervención de un experto con cuyo criterio se discierna el casi siempre confuso límite entre lo normal y lo atípico. Sin embargo, muchas veces la tarea del experto se dificulta ante determinada patología cuyos efectos pueden ser: i) desconocidos, por la ausencia de literatura previa relacionada, o ii) poco evidenciables a simple vista, debido a complejidades asociadas a la observación objetiva de la anomalía correspondiente. Esta difícil situación ocurre con frecuencia ante muchas patologías neurológicas, como en el caso de la Esclerosis Múltiple o la Enfermedad de Alzheimer, donde un comportamiento determinado del sujeto y la evaluación de variables cognitivas relacionadas inducen a considerar la presencia o agravamiento de alguna patología específica, pero no es posible confirmar las sospechas debido a la falta de evidencia estructural sobre afectaciones concretas a los tejidos que suelen ser modificados por esa patología. En el caso específico de la enfermedad de Alzheimer, el diagnóstico definitivo sólo se alcanza mediante una biopsia cerebral, que pocas veces se realiza, debido al desbalance entre coste-beneficio (es muy invasiva). El diagnóstico queda por tanto en un punto de incertidumbre intermedio, donde, pese a la falta de evidencia científica suele arriesgarse un tratamiento clínico, en ocasiones para no dejar de hacer “algo”, cuya efectividad queda a merced de la futura mejora o empeoramiento del paciente.

Serían de gran ayuda entonces herramientas que contribuyan a hacer el diagnóstico por sí solas o al menos a mejorar significativamente al diagnóstico del especialista. Pero, siendo objetivos, ¿podría una de estas herramientas decirnos cuantitativamente si un sujeto ha dejado de ser saludable, o si empeora o progresa ante un determinado tratamiento clínico? El anhelo de contar con tales herramientas se refleja desde hace años en la comunidad científica a

través de la búsqueda de *biomarcadores*: características que son evaluadas y medidas como indicadores de procesos biológicos normales, procesos patológicos o respuestas farmacológicas, con el fin de contribuir a la intervención terapéutica [http://www.fnih.org/work/key-initiatives/biomarkers-consortium]. Pero, específicamente, ¿cómo pueden contribuir las neuroimágenes a la creación de biomarcadores asociados a patologías cerebrales?, y, en el caso de las neuroimágenes basadas en RMN, como ya habíamos visto en la introducción de esta tesis, ¿se tendría la ventaja de crear biomarcadores *no invasivos,* con una interpretación cualitativa y cuantitativa a la vez?

La creación de un biomarcador no es trivial, pues requiere de una amplia validación, donde este debe resultar capaz, con relativa independencia del especialista que lo aplique, de manifestar distintos aspectos de cada patología o estado de salud para el que ha sido diseñado. Su creación es, por tanto, un propósito ambicioso que sólo pocas veces se consuma luego de la definición inicial de una herramienta, la exploración preliminar de sus resultados, y la posterior validación más amplia y rigurosa en una muestra representativa. Por ejemplo, en el caso de la Esclerosis Múltiple, anomalía cerebral que provoca afectaciones estructurales ubicadas con frecuencia en la materia blanca, muchas de las herramientas de diagnóstico tradicionales, como los criterios de McDonald (McDonald y col., 2001), requieren de parámetros subjetivos que pueden variar en dependencia del experto que realiza el análisis, entre ellos el número de lesiones que se exige en la imagen de RMN ponderada en T2 para confirmar luego el diagnóstico. Por tanto, pese al uso extendido que tienen para la evaluación de la Esclerosis Múltiple, estos criterios de diagnóstico tradicionales, como los de McDonald, no podrían ser considerados biomarcadores, pues están aún lejos de ser una herramienta objetiva que aporte medidas cuantitativas e interpretables sobre las afectaciones provocadas por la enfermedad (Filippi and Agosta, 2010). Sin embargo, en los últimos años han ido desarrollándose un conjunto de modalidades neuroimagenológicas no convencionales, como las neuroimágenes de espectroscopía, las técnicas

funcionales de RMN, o las mismas neuroimágenes de la difusión, que han contribuido a perfeccionar algunas de las limitaciones propias de las neuroimágenes clásicas y de las que se podría esperar por tanto una contribución considerable en la creación de herramientas objetivas para el diagnóstico clínico.

En el Artículo 4, tratamos de colaborar con la creación de herramientas que permitan evaluar la integridad de los tejidos cerebrales con el propósito de clasificar cuantitativamente a los individuos en sujetos normales o patológicos. Para ello, partimos de la hipótesis de que cambios en las propiedades topológicas de la red estructural, definida por el conjunto de las conexiones anatómicas cerebrales, reflejan el estadío individual provocado por determinada anomalía cerebral. Las neuroimágenes de la difusión y la información que estas contienen son, nuevamente, la piedra angular sobre la cual nos basamos para evaluar nuestra hipótesis, proponiendo investigar posibles cambios topógicos en las redes anatómicas cerebrales provocados por una anomalía donde la materia blanca es afectada con severidad. Específicamente, exploramos alteraciones en seis parámetros topológicos básicos de las redes anatómicas estimadas para ratones temblorosos, un modelo animal de enfermedades que afectan la mielina de los axones, y ratones controles de similar rango de edad. Los parámetros evaluados (grado de *clusterización, longitud del camino medio, modularidad, eficiencia global/local y grado de mundo-pequeño*) son escogidos por sus facultades para reflejar la cantidad de información neural que puede ser intercambiada en los cerebros analizados y qué tan optimizadamente pueden ser estos procesos.

En un primer análisis, comprobamos que las redes anatómicas cerebrales de los ratones controles son significativamente más agrupadas o clusterizadas, compuestas por módulos básicos, eficientes y optimizadas que las de los ratones temblorosos, los cuales presentaron un camino medio incrementado entre regiones. Estos resultados concuerdan con los reportados para estudios funcionales y anatómicos asociados a patologías específicas en humanos, en

específico con aquellos estudios que han hallado una red cerebral más desorganizada e ineficiente en la Esclerosis Múltiple (He y col., 2009), la esquizofrenia (Micheloyannis y col., 2006; Rubinov y col., 2009), el Alzheimer (Chun-Yi Lo y col., 2010; Stam y col., 2007), y el accidente vascular encefálico (Crofts and Higham, 2009; Wang y col., 2010).

Luego, ya evidenciada una diferencia considerable entre las características topológicas de las redes cerebrales de los sujetos patológicos y normales, se pasó entonces a clasificar a cada sujeto según sus características individuales. Para ello se introdujo el concepto de *representación espacial de una medida de red* (*Network Measure Spatial Representation*, en inglés), en el cual para cada medida topológica de las seis consideradas, cada sujeto es representado y determinado en el espacio por un punto único cuyas coordenadas dependen de los valores individuales obtenidos para esta medida. Entonces, se emplearon técnicas de clasificación para subdividir el espacio original de representación de cada medida en dos subespacios, separando así en dos grupos a los sujetos que presentaron similares características topológicas (hipotéticamente, en un grupo deberían estar los sujetos patológicos y en el otro los sujetos controles), y obteniendo a la par un valor de probabilidad individual de pertenecer a un grupo u a otro, como un clasificador anatómico.

Para cuatro de las seis medidas topológicas consideradas se obtuvieron valores de predicción patológica elevados, entre 91.6 y 100 %, lo cual, al observar además las correctas subdivisiones obtenidas para los espacios de representación de cada medida, sostiene nuestra hipótesis de que las propiedades topológicas de la red estructural definida por el conjunto de las conexiones anatómicas cerebrales reflejan el estadío individual provocado por determinada anomalía cerebral. Pese a que requiere aún de una profunda validación, la metodología propuesta tiene aplicaciones clínicas potenciales, pues aporta nuevos elementos a la comprensión de las propiedades topológicas cerebrales en cuanto a su relación con el diagnóstico clínico, la discriminación

de estadíos patológicos y la futura obtención de biomarcadores interpretables basados en las técnicas de RMN.

3. ARTÍCULOS

3.1. ARTÍCULO 1

Yasser Iturria-Medina, E. J. Canales-Rodríguez, L. Melie-García, P. A. Valdés-Hernández, Martínez-Montes, E., Alemán-Gómez, A., and Bornot, J. M., 2007. Characterizing Brain Anatomical Connections using Diffusion Weighted MRI and Graph Theory. Neuroimage, 36, 645-660.

ELSEVIER

NeuroImage

www.elsevier.com/locate/ynimg
NeuroImage 36 (2007) 645–660

Characterizing brain anatomical connections using diffusion weighted MRI and graph theory

Y. Iturria-Medina,[a,*] E.J. Canales-Rodríguez,[a] L. Melie-García,[a] P.A. Valdés-Hernández,[a] E. Martínez-Montes,[b] Y. Alemán-Gómez,[a] and J.M. Sánchez-Bornot[b]

[a]*Neuroimaging Department, Cuban Neuroscience Center, Avenue 25, Esq 158, #15202, PO Box 6412, Cubanacán, Playa, Havana, Cuba*
[b]*Neurostatistic Department, Cuban Neuroscience Center, Havana, Cuba*

Received 24 July 2006; revised 1 February 2007; accepted 6 February 2007
Available online 15 February 2007

A new methodology based on Diffusion Weighted Magnetic Resonance Imaging (DW-MRI) and Graph Theory is presented for characterizing the anatomical connections between brain gray matter areas. In a first step, brain voxels are modeled as nodes of a non-directed graph in which the weight of an arc linking two neighbor nodes is assumed to be proportional to the probability of being connected by nervous fibers. This probability is estimated by means of probabilistic tissue segmentation and intravoxel white matter orientational distribution function, obtained from anatomical MRI and DW-MRI, respectively. A new tractography algorithm for finding white matter routes is also introduced. This algorithm solves the most probable path problem between any two nodes, leading to the assessment of probabilistic brain anatomical connection maps. In a second step, for assessing anatomical connectivity between K gray matter structures, the previous graph is redefined as a K+1 partite graph by partitioning the initial nodes set in K non-overlapped gray matter subsets and one subset clustering the remaining nodes. Three different measures are proposed for quantifying anatomical connections between any pair of gray matter subsets: Anatomical Connection Strength (ACS), Anatomical Connection Density (ACD) and Anatomical Connection Probability (ACP). This methodology was applied to both artificial and actual human data. Results show that nervous fiber pathways between some regions of interest were reconstructed correctly. Additionally, mean connectivity maps of ACS, ACD and ACP between 71 gray matter structures for five healthy subjects are presented.

Keywords: Brain connectivity; Diffusion weighted magnetic resonance imaging; Graph model; Tractography

Introduction

Random motion of water molecules inside the brain is influenced by the architectural properties of tissues. Water diffusion is known to be highly anisotropic in certain white matter regions, with preferential movement along the nervous fibers. A recent development of a non-invasive technique which quantifies water diffusion process, known as Diffusion Weighted Magnetic Resonance Imaging (DW-MRI), has allowed to obtain structural information about the intravoxel axon arrangement (Basser et al., 1994; LeBihan, 2003). Based on this information, fiber tractography arises as a crucial technique to attain a better in vivo anatomical characterization of the brain (Mori et al., 1999; Conturo et al., 1999; Tuch, 2002; Parker et al., 2002; Koch et al., 2002; Behrens et al., 2003). Also, quantification of the anatomical connectivity between different gray matter structures would be a significant contribution to the understanding of functional integration of the human brain (LeBihan et al., 2001; Koch et al., 2002; Ramnani et al., 2004; Sporns et al., 2005; Sotero et al., 2007).

Reconstruction of nervous fiber trajectories is an extensively treated topic. In the traditional Streamline Tractography (SLT) approach (Mori et al., 1999; Conturo et al., 1999; Basser et al., 2000), a continuous trajectory is traced tangential to the direction of the principal eigenvector of the diffusion tensor measured at each voxel using a discretization step smaller than the size of the voxel. This approach usually fails in voxels where fibers cross each other, merge, kiss or diverge, and it is very sensitive to the influence of MR signal noise (Basser and Pajevic, 2000; Lori et al., 2002). In those situations, traced path strays from the real trajectory of nervous fibers. To overcome these limitations, modified Streamline Tractography (mSLT) methods based on Diffusion Tensor Deflection (Weinstein et al., 1999; Lazar et al., 2003) and Probabilistic Monte-Carlo Method (Parker and Alexander, 2003) have been proposed. The former uses the entire diffusion tensor to deflect the propagation direction computed in the previous step. The latter uses the uncertainty of the estimated nervous fiber orientation to compute a large number of possible paths from the seed point; a quantity can be assigned to each path reflecting some connectivity relationship between seed and target points.

In recent years, many other mSLT methods have been proposed (Tuch, 2002; Tench et al., 2002; Behrens et al., 2003; Hagmann et al., 2003). Usually, they define the anatomical connection pro-

* Corresponding author. Fax: +53 7 208 6707.
E-mail address: iturria@cneuro.edu.cu (Y. Iturria-Medina).
Available online on ScienceDirect (www.sciencedirect.com).

1053-8119/$ - see front matter © 2007 Elsevier Inc. All rights reserved.
doi:10.1016/j.neuroimage.2007.02.012

bability between seed and target voxels as the ratio between the number of shared paths and the number of generated paths.

In contrast to SLT and mSLT methods, Level Set-Based Fast Marching (FM) techniques (Parker et al., 2002; Staempfli et al., 2006) express the tractography in terms of a wave front that emanates from a source point and whose evolution is controlled by the diffusion data. FM methods have two advantages over the SLT and mSLT methods: 1, better performance in situations of branching and fiber crossing, and 2, direct estimation of the probability of white matter connectivity between two points (Jun Zhang et al., 2005).

In FM methods, front evolution speed and direction in a voxel depend on the measured diffusion tensor. Generally, all proposed FM algorithms have used only the principal eigenvector of the diffusion tensor, therefore these methods fail to reconstruct fiber pathways in those places where fibers cross, merge, kiss or diverge. For dealing with this limitation, recently Staempfli et al. (2006) proposed an advanced implementation of FM (aFM), combining the advantages of classical FM and the tensor deflection approach. The objective is to take into account the entire information contained in the diffusion tensor. As an intrinsic limitation, aFM needs an empirical threshold value to classify geometrically the diffusion tensor ellipsoid (i.e. prolate, oblate or spherical tensor) and therefore to set the corresponding speed function. Also, only four possible situations of voxel transitions are considered, which are those involving prolate and oblate cases. Thus, some combinations of more than two fibers crossing may be ignored.

On the other hand, although probability of connection between seed and target voxels has been previously used (Tuch, 2002; Parker et al., 2002; Koch et al., 2002; Parker et al., 2003; Behrens et al., 2003; Staempfli et al., 2006), the generalization of this concept to characterize anatomical connections between different brain gray matter structures is not straightforward. An initial approach (Iturria-Medina et al., 2005) was proposed to quantify the anatomical connection strength (ACS) between two gray matter structures using geometrical information from probabilistic fiber paths. ACS was considered proportional to the total area comprised by the fiber connector volume over the surfaces of the two connected structures. This was evaluated by counting the number of superficial voxels involved in the connection, where each voxel is weighted according to the validity of the paths that connect it with the second structure. A connectivity matrix estimated using the aforementioned approach was employed to couple several brain areas in a realistic neural mass model for the EEG generation, obtaining physiologically plausible results (Sotero et al., 2007).

In addition, recently Hagmann et al. (2006) proposed a technique based on graph theory to study the connectivity between small cortical areas. Nodes of a graph correspond to small cubic regions of interest (ROI) covering the brain gray matter. Fiber tractography is performed by initiating fibers over the whole brain and arc weight between any two ROIs is assigned according to the connection density between them. An unweighted version of this graph was constructed in order to analyze its small world and hierarchical properties.

In this work, our interest lies in the development of a DW-MRI-based methodology, capable of characterizing directly anatomical connections between brain gray matter structures, which can be defined according to cytoarchitectonic, histological or other sort of anatomical and functional information. In order to accomplish this, the graph framework is employed to introduce a new anatomical connectivity model. Firstly, each voxel of the cerebral volume is assumed to be a node of a non-directed weighted graph. In this case, the weight of an arc is considered to be proportional to the probability of the existence of a nervous fiber connecting its corresponding nodes. Probabilistic tissue segmentation and intravoxel white matter orientational distribution function (ODF) are combined to compute the arc weight. Secondly, an iterative algorithm is used to solve the most probable path problem between any two nodes in the graph, which we will indistinctly refer to as the most reliable connection route between these nodes. This approach allows to asses probabilistic anatomical connectivity maps between brain voxels. Finally, in order to assessing anatomical connectivity between K gray matter structures, the graph is partitioned in the corresponding K non-overlapped subsets and one subset containing the remaining nodes. This allowed for the definition of three different anatomical connectivity measures between any pair of gray matter structures: Anatomical Connection Strength (ACS), Anatomical Connection Density (ACD) and Anatomical Connection Probability (ACP).

Methods

This section will be devoted to present some basic elements of graph theory, as well as the principal steps of the proposed methodology: 1, definition of a Brain Graph, 2, introduction of an iterative fiber tracking algorithm and quantification of node–node connectivity and 3, definition of anatomical connectivity measures between gray matter areas. Details on experimental data to be used and its preprocessing will also appear.

Elements of graph theory

A graph $G=[N,A]$ is defined by a set N of n elements called nodes and a set A of elements called arcs (Gondran and Minoux, 1984). Arcs link pairs of nodes. The number of elements of a set N is known as the cardinality of N and it is denoted by $|N|$. Given an arc $a_{i,j}$ linking r_i and r_j nodes ($i, j=1,\ldots,n$), we will refer to r_i as the initial endpoint and to r_j as the terminal endpoint of $a_{i,j}$. A non-directed graph is that in which the direction of the arcs (i.e. distinction between initial and terminal nodes) is not established. Graphically, nodes are represented by points and arcs by lines (without arrow) joining them.

A graph $G=[N,A]$ is called K partite if the set of its n nodes admits a partition into K pairwise disjoint independent subsets (see Fig. 1). A path $\rho_{i_1\ldots iL}$, with $L-1$ steps, between nodes r_{i_1} and r_{i_L} is an ordered subset of $L-1$ arcs $\{a_{i_1i_2}; a_{i_2i_3};\ldots; a_{i_{L-1}i_L}\}$.

Each arc $a\in A$ is assigned a number $w(a)\in\mathcal{R}$, denominated the weight of the arc. A very large number of path finding problems in graph theory use the weight of the arc to optimize convenient cost functions. For example, if the weight of an arc is defined as its length, the problem of the shortest path between two nodes is equivalent to find the path with the minimum sum of its arc weights. Similarly, the weight of the arc can be interpreted as the cost of transportation along it, the time required to pass through it or the probability of its existence. Specifically, in a weighted non-directed graph, where each arc weight is considered as the probability of its existence, the problem of searching the most probable path between nodes r_{i_1} and r_{i_L} is equivalent to find the path $\rho_{i_1\ldots iL}$ with maximum total probability:

$$P[\rho_{i_1\ldots i_L}] = w(a_{i_1i_2}) \prod_{k=2}^{L-1} w^{\mathrm{cond}}(a_{i_ki_{k+1}}|a_{i_{k-1}i_k}), \quad (1)$$

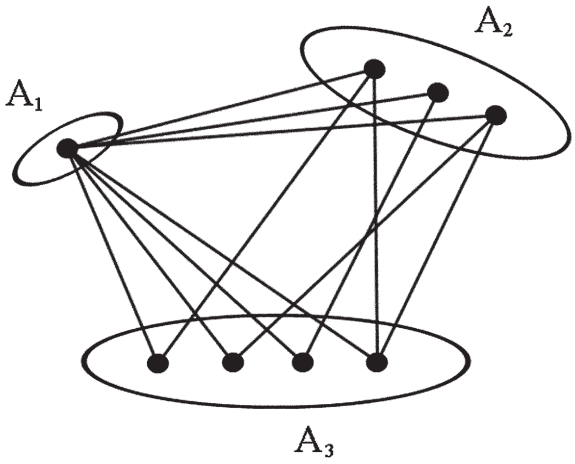

Fig. 1. Schematic representation of a multi partite graph (specifically, a tripartite graph). An initial graph of 8 nodes is partitioned in three disjoint independent node subsets, A1, A2 and A3, with 1, 3 and 4 nodes, respectively.

where the term $w^{\text{cond}}\left(a_{i_k i_{k+1}} | a_{i_{k-1} i_k}\right)$ is the conditional weight of the arc $a_{i_k i_{k+1}}$ given arc $a_{i_{k-1} i_k}$.

Defining a brain graph

Consider an orthogonal grid defining voxels $\{\vec{r}_i=(x_i,y_i,z_i); i=1..n\}$ in the space of a magnetic resonance image (or other neuroimaging technique) with anatomical information about the brain (e.g. a T1-weighted image or a Computer Tomography image). Let N be the set of voxels having a non-zero probability of belonging to some cerebral tissue. Then, we define as a Brain Graph the weighted non-directed graph $G_{\text{brain}}=[N,A]$ where A is the set of white matter links between contiguous voxels in N. Graphically, G_{brain} is a discrete set of points (nodes) representing voxels and a set of lines (arcs) representing connections between contiguous voxels (see Fig. 2a).

The weight of an arc is chosen so that it represents the probability that linked nodes are really connected by nervous fibers. A nearest neighborhood of the i-th node, denoted as N_i^{neig}, is the set of all its contiguous nodes. In our orthogonal grid, the maximum cardinality of N_i^{neig} is 26.

In the present approach, arc weight $w(a_{ij})$ $(a_{ij}\in A)$ is proposed to take into account both the probability of nodes $\vec{r}_i$ and $\vec{r}_j$ to belong to gray/white matter and the probability of nervous fibers to be oriented around the direction of the arc a_{ij}. Mathematically:

$$\begin{aligned} w(a_{ij}) &\equiv w(a_{ji}) \\ &= P_{\text{mat}}(\vec{r}_i) P_{\text{mat}}(\vec{r}_j)\left[P_{\text{diff}}(\vec{r}_i,\Delta\vec{r}_{ij}) + P_{\text{diff}}(\vec{r}_j,\Delta\vec{r}_{ji})\right], \end{aligned} \tag{2}$$

where the two basics functions P_{mat} and P_{diff} enclose anatomical and diffusion information respectively (Fig. 2b). The first of these functions is defined as follows:

$$P_{\text{mat}}(\vec{r}) = \frac{\alpha P_{\text{WM}}(\vec{r}) + P_{\text{GM}}(\vec{r})}{1+(\alpha-1)P_{\text{WM}}(\vec{r})}, \tag{3}$$

where P_{WM} and P_{GM} are probabilistic maps of white and gray matter (WM and GM) respectively and α is a tuning parameter. As we hope to associate arcs in G_{brain} to probable nervous fiber pathways, the presence of white matter (given by P_{WM}) to arc weights could be enhanced by making $\alpha \geq 1$.

The other function, $P_{\text{diff}}(\vec{r}_j,\Delta\vec{r}_{ij})$, characterizes fiber coherence along $\Delta\vec{r}_{ij}=\vec{r}_j-\vec{r}_i$, which is the direction of the arc a_{ij}, and can be inferred from DW-MRI images using methods for the description of the intravoxel white matter structure. Here, $P_{\text{diff}}(\vec{r}_j,\Delta\vec{r}_{ij})$ is assumed to be the integral of the ODF over a solid angle β around $\Delta\vec{r}_{ij}$ (Fig. 3):

$$P_{\text{diff}}(\vec{r}_i,\Delta\vec{r}_{ij}) = \frac{1}{Z}\int_{\beta} \text{ODF}(\vec{r}_i,\Delta\vec{r}_{ij})\text{d}S. \tag{4}$$

Z is a normalization constant chosen to fix to 0.5 the maximum value of the set $\left\{P_{\text{diff}}(\vec{r}_i,\Delta\vec{r}_{ij})\right\}_{\forall\vec{r}_j\in N_i^{\text{neig}}}$. Note that generally $P_{\text{diff}}(\vec{r}_i,\Delta\vec{r}_{ij}) \neq P_{\text{diff}}(\vec{r}_j,\Delta\vec{r}_{ji})$.

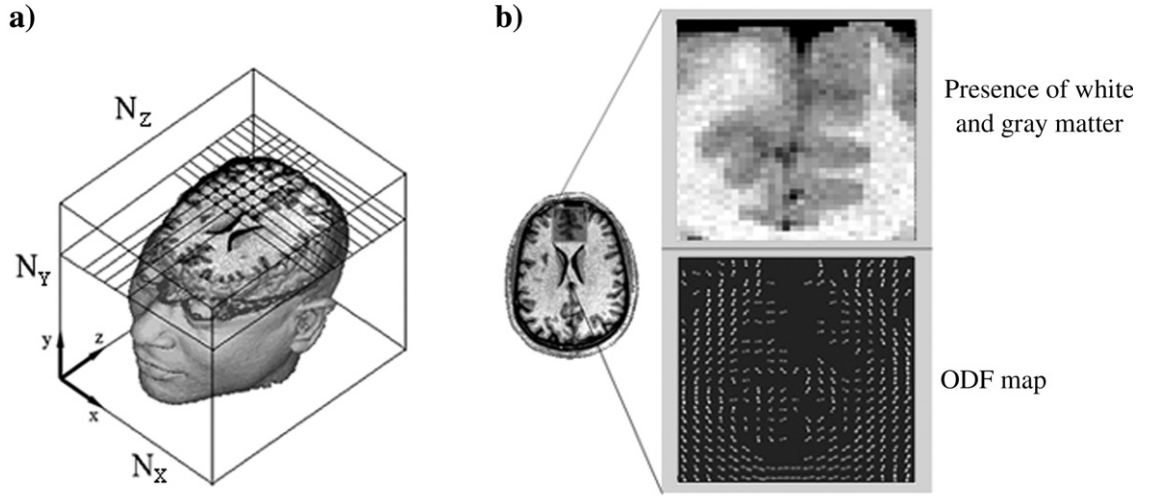

Fig. 2. Basic elements of the non-directed weighted Brain Graph G_{brain}. (a) Each voxel of the T1-weighted image volume (of dimensions N_X, N_Y, $N_Z\in\mathbb{N}$) belonging to the brain tissue is considered a node in G_{brain}. (b) Anatomical information about the presence of white and gray matter and orientational distribution function (ODF) maps are used to define the weights of the arcs in G_{brain}. Each ODF is a 3-D representation of the fiber orientation within a single voxel.

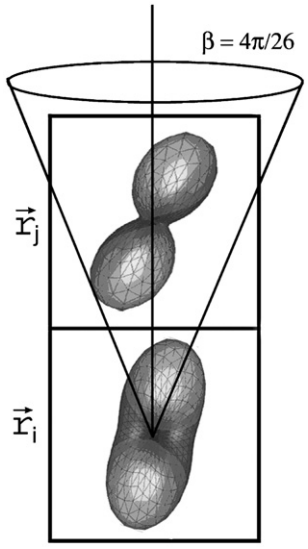

Fig. 3. The solid angle β around vector $\Delta\vec{r}_{ij}$ defines a cone in which the nervous fibers passing from node $\vec{r}_i$ to node $\vec{r}_j$ should be contained. It is defined for all 26 nearest neighbors in the same way.

Eq. (2) quantitatively combines the information of probabilistic tissue segmentation of the brain and diffusion weighted MRI data. This ensures that only those pairs of nodes with high probability of belonging to gray/white matter and high probability of sharing fibers will have higher weights, which is equivalent to have high probability of being connected. It should be kept in mind that the DW-MRI profile is symmetric under the transformation: $\vec{r} \rightarrow -\vec{r}$. This hinders the possibility to distinguish between efferent and afferent projections in a nervous tracking process.

Fiber tracking and node–node connectivity

In this work, the key idea on which fiber tracking and node-node connectivity is based derives from "the most probable path problem" between nodes of interest in the defined Brain Graph. Initially, we assumed that any possible path between these nodes corresponds to the anatomic trajectory of a probable nervous fiber. Then, an iterative algorithm is employed for finding the most probable trajectory, which is considered to evaluate the real existence of fiber pathways between these points.

Considering a given path $\rho_{s\ldots p}$, with L-1 steps, that belongs to the set of all possible paths between nodes $\vec{r}_s$ and $\vec{r}_p$; the weights of any two consecutives arcs $a_{i_{k-1}i_k}$ and $a_{i_k i_{k+1}}$ are not independent, since they share the term $P_{mat}(\vec{r}_{i_k})$. Given the existence of arc $a_{i_{k-1}i_k}$, the conditional weight of arc $a_{i_k i_{k+1}}$ results:

$$w^{cond}(a_{i_k i_{k+1}}|a_{i_{k-1}i_k}) = P_{mat}(\vec{r}_{i_{k+1}})\cdot\left[P_{diff}(\vec{r}_{i_k},\Delta\vec{r}_{i_k i_{k+1}}) + P_{diff}(\vec{r}_{i_{k+1}},\Delta\vec{r}_{i_{k+1}i_k})\right]. \quad (5)$$

In order to consider physiological and anatomical evidences about fiber bundles shape in the brain as a priori information, a modified version of Eq. (1) includes a function ψ which penalizes path curvature, as used in other tracking methods (see for example Tuch, 2002):

$$P[\rho_{s\ldots p}] = w(a_{s,i_2})\prod_{k=2}^{L\text{-}1} w^{cond}(a_{i_k i_{k+1}}|a_{i_{k-1}i_k})\,\Psi(\rho_{i_{k-1}\ldots i_{k+1}}), \quad (6)$$

where

$$\Psi(\rho_{i_{k-1}\ldots i_{k+1}}) = \begin{cases} f(\phi) & \text{if } \phi < \phi_{critical} \\ 0 & \text{otherwise} \end{cases}.$$

The angle ϕ is defined using the two arcs of the subpath $\rho_{i_{k-1}\ldots i_{k+1}}$:

$$\phi = \arccos\left(\frac{\Delta\vec{r}_{i_k i_{k+1}}\Delta\vec{r}_{i_{k-1}i_k}}{\left|\Delta\vec{r}_{i_k i_{k+1}}\right|\left|\Delta\vec{r}_{i_{k-1}i_k}\right|}\right) \quad (7)$$

were $\phi_{critical}$ is a critical threshold curvature angle and $f(\phi)$ is a curvature function. Otherwise stated, in this study we will choose $\phi_{critical}=\pi/2$ and $f(\phi)=1$, which is equivalent to allow only those trajectories with curvature angles smaller than 90°.

In order to illustrate formulation (6), Fig. 4 shows a hypothetical 2D graph. Probability of path ρ_2 is zero because it has a curvature in one of its nodes that exceed the critical angle $\phi_{critical}$, and therefore the path ρ_1 is more reliable than ρ_2.

The estimated nervous fiber trajectory running from $\vec{r}_s$ to $\vec{r}_p$ will be given by the most reliable path:

$$\tilde{\rho}_{s\ldots p} = \underset{\forall_{\rho_{s\ldots p}}}{\operatorname{argmax}}\left(P[\rho_{s\ldots p}]\right). \quad (8)$$

To solve Eq. (8) we propose an iterative algorithm (see Appendix A), which is an adaptation of the Moore and Dijstra algorithm (Dijkstra, 1959; Moore, 1959; Gondran and Minoux,

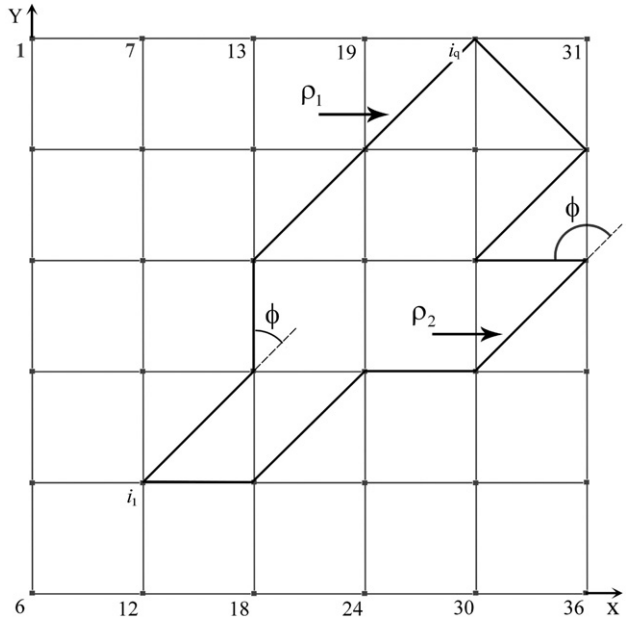

Fig. 4. Hypothetical simple 2D graph. The set of 36 nodes is consecutively enumerated, the nodes i_1=11 and i_q=25 in the figure are linked by two paths $\rho_1(\vec{r}_{i_1},\vec{r}_{i_q})$ and $\rho_2(\vec{r}_{i_1},\vec{r}_{i_q})$. For path $\rho_1(\vec{r}_{i_1},\vec{r}_{i_q}) = \{u(\vec{r}_{i_1},\vec{r}_{i_2}); u(\vec{r}_{i_2},\vec{r}_{i_3}); \ldots; u(\vec{r}_{i_{q-1}},\vec{r}_{i_q})\}$ the sequence of nodes i_1, i_2, … , i_{q-1}, i_q is 11, 16, 15, 20, and 25. For $\rho_2(\vec{r}_{i_1},\vec{r}_{i_q})$ the sequence is: 11, 17, 22, 28, 33, 27, 32 and 25. The probability of path ρ_2 is null, $P[\rho_2\ (r_{i_1}, r_{i_q})]=0$, because this path has a curvature in node 33 that exceeds the critical angle $\phi_{critical}=\frac{\pi}{2}$. In particular $\phi = \arccos\left(\frac{\Delta\vec{r}_{i_5,i_6},\Delta\vec{r}_{i_4,i_5}}{|\Delta\vec{r}_{i_5,i_6}||\Delta\vec{r}_{i_4,i_5}|}\right) = \frac{3\pi}{4}$, where i_4=28, i_5=33 and i_6=27. In this case path ρ_1 is more probable than ρ_2.

1984) to solve the shortest path problem in a graph. The resulting map $M(\vec{r}_s,\vec{r}_p)$ is the probability of the path between nodes $\vec{r}_s$ and $\vec{r}_p$ of maximum reliability, which is the solution of Eq. (8).

In general, the anatomical connectivity between nodes $\vec{r}_s$ and $\vec{r}_p$ can be defined as a function 'g' of the arc weights of $\tilde{\rho}_{s\ldots p}$ and the a priori term $C_{prior}(\vec{r}_s,\vec{r}_p)$:

$$C_{node}(\vec{r}_s,\vec{r}_p) = g\big(w(a_{s\ i_2}),\ldots,\ w(a_{i_{L-1}p}),\ C_{prior}(\vec{r}_s,\vec{r}_p)\big), \tag{9}$$

$C_{prior}(\vec{r}_s,\vec{r}_p)$ represents the a priori information about the connectivity between nodes $\vec{r}_s$ and $\vec{r}_p$, which could come from histological tracing methods or other neuroimaging techniques (e.g. fMRI, EEG/MEG tomography, PET, etc.). When there is not prior information available, $C_{prior}(\vec{r}_s,\vec{r}_p)$ may be a non-informative prior or not evaluated at all, as will be the case in this work.

A straightforward definition of the function 'g' could be $M(\vec{r}_s,\vec{r}_p)$. However, this measure decreases strongly with the path longitude, stating a high contrast in connectivity values between pairs of near and distant nodes. In this work, similarly to Parker et al. (2002) and Staempfli et al. (2006), the anatomical connectivity measure is defined as the lowest weight of the arcs belonging to the most probable path, i.e. 'g' is the minimum function and equation (9) becomes:

$$C_{node}(\vec{r}_s,\vec{r}_p) = \min_{\forall a\in\tilde{\rho}_{s\ldots p}}(w(a)). \tag{10}$$

Zone-zone connectivity

In the graph framework presented here, the evaluation of connectivity between clusters of nodes in G_{brain} will be used for defining of connectivity measures between brain anatomical areas.

Let the graph $G_{brain}=[N,A]$ be redefined as a $K+1$ partite undirected graph where the nodes set N is partitioned in K non-overlapped gray matter subsets N_k, $k=1,\ldots,K$, and one subset N_{rest} clustering all voxels not belonging to brain gray matter (i.e. cerebral spinal fluid and white matter). The K gray matter clusters represent the anatomical areas, denoted by $A_1,\ldots,A_K$. Generally those areas are segmented based upon cytoarchitectonic, histological or other sort of anatomic and functional information (e.g. Broadmann areas) through manual, automatic or semi automatic procedures.

In this context the arcs are defined directly between nodes of different areas. The term $a_{ij}(\vec{r}_m,\vec{r}_n)$ represents the arc that links node $\vec{r}_m\in N_i$ with node $\vec{r}_n\in N_j$. The weight of this arc $\omega\big(a_{ij}(\vec{r}_m,\vec{r}_n)\big)$ will be a function of the node–node connectivity measure defined previously by Eq. (10). This can be expressed in general by the following formula:

$$\omega\big(a_{ij}(\vec{r}_m,\vec{r}_n)\big) = h\big(C_{node}(\vec{r}_m,\vec{r}_n),\ P_i(\vec{r}_m),\ P_j(\vec{r}_n)\big). \tag{11}$$

This expression also includes the uncertainty of each node $\vec{r}_s\in N_{\bar{k}}$ to be a member of its anatomical area $\bar{k}$ through a probability term $P_{\bar{k}}(\vec{r}_s)$. This probability comes from a Maximum Probability Segmentation Map (Mazziotta et al., 1995), which means that $P_{\bar{k}}(\vec{r}_s) = \max_{k=1..K}(P_k(\vec{r}_s))$.

Particularly, for the sake of simplicity, we will assume the following expression for the weight of the arc:

$$\omega\big(a_{ij}(\vec{r}_m,\vec{r}_n)\big) = C_{node}(\vec{r}_m,\vec{r}_n)P_i(\vec{r}_m)P_j(\vec{r}_n). \tag{12}$$

Additionally, it is necessary to define a subdivision of each cluster N_k into a boundary nodes set N_k^s and a core nodes set N_k^c, such that $N_k^s\cup N_k^c=N_k$. The boundary nodes set N_k^s comprises those voxels having at least one neighbor that does not belong to N_k. Finally, a general definition for zone–zone connectivity is established as:

$$C_{zone}(A_i,A_j) = t\big(\omega\big(a_{ij}(\vec{r}_m,\vec{r}_n)\big),C_{prior}(A_i,\ A_j)\big) \tag{13}$$

for all $\vec{r}_m\in N_i$ and $\vec{r}_n\in N_j$. Similar as in Eq. (9), the term $C_{prior}(A_i,A_j)$ represents the a priori information about the connection between areas A_i and A_j.

The general zone-zone connectivity measure (13) can be reasonably restricted to white matter connections. This is accomplished by taking into account only connectivity between voxels of the surface of the corresponding anatomical areas, since voxels in the core nodes set N_k^c belong to gray matter and connections to (and among) them are beyond the scope of the present methodology. Based on this, we introduce three different anatomical connectivity measures, namely: Anatomical Connection Strength (ACS), Anatomical Connection Density (ACD) and Anatomical Connection Probability (ACP). Let us explain each in detail:

- ACS is required to be a measure of the potential information flow between the connected areas A_i and A_j. This would be related to the cross sectional area of the fiber bundle connecting the surfaces of the zones, which will give an estimate of the amount of nervous fibers shared by these areas. Therefore, we propose to estimate the ACS by counting the nodes on the surface of A_i and A_j involved in the connection, where each node is weighted by its anatomical connectivity value with the surface of the second zone. The connectivity value of node $\vec{r}_n\in N_j^s$ will be denoted as $\zeta_{\vec{r}_n}\big(0\le\zeta_{\vec{r}_n}\le1\big)$ and defined as the maximum arc weight among all connections between $\vec{r}_n$ and any $\vec{r}_m\in N_i^s$:

$$\zeta_{\vec{r}_n} = \max_{\forall\ \vec{r}_m\in N_i^s}\big(\omega\big(a_{ij}(\vec{r}_n,\vec{r}_m)\big)\big). \tag{14}$$

  Then, the final expression for the ACS reads:

$$C_{Zone}^{ACS}(A_i,A_j) = \sum_{\forall\vec{r}_m\in N_i^s}\zeta_{\vec{r}_m} + \sum_{\forall\vec{r}_n\in N_j^s}\zeta_{\vec{r}_n}, \tag{15}$$

  where we have explicitly written two terms, one quantifying connections of the region A_i with A_j, and the other quantifying connections of the region A_j with A_i.
- ACD is searched as a measure of the fraction of the surface involved in the connection with respect to the total surface of both areas. Thus, it can be estimated as the ACS relative to the number of nodes belonging to the surfaces of A_i and A_j:

$$C_{Zone}^{ACD}(A_i,A_j) = \frac{C_{Zone}^{ACS}(A_i,A_j)}{|N_i^s|+|N_j^s|}. \tag{16}$$

- ACP is searched as a measure of the probability of two areas to be connected at least by a single connection. Then, we define it as the maximum connectivity value between nodes of areas A_i and A_j:

$$C_{Zone}^{ACP}(A_i,A_j) = \max\left(\max_{\forall\vec{r}_m\in N_i^s}\zeta_{\vec{r}_m},\ \max_{\forall\vec{r}_n\in N_j^s}\zeta_{\vec{r}_n}\right). \tag{17}$$

Experimental data

Artificial data

Diffusion tensor phantom simulated data sets were obtained from the Centre for Neuroimaging Sciences, Institute of Psychiatry, King's College London. The DW-MRI data were simulated using a spin-echo sequence with the following parameters: 30 diffusion encoding directions (Jones et al., 1999); $b=1000$ s/mm^2; image resolution $2\times2\times2$ mm^3; TE=160 ms. T2 values for the tract and background were assumed to be the same as white matter (65 ms) and grey matter (95 ms) at 1.5 T, respectively. Three data sets are available with varying levels of SNR (7, 15 and 31).

Three out of ten different tract configurations were selected to evaluate the performance of the proposed methodology (see Fig. 5): straight crossing, curved crossing and the tract inspired in the maple leaf (Feuille trajectory). For each of them, the six diffusion elements, the eigenvectors and the corresponding T2-weighted images for each SNR data set were provided. The corresponding ODF maps were estimated using a simple procedure described in Appendix B. A threshold value was applied to the T2-weighted image in order to create a binary mask (P_{mat}) expressing the presence or not of gray/white matter tissue.

Additionally, two other artificial diffusion data sets were created using the following geometric parameters: $55\times55\times55$ voxels; image resolution $2\times2\times2$ mm^3. The first artificial data set represents a branching fiber tract (Fig. 6a). In branching areas, the first and second eigenvalues of the diffusion tensor were assumed to be equal (i.e. oblate tensor). The second artificial data set represents a fiber crossing of three orthogonal tracts (Fig. 6b). In crossing areas, the three tensor's eigenvalues were assumed to be approximately the same (i.e. spherical tensor). In both configurations, three different SNR (7, 15 and 31) were considered to create the diffusion tensor elements. ODF maps were estimated using the procedure described in Appendix B.

Human data

Using a standard diffusion gradient direction scheme (twelve diffusion-weighted images and a $b=0$ image), DW-MRI data were acquired from 5 healthy subjects using a MRI scanner Siemens Symphony 1.5 T (Erlangen, Germany) and a single shot EPI sequence. To each subject, two interleaved sets of 25 slices of 6 mm thickness with a distance factor of 100% were acquired with the following parameters: $b=1200$ s/mm^2; FOV=256×256 mm^2; acquisition matrix=128×128; corresponding to an 'in plane' spatial resolution of 2×2 mm^2; TE/TR=160 ms/7000 ms. Two interleaved sets were necessary because it was impossible to cover the whole head with a good spatial resolution using a single set due to a pulse sequence limitation (max: 35 slices). Both sets were joined to form a volume of 50 contiguous slices of 3 mm thickness covering the whole brain for each subject. The aforementioned acquisition was repeated 5 times to improve signal to noise ratio (SNR). In order to improve EPI quality, magnitude and phase difference images of a T2 gradient echo field mapping sequence were acquired with TE=7.71 ms and 12.47 ms.

Also, a 3D high resolution T1-weighted image (MPRAGE) covering the whole brain was acquired with the following parameters: 160 contiguous slices of 1 mm thickness in sagittal orientation; in plane FOV=256×256 mm^2, corresponding to an in plane spatial resolution of 1×1 mm^2; TE/TR=3.93 ms/3000 ms.

Although the scanner sequence performs an eddy current automatic correction, in order to remove remaining distortions an affine 3D mutual normalized information-based registration method (Studholme et al., 1998) was used. The DW-MRI images were attempted to be corrected from EPI distortions using the SPM FieldMap toolbox (Hutton et al., 2002).

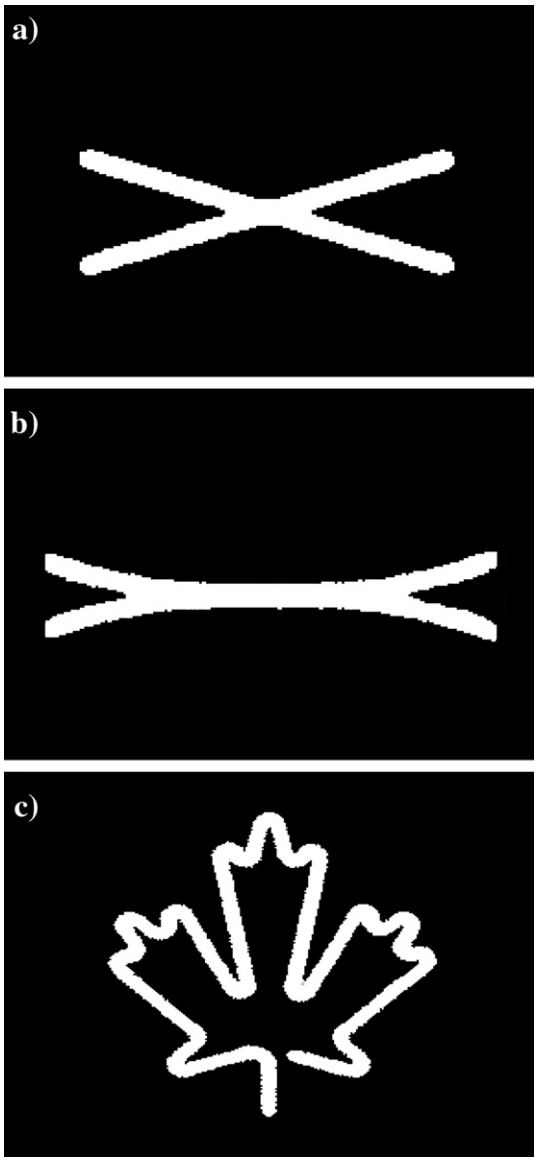

Fig. 5. Phantom tract configurations obtained from the Centre for Neuroimaging Sciences, Institute of Psychiatry, King's College London (http://neurology.iop.kcl.ac.uk/dtidataset/Common_DTI_Dataset.htm). The configurations used in this study were: (a) straight crossing, (b) curve crossing, and (c) tract inspired in the maple leaf (Feuille trajectory).

T1-weighted 3D anatomical image was registered to the $b=0$ image using a normalized mutual information method (Studholme et al., 1998). Using the SPM2 toolbox (available at http://www.fil.ion.ucl.ac.uk/spm/software/spm2), a low dimensional normalization (Ashburner and Friston, 1999) to a stereotaxic space MNI (Evans and Collins, 1993) was estimated for the registered T1-weighted image, which was written with an spatial resolution of $2\times2\times2$ mm^3. Employing the aforementioned transformation, DW-MRI data were fitted to a diffusion tensor (Basser et al., 1994) in each voxel of the stereotaxic space. Tensors were rotated

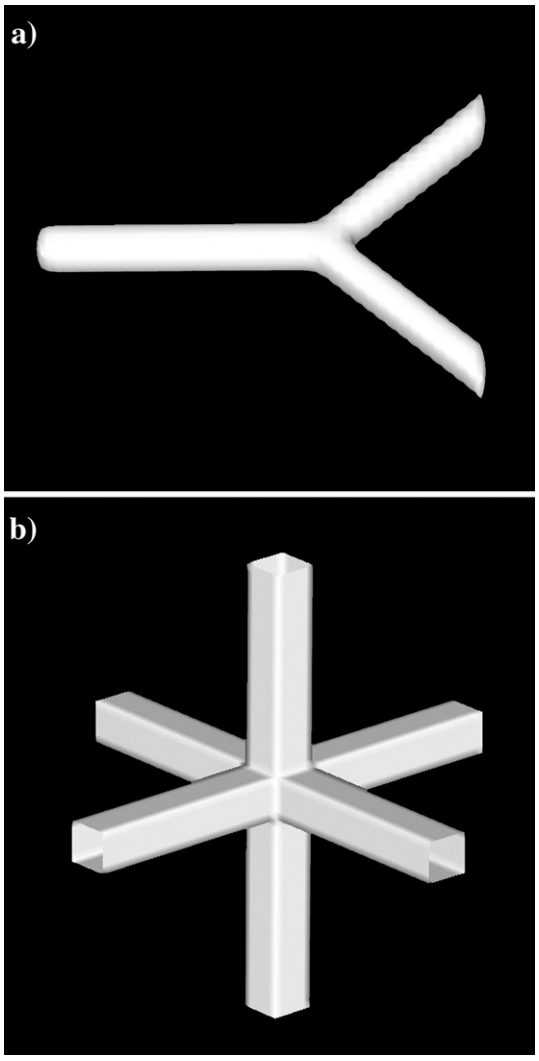

Fig. 6. Additional artificial tract configurations created to explore the performance of the proposed methodology. (a) Branching fiber tract. (b) Fiber crossing of three orthogonal tracts.

according to the method presented by Alexander and coworkers (Alexander et al., 2001).

Probabilistic tissues segmentations of gray matter, white matter and cerebral spinal fluid (Ashburner and Friston, 2000) were obtained from the normalized T1-weigthed image using the SPM2 toolbox. The gray and white matter segmentation probabilistic maps (P_{GM} and P_{WM}, respectively) were used to construct the anatomical information function P_{mat} evaluating Eq. (3), with $\alpha=1$. Also, the normalized T1-weigthed image was automatically segmented into 71 gray matter structures using the IBASPM toolbox (available at http://www.fil.ion.ucl.ac.uk/spm/ext/#IBASPM) (Alemán-Gómez et al., 2006) and the average Probabilistic MRI Atlas created by the Montreal Neurological Institute (Collins et al., 1994; Evans et al., 1994). For evaluating the arcs weight in expression (11), the probability of each voxel $\vec{r}_s \in N_k$ to belong to k-th anatomical area was set to unity ($P_k(\vec{r}_s)=1$), although as it was mentioned in Section 2.4, this probability can be more realistically evaluated employing Maximum Probability Segmentation Maps (Mazziotta et al., 1995). Again, the ODF maps were estimated using the procedure described in Appendix B.

Results

Artificial data

The performance of the proposed methodology was explored using artificial DW-MRI data. Firstly, anatomical connections between different regions of interest (ROIs), defined for the straight crossing, curve crossing and Feuille trajectory were estimated (see Fig. 7). Each ROI consists of seven contiguous voxels representing a line perpendicular to the fiber tract being analyzed. Left column (Figs. 7a, c and e) shows the reconstructed connection routes (most probable paths) between ROI1 and the others, with SNR level of 15. These results illustrate the ability of our method to reconstruct complex fiber tracts configurations (see for example the Feuille trajectory results, Fig. 7e). Complementarily, right column (Figs. 7b, d and f) shows the corresponding maximum voxel–voxel connectivity values with ROI1 (i.e. each voxel of the image volume was assigned its maximum voxel–voxel connectivity value with the voxels of ROI1). Note that, although for the straight crossing and curve crossing the method provides anatomical connection routes between ROI1 and ROI4, the corresponding voxel–voxel connectivity values indicate the low probability of connection between these ROIs, which is in accordance with the characteristics of the tracts configurations. In contrast, the obtained voxel–voxel connectivity values between ROI1–ROI2 and ROI1–ROI3 indicate the high probability of connection between these ROIs.

Secondly, we analyzed the branching configuration shown in Fig. 6a. Both Fig. 8 and Table 1 show the results before and after a hypothetical loss of the white matter integrity. Three different ROIs were defined (Fig. 8a): ROI1 consists of two contiguous voxels at the left end of the fiber tract, ROI2 consists of four contiguous voxels at the upper right end of the tract and ROI3 is conformed by a single voxel at the bottom right end of the tract. For simulating a hypothetical loss of the white matter integrity (hereinafter, WM-affectation, for brevity), the values of two voxels in the binary mask (P_{mat}) were set to zero (each voxel located symmetrically at the upper right tract or at the bottom right tract, see Fig. 8b). Figs. 8c and d correspond to the maximum voxel–voxel connectivity values between the voxels of ROI1 and the rest of voxels before and after the WM-affectation, respectively. Also, Table 1 helps us to understand the interrelationship between the ACS, ACD and ACP measures and their sensitivity to white matter affectation. For example, note that before WM-affectation the C^{ACS}_{Zone} (ROI1, ROI2) is around twice the C^{ACS}_{Zone} (ROI1, ROI3) since the total number of superficial voxels in ROI1 and ROI2 duplicates the total number of superficial voxels in ROI1 and ROI3 (i.e. 6 and 3 voxels, respectively). However, C^{ACD}_{Zone} (ROI1, ROI2) and C^{ACD}_{Zone} (ROI1, ROI3) are similar and the small difference between them can be explained by the different geometrical characteristics of the defined ROIs. In this case, both ROI2 and ROI3 present very high probabilities of connection with ROI1 for all SNR levels. After the WM-affectation, these probabilities of connection as well as the ACS and ACD measures decrease considerably.

Finally, the performance of our model in comparison with SLT and aFM methods was studied in the case of fiber crossing of three orthogonal tracts, as shown in Fig. 9. Starting and ending ROIs were defined as planes of 5×5 voxels (i.e. each ROI containing 25 voxels) at the two ends of the fiber tract being analyzed. Most of the fiber paths generated from ROI1 using SLT method terminate in the crossing fiber region or go to the perpendicular tracts (Fig.

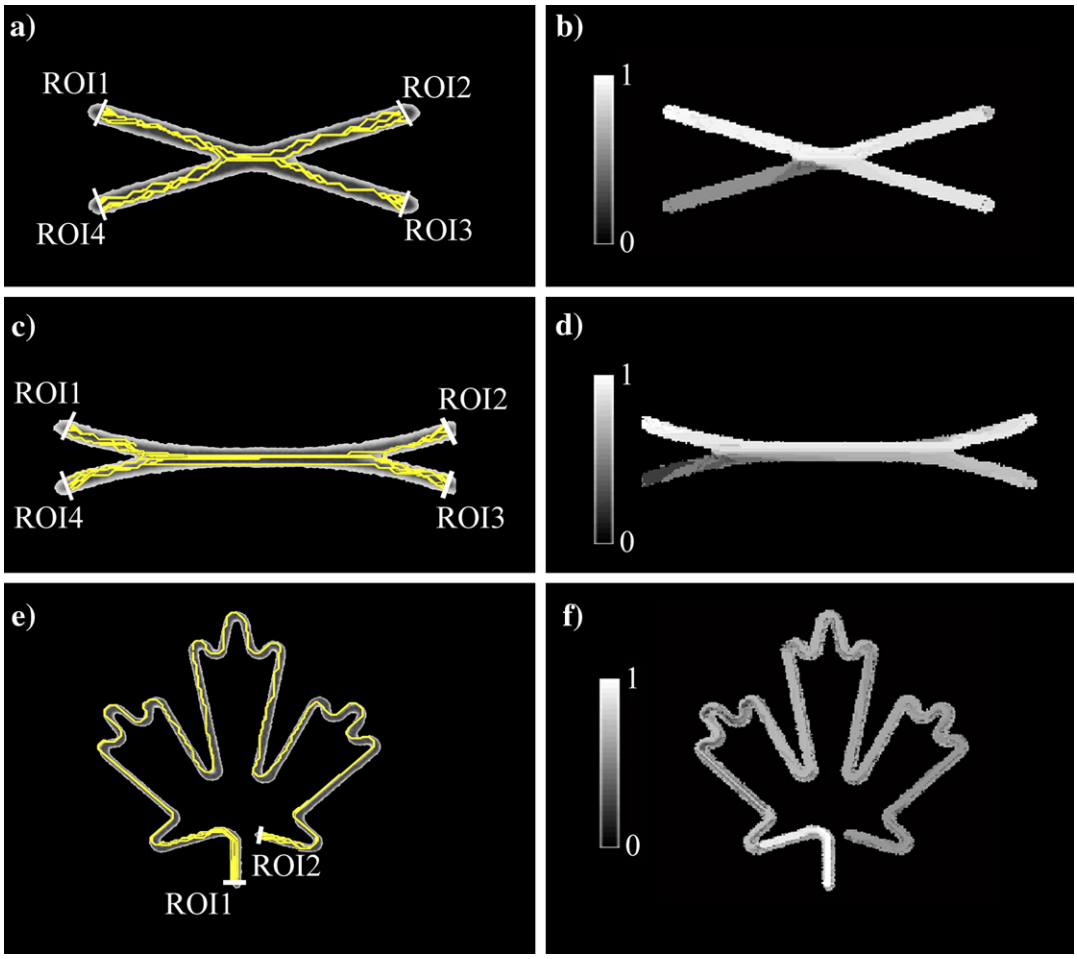

Fig. 7. Resulting anatomical connections between different regions of interest (ROIs) defined for straight crossing, curve crossing and Feuille trajectory. Each defined ROI consists of seven contiguous voxels defining a perpendicular line to the corresponding fiber tract. Left column (Figs. 7a, c and e): reconstructed connection routes (most probable paths) between ROI1 and the other defined ROIs, with SNR level of 15. Right column (Figs. 7b, d and f): corresponding maximum voxel–voxel connectivity values between the image volume voxels and the ROI1 voxels. The color code represents the index of connectivity. (For interpretation of the references to colour in this figure legend, the reader is referred to the web version of this article.)

9a). In contrast, both aFM and our graph-based tractography method reconstructed tracts between ROI1 and ROI2 (Figs. 9b and c, respectively). However, some fiber paths found by aFM failed to follow the correct fiber tract (e.g. some of them strayed from the fiber tract being analyzed at the level of the crossing region, going to the other perpendicular tracts and doing a U-turn before coming back to the main fiber to eventually reach the ending ROI).

Complementarily, Table 2 presents the obtained ACS, ACD and ACP measures using aFM and the proposed approach. Notice that although the zone–zone connectivity measures were not defined in the aFM, we used the voxel–voxel connectivity provided by this method to evaluate Eqs. (15), (16) and (17). The resulting C^{ACP}_{Zone} (ROI1, ROI2) using aFM is lower than that provided by our approach. Similarly, C^{ACS}_{Zone} (ROI1, ROI2) and C^{ACD}_{Zone} (ROI1, ROI2) measures for the aFM method are more distant from their ideal values (50 for the ACS, and 1 for the ACD measure).

It is interesting to note that in this experiment, the fiber paths obtained by our method look rougher or noisier (i.e. changing directions from voxel to voxel) inside the crossing region (Fig. 9c). This effect is explained by the fact that in this region the diffusion tensor is nearly spherical, and any fiber tracking method relying on estimating an ODF will be affected by the goodness of this estimation. In this work, the ODF is estimated from the Diffusion tensor model (Appendix B). This is a very simple method which is usually not able to describe complex fiber configurations, as is the case in crossing regions. In the Summary and discussions section the advantages of using more advanced models to infer the ODF will be illustrated.

Human data

In order to explore the performance of the proposed method in real data, we tried to replicate three well known brain anatomical connections. First, anatomical connections between voxels of the occipital pole surfaces (OCCs) and voxels belonging to the white matter and to the gray matter regions surfaces (WM-GMs) were estimated. The reconstructed connection routes (most probable paths) between left and right OCCs are shown in Fig. 10a. Figs. 10b and c show axial maps of the node–node connectivity values at the level of the splenium of the corpus callosum and the lateral geniculate nucleus, respectively. In these maps, each voxel was assigned the maximum of all possible connectivity values between it and the voxels of both OCC areas. Fig. 10a illustrates how the connection routes pass correctly through the splenium of the corpus

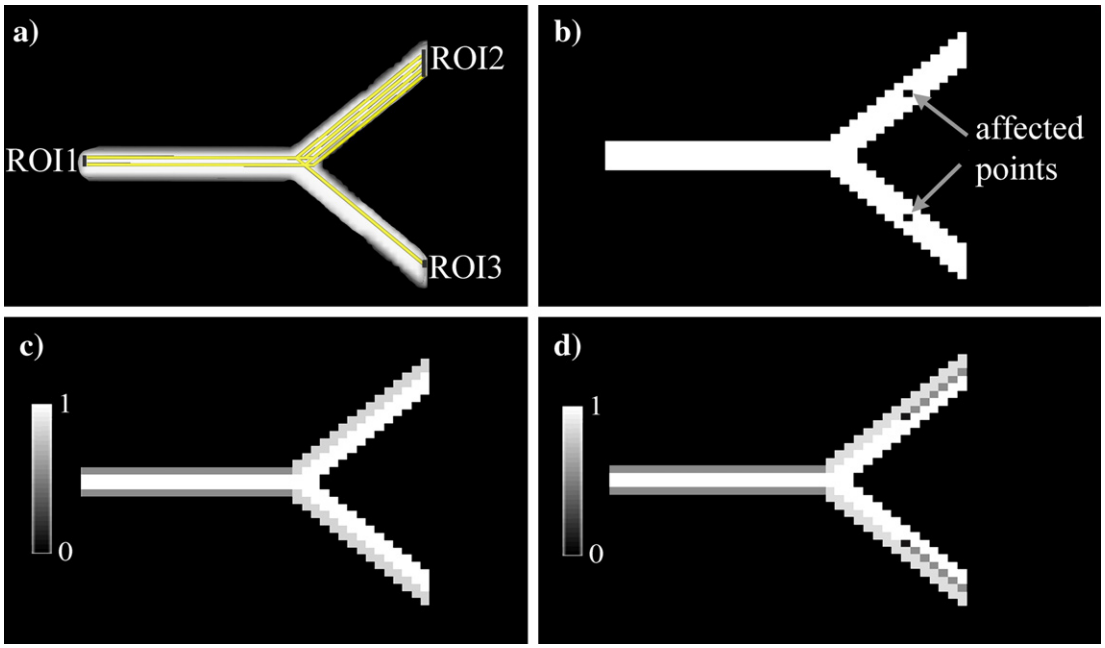

Fig. 8. Anatomical connections for the branching configuration before and after a hypothetical loss of the white matter integrity. (a) Three different ROIs were defined: ROI1 consists of two contiguous voxels at the left end of the fiber tract, ROI2 consists of four contiguous voxels at the upper right end of the tract, and ROI3 is conformed by a single voxel located at the bottom right end of the tract. Reconstructed connection routes (most probable paths) between ROI1–ROI2 and ROI1–ROI3 are also represented. (b) To simulate a hypothetical loss of the white matter integrity, the values of two voxels in the binary mask (P_{mat}) were set to zero (each voxel located symmetrically at the upper right tract or at the bottom right tract). (c) Obtained maximum voxel–voxel connectivity values between the image volume voxels and the ROI1 voxels before the hypothetical loss of the white matter integrity. The color code represents the index of connectivity. (d) Similar to (c), but after the hypothetical loss of the white matter integrity. (For interpretation of the references to colour in this figure legend, the reader is referred to the web version of this article.)

callosum and Figs. 10b and c confirm the expected high connectivity values for this region and the optic radiation, respectively. These results are in accordance with existing anatomical knowledge (Gómez-Padrón et al., 1985; Witelson, 1989; Standring, 2004).

The anatomical connections between voxels of an axial seed plane (ASP) placed in the corticospinal tract at the level of the pons (which is considered as a region) and voxels belonging to the WM-GMs were also estimated. Fig. 10d shows the reconstructed routes connecting the ASP and the left and right postcentrals gyrus, passing through the internal capsule. Moreover, Figs. 10e and f illustrate how regions of highest connectivity belong to the internal capsule, the corona radiata and the motor cortex (Gómez-Padrón et al., 1985; Standring, 2004).

Table 1
Results for branching configuration using the proposed connectivity graph model

SNR	C^{ACS}_{Zone} (ROI1, ROI2)	C^{ACS}_{Zone} (ROI1, ROI3)	C^{ACD}_{Zone} (ROI1, ROI2)	C^{ACD}_{Zone} (ROI1, ROI3)	C^{ACP}_{Zone} (ROI1, ROI2)	C^{ACP}_{Zone} (ROI1, ROI3)
Connectivity measures in branching configuration						
7	5.56	2.60	0.92	0.87	0.99	1
15	5.57	2.58	0.92	0.86	0.99	0.99
31	5.58	2.59	0.93	0.86	1	1
Connectivity measures after affecting the white matter mask						
7	3.98	1.58	0.66	0.52	0.98	0.59
15	3.96	1.57	0.66	0.52	0.99	0.59
31	3.96	1.57	0.66	0.53	0.99	0.60

In a similar way, anatomical connections between voxels of the middle frontal gyrus (MFGs) and the WM-GMs voxels were estimated (see Figs. 10g–i). We tried to obtain the fibers trajectories first between the thalamus and the MFGs, and finally between the left and right MFGs. In both cases, the main difficulty lies in the fact that the connecting fibers should pass through the crossing of three major bundles (i.e. intersection of the superior longitudinal fasciculus, the corona radiata and the corpus callosum). Note that the obtained routes connecting the thalamus and the MFGs (Fig. 10g) pass through the internal capsule and the corona radiata in accordance with previous anatomical studies (Gómez-Padrón et al., 1985; Standring, 2004). Also, those connection routes between the left and right MFGs (Fig. 10g) pass specifically through the genu and the rostral body of the corpus callosum and Figs. 10h and i confirm the expected high connectivity values for these regions, agreeing with Witelson's corpus callosum subdivision (Witelson, 1989).

Fig. 11 shows the mean ACS, ACD and ACP maps between 71 brain gray matter regions for five healthy subjects. For each subject, ACS, ACD and ACP measures were computed after eliminating not significant connectivity values between the WM-GMs voxels and the set of defined gray matter structures. Significant values were found by a z-test (H_0: $z \leq 0$) with a 0.05 significance level. In each map, the element $C_{i,j}$ is the mean connectivity value between regions i and j. Note that as we defined non-directed ACS, ACD and ACP measures, the resulting maps are symmetrical. Also, it can be spotted 2 black lines (4 with the symmetry) in all maps. These correspond with the left and right subthalamic nucleus, which were not correctly defined by the automatic parcellation method due to their very small sizes.

According to the mean ACS map (Fig. 11a), the precentral gyrus left and the postcentral gyrus left are the most connected regions (i.e. they present the maximum ACS value, 387.16± 97.87). These regions play an important role in a wide variety of the brain functions (e.g. motor and somatosensory functions). In general, frontal and temporal structures are the most connected structures. On the other hand, the most densely connected regions are the caudate nucleus right and the thalamus right (connecting around the 10±3% of their surfaces). It is known that the caudate nucleus is involved in the control of voluntary movement and in learning and memory systems. Taking into account the mean ACP map (Fig. 11c), the average connection density (i.e. the number of all non-zero connections divided by the maximum possible number of connections) was 0.7. This means that about the 70% of all possible connections between any two of the defined brain structures have a non-zero probability.

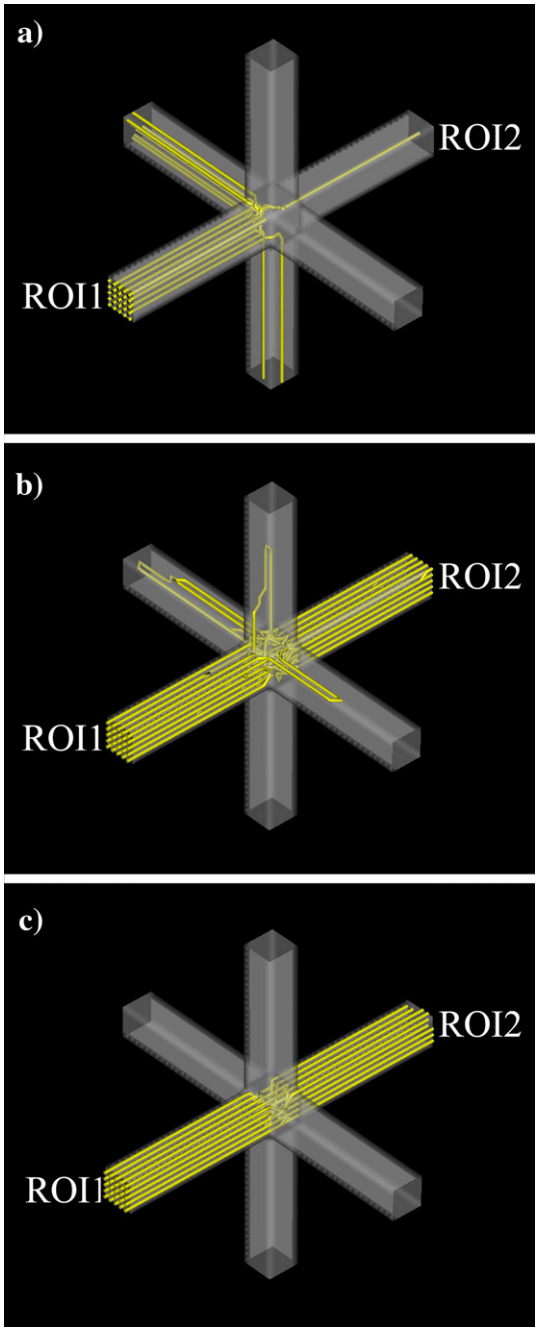

Fig. 9. Tracking results for the fiber crossing of three orthogonal tracts with SNR level of 15. ROI1 and ROI2 were defined as planes of 5×5 voxels at the two ends of the fiber tract being analyzed. (a) All paths generated from ROI1 using the SLT method. (b) Obtained connection routes between ROI1 and ROI2 using the aFM method. (c) Obtained connection routes between ROI1 and ROI2 using the proposed methodology.

Table 2
Results for orthogonal crossing of three fiber tracts using aFM and the proposed connectivity graph model

Connectivity measures in orthogonal crossing using aFM and the connectivity graph model

SNR	aFM			Graph model		
	C_{Zone}^{ACS} (ROI1, ROI2)	C_{Zone}^{ACD} (ROI1, ROI2)	C_{Zone}^{ACP} (ROI1, ROI2)	C_{Zone}^{ACS} (ROI1, ROI2)	C_{Zone}^{ACD} (ROI1, ROI2)	C_{Zone}^{ACP} (ROI1, ROI2)
7	23.53	0.47	0.50	36.41	0.72	0.90
15	23.80	0.48	0.50	37.78	0.76	0.91
31	24.63	0.49	0.51	42.73	0.85	0.98

In order to evaluate (dis)similarity between the different subjects, correlation coefficients between their corresponding ACS, ACD and ACP maps were estimated (see Table 3). Results show significant correlations in all cases (the maximum p value obtained was in the order of 10^{-209}), supporting the hypothesis that healthy subjects present similar ACS, ACD and ACP patterns for the gray matter parcellation used in this study.

Summary and discussions

In this work, we developed a diffusion imaging methodology capable to characterize anatomical connections between different brain gray matter structures. It consists of three basic steps: 1, definition of a Brain Graph model in which each voxel is considered as a node of a non-directed weighted graph; 2, the use of an iterative algorithm based on analysis of the voxels neighborhood to find the route of maximum probability between two nodes and the subsequent definition of the anatomical connectivity measure between them; 3, the definition of three anatomical connectivity measures between different gray matter regions, which are individually considered as clusters of nodes in the graph.

In step 1, the probabilistic tissue segmentation of the anatomical MR image and the intravoxel white matter orientational distribution function (ODF), obtained from DW-MRI, are combined to estimate the probability of nervous fibers connection between two contiguous nodes (voxels), which is associated to the weight of the arc connecting these nodes.

Generally, in the diffusion tracking framework, the fractional anisotropy (FA) map is used to construct a binary mask which is employed to constraint the fiber trajectories space (Conturo et al., 1999; Mori and van Zijl, 2002; Staempfli et al., 2006). Assuming that nervous fibers are present only in those regions with high anisotropy, this mask is defined by an empirical threshold on the FA map, which implies that regions where two or more fibers cross each other will be ignored. To our knowledge, this work introduces for the first time, the use of probabilistic brain tissue segmentations of the anatomical MR images as a priori information to find anatomically plausible connection routes between any two voxels.

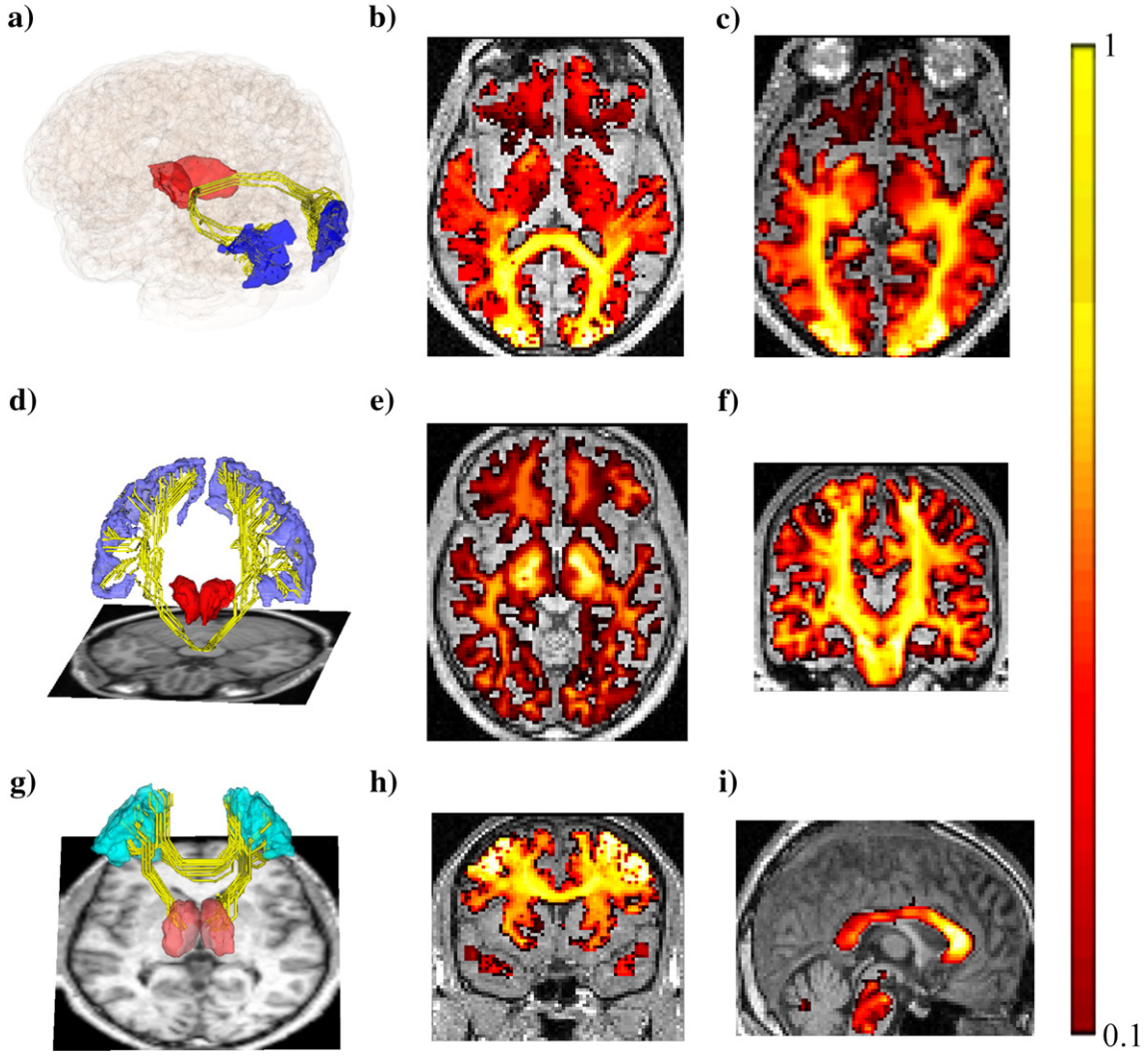

Fig. 10. (a) Obtained anatomical connection routes between the left and right occipital poles. Both thalami are represented as anatomical references. (b) Axial map at the level of the splenium of the corpus callosum representing maximum voxel–voxel connectivity values between the WM-GMs voxels and the OCCs voxels. (c) Axial map at the level of the lateral geniculate nucleus representing maximum voxel–voxel connectivity values between the WM-GMs voxels and the OCCs voxels. (d) Reconstructed connection routes between the ASP and the left and right postcentral gyrus. (e) Axial map representing maximum voxel–voxel connectivity values between the WM-GMs voxels and the voxels of the ASP. (f) Coronal map representing maximum voxel–voxel connectivity values between the WM-GMs and the ASP voxels. (g) Obtained connection routes among the left and right MFGs, and between each MFGs and the ipsilateral thalamus. (h) Coronal map representing maximum voxel–voxel connectivity values between the WM-GMs voxels and the MFGs voxels. (i) Inter-hemispheric plane representing maximum voxel–voxel connectivity values between the WM-GMs voxels and the MFGs voxels. In (b), (c), (e), (f), (h) and (i) the color code represents the index of connectivity. Each connectivity map was overlaid on the corresponding T1-weighted image. (For interpretation of the references to colour in this figure legend, the reader is referred to the web version of this article.)

Additionally, we allow for tuning the relative importance between the probabilistic gray and white matter segmentations through the α parameter (see Eq. (3)). For $\alpha \geq 1$, the segmentation of white matter will have equal or bigger weight than the gray matter segmentation, which agrees with the fact that nervous fibers are mostly in the white matter. However, α should not be considerably greater than one (for example: $\alpha = 10$), because voxel–voxel connections around gray matter can be rejected. Thus, although in this study we chose $\alpha = 1$, the appropriate selection of this parameter requires detailed future analysis.

On the other hand, the weight of the arc connecting two neighboring nodes is defined by taking into account the fibers coherence along its direction. The probability that a fiber is present around a particular arc is evaluated by computing the integral of the ODF in a solid angle along its direction (see Fig. 3), which contributes to reduce discretization errors at the same time that complex structural fiber distributions can be considered. However, the ODF is just one of several measures that implicitly reflect fiber coherence. In this sense, the graph-based approach has the advantage that other functions can be used for this purpose, such as those characterizing fiber distribution with various maxima of orientation (Jansons and Alexander, 2003; Tuch, 2004; Alexander, 2005) or even the ellipsoids given by the diffusion tensors (Basser et al., 1994).

In order to find the anatomical connection route between two nodes in the defined Brain Graph, we explored the set of all

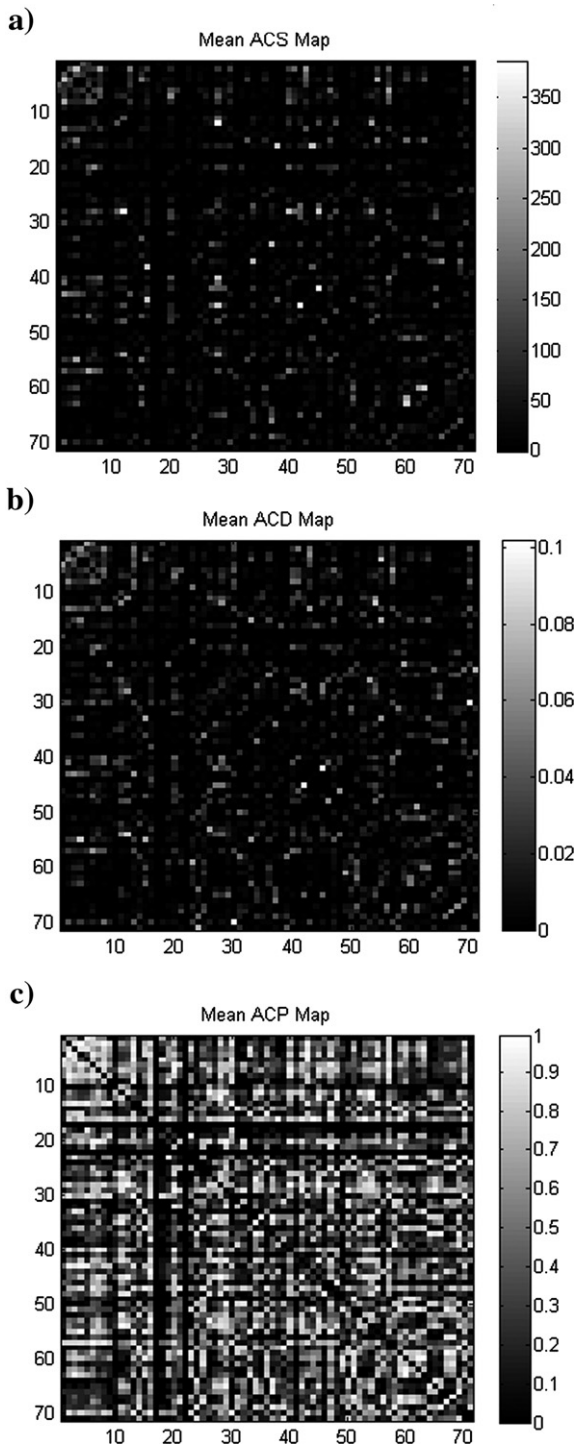

Fig. 11. Mean connectivity results for 71 gray matter regions defined on the brain of five healthy subjects: (a) ACS, (b) ACD and (c) ACP. In each map, the element $C_{i,j}$ is the mean connectivity across subjects between regions i and j. The color code represents the index of connectivity.

possible discrete paths to select the route which optimize certain function designed according to physiological criteria. A similar example of this type of procedure are the Fast Marching (FM) tractography techniques (Parker et al., 2002; Staempfli et al., 2006), in which the route connecting two voxels should minimize the "time" necessary to arrive from one voxel to the other. In our case, the fiber tractography is expressed in terms of the most probable path in the defined Brain Graph. Figs. 7–9 illustrate the performance of the proposed tractography method in the artificial DW-MRI data. The results show that the methodology we have introduced here is able to reconstruct correctly complex fiber configurations such as straight crossing, curve crossing, Feuille trajectory, branching tract and orthogonal crossing of three tracts. Also, the obtained connection routes between the left and right OCCs (Fig. 10a), the defined ASP and both postcentral gyrus (Fig. 10d), the thalamus and left and right MFGs (Fig. 10g) were presented. These results agree with existing anatomical knowledge (Gómez-Padrón et al., 1985; Witelson, 1989; Standring, 2004).

Quantification of the anatomical connectivity between two voxels can be defined according to the parameters of the connection route among them and also taking into account the a priori information about the connectivity between these voxels, which could come from previous anatomical and functional studies based on histological tracing methods or neuroimaging techniques (e.g. fMRI, EEG/MEG tomography, PET, etc.). This allows the integration between different anatomical and functional connectivity measures. In this work, similar to Parker et al. (2002) and Staempfli et al. (2006), an anatomical connectivity measure is defined as the lowest weight of the arcs set belonging to the most probable path. However, we consider that other node–node (voxel–voxel) connectivity measures should be explored.

To characterize anatomical connections between K brain gray matter structures, the previous Brain Graph was redefined as a $K+1$ partite graph by partitioning the initial nodes set in K non-overlapped gray matter subsets and one subset clustering the remaining nodes. Based on the latter, three connectivity measures were defined: Anatomical Connection Strength (ACS), Anatomical Connection Density (ACD) and Anatomical Connection Probability (ACP). ACS provides an estimation of the potential information flow between any pair of regions. It is considered

Table 3
Correlations between the ACS, ACD and ACP maps of the 5 subjects

Subject	1	2	3	4	5
ACS correlation					
1	–	0.71	0.76	0.78	0.85
2		–	0.69	0.72	0.64
3			–	0.79	0.74
4				–	0.79
5					–
ACD correlation					
1	–	0.64	0.76	0.71	0.82
2		–	0.61	0.61	0.56
3			–	0.73	0.73
4				–	0.69
5					–
ACP correlation					
1	–	0.64	0.64	0.59	0.69
2		–	0.68	0.66	0.60
3			–	0.64	0.63
4				–	0.60
5					–

For each connectivity measure, the elements above the main diagonal are the correlation coefficients.
All the correlations are significant; the maximum p value obtained was in the order of 10^{-209}.

proportional to the amount of nervous fibers shared by these regions. To estimate it we considered that, similar as in a system of tubes in which the liquids flow in one extreme of a specific tube depends on its cross section area and on the rate of liquids, the potential nervous information flow can be reflected by the cross section area of the fiber connector volume on the surfaces of the two regions. Here, the ACS is estimated by counting the "effective" number of nodes on the surfaces of the zones involved in the connection, where each node is counted according to a function which represents its anatomical connectivity value with the surface of the second zone (this function ranges between 0, no connected, and 1, completely connected). When the zones of interest present a high number of superficial nodes, the proposed ACS estimation has the inconvenient that, even if the superficial nodes of the zones are not well connected, the accumulation of a great number of small node–node connectivity values can cause a high ACS. To avoid this, it is reasonable to eliminate those node–node connections with values below a specified threshold before computing the ACS, which also contributes to eliminate the nuisance connections. Although in this work we used a z-test in order to eliminate non-significance connectivity values between the WM-GMs voxels and the set of defined gray matter structures, the selection of the threshold could be carried out using more advanced local and global thresholding models, such as local false discovery rate technique (Efron, 2004, 2005) or image thresholding based on the EM algorithm (Yakoub et al., 2006). This will be the subject of future work.

On the other hand, ACD is a measure of the fraction of the connected superficial nodes with respect to the total number of superficial nodes of both areas. It permits, for example, to know if a pair of zones has more or less density of connection than other pair of zones with different or equal number of superficial nodes. Two regions with a high ACS value (compared with the ACS between others pairs of regions) not necessarily have to present a high ACD value. This situation could take place when two regions of interest contain a high number of superficial nodes. Similarly, a pair of zones with a low ACS value can present a high ACD value, which occurs specifically when the zones contain a small number of superficial nodes (each node having an anatomical connectivity value close to 1 with the surface of the other zone).

While ACS and ACD quantify the strength and density of the possible connection respectively, ACP measures the maximum probability of two regions to be connected at least by a single connection. It allows to infer if any two gray matter regions can be functionally related independently of the strength and density of the possible connection. Additionally, other zone–zone connectivity measures can be defined and some of them could be directly formulated as the combination of the three proposed measures.

Fig. 11 show the mean maps of ACS, ACD and ACP obtained between 71 gray matter structures for five healthy subjects. Significant correlations among the connectivity matrixes of the different subjects were found (Table 3), which could support the hypothesis that healthy subjects present similar ACS, ACD and ACP patterns for the used gray matter parcellation. Before presenting the aforementioned results, the anatomical connections obtained for the branching configuration before and after a hypothetical loss of the white matter integrity were presented (Fig. 8 and Table 1), illustrating how the ACS, ACD and ACP measures reflect the white matter affectation. In a similar way, more detailed comparisons between normal and pathological ACS, ACD and ACP maps (or its combinations) could be a potential procedure to detect and diagnose pathologies causing functional cognitive deficiencies related to white matter injury, such as: Alzheimer, Schizophrenia and Dyslexia. Compared to connectivity maps of normal subjects, abnormal ones can reveal certain damage in the anatomical interconnectivity between multiple functional cognitive brain areas, allowing to find those regions that are not wired properly. Other possible application of the aforementioned connectivity maps is to use them as a priori or complementary information in brain functional connectivity studies (see for example Sotero et al., 2007).

However, the lack of information about the direction of nervous fibers in DW-MRI data hinders the possibility of distinguishing between efferent and afferent projections. Thus, in the defined non-directed weighted graph, the direction of the arcs (distinction between initial and terminal nodes) is irrelevant and making the measures ACS, ACD and ACP to be bidirectional. This constitutes an inherent important limitation of DW-MRI techniques. Nevertheless, in a previous work (Young, 1993) a connectivity matrix of the primate cerebral cortex was reported where approximately only the 15% of the total possible connections between 73 brain areas were not reciprocals.

An important element in the Brain Graph model is the voxel size of the MR images (1/resolution). Reduction of the voxel size (which can be achieved directly in the data acquisition) implies a more accurate description of the brain structure, i.e. a better characterization of the intravoxel anisotropy as well as a more reliable tissue segmentation. However, the decrease of the voxel size leads to a worse SNR and implies an increase in the computational cost of the methodology.

Other important element is the angular resolution of the diffusion weighted images. In this work, we have achieved competitive results with the use of low angular resolution data, but certainly a better performance of the methodology can be obtained using high angular resolution techniques, for example Q-ball Imaging (Tuch, 2004) and diffusion spectrum MRI (Wedeen et al., 2005). A better estimation of the ODF implies a precise characterization of the intravoxel white matter disposition and thus an accurate evaluation of the fibers coherence along arcs direction, which subsequently implies a more realistic characterization of the brain structure. In order to illustrate this, in Fig. 12 a comparison of the fiber crossing of three orthogonal tracts using the introduced graph-based tractography with ODF maps estimated from (a) the Diffusion tensor model (same results that in Fig. 9c) and (b) the Q-ball Imaging technique (Tuch, 2004) is shown. Close-ups of the fiber crossing region are shown, illustrating that the calculated routes using the Diffusion tensor model (Fig. 12a) are considerably rougher or noisier than those routes obtained using the Q-ball Imaging technique (Fig. 12b). This supports the idea that high angular resolution-based techniques allow to get better results.

The Graph Theory constitutes an ideal framework for modeling diverse system situations. Given the wide use of the graph framework in several areas of physics and mathematics, multiple problems and practical applications have been undergone. In this study, this framework is applied for the first time to the fiber tracking problem and to the subsequent quantification of the brain anatomical connections from DW-MRI data. However, open problems remain related to the recognition of false fiber trajectories and to the corresponding elimination of nuisance connections. Statistical models, in which a relative high number of subjects should be considered, can be useful to investigate the variability of the connectivity maps in order to eliminate non-significant and superfluous connections. Also, as was

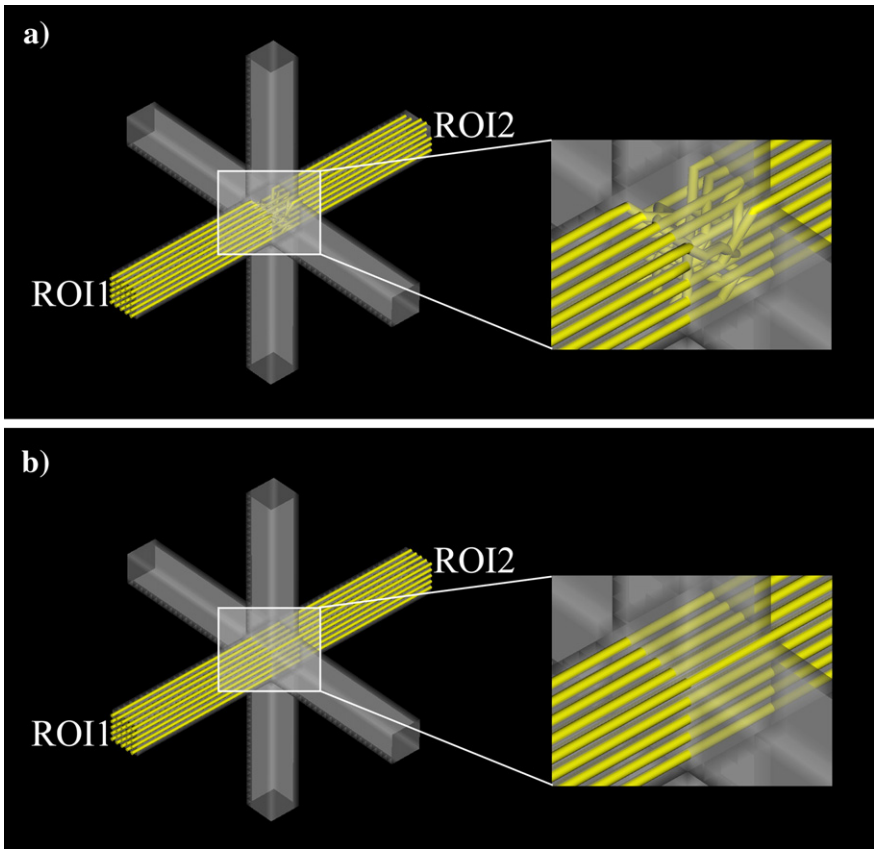

Fig. 12. Comparison of the fiber crossing of three orthogonal tracts using the graph-based tractography method with SNR level of 15 and ODF maps estimated according to: (a) Diffusion tensor model, (b) Q-ball Imaging technique. Close-ups of the fiber crossing region are shown.

mentioned in Section 2.4, the probability that a node belongs to a given gray matter structure can be specified employing Maximum Probability Segmentation Maps or even using Spatial Probabilistic Anatomical Maps (Mazziotta et al., 1995). In the future, more advanced graph models should be able to employ both this probability and the uncertainty in the estimation of the fiber orientation distribution function. This, in turn, could be used to estimate the error associated to arc weights, node–node and zone–zone connectivity measures. Additionally, future studies in animals should be addressed to further testing of the performance of the proposed methodology.

Acknowledgments

Authors would like to thank Nelson Rubal Lorenzo, Agustín Lage-Castellanos and Erick C. Jones for their useful comments on the anatomical, statistical and algorithmic aspects of this work, respectively. Also, we thank to Roberto C. Sotero and Thomas Koenig, for the final revision of the manuscript.

Appendix A. Algorithm to solve the most probable path problem

Given a Brain Graph $G_{\text{brain}}=[N,A]$, let us define some quantities before setting up the algorithm:

$|N|$: Cardinality of the set N, i.e. the number of elements belonging to set N.

N^{-s}: Set of nodes that belong to G_{brain} except node 's', $N^{-s}=N/\{\vec{r}_s\}$.

$M(\vec{r}_v)$: Map of probabilities of the path between node 's' and all nodes $\vec{r}_v \in N^{-s}, M(\vec{r}_v)=P[\rho(\vec{r}_s,\vec{r}_v)]$ and $M(\vec{r}_s)=1$.

N_i^{neig}: Nearest neighborhood of the i-th node.

This algorithm proceeds in $|N|-1$ iterations as follows:

a) Set initially:

a.1) $\tilde{S}=N^{-s}$

a.2) $$M(\vec{r}_i)=\begin{cases}1, & \vec{r}_i=\vec{r}_s,\\ w(a_{si}), & \vec{r}_i\in N_i^{\text{neig}}\\ 0, & \text{otherwise.}\end{cases}$$

a.3) $\tilde{\rho}(\vec{r}_s,\vec{r}_i)=a_{si}, \quad \forall \vec{r}_i \in N_s^{\text{neig}}$

b) Find $\vec{r}_j \in \tilde{S}$ such that $M(\vec{r}_j)=\max_{\forall \vec{r}_i \in \tilde{S}} M(\vec{r}_i)$

b.1) Set a new $\tilde{S} \leftarrow \tilde{S}/\{\vec{r}_j\}$

b.2) If $\tilde{S}=\emptyset$, then **Stop**; else continue

c) For all $\vec{r}_m \in N_j^{\text{neig}}$ and $\vec{r}_m \in \tilde{S}$, set

c.1) $\rho(\vec{r}_s,\vec{r}_m)=\{\tilde{\rho}(\vec{r}_s,\vec{r}_j)\cup a_{jm}\}$,

c.2) If $P[\rho(\vec{r}_s,\vec{r}_m)]>M(\vec{r}_m)$ then

$$\tilde{\rho}(\vec{r}_s,\vec{r}_m)=\rho(\vec{r}_s,\vec{r}_m),\ M(\vec{r}_m)=P[\tilde{\rho}(\vec{r}_s,\vec{r}_m)]$$

c.3) **go to b**.

Finally, the map $M(\vec{r}_p)$ for $\vec{r}_p \in N^{-s}$ represents the final probability of the path of maximum reliability according to Eq. (8) between nodes $\vec{r}_s$ and $\vec{r}_p$ denoted by $\tilde{\rho}(\vec{r}_s, \vec{r}_p)$.

Appendix B. White matter orientational distribution function

The intravoxel white matter orientational distribution function (ODF) $\Psi(\hat{u})$ is defined as the radial projection of the probability density function (PDF) $P(\vec{R})$ (Wedeen et al., 2005):

$$\psi(\hat{u}) = \int_0^{+\infty} R^2 P(\hat{u}R)\mathrm{d}R, \tag{B1}$$

being $\hat{u}$ a unitary vector and $\vec{R} = \hat{u}R$ the relative spin displacement.

Considering the PDF for anisotropic Gaussian diffusion:

$$P\left(\vec{R}\right) = (4\pi t)^{-3/2}(|D|)^{-1/2} e^{\frac{-\vec{R}^T D^{-1}\vec{R}}{4t}}, \tag{B2}$$

Then, substituting in Eq. (B1) and using the identity:

$$\int_0^{+\infty} x^m e^{ax^2} dx = \frac{\Gamma\left(\frac{(m+1)}{2}\right)}{2a^{\frac{m+1}{2}}}, \tag{B3}$$

where Γ is the Gamma function, we can obtain the ODF as:

$$\psi(\hat{u}) = \frac{1}{C}\left(\hat{u}^T D^{-1}\hat{u}\right)^{-\frac{3}{2}} \tag{B4}$$

Here, C is a normalization constant which ensures that the ODF is properly normalized to unit mass.

References

Alemán-Gómez, Y., Melie-García, L., Valdes-Hernández, P., 2006. IBASPM: Toolbox for automatic parcellation of brain structures. Presented at the 12th Annual Meeting of the Organization for Hum. Brain Mapp., June 11–15, 2006, Florence, Italy. Available on CD-Rom in NeuroImage, Vol. 27, No.1.

Alexander, D.C., 2005. Multiple-fiber reconstruction algorithms for diffusion MRI. Ann. N. Y. Acad. Sci. 1064, 113–133.

Alexander, D.C., Pierpaoli, C., Basser, P.J., Gee, J.C., 2001. Spatial transformations of diffusion tensor magnetic resonance images. IEEE Trans. Med. Imag. 20, 1131–1139.

Ashburner, J., Friston, K.J., 1999. Nonlinear spatial normalization using basis functions. Hum. Brain Mapp. 7, 254–266.

Ashburner, J., Friston, K.J., 2000. Voxel-based morphometry-the methods. NeuroImage 11, 805–821.

Basser, P.J., Pajevic, S., 2000. Statistical artifacts in diffusion tensor MRI (DT-MRI) caused by background noise. Magn. Reson. Med. 44, 41–50.

Basser, P.J., Mattiello, J., LeBihan, D., 1994. Estimation of the effective self-diffusion tensor from the NMR spin echo. J. Magn. Reson., Ser. B. 103, 247–254.

Basser, P.J., Pajevic, S., Pierpaoli, C., Duda, J., Aldroubi, A., 2000. In vivo fiber tractography using DT-MRI data. Magn. Reson. Med. 44, 625–632.

Behrens, T.E., Johansen-Berg, H., Woolrich, M.W., Smith, S.M., Wheeler-Kingshott, C.A., Boulby, P.A., Barker, G.J., Sillery, E.L., Sheehan, K., Ciccarelli, O., Thompson, A.J., Brady, J.M., Matthews, P.M., 2003. Non-invasive mapping of connections between human thalamus and cortex using diffusion imaging. Nat. Neurosci. 6, 750–757.

Collins, D.L., Neelin, P., Peters, T.M., Evans, A.C., 1994. Automatic 3D intersubject registration of MR volumetric data in standardized Talairach space. J. Comput. Assist. Tomogr. 18, 192–205.

Conturo, T.E., Lori, N.F., Cull, T.S., Akbudak, E., Snyder, A.Z., Shimony, J.S., McKinstry, R.C., Burton, H., Raichle, M.E., 1999. Tracking neuronal fiber pathways in the living human brain. Proc. Natl. Acad. Sci. U. S. A. 96, 10422–10427.

Dijkstra, E.W., 1959. A note on two problems in connexion with graphs. Numer. Math. 269–271.

Efron, B., 2004. Large-scale simultaneous hypothesis testing: the choice of a null hypothesis. J. Am. Stat. Assoc. 99, 96–104.

Efron, B., 2005. Local false discovery rates. http://www-stat.stanford.edu/~brad/papers/.

Evans, A.C., Collins, D.L., 1993. A 305-member MRI-based stereotactic atlas for CBF activation studies. Proceedings of the 40th Annual Meeting of the Society for Nuclear Medicine.

Evans, A.C., Collins, D.L., Neelin, P., MacDonald, D., Kamber, M., Marrett, T.S., 1994. Three-dimensional correlative imaging: applications in human brain mapping. In: Thatcher, R.W., Hallett, M., Zeffiro, T., John, E.R., Huerta, M. (Eds.), Functional Neuroimaging. Technical Foundations, pp. 145–162.

Gómez-Padrón, I., Silva Loynaz, C., Seuc Chiu, A., 1985. Anatomía II. Folleto complementario. Ministerio de salud pública, Cuba.

Gondran, M., Minoux, M., 1984. Graphs and Algorithms. John Wiley and Sons Ltd., Chichester.

Hagmann, P., Thiran, J.P., Jonasson, L., Vandergheynst, P., Clarke, S., Maeder, P., Meuli, R., 2003. DTI mapping of human brain connectivity: statistical fibre tracking and virtual dissection. NeuroImage 19, 545–554.

Hagmann, P., Kurant, M., Gigandet, X., Thiran, P., Wedeen, V.J., Meuli, R., Thiran, J.P., 2006. Imaging the brain neuronal network with diffusion MRI: a way to understand its global architecture. Proc. ISMRM 436.

Hutton, C., Bork, A., Josephs, O., Deichmann, R., Ashburner, J., Turner, R., 2002. Image distortion correction in fMRI: a quantitative evaluation. NeuroImage 16, 217–240.

Iturria-Medina, Y., Valdes-Hernandez, P., Canales-Rodriguez, E., 2005. Measures of anatomical connectivity obtained from neuro diffusion images. Available on CD-Rom in NeuroImage, Vol. 26, No.1; Presented at the 11th Annual Meeting of the Organization for Hum. Brain Mapp., June 12–16, 2005, Toronto, Ontario, Canada.

Jansons, K.M., Alexander, D.C., 2003. Persistent angular structure: new insights from diffusion MRI data. Dummy version. Inf. Process. Med. Imag. 18, 672–683.

Jones, D.K., Horsfield, M.A., Simmons, A., 1999. Optimal strategies for measuring diffusion in anisotropic systems by magnetic resonance imaging. Magn. Reson. Med. 42, 515–525.

Jun Zhang, Hao Ji, Ning Kang and Ning Cao, 2005. Fiber Tractography in Diffusion Tensor Magnetic Resonance Imaging: A Survey and Beyond. Technical Report No. 437-05 ed., Department of Computer Science; University of Kentucky; Lexington; KY.

Koch, M.A., Norris, D.G., Hund-Georgiadis, M., 2002. An investigation of functional and anatomical connectivity using magnetic resonance imaging. NeuroImage 16, 241–250.

Lazar, M., Weinstein, D.M., Tsuruda, J.S., Hasan, K.M., Arfanakis, K., Meyerand, M.E., Badie, B., Rowley, H.A., Haughton, V., Field, A., Alexander, A.L., 2003. White matter tractography using diffusion tensor deflection. Hum. Brain Mapp. 18, 306–321.

LeBihan, D., 2003. Looking into the functional architecture of the brain with diffusion MRI. Nat. Rev., Neurosci. 4, 469–480.

LeBihan, D., Mangin, J.F., Poupon, C., Clark, C.A., Pappata, S., Molko, N., Chabriat, H., 2001. Diffusion tensor imaging: concepts and applications. J. Magn. Reson. Imaging 13, 534–546.

Lori, N.F., Akbudak, E., Shimony, J.S., Cull, T.S., Snyder, A.Z., Guillory, R.K., Conturo, T.E., 2002. Diffusion tensor fiber tracking of human brain connectivity: acquisition methods, reliability analysis and biological results. NMR Biomed. 15, 494–515.

Mazziotta, J.C., Toga, A.W., Evans, A., Fox, P., Lancaster, J., 1995. A probabilistic atlas of the human brain: theory and rationale for its development. The International Consortium for Brain Mapping (ICBM). NeuroImage 2, 89–101.

Moore, E.F., 1959. The Shortest Path Through a Maze. Harvard University Press, Cambridge, Massachusetts, pp. 285–292.

Mori, S., van Zijl, P.C., 2002. Fiber tracking: principles and strategies—A technical review. NMR Biomed. 15, 468–480.

Mori, S., Crain, B.J., Chacko, V.P., van Zijl, P.C., 1999. Three-dimensional tracking of axonal projections in the brain by magnetic resonance imaging. Ann. Neurol. 45, 265–269.

Parker, G.J., Alexander, D.C., 2003. Probabilistic Monte Carlo based mapping of cerebral connections utilising whole-brain crossing fibre information. Inf. Process. Med. Imag. 18, 684–695.

Parker, G.J., Wheeler-Kingshott, C.A., Barker, G.J., 2002. Estimating distributed anatomical connectivity using fast marching methods and diffusion tensor imaging. IEEE Trans. Med. Imag. 21, 505–512.

Parker, G.J., Haroon, H.A., Wheeler-Kingshott, C.A., 2003. A framework for a streamline-based probabilistic index of connectivity (PICo) using a structural interpretation of MRI diffusion measurements. J. Magn. Reson. Imaging 18, 242–254.

Ramnani, N., Behrens, T.E., Penny, W., Matthews, P.M., 2004. New approaches for exploring anatomical and functional connectivity in the human brain. Biol. Psychiatry 56, 613–619.

Sotero, R.C., Trujillo-Barreto, N.J., Iturria-Medina, Y., Carbonell, F., Jimenez, J.C., 2007. Realistically coupled neural mass models can generate EEG rhythms. Neural Comput. 19, 478–512.

Sporns, O., Tononi, G., Kotter, R., 2005. The human connectome: a structural description of the human brain. PLoS. Comput. Biol. 1, e42.

Staempfli, P., Jaermann, T., Crelier, G.R., Kollias, S., Valavanis, A., Boesiger, P., 2006. Resolving fiber crossing using advanced fast marching tractography based on diffusion tensor imaging. NeuroImage 30, 110–120.

Standring, S., 2004. Gray's Anatomy: The Anatomical Basis of Medicine and Surgery, 39th edition. Churchill Livingstone.

Studholme, Hill, Hawkes, 1998. A normalized entropy measure of 3-D medical alignment. Proc. Med. Imaging, vol. 3338. SPIE Press, San Diego, CA, pp. 132–143.

Tench, C.R., Morgan, P.S., Blumhardt, L.D., Constantinescu, C., 2002. Improved white matter fiber tracking using stochastic labeling. Magn. Reson. Med. 48, 677–683.

Tuch, D.S, 2002. MRI of complex tissue structure. PhD Thesis.

Tuch, D.S., 2004. Q-ball imaging. Magn. Reson. Med. 52, 1358–1372.

Wedeen, V.J., Hagmann, P., Tseng, W.Y., Reese, T.G., Weisskoff, R.M., 2005. Mapping complex tissue architecture with diffusion spectrum magnetic resonance imaging. Magn. Reson. Med. 54, 1377–1386.

Weinstein, D., Kindlmann, G., Lundberg, E., 1999. Tensorlines: advection-diffusion based propagation through diffusion tensor fields. Proc. IEEE Visualization, San Francisco, CA, pp. 249–253.

Witelson, S.F., 1989. Hand and sex differences in the isthmus and genu of the human corpus callosum. A postmortem morphological study. Brain 112 (Pt. 3), 799–835.

Yakoub, B., Lorenzo, B., Farid, M., 2006. Image thresholding based on the EM algorithm and the generalized Gaussian distribution. Pattern Recogn. 40, 619–634.

Young, M.P., 1993. The organization of neural systems in the primate cerebral cortex. Proc. Biol. Sci. 252, 13–18.

3.2. ARTÍCULO 2

Yasser Iturria-Medina, Roberto C. Sotero, Erick J. Canales-Rodríguez, Yasser Alemán-Gómez and Lester Melie-García, 2008. Studying the Human Brain Anatomical Network via Diffusion-Weighted MRI and Graph Theory. Neuroimage, 40, 1064-1076.

ELSEVIER

NeuroImage

www.elsevier.com/locate/ynimg
NeuroImage 40 (2008) 1064–1076

Studying the human brain anatomical network via diffusion-weighted MRI and Graph Theory

Yasser Iturria-Medina,[a,*] Roberto C. Sotero,[b] Erick J. Canales-Rodríguez,[a] Yasser Alemán-Gómez,[a] and Lester Melie-García[a]

[a]*Neuroimaging Department, Cuban Neuroscience Center, Avenue 25, Esq 158, #15202, PO Box 6412, Cubanacán, Playa, Havana, Cuba*
[b]*Brain Dynamics Department, Cuban Neuroscience Center, Havana, Cuba*

Received 20 June 2007; revised 18 October 2007; accepted 30 October 2007
Available online 19 November 2007

Our goal is to study the human brain anatomical network. For this, the anatomical connection probabilities (ACP) between 90 cortical and subcortical brain gray matter areas are estimated from diffusion-weighted Magnetic Resonance Imaging (DW-MRI) techniques. The ACP between any two areas gives the probability that those areas are connected at least by a single nervous fiber. Then, the brain is modeled as a non-directed weighted graph with continuous arc weights given by the ACP matrix. Based on this approach, complex networks properties such as small-world attributes, efficiency, degree distribution, vulnerability, betweenness centrality and motifs composition are studied. The analysis was carried out for 20 right-handed healthy subjects (mean age: 31.10, S.D.: 7.43). According to the results, all networks have small-world and broad-scale characteristics. Additionally, human brain anatomical networks present bigger local efficiency and smaller global efficiency than the corresponding random networks. In a vulnerability and betweenness centrality analysis, the most indispensable and critical anatomical areas were identified: putamens, precuneus, insulas, superior parietals and superior frontals. Interestingly, some areas have a negative vulnerability (e.g. superior temporal poles, pallidums, supramarginals and hechls), which suggest that even at the cost of losing in global anatomical efficiency, these structures were maintained through the evolutionary processes due to their important functions. Finally, symmetrical characteristic building blocks (motifs) of size 3 and 4 were calculated, obtaining that motifs of size 4 are the expanded version of motif of size 3. These results are in agreement with previous anatomical studies in the cat and macaque cerebral cortex.

Introduction

The brain is one of the most challenging systems found in nature. It can be viewed as a complex network consisting of highly interconnected processing regions. Its response to any external stimulus relies on the cooperation among these specialized centers, which can be classified according to their anatomical and functional properties (Brodmann, 1909; Mazziotta et al., 1995; Toga et al., 2006; Mountcastle, 2007). Thus, the study of their anatomical and functional connectivity constitutes an indispensable step towards the understanding of the brain specialization and integration (Sporns et al., 2005).

Previous works in mammalian species (i.e. cat and macaque monkey) have shown that cortical anatomical connection matrices, obtained post-mortem, exhibit "small-world" attributes (Sporns and Zwi, 2004; Hilgetag and Kaiser, 2004). That is, anatomical brain connection patterns are characterized by a high clustering index and a short average distance between any two regions. Small-world topology is generally associated with global and local parallel information processing, sparse connectivity between nodes and low wiring costs (Bassett and Bullmore, 2006). Using this same connectivity datasets, structural and functional motifs composition (characteristic network building blocks) were studied (Sporns and Kotter, 2004). The results supported the hypothesis that while brain networks maximize both the number and the diversity of functional motifs, the repertoire of structural motifs is relatively small.

Functional human brain networks derived from functional Magnetic Resonance Imaging (fMRI), Electroencephalogram (EEG) and Magnetoencephalographic (MEG) data also exhibit small-world properties (Stam, 2004; Eguiluz et al., 2005; Salvador et al., 2005; Achard et al., 2006; Bassett et al., 2006). However, characteristics of the human brain anatomical network have been poorly investigated. This is due to difficulties in defining the basic structural elements of the human brain in terms of nodes and connections (Sporns et al., 2005) and also because the common invasive tracer methods cannot be applied. Recent steps in that direction were given by He et al. (2007), which investigated anatomical connections patterns in the human cerebral cortex in vivo using cortical thickness measurements from magnetic resonance images. For this, the cerebral cortex was segmented into 54 different areas for 124 normal brains, and any two areas

* Corresponding author. Fax: +53 7 208 6707.
E-mail address: iturria@cneuro.edu.cu (Y. Iturria-Medina).
Available online on ScienceDirect (www.sciencedirect.com).

1053-8119/$ - see front matter © 2008 Published by Elsevier Inc.
doi:10.1016/j.neuroimage.2007.10.060

were considered anatomically connected if they had statistically significant correlations in cortical thickness. This is based on studies suggesting that interregional statistical associations in cortical thickness provide important connectivity information (Worsley et al., 2005; Lerch et al., 2006). Then, a threshold value was applied to interregional correlation matrix in order to construct a binary undirected graph and estimate its properties, principally small-world properties and the connectivity degree distribution. Their results supported the hypothesis that human brain anatomical networks present small-world attributes and follow a degree distribution characterized by an exponentially truncated power-law. However, as their approach was limited to cortical networks, important subcortical structures such as the thalamus or the amygdales, which keep vital connections with cortical areas, were not taken into account.

On the other hand, the development of diffusion-weighted Magnetic Resonance Imaging (DW-MRI) techniques in the last decade makes possible the noninvasive study of the anatomical circuitry of the living human brain (Mori et al., 1999; Conturo et al., 1999; Tuch, 2002; Parker et al., 2002; Koch et al., 2002; Behrens et al., 2003; Hagmann et al., 2006; Iturria-Medina et al., 2007). In this context, Hagmann et al. (2006) reported for the first time small-world attributes in networks of small human cortical areas estimated from DW-MRI techniques. In that study, nodes of the analyzed network corresponded to small cubic regions of interest (ROI) covering the gray matter tissue, while arc weights were assigned according to the estimated fiber densities between nodes, which had been previously computed using an in vivo probabilistic nervous fiber tracking procedure (Wedeen et al., 2005). By applying a threshold to the created graph, an unweighted version was constructed and its small-world and hierarchical properties were analyzed. Their results show similar small-world topologies to those obtained for the rat and macaque monkey brain networks, which were created using post-mortem tracing techniques.

In the present paper we continue the characterization of the human brain anatomical connections by extending previous works in several ways. First, instead of an unweighted graph as in Hagmann et al. (2006) and He et al. (2007), a weighted version will be used for modeling the brain anatomical network. In this approach, the weights are obtained from the anatomical connections probability (ACP) matrix which gives the probability that any two areas are connected at least by a single nervous fiber. For obtaining the ACP matrix, anatomical connections patterns between 90 different anatomical gray matter regions will be estimated using DW-MRI techniques and Graph Theory (Iturria-Medina et al., 2007). These regions include both cortical and subcortical structures as defined by Tzourio-Mazoyer et al. (2002) according to functional and anatomical criteria. Finally, in addition to previous small-world and degree distribution analysis, other important network properties, such as efficiency, vulnerability, betweenness centrality and motif composition will be investigated.

The remainder of the paper is organized as follows. In the Materials and methods section the DW-MRI methodology used for estimating brain anatomical connections is briefly described, and it is shown that the obtained anatomical network can be viewed as a weighted non-directed graph. After that, concepts like small-world and network efficiency, degree distribution, vulnerability, betweenness centrality and motifs composition are briefly exposed. The experimental data and its preprocessing are also described. In the Results section significant findings are presented. Finally, the last section summarizes and discusses the principal results, and proposes some open problems to be considered in future studies.

Materials and methods

Mapping zone-zone brain anatomical connections using DW-MRI

DW-MRI techniques have being widely used to estimate the nervous fiber pathways connecting brain regions of interest (Mori et al., 1999; Conturo et al., 1999; Tuch, 2002; Parker et al., 2002; Koch et al., 2002; Behrens et al., 2003; Hagmann et al., 2006; Iturria-Medina et al., 2007). Recently, a novel DW-MRI and Graph Theory methodology (Iturria-Medina et al., 2007) was introduced with the principal purpose of summarizing anatomical connections patterns between brain gray matter areas. The proposed procedure consists of three major steps:

1. The cerebral volume is represented as a non-directed weighted graph $G_{brain,0}=[N_0, A_0, W_0]$, where N_0 is the set of voxels (nodes) having a non-zero probability of belonging to some cerebral tissue, A_0 is the set of white matter links (arcs) between contiguous voxels in N_0, and W_0 is a set of real numbers representing arcs weights. The weight of an arc is chosen so that it represents the probability that contiguous linked nodes are really connected by nervous fibers. It is defined by taken into account both the probability that linked nodes belong to gray/white matter (evaluated according to the probabilistic tissues segmentation of the corresponding anatomic T1-weighted image) and the probability of nervous fibers to be oriented around the direction of the arc (evaluated using the intravoxel white matter Orientational Distribution Function [ODF] estimated via DW-MRI techniques) (see Eq. (A1)). This ensures that only those pairs of contiguous nodes with high probability of belonging to gray/white matter and high probability of sharing fibers will have high arc weights, which is equivalent to have high probability of being connected. Also, since the DW-MRI profile is symmetric (efferent and afferent projections can not be distinguished) $G_{brain,0}$ is modeled as a non-directed graph (i.e. distinction between initial and terminal arc nodes is irrelevant).
2. In this step, an iterative algorithm (see Appendix C) is employed for finding the most probable trajectory (see Eq. ((A6)) between any two nodes, which is assumed to be the hypothetical nervous fiber pathway running between these points. Thus, quantification of the anatomical connectivity between both points is carried out according to the intrinsic information of this estimated connection route. Specifically, the node-node anatomical connectivity measure (ranging between 0, not connected, and 1, perfectly connected) is defined as the lowest weight of the arcs set belonging to the most probable path (see Eq. (A7)). This ensures that only those brain points with high arc weights (probability of white matter connection) of all the arcs belonging to their connection route will have a high connectivity value.
3. In order to characterize anatomical connections between n brain gray matter structures, the previous graph $G_{brain,0}$ is redefined as a $n+1$ partite graph G_{brain} by partitioning the initial nodes set N_0 into n non-overlapped gray matter subsets and one subset clustering the remaining nodes. In this context, the new weighted non-directed brain graph $G_{brain}=[N, A, W]$ consist of a set N of n nodes (gray matter regions), a set A of arcs (direct white matter connections between gray matter regions) and a set W of arc

weights (probability of connections between the gray matter regions). Graphically, G_{brain} is a discrete set of points (nodes) representing anatomic regions and a set of lines without arrow (arcs) representing connections between the regions. Based on the latter, three connectivity measures were defined: Anatomical Connection Strength (ACS), Anatomical Connection Density (ACD) and Anatomical Connection Probability (ACP). The interpretation of these measures is as follows. ACS provides an estimation of the potential information flow between any pair of regions, which is considered proportional to the amount of nervous fibers shared by these regions. As an indicator of the latter, we took the cross section area of the fiber connector volume on the surfaces of the two regions. This is estimated by counting the "effective" number of nodes on the surfaces of the zones involved in the connection, where each node is counted according to its maximum probability of being connected with the nodes in the surface of the second zone (see Eq. (A8)). On the other hand, ACD is a measure of the fraction of the connected superficial nodes with respect to the total number of superficial nodes of both areas (see Eq. (A10)). It allows, for example, to know if a pair of zones has more or less connection density than other pair of zones with different or equal number of superficial nodes. Finally, ACP measures the maximum probability of any two regions to be connected at least by a single nervous fiber connection. It is estimated as the maximum connectivity value between the superficial nodes of both involved areas (see Eq. (A11)) and allows to infer if any two gray matter regions can be functionally related independently of the strength and density of their possible anatomical connection.

In the present study, as our goal is to analyze a map of possible brain anatomical connections implying potential functional interchange between gray matter areas (i.e. which areas are directly connected or not), we employ the ACP measure for weighting zone-zone connections in G_{brain}. Further works might include ACS and ACD measures in order to complement the description of the brain anatomical network.

Graph analysis to characterize brain anatomical connections

A great number of natural systems can be represented by complex networks. Graph Theory is usually considered the most appropriate framework for the mathematical treatment of complex networks. In general, a complex network can be represented as a graph in which nodes correspond to the elements of the system and arcs to the interactions between them (Boccaletti et al., 2006). In our specific case, we want to study the weighted brain network $G_{brain}=[N, A, W]$, which model the anatomical connections between 90 cortical and subcortical gray matter regions. G_{brain} will be characterized attending to six basic aspects: small-world, network efficiency, degree distribution, vulnerability, betweenness centrality and motifs composition.

Small-world and network efficiency

The concept of "small-world" is strongly related to the average shortest path length (L) and clustering coefficient (C) concepts. Let us explain these in detail: the average shortest path length (L) of a given graph $G=[N, A, W]$, is a measure of the typical separation between two nodes i and j ($\forall i, j \in N$), and it is defined as the mean of geodesic lengths d_{ij} over all pairs of nodes (Watts and Strogatz, 1998; Watts, 1999; Boccaletti et al., 2006):

$$L = \frac{1}{n(n-1)} \sum_{\substack{i,j \in G \\ i \neq j}} d_{ij} \tag{1}$$

In the unweighted network context ($w_{ij}=[0,1] \in \mathbb{N}$), the geodesic length d_{ij} is defined as the number of arcs along the shortest path connecting nodes i and j. In the case of weighted networks ($w_{ij} \in \mathbb{R}$), the path with the minimum number of nodes is not necessarily the optimal d_{ij} and in some cases it is necessary to define a physical length associated to each arc (this should be a function of the characteristics of the hypothetical link among any nodes i and j). In this work, we follow the suggestion of Boccaletti et al. (2006), and assume that the physical length of an arc connecting nodes i and j is inversely proportional to the probability of the analyzed connection, i.e. $l_{ij} = \frac{1}{w_{ij}}$. That is, as the probability of nervous fiber connection is lower the nodes are more distant. Note that this assumption do not penalizes arc length according to the real spatial separation between the position of the modeled gray matter regions or according to the longitude of the connecting fiber pathway. This is because the defined probability of nervous fiber connection only depends on the "diffusion data coherence" and the white/gray matter presence along the estimated connection routes, and not on its longitude. Thus, long range connections (such as those maintained by the optic radiation and the occipital–frontal fascicule) can have arc length values similar to short range connections, only depending of their corresponding connection probabilities. The geodesic length d_{ij} is finally defined as the smallest sum of the arc lengths throughout all the possible paths from node i to node j. Note that for the particular case of unweighted graphs, $l_{ij}=1$ for all arcs and the geodesic lengths d_{ij} reduces to the minimum number of arcs traversed to get from i to j.

On the other hand, the clustering coefficient is a measure of the inherent tendency to cluster nodes into strictly connected neighborhoods (Watts and Strogatz, 1998). In a weighted graph, the clustering around a node i can be calculated as the geometric average of subgraph node weights (Onnela et al., 2005):

$$C_i = \frac{1}{k_i(k_i-1)} \sum_{\substack{j,k \in G \\ j,k \neq i}} \left(\tilde{w}_{ij} \cdot \tilde{w}_{jk} \cdot \tilde{w}_{ki}\right)^{\frac{1}{3}}, \tag{2}$$

where k_i is the number of arcs connecting node i (named degree of the node i) and the weights are scaled by the largest weight in the network, $\tilde{w}_{ij} = \frac{w_{ij}}{\max(w_{ij})}$. The clustering coefficient for the whole graph G is defined as the average of clustering around each node (Watts and Strogatz, 1998):

$$C = \frac{1}{n} \sum_{i \in G} C_i. \tag{3}$$

Formally, Watts and Strogatz (1998) defined small-world networks as those having small average shortest path length, like random networks ($\lambda \equiv \frac{L^{real}}{L^{rand}} \sim 1$), and high clustering coefficient, much larger than random networks ($\gamma \equiv \frac{C^{real}}{C^{rand}} \gg 1$). Additionally, the small-worldness condition lies in satisfying that $\sigma \equiv \frac{\gamma}{\lambda} > 1$ (Humphries et al., 2006).

The concept of small-world has been also expressed in terms of the information flow (Latora and Marchiori, 2001). That is, small-world networks are very efficient in terms of global and local communication (they have high global and local efficiency E_{glob} and E_{loc}, respectively). The E_{glob} of a graph G is defined as:

$$E_{glob} = \frac{1}{n(n-1)} \sum_{\substack{i,j \in G \\ i \neq j}} \frac{1}{d_{ij}}. \quad (4)$$

This measure reflects how efficiently information can be exchanged over the network, considering a parallel system in which each node sends information concurrently along the network. On the other hand, the E_{loc} of G is defined as the average efficiency of the local subgraphs:

$$E_{loc} = \frac{1}{n} \sum_{i \in G} E_{glob}(G_i), \quad (5)$$

where G_i is the subgraph of the neighbors of i. This measure reveals how much the system is fault tolerant, showing how efficient the communication is among the first neighbors of i when it is removed. That is, the efficiency formalization gives a clear physical meaning to the concept of small-world, and allows a precise quantitative analysis of weighted networks (Latora and Marchiori, 2001).

In order to compare the efficiency of a given real network with the efficiency of its equivalent random network (characterized by the same number of nodes and arcs placed randomly), from now on we will refer to the relative local efficiency (E^*_{loc}) and the relative global efficiency (E^*_{glob}) measures (i.e. the ratio between the local and global efficiencies of the real and random networks respectively).

Degree distribution

Since not all nodes in a complex network have the same degree, usually a degree distribution $P(k)$ is defined. This gives the probability that a randomly selected node has k arcs (Erdös and Rényi, 1959). The degree distribution properties are commonly employed to classify networks into different categories. Amaral et al. (2000) presented evidences of the occurrence of three classes of small-world networks attending to their degree distribution properties: 1) scale-free networks, 2) broad-scale networks, and 3) single-scale networks.

Scale-free networks, for example the World-Wide Web (Albert et al., 1999), are characterized by a degree distribution that decays as a power law, i.e. $P(k) \sim k^{-\alpha}$, with exponents varying in the range $2 < \alpha < 3$. This power law indicates the preferential attachment of the nodes in the network to some specific hub nodes.

Broad-scale networks are characterized by a degree distribution that has a power law regime followed by a sharp cutoff, i.e. $P(k) \sim k^{\alpha-1} f(k/k_{crit})$. The function $f(k/k_{crit})$ has a sharp cut-off for degrees $k > k_{crit}$, constraining the number of nodes that can be connected to the hub nodes.

Finally, single-scale networks are characterized by a degree distribution with a fast decaying tail, i.e. $P(k) \sim f(k/k_{crit})$. Commonly for single-scale and broad-scale regime the sharp cutoff functions $f(k/k_{crit})$ are exponential or Gaussian (Amaral et al., 2000).

The information expressed by the degree distribution function is often presented by the cumulative degree distribution $P_c(k) = \sum_{k'=k}^{\infty} P(k')$, which is usually used to reduce the effects of noise corresponding to small networks (Strogatz, 2001; He et al., 2007).

Vulnerability

The vulnerability analysis of complex networks provides valuable quantitative information about the possible damage caused by the hypothetical failure of its elements. That is, this type of analysis allows to identify which are the most critical or indispensable structures for the appropriate operation of the network, and in the specific case of brain networks, it could be useful to evaluate the damage caused by illness known to affect gray matter connections such as Alzheimer Disease (Pearson et al., 1985; Morrison et al., 1986) and Schizophrenia (Mitelman et al., 2007).

By associating the performance of a network with its global efficiency, the vulnerability V_i of a node i can be defined as the drop in network performance when node i and its connections are removed (Newman and Park, 2003; Goldshtein et al., 2004; L.da F. Costa et al., 2006):

$$V_i = \frac{E_{glob} - E^i_{glob}}{E_{glob}}, \quad (6)$$

where E_{glob} and E^i_{glob} are the global efficiency of the network with and without node i.

Then, the vulnerability of the entire network G is defined as the maximum vulnerability for all of its nodes (Latora and Marchiori, 2005; L.da F.Costa et al., 2006):

$$V = \max_i V_i. \quad (7)$$

Betweenness centrality

Betweenness centrality is a widely used measure to identify the most central nodes in a graph, which are associated to those nodes that acts as bridges between the others nodes (Freeman, 1977; Dall'Asta et al., 2006; Bassett et al., 2006; Honey et al., 2007). It is defined as the fraction of shortest paths between pairs of nodes that passes through a given node. Mathematically, for weighted networks, if σ^w_{kj} is the total number of shortest paths from k to j and $\sigma^w_{kj}(i)$ is the number of these paths passing through node i, the weighted betweenness centrality of node i is (Dall'Asta et al., 2006):

$$b^w_i = \sum_{\substack{k,j \in G \\ k \neq j}} \frac{\sigma^w_{kj}(i)}{\sigma^w_{kj}}. \quad (8)$$

Motifs composition

Network motifs are subgraphs that appear more frequently in a real network than could be statistically expected, and are associated to the network evolution (Milos et al., 2002; Sporns and Kotter, 2004; Onnela et al., 2005). To detect those motifs that are likely to be important, Milos et al. (2002) proposed to compare the analyzed real network to suitably randomized networks and to select patterns appearing in the real network at numbers significantly higher than those in the randomized networks. Different motifs classes are

generally distinguished according to the motif's size (M), representing the number of involved nodes, and the number and pattern of interconnections.

In the case of weighted networks, Onnela et al. (2005) defined the *intensity* (I_M) of motif M as the geometric mean of its arc weights, and the *coherence* (Q_M) of motif M as the ratio of the geometric to the corresponding arithmetic mean. Based on these measures, motif scores were defined as:

$$ZI_M = \frac{(I_M - \langle i_M \rangle)}{\left(\langle i_M^2 \rangle - \langle i_M \rangle^2\right)^{\frac{1}{2}}}, \qquad ZQ_M = \frac{(Q_M - \langle q_M \rangle)}{\left(\langle q_M^2 \rangle - \langle q_M \rangle^2\right)^{\frac{1}{2}}}, \tag{9}$$

where ZI_M and ZQ_M are the motif intensity and coherence score respectively; i_M and q_M are the total intensity and coherence of motif M in one realization of the random regime, respectively.

Experimental data

DW-MRI datasets corresponding to 20 right-handed healthy subjects (mean age: 31.10, S.D.: 7.43) were acquired using a MRI scanner Siemens Symphony 1.5 T (Erlangen, Germany) and a single shot EPI sequence. Each dataset consists of 12 diffusion-weighted images and a $b=0$ image, with the following parameters: 50 contiguous slices of 3 mm thickness; $b=1200$ s/mm^2 for the weighted images; FOV=256×256 mm^2; acquisition matrix=128×128; corresponding to an 'in plane' spatial resolution of 2×2 mm^2; TE/TR=160 ms/7000 ms. The aforementioned acquisition was repeated 5 times to improve signal to noise ratio (SNR). In order to improve EPI quality, magnitude and phase difference images of a T2 gradient echo field mapping sequence were acquired with TE=7.71 ms and 12.47 ms. Also, for each subject a 3D high resolution T1-weighted image (MPRAGE) covering the whole brain was acquired with the following parameters: 160 contiguous slices of 1 mm thickness in sagittal orientation; in plane FOV=256×256 mm^2, corresponding to an in plane spatial resolution of 1×1 mm^2; TE/TR=3.93 ms/3000 ms.

In order to remove remaining distortions an affine 3D mutual normalized information-based registration method (Studholme et al., 1998) was used. The DW-MRI images were corrected from EPI distortions using the SPM FieldMap toolbox (Hutton et al., 2002). The T1-weighted 3D anatomical image was registered to the $b=0$ image using a normalized mutual information method (Studholme et al., 1998). Both diffusion-weighted images and T1-weighted images were interpolated and written with a spatial resolution of 2×2×2 mm^3. The registered interpolated T1-weighted image was automatically segmented into 90 gray matter structures (Tzourio-Mazoyer et al., 2002) using the IBASPM toolbox (available at http://www.fil.ion.ucl.ac.uk/spm/ext/#23IBASPM) (Alemán-Gómez et al., 2006). ODF maps were estimated using the procedure described in Appendix B.

Additionally, a set of three brain anatomical connectivity matrices were obtained from the Computational Cognitive Neuroscience Laboratory, Indiana University Bloomington (http://www.indiana.edu/~cortex/CCNL.html). These datasets correspond to the cat cerebral cortex, the macaque monkey visual cortex and the macaque monkey cerebral cortex, and consist of unweighted matrices with number of nodes 95, 30 and 73, respectively.

In all cases, randomized counterpart versions of the original networks were created using a rewiring algorithm (Maslov and Sneppen, 2002). This algorithm preserves the degree of each individual node, but connection weights are randomized until weight correlations with the original network are lost.

Results

Fiber tracking and zone–zone connectivity

Using the DW-MRI methodology described above, anatomical connections between the defined 90 brain gray matter structures were estimated for the 20 healthy subjects. Fig. 1 presents the obtained mean intersubject ACP matrix. The element C_{ij} is the connectivity value between regions i and j. As previously mentioned, this map is symmetric. Self connections are excluded, which implies a diagonal black line in the matrix. Also, it should be kept in mind that for each subject the anatomical reconstruction consisted of the whole brain with the two hemispheres (i.e. including callosal connections). Note for example the high connectivity values between the left and right superior frontal gyrus, or between the left and right superior occipital poles, which is in accordance with existing anatomical knowledge (Gómez-Padrón et al., 1985; Witelson, 1989; Standring, 2004).

In order to evaluate intersubject dis(similarity), correlations coefficients between their corresponding ACP matrices were calculated. Significant correlations coefficients were obtained (ranging between 0.65 and 0.88) with corresponding p values in the order of 10^{-220}.

Small-world and network efficiency analysis

First, the relative clustering coefficient γ, the relative average shortest path length λ and the small-worldness parameter σ were calculated for each subject. The results (first three columns of Table 1) confirm the expected small-world attributes of the studied brain anatomical networks according to the Watts-Strogatz (1998) and Humphries et al. (2006) conditions (i.e. $\lambda \sim 1$, $\gamma \gg 1$ and $\sigma > 1$). The obtained mean parameters of interest were $\gamma_{mean}=1.85$, $\lambda_{mean}=1.12$ and $\sigma_{mean}=1.64$, satisfying the previous conditions.

In a second statistical analysis, a network efficiency study revealed that, compared with the corresponding random networks, the human brain architectural network (as well as other mammalian species brain networks, as we will see later) presents smaller global efficiency and bigger local efficiency, i.e. both individual and mean values of E^*_{glob} are under 1, while the corresponding E^*_{loc} values are always above 1 (see columns 4 and 5 of Table 1, respectively). These results are in accordance with those obtained for brain functional networks corresponding to the same gray matter parcellation scheme (Achard and Bullmore, 2007). In the Summary and discussion section we will comment more about this, including the analysis of other mammalian brain species results.

Degree distribution analysis

A degree distribution analysis revealed that the studied brain anatomical networks correspond to a power law regime followed by a sharp cutoff, as broad-scale networks. Table 1 (columns 6 and 7) presents the obtained α and k_{crit} parameters corresponding to a broad-scale regime following the form $P(k) \sim k^{\alpha-1} \exp(k/k_{crit})$.

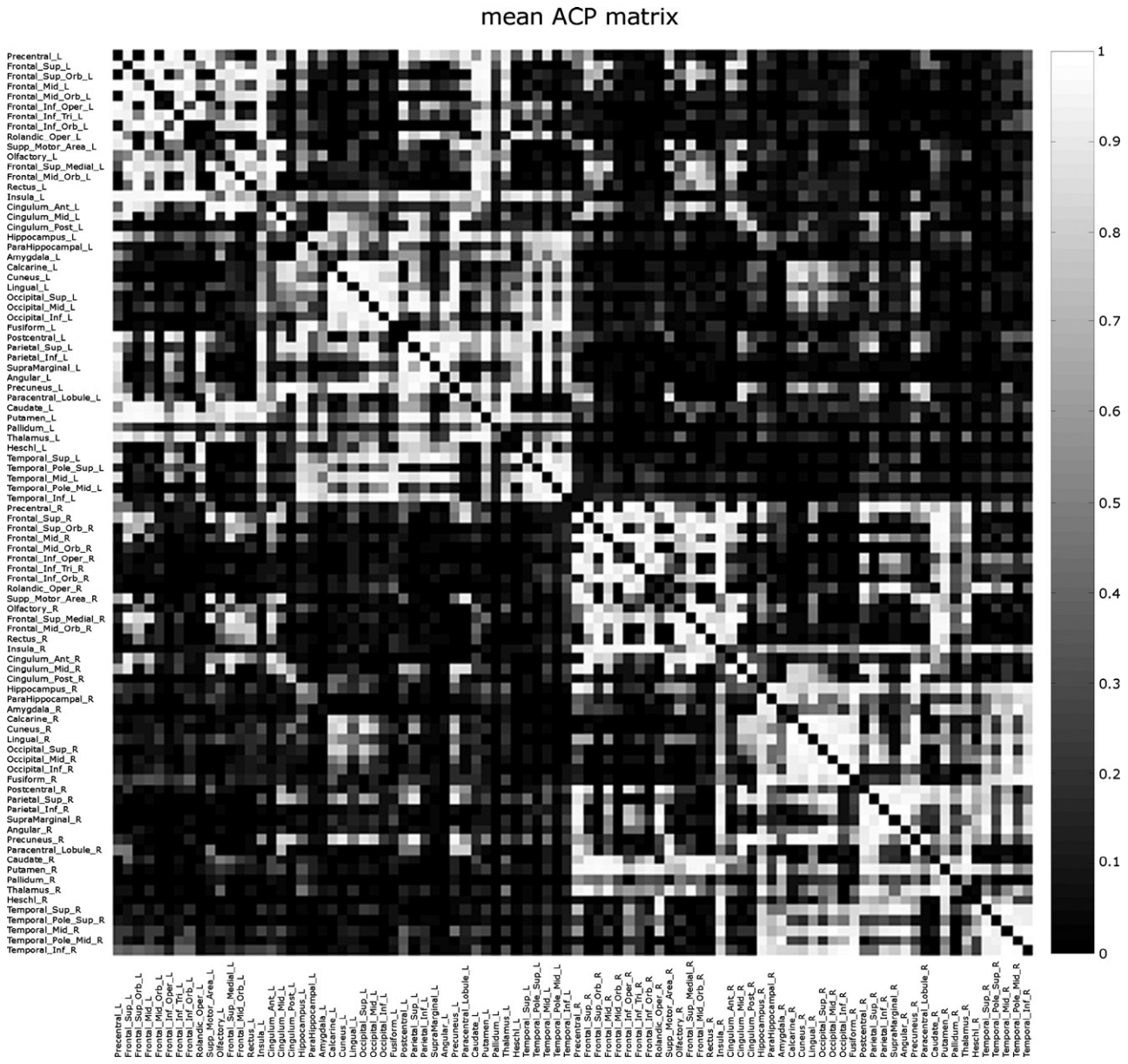

Fig. 1. Mean ACP matrix for 90 gray matter regions defined on the brain of 20 healthy subjects. The element $C_{i,j}$ is the connectivity value between regions i and j. Self connections are excluded, which implies a diagonal black line in the matrix. As previously mentioned, this map is symmetric. The color code represents the index of connectivity.

Fig. 2 illustrates the inter-subject mean cumulative degree distribution and its standard deviation. All the corresponding multiple determination coefficients, R-square (i.e. a measure of how successful the fit is in explaining the variation of the data, a value closer to 1 indicates a better fit), were in the order of 0.99. The mean estimated exponent α was 1.34. Additionally, the resulting mean parameter k_{crit} indicate that even the most connected areas in the brain have a physical constraint of around 5.81 inter-regional connections according to the used gray matter parcellation. These results are similar to those reported in Achard et al. (2006) for a human functional network involving the same gray matter areas (i.e. a degree distribution followed an exponentially truncated power law with an exponent parameter $\alpha=1.80$ and a cutoff degree $k_{crit}=5$).

Vulnerability and betweenness centrality analysis

In order to make a first inference about the most critical or indispensable structures in the brain anatomical networks, the vulnerability of the 90 defined brain gray matter areas for each subject were computed using expression (6). Fig. 3a summarizes the obtained mean vulnerability results. The identified most vulnerable areas are: putamens, precuneus, insulas, superior parietals and superior frontals. In a complementary analysis, the betweenness centrality of each gray matter area was estimated using expression (8). The identified most central areas agree totally with the obtained in the previous vulnerability analysis (see Fig. 3b). In both cases, the selected regions were identified by applying a z-test (H_0: $z=0$) with a 0.05 significance level to the resulting

Table 1
Obtained human brain networks attributes

Subjects	γ	λ	σ	E^*_{glob}	E^*_{loc}	α	k_{crit}
1	1.65	1.11	1.48	0.94	1.15	1.38	6.49
2	1.52	1.10	1.37	0.94	1.11	1.33	6.11
3	1.64	1.12	1.46	0.93	1.14	1.36	6.13
4	1.83	1.13	1.62	0.92	1.24	1.37	5.72
5	1.67	1.12	1.48	0.93	1.19	1.40	5.85
6	2.00	1.13	1.77	0.92	1.28	1.36	5.72
7	1.69	1.11	1.52	0.93	1.17	1.52	6.62
8	1.92	1.12	1.71	0.93	1.32	1.28	5.35
9	1.51	1.08	1.39	0.95	1.13	1.40	6.47
10	2.37	1.16	2.04	0.90	1.42	1.28	5.34
11	1.77	1.12	1.57	0.93	1.17	1.31	5.52
12	2.19	1.15	1.90	0.91	1.37	1.33	5.50
13	1.61	1.11	1.44	0.93	1.18	1.30	5.86
14	2.13	1.14	1.86	0.92	1.31	1.38	6.01
15	1.83	1.13	1.61	0.92	1.25	1.33	5.59
16	1.91	1.13	1.67	0.92	1.24	1.31	5.65
17	2.05	1.14	1.79	0.92	1.27	1.29	5.43
18	1.87	1.13	1.64	0.92	1.23	1.30	5.32
19	1.73	1.11	1.56	0.93	1.19	1.28	5.78
20	2.11	1.16	1.81	0.91	1.36	1.32	5.81
Mean	1.85	1.12	1.64	0.93	1.24	1.34	5.81
S.D.	0.23	0.02	0.18	0.01	0.08	0.05	0.38

mean vulnerability and mean betweenness centrality vectors respectively.

Motifs composition

Since the human brain anatomical networks studied here are symmetrical, our motifs composition analysis was restricted to find only those symmetrical motifs that appear significantly increased in the analyzed networks (let us say motifs with identity number [ID] 9 and 13 for motifs of size 3, and motifs with ID 75, 95, 159, 178, 194 and 199 for motifs of size 4; see Fig. 4a). In order to carry out the motifs analysis, 30 reference random matrices were generated. Fig. 4b and c show the obtained motifs intensity and motifs coherence scores for each subject, with motifs sizes 3 and 4, respectively. Notice that for $M=3$ (Fig. 4b), only a candidate motif with ID=13 seems to appear significantly increased while for $M=4$ (Fig. 4c) candidate motifs with ID=159, 194 and 199 are those that seem to appear significantly increased. Using a 0.05 significance level, we confirmed that the mentioned candidate motifs show statistically significant intensity and coherence deviation from the reference system, being them the obtained symmetrical human brain motifs of size 3 and 4.

Summary and discussion

In this work some basic statistical aspects of the human brain anatomical network were analyzed. The studied networks consisted of white matter connections between 90 cortical and subcortical gray matter regions, which were defined according to functional and anatomical criterions (Tzourio-Mazoyer et al., 2002). Connections among the different regions were estimated for 20 healthy subjects according to a graph-based DW-MRI procedure (Iturria-Medina et al., 2007) and the weighted networks analysis was centered in their small-world attributes, efficiency, degree distribution, vulnerability, betweenness centrality and motifs composition properties.

To our knowledge, until now only two previous works have being presented with a similar purpose. In the first previous study (Hagmann et al., 2006), the analyzed brain network consisted of a lot of gray matter cubic regions defining nodes whose corresponding arc weights connections were assigned according to the estimated nervous fiber density (Hagmann et al., 2004) between them. An unweighted version of the created graph was analyzed taking into account its small-world and hierarchical properties. In the second previous study (He et al., 2007), the network summarized the obtained connectivity patterns between 54 cortical areas segmented for 124 normal brains. Connections between areas were estimated using cortical thickness measurements from magnetic resonance images. The brain anatomical unweighted network analysis was centered principally in its small-world attributes and degree distribution properties.

In our first brain anatomical network statistical analysis, small-world and efficiency properties were studied. The results confirm the small-world attributes of the human brain anatomical network (Table 1). The obtained mean parameters of interest were $\gamma_{mean}=1.85$, $\lambda_{mean}=1.12$, with a resulting small-worldness parameter of $\sigma_{mean}=1.64$, satisfying the Watts-Strogatz (1998) and Humphries et al. (2006) conditions (i.e. $\lambda\sim1$, $\gamma\gg1$ and $\sigma>1$). However, it is important to notice that according to Hagmann et al. (2006), small-worldness parameter as well as the relative clustering coefficient should increases significantly when the number of brain network nodes increases. Although our results are in agreement with the results reported by Hagmann et al. (2006) and He et al. (2007) it should be noted that the used gray matter parcellation procedures differ in these studies. Additionally, our analysis was based on a weighted network scheme in contrast to an unweighted scheme as in previous works. Unfortunately, these procedure differences hinder a reliable quantitative parameter comparison between these three human anatomical studies.

Other brain mammalian species (cat and macaque monkey) present similar small-world anatomical attributes (Sporns and Zwi, 2004; Hilgetag and Kaiser, 2004). Nevertheless, as happens with previous human studies, a quantitative parameters comparison between our results and the reported by these post-mortem tracing animal studies it is not straightforward due to differences in the employed procedures (mainly the different used gray matter segmentation schemes).

In addition, the network efficiency analysis provided an interesting result: compared with the corresponding random networks, human brain anatomical networks present bigger local efficiency and smaller global efficiency. These results agree with that obtained by Achard and Bullmore (2007) for human brain functional networks, and also with those obtained by us for the cat cerebral cortex ($E^*_{loc}=1.37$ and $E^*_{glob}=0.96$), the macaque monkey visual cortex ($E^*_{loc}=1.24$ and $E^*_{glob}=0.97$) and the macaque monkey cerebral cortex ($E^*_{loc}=1.86$ and $E^*_{glob}=0.93$). In our opinion, this suggests that mammalian brains evolved trying to maintain a high local efficiency, which is equivalent to prioritize the integration among regions specialized in similar types of functional information and, also, guaranties the tolerance to possible fails at the local level. On the other hand, the global efficiency (i.e. the capacity to exchange information among all the regions) is small compared with corresponding random networks. A reason for this could be that the global exchange may not be completely necessary, a fact related to the optimization of the brain integration process.

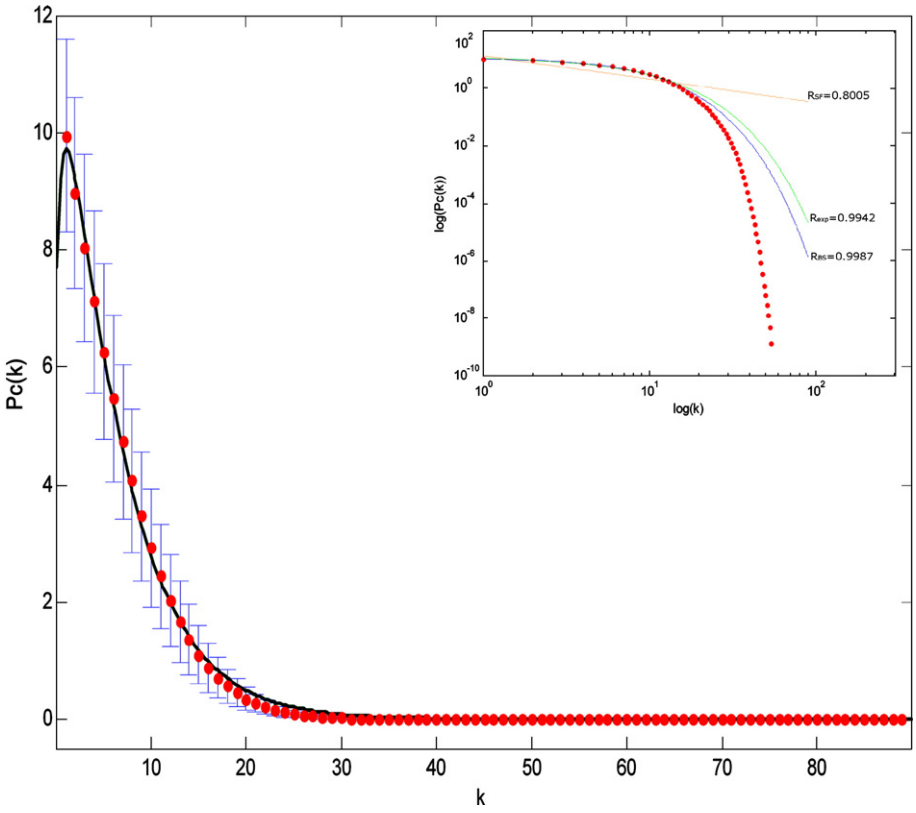

Fig. 2. Estimated inter-subject mean cumulative degree distribution (red points) and standard deviation (blue error bars). The green line represents the fitted exponential truncated power law corresponding to a broad scale regime of the form $P(k) \sim k^{\alpha-1}\exp(k/k_{crit})$, with $\alpha=1.34$ and $k_{crit}=5.81$. Inset: log–log plot of the mean cumulative degree distribution. The red points indicate observed data, the blue line is the best fitted exponential truncated power law ($R_{BS}=0.9987$), the green line is an exponential ($R_{exp}=0.9942$), and the orange line is a power law ($R_{SF}=0.8005$).

A degree distribution analysis revealed that the studied brain networks present a power-law regime followed by a sharp cutoff (Fig. 2), as broad-scale networks. In this kind of networks, the preferential attachment to the hub nodes has a physical constraint, which in terms of brain anatomical connections is related to the maximum number of areas connected to the hub nodes and responds to structural cost optimization process (e.g. optimization of the axonal volume covering inter-regional brain connections). In addition, other anatomical and functional human brain studies have presented similar degree distribution results (Achard et al., 2006; He et al., 2007). This supports the broad-scale attributes of the human brain network; however, final conclusions about this topic require future analysis to much larger brain networks with thousands of nodes.

The vulnerability and betweenness centrality analysis allowed identifying the most critical anatomical nodes in the brain, reveling quantitative information about the global damage caused by the hypothetical failure of these nodes. According to the gray matter parcellation that was used, the most vulnerable and central areas were (see Fig. 3): putamens, precuneus, insulas, superior parietals and superior frontals. On the other hand, note that some areas cause a negative vulnerability to the studied brain networks, which means that the anatomical brain system can be more efficient without them (the most representative are: superior temporal poles, pallidums, supramarginals and hechls). This can be related to the anatomical cost of their existence, and suggest that even implying a possible loss in global anatomical efficiency, these structures were maintained in the brain circuitry through the evolutionary processes due to their specific important functions. Also, as an interesting point, we may have expected that thalamic regions belong to the most critical or indispensable gray matter centers in the brain. However, the used vulnerability and betweenness centrality measures are strongly related to the number of connections of the analyzed areas, and the obtained results indicate that thalamic regions are not the most connected areas although surely they have important connections with some specific anatomic regions.

In the context of brain networks, a structural (anatomical) motif may consist of a set of brain areas and pathways that can be potentially engage in different patterns of interactions (Sporns and Kotter, 2004). In practice, networks motifs are identified as those subgraphs appearing more frequently in a real network than could be statically expected (Milos et al., 2002; Onnela et al., 2005). In this work, it was looked for the first time into the structural motif composition of the human brain anatomical network. According to the used gray matter parcellation and the employed weighted motif detection procedures (Onnela et al., 2005), the obtained structural motifs were those with ID=13, for $M=3$, and with ID=159, 194 and 199, for $M=4$ (see Fig. 4). This result keeps some essential similarities with the obtained for cat and macaque cerebral cortex by Sporns and Kotter (2004), that is: motifs at $M=4$ are the expanded versions of the obtained motif at $M=3$, forming a reciprocally connected nodes chain, where pairs of connections linking the ends of the chain can be absent; thus, nodes in the

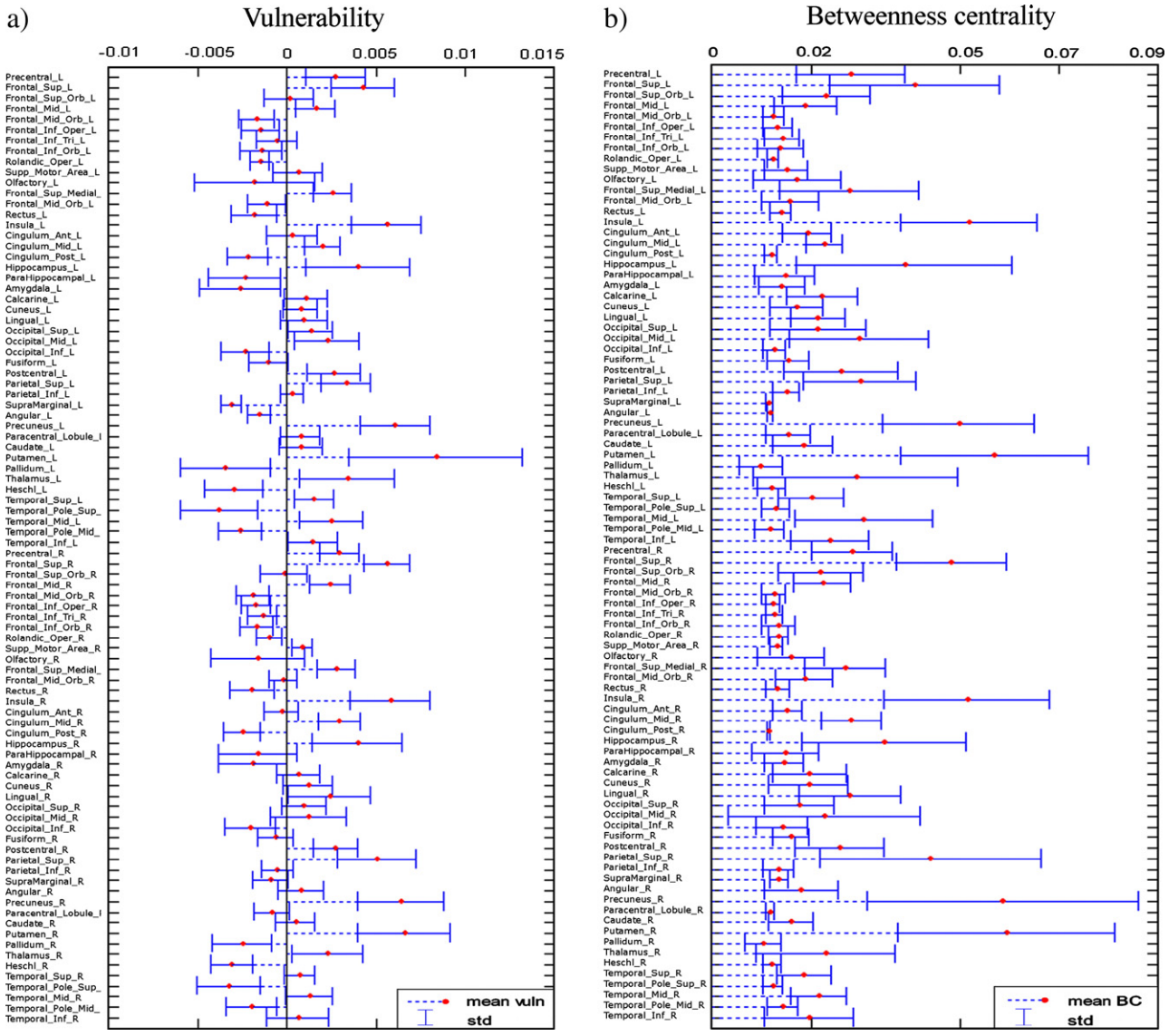

Fig. 3. Mean inter-subject vulnerability (a) and betweennes centrality (b) results for the 90 defined brain gray matter areas. Additionally, using a z-test (H_0: $z=0$) with a 0.05 significance level, the most vulnerable and central areas were identified. In both cases, these areas are: putamens, precuneus, insulas, superior parietals, and superior frontals.

motifs are highly integrated with their neighbors although some of them do not communicate directly, reflecting the basic principles of integration and segregation in the brain.

A limitation of the presented study is the symmetrical configuration of the analyzed brain connectivity matrices, which is a consequence of the inherent symmetrical properties of DW-MRI techniques (distinction between afferent and efferent fiber projections it is not possible yet). This fact causes, for example, the restriction of the motif composition analysis to consider only those symmetrical candidate motifs. Nevertheless, a previous work (Young, 1993) reported that around 85% of the total possible connections between 73 primate brain areas are reciprocals.

An important element in the DW-MRI Graph-Based methodology employed here for estimating brain anatomical connections (Iturria-Medina et al., 2007) is the angular resolution of the diffusion-weighted images. In this work we used low angular resolution data due to a system limitation, but certainly more reliable results can be obtained using high angular resolution techniques, which allows a more precise characterization of the intravoxel white matter orientation (Tuch, 2004; Wedeen et al., 2005) and thus a more realistic characterization of the brain structure. Other relevant matter is how to use the obtained ACP matrices to elucidate which gray matter areas are actually connected or not. A tentative alternative could be the selection of a threshold value to create unweighted connectivity matrices. However, the choice of the appropriate threshold is generally an elusive point, and that's why in this study we chose to work only with probability of connections between zones instead of the simpler on–off connectivity analysis. Additionally, future works might be directed to explore the effects of different tracking methods on the network attributes. Surely, common findings across different tracking methods would provide more confidence for the anatomical network graphical description. Nonetheless, in recent studies (unconcluded) we have obtained significant similarity

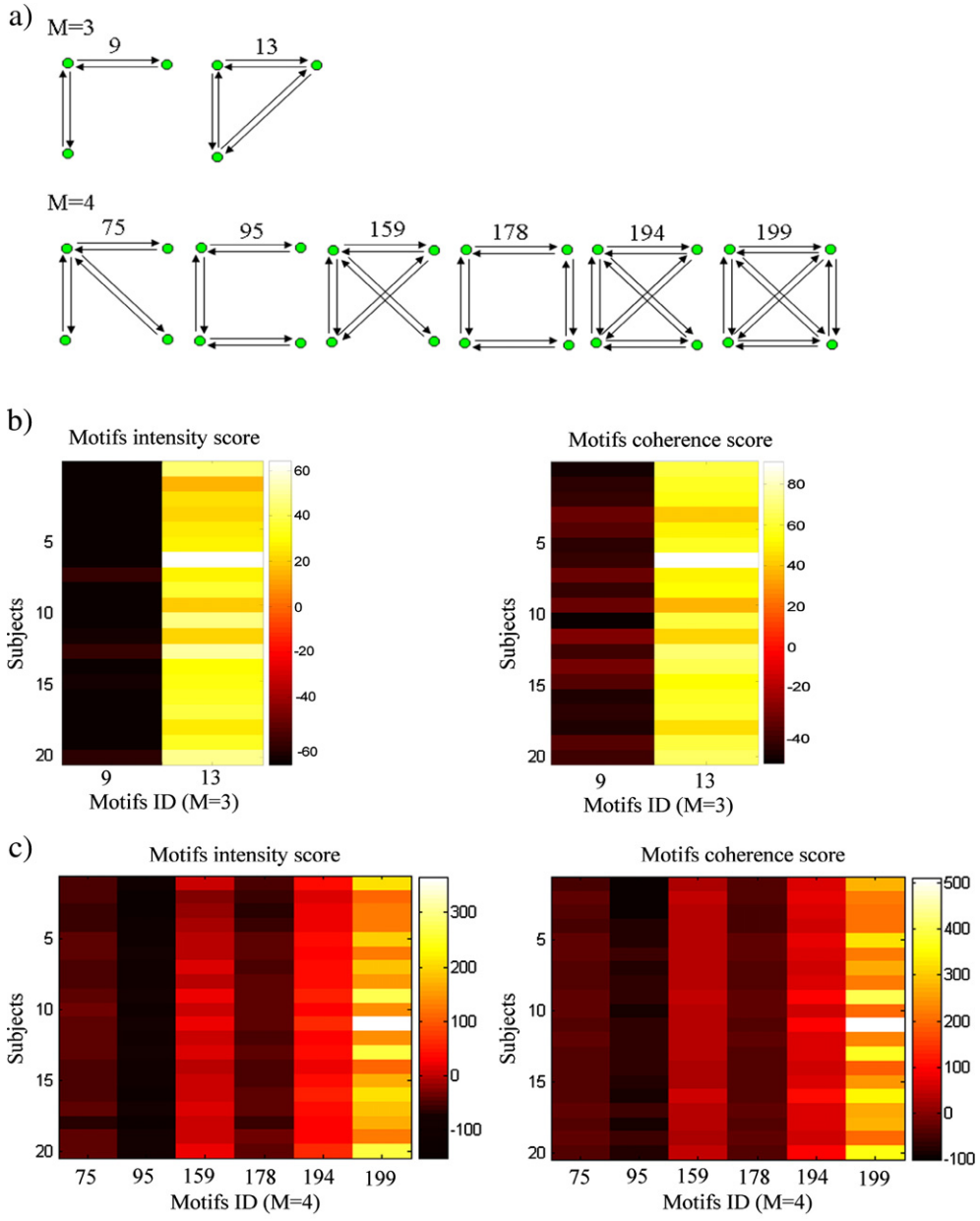

Fig. 4. Motifs results for motifs size $M=3$ and $M=4$. (a) Candidate symmetrical motifs of size 3 and 4. Numbers refer to the motif's identity number (ID). (b) Obtained motifs intensity and motifs coherence scores for each subject, with $M=3$. (c) Obtained motifs intensity and motifs coherence scores for each subject, with $M=4$. In panels (b) and (c), the color code represents the z-score index. Using a 0.05 significance level, significant motifs found in the analyzed human brain networks were those with ID=13, for $M=3$, and with ID=159, 194 and 199, for $M=4$.

among the connectivity patterns of healthy subjects using two different fiber tractography procedures (i.e. the Graph-based method employed here and the probabilistic tracking method implemented in the FSL software package [http://www.fmrib.ox.ac.uk/fsl]). This will be the subject of a separate publication.

Reliable gray matter parcellation is crucial for obtaining consistent connectivity patterns between individuals. Therefore, a key element of the used methodology to create the brain anatomical network is its high dependency on the employed atlas. Although the atlas used here was carefully created taking into account relevant anatomical and functional details (Tzourio-Mazoyer et al., 2002), in the future it might be more meaningful to use advanced integrative atlases based on finer cytoarchitecture, myeloarchitecture and MRI procedures (Toga et al., 2006; He et al., 2007).

Further studies should focus on: improving the characterization of the brain anatomical connections (using for example high angular resolution DW-MRI techniques, a priori connectivity information and others fiber tracking methodologies), extending the analysis to other interesting network properties (such as brain complexity, hierarchical features and functional motif composition) and to other brain connection measures (such as ACS and ACD), as well as exploring sex and right–left handed (dis)similarities.

Appendix A. Mathematical expressions of the used DW-MRI and Graph-based connectivity model

Arc weights

Given the weighted non-directed graph $G_{\text{brain},0}=[N_0,\ A_0,\ W_0]$, the weight of an arc $a_{ij}\in A_0$ linking two contiguous nodes i and j ($i,j\in N_0$), with spatial vectors position $\overrightarrow{r_i}$ and $\overrightarrow{r_j}$ respectively, is defined as:

$$w(a_{ij})\equiv w(a_{ji}) = P_{\text{mat}}(\overrightarrow{r_i})P_{\text{mat}}(\overrightarrow{r_j})[P_{\text{diff}}(\overrightarrow{r_i},\Delta\overrightarrow{r_{ij}}) + P_{\text{diff}}(\overrightarrow{r_j},\Delta\overrightarrow{r_{ji}})], \tag{A1}$$

where the two basics functions P_{mat} and P_{diff} enclose anatomical and diffusion information respectively. The first of these functions was defined as follows:

$$P_{\text{mat}}(\overrightarrow{r}) = \frac{\alpha P_{\text{WM}}(\overrightarrow{r}) + P_{\text{GM}}(\overrightarrow{r})}{1+(\alpha-1)P_{\text{WM}}(\overrightarrow{r})}, \tag{A2}$$

where P_{WM} and P_{GM} are probabilistic maps of white and gray matter (WM and GM) respectively and α is a tuning parameter.

The other function, $P_{\text{diff}}(\overrightarrow{r_i},\Delta\overrightarrow{r_{ij}})$, characterizes fiber coherence along $\Delta\overrightarrow{r_{ij}} = \overrightarrow{r_j} - \overrightarrow{r_i}$, which is the direction of the arc a_{ij}, and can be inferred from DW-MRI images using methods for the description of the intravoxel white matter structure. Here, $P_{\text{diff}}(\overrightarrow{r_i},\Delta\overrightarrow{r_{ij}})$ is assumed to be the integral of the fiber Orientational Distribution Function (ODF) over a solid angle β around $\Delta\overrightarrow{r_{ij}}$:

$$P_{\text{diff}}(\overrightarrow{r_i},\Delta\overrightarrow{r_{ij}}) = \frac{1}{Z}\int_{\beta}\text{ODF}(\overrightarrow{r_i},\Delta\overrightarrow{r_{ij}})\text{d}S. \tag{A3}$$

Z is a normalization constant chosen to fix to 0.5 the maximum value of the set $\{P_{\text{diff}}(\overrightarrow{r_i},\Delta\overrightarrow{r_{ij}})\}_{\forall\overrightarrow{r_j}\in N_i^{\text{neig}}}$. Note that generally $P_{\text{diff}}(\overrightarrow{r_i},\Delta\overrightarrow{r_{ij}})\neq P_{\text{diff}}(\overrightarrow{r_j},\Delta\overrightarrow{r_{ji}})$.

Fiber tracking and node–node connectivity

In the previous graph $G_{\text{brain},0}$, where each arc weight is considered as the probability of its existence, the problem of searching the most probable path between nodes $\overrightarrow{r_{i_1}}$ and $\overrightarrow{r_{i_L}}$ is equivalent to find the path $\rho_{i_1\ldots i_L}=\{a_{i_1i_2};a_{i_2i_3};\ldots;a_{i_{L-1}i_L}\}$ with maximum total probability:

$$P[\rho_{i_1\ldots i_L}] = w(a_{i_1,i_2})\prod_{k=2}^{L-1}w^{\text{cond}}(a_{i_ki_{k+1}}|a_{i_{k-1}i_k})\Psi(\rho_{i_{k-1}\ldots i_{k+1}}), \tag{A4}$$

where the term $w^{cond}(a_{i_ki_{k+1}}|a_{i_{k-1}i_k})$ is the conditional weight of the arc $a_{i_ki_{k+1}}$ given arc $a_{i_{k-1}i_k}$:

$$w^{\text{cond}}(a_{i_ki_{k+1}}|a_{i_{k-1}i_k}) = P_{\text{mat}}(\overrightarrow{r_{i_{k+1}}})[P_{\text{diff}}(\overrightarrow{r_{i_k}},\Delta\overrightarrow{r_{i_ki_{k+1}}}) + P_{\text{diff}}(\overrightarrow{r_{i_{k+1}}},\Delta\overrightarrow{r_{i_{k+1}i_k}})]. \tag{A5}$$

The function Ψ penalizes path curvature between any three consecutive steps of the path and is selected in a way that allows only those fiber trajectories with curvature angles smaller than 90°.

Based on this, the estimated nervous fiber trajectory running from $\overrightarrow{r_{i_1}}$ and $\overrightarrow{r_{i_L}}$ will be given by the most probable path:

$$\tilde{\rho}_{i_1\ldots i_L} = \underset{\forall\rho_{i_1\ldots i_L}}{\text{argmax}}(P[\rho_{i_1\ldots i_L}]). \tag{A6}$$

To solve previous Eq. (A6) an iterative algorithm was proposed (see Appendix C). Then, quantification of the anatomical connectivity between nodes $\overrightarrow{r_{i_1}}$ and $\overrightarrow{r_{i_L}}$ is defined according to the parameters of the connection route among them, specifically as the lowest weight of the arcs belonging to it:

$$C_{\text{node}}(\overrightarrow{r_{i_1}},\overrightarrow{r_{i_L}}) = \min_{\forall a\in\tilde{\rho}_{i_1\ldots i_L}}(w(a)). \tag{A7}$$

Zone–zone connectivity

The expression for the ACS measure between any two gray matter regions R_1 and R_2 reads:

$$C_{\text{Zone}}^{\text{ACS}}(R_1,R_2) = \sum_{\forall\overrightarrow{r_m}\in N_2^s}\zeta_{\overrightarrow{r_m}} + \sum_{\forall\overrightarrow{r_n}\in N_1^s}\zeta_{\overrightarrow{r_n}}, \tag{A8}$$

where the term $\zeta_{\overrightarrow{r_n}}(0\leq\zeta_{\overrightarrow{r_n}}\leq 1)$ denotes the connectivity value of a node $\overrightarrow{r_n}\in N_1^s$ (being N_1^s the set of superficial nodes of R_1) with R_2. It is defined as the maximum node–node connectivity value (see Eq. (A7)) among all connections between $\overrightarrow{r_n}$ and any $\overrightarrow{r_m}\in N_2^s$ (being N_2^s the set of superficial nodes of R_2):

$$\zeta_{\overrightarrow{r_n}} = \max_{\forall\overrightarrow{r_m}\in N_2^s}(C_{\text{node}}(\overrightarrow{r_n},\overrightarrow{r_m})). \tag{A9}$$

Similarly, $\zeta_{\overrightarrow{r_m}}$ denotes the connectivity of any node $\overrightarrow{r_m}\in N_2^s$ with R_1. Note that the first term of expression (A8) quantifies connections of the region R_2 with R_1, and the second term quantifies connections of the region R_1 with R_2.

ACD measure is estimated as the ACS relative to the number of nodes belonging to the surfaces of R_1 and R_2:

$$C_{\text{Zone}}^{\text{ACD}}(R_1,R_2) = \frac{C_{\text{Zone}}^{\text{ACS}}(R_1,R_2)}{|N_1^s|+|N_2^s|}. \tag{A10}$$

ACP represents the probability of regions R_1 and R_2 to be connected at least by a single fiber connection. It is estimated as the maximum connectivity value between nodes of these regions:

$$C_{\text{Zone}}^{\text{ACP}}(r_1,r_2) = \max\left(\max_{\forall\overrightarrow{r_m}\in N_2^s}\zeta_{\overrightarrow{r_m}},\max_{\forall\overrightarrow{r_n}\in N_1^s}\zeta_{\overrightarrow{r_n}}\right). \tag{A11}$$

Appendix B. White matter Orientational Distribution Function

The intravoxel white matter orientational distribution function (ODF) $\psi(\hat{u})$ is defined as the radial projection of the probability density function (PDF) $P(\overrightarrow{R})$ (Wedeen et al., 2005):

$$\psi(\hat{u}) = \int_0^{+\infty}R^2P(\hat{u}R)\text{d}R, \tag{B1}$$

being $\hat{u}$ a unitary vector and $\overrightarrow{R}=\hat{u}R$ the relative spin displacement.

Considering the PDF for anisotropic Gaussian diffusion:

$$P\left(\overrightarrow{R}\right) = (4\pi t)^{-3/2}(|\mathbf{D}|)^{-1/2}\text{e}^{\frac{-\overrightarrow{R}^T\mathbf{D}^{-1}\overrightarrow{R}}{4t}}, \tag{B2}$$

Then, substituting in Eq. (B1) and using the identity:

$$\int_0^{+\infty}x^m\text{e}^{ax^2}\text{d}x = \frac{\Gamma\left(\frac{(m+1)}{2}\right)}{2a^{\frac{m+1}{2}}}, \tag{B3}$$

where Γ is the Gamma function, we can obtain the ODF as:

$$\psi(\hat{u}) = \frac{1}{C}\left(\hat{u}^T\mathbf{D}^{-1}\hat{u}\right)^{-\frac{3}{2}}. \tag{B4}$$

Here, C is a normalization constant which ensures that the ODF is properly normalized to unit mass.

Appendix C. Algorithm to solve the most probable path problem

Given a Brain Graph $G_{\text{brain},0}=[N_0, A_0, W_0]$, let us define some quantities before setting up the algorithm:

$|N_0|$: Cardinality of the set N_0, i.e. the number of elements belonging to set N_0.
N_0^{-s}: Set of nodes that belong to $G_{\text{brain},0}$ except node 's', $N_0^{-s} = N_0/\{\overrightarrow{r_s}\}$.
$\mathrm{M}(\overrightarrow{r_v})$: Map of probabilities of the path between node 's' and all nodes $\overrightarrow{r_v}\in N_0^{-s}, \mathrm{M}(\overrightarrow{r_v}) = P[\rho(\overrightarrow{r_s}, \overrightarrow{r_v})]$ and $\mathrm{M}(\overrightarrow{r_s})=1$.
N_i^{neig}: Nearest neighborhood of the ith node.

This algorithm proceeds in $|N_0|-1$ iterations as follows:

a) Set initially:
$a.1)$ $\tilde{S}=N_0^{-s}$,
$a.2)$ $\mathrm{M}(\overrightarrow{r_i}) = \begin{cases} 1, & \overrightarrow{r_i}=\overrightarrow{r_s}, \\ w_0(a_{si}), & \overrightarrow{r_i}\in N_i^{\text{neig}} \\ 0, & \text{otherwise.} \end{cases}$
$a.3)$ $\tilde{\rho}(\overrightarrow{r_s}, \overrightarrow{r_i}) = a_{si}, \quad \forall \overrightarrow{r_i}\in N_s^{\text{neig}}$
b) Find $\overrightarrow{r_j}\in \tilde{S}$ such that $\mathrm{M}(\overrightarrow{r_j}) = \max_{\forall r_i\in\tilde{S}} \mathrm{M}(\overrightarrow{r_i})$
b.1) Set a new $\tilde{S}\leftarrow\tilde{S}/\{\overrightarrow{r_j}\}$
b.2) If $\tilde{S}=\varnothing$, then Stop; else continue
c) For all $\overrightarrow{r_m}\in N_j^{\text{neig}}$ and $\overrightarrow{r_m}\in S$, set
c.1) $\rho(\overrightarrow{r_s}, \overrightarrow{r_m}) = \{\tilde{\rho}(\overrightarrow{r_s}, \overrightarrow{r_j}) \cup a_{jm}\}$,
c.2) If $P[\rho(\overrightarrow{r_s}, \overrightarrow{r_m})]>\mathrm{M}(\overrightarrow{r_m})$ then
$\tilde{\rho}(\overrightarrow{r_s}, \overrightarrow{r_m})= \rho(\overrightarrow{r_s}, \overrightarrow{r_m}), \quad \mathrm{M}(\overrightarrow{r_m})= P[\tilde{\rho}(\overrightarrow{r_s}, \overrightarrow{r_m})]$
c.3) go to b).

Finally, the map $\mathrm{M}(\overrightarrow{r_p})$ for $\overrightarrow{r_p}\in N_0^{-s}$ represents the final probability of the path of maximum reliability according to (A6) between nodes $\overrightarrow{r_s}$ and $\overrightarrow{r_p}$ denoted by $\rho(\overrightarrow{r_s}, \overrightarrow{r_p})$.

References

Achard, S., Bullmore, E., 2007. Efficiency and cost of economical brain functional networks. PLoS Comput. Biol. 3 (2), e17 (Feb. 2).

Achard, S., Salvador, R., Whitcher, B., Suckling, J., Bullmore, E., 2006. A resilient, low-frequency, small-world human brain functional network with highly connected association cortical hubs. J. Neurosci. 26, 63–72.

Albert, R., Jeong, H., Barabasi, A.-L., 1999. Diameter World-Wide Web 130–131.

Alemán-Gómez, Y., Melie-García, L., Valdes-Hernández, P., 2006. IBASPM: Toolbox for automatic parcellation of brain structures. Presented at the 12th Annual Meeting of the Organization for Human Brain Mapping, June 11–15, 2006, Florence, Italy. Available on CD-Rom in NeuroImage, Vol. 27, No. 1.

Amaral, L.A., Scala, A., Barthelemy, M., Stanley, H.E., 2000. Classes of small-world networks. Proc. Natl. Acad. Sci. U. S. A. 97, 11149–11152.

Bassett, D.S., Bullmore, E., 2006. Small-world brain networks. Neuroscientist 12, 512–523.

Bassett, D.S., Meyer-Lindenberg, A., Achard, S., Duke, T., Bullmore, E., 2006. Adaptive reconfiguration of fractal small-world human brain functional networks 1. Proc. Natl. Acad. Sci. U. S. A. 103, 19518–19523.

Behrens, T.E., Johansen-Berg, H., Woolrich, M.W., Smith, S.M., Wheeler-Kingshott, C.A., Boulby, P.A., Barker, G.J., Sillery, E.L., Sheehan, K., Ciccarelli, O., Thompson, A.J., Brady, J.M., Matthews, P.M., 2003. Non-invasive mapping of connections between human thalamus and cortex using diffusion imaging. Nat. Neurosci. 6, 750–757.

Boccaletti, S., Latora, V., Moreno, Y., Chavez, M., Hwang, D.-U., 2006. Complex networks: structure and dynamics. Phys. Rep. 424, 175–308.

Brodmann, K., 1909. Vergleichende Lokalisationslehre der Grosshirnrinde in ihren Prinzipien dargestellt auf Grund des Zellenbaues, Barth, Leipzig. Thomas, Springfield, IL, 1960, pp. 201–230.

Conturo, T.E., Lori, N.F., Cull, T.S., Akbudak, E., Snyder, A.Z., Shimony, J.S., McKinstry, R.C., Burton, H., Raichle, M.E., 1999. Tracking neuronal fiber pathways in the living human brain. Proc. Natl. Acad. Sci. U. S. A. 96, 10422–10427.

Dall'Asta, L., Barrat, A., Barthelemy, M., Vespignani, A., 2006. Vulnerability of Weighted Networks. Dynamically Evolving, Large-scale Information Systems, TR-0340.

Eguiluz, V.M., Chialvo, D.R., Cecchi, G.A., Baliki, M., Apkarian, A.V., 2005. Scale-free brain functional networks. Phys. Rev. Lett. 94 (018102).

Erdös, P., Rényi, A., 1959. On random graphs. Publ. Math. Debrecen 6, 290.

Freeman, L., 1977. A set of measures of centrality based upon betweenness. Sociometry 40, 35–41.

Goldshtein, V., Koganov, G.A., Surdutovich, G.I., 2004. Vulnerability and Hierarchy of Complex Networks. Cond-mat/0409298.

Gómez-Padrón, I., Silva Loynaz, C., Seuc Chiu, A., 1985. Anatomía II. Folleto complementario. Ministerio de salud publica, Cuba.

Hagmann, P., Reese, T.G., Tseng, W.Y., Meuli, R., Thiran, J.P., Wedeen, V.J., 2004. Diffusion Spectrum Imaging tractography in complex cerebral white matter: aninvestigation of the centrum semiovale. Proc. ISMRM 623.

Hagmann, P., Kurant, M., Gigandet, X., Thiran, P., Wedeen, V.J., Meuli, R., Thiran, J.P., 2006. Imaging the brain neuronal network with diffusion MRI: a way to understand its global architecture. Proc. ISMRM 436.

He, Y., Chen, Z.J., Evans, A.C., 2007. Small-world anatomical networks in the human brain revealed by cortical thickness from MRI. Cereb. Cortex, doi:10.1093/cercor/bhl149.

Hilgetag, C.C., Kaiser, M., 2004. Clustered Organization of Cortical Connectivity, pp. 353–360 (2nd ed.).

Honey, C.J., Kotter, R., Breakspear, M., Sporns, O., 2007. Network structure of cerebral cortex shapes functional connectivity on multiple time scales. Proc. Natl. Acad. Sci. U.S.A. 104, 10240–10245.

Humphries, M.D., Gurney, K., Prescott, T.J., 2006. The brain stem reticular formation is a small-world, not scale-free, network. Proc. Biol. Sci. 273, 503–511.

Hutton, C., Bork, A., Josephs, O., Deichmann, R., Ashburner, J., Turner, R., 2002. Image distortion correction in fMRI: aquantitative evaluation. NeuroImage 16, 217–240.

Iturria-Medina, Y., Canales-Rodríguez, E.J., Melie-García, L., Valdes-Hernández, P.A., Martínez-Montes, E., Alemán-Gómez, Y., Sánchez-Bornot, J.M., 2007. Characterizing brain anatomical connections using diffusion weighted MRI and Graph Theory. NeuroImage 36, 645–660.

Koch, M.A., Norris, D.G., Hund-Georgiadis, M., 2002. An investigation of functional and anatomical connectivity using magnetic resonance imaging. NeuroImage 16, 241–250.

L. da F. Costa, Rodrigues, F.A., Travieso, G., Villas, P.R., 2006. Characterization of Complex Networks: A Survey of Measurements. (arXiv:cond-mat/0505185v5).

Latora, V., Marchiori, M., 2001. Efficient behavior of small-world networks5. Phys. Rev. Lett. 87 (198701).

Latora, V., Marchiori, M., 2005. Vulnerability and protection of infrastructure networks. Phys. Rev., EStat. Nonlinear Soft Matter Phys. 71 (1Pt2) (Jan; 015103).

Lerch, J.P., Worsley, K., Shaw, W.P., Greenstein, D.K., Lenroot, R.K., Giedd, J., Evans, A.C., 2006. Mapping anatomical correlations across cerebral cortex (MACACC) using cortical thickness from MRI. NeuroImage 31, 993–1003.

Maslov, S., Sneppen, K., 2002. Specificity and stability in topology of protein networks. Science 296 (5569), 910–913 (May 3).

Mazziotta, J.C., Toga, A.W., Evans, A., Fox, P., Lancaster, J., 1995. A probabilistic atlas of the human brain: theory and rationale for its development. The International Consortium for Brain Mapping (ICBM). NeuroImage 2, 89–101.

Milos, R., Shen-Orr, S., Itzkovitz, S., Kashan, N., Chklovskii, D., Alon, U., 2002. Network motifs: simple building blocks of complex networks. Science 298, 824–827.

Mitelman, S.A., Brickman, A.M., Shihabuddin, L., Newmark, R.E., Hazlett, E.A., Haznedar, M.M., Buchsbaum, M.S., 2007. A Comprehensive Assessment of Gray and White Matter Volumes and their Relationship to Outcome and Severity in Schizophrenia, doi:10.1016/j.neuroimage.2007.04.070.

Mori, S., Crain, B.J., Chacko, V.P., vanZijl, P.C., 1999. Three-dimensional tracking of axonal projections in the brain by magnetic resonance imaging. Ann. Neurol. 45, 265–269.

Morrison, J.H., Scherr, S., Lewis, D.A., Campbell, M.J., Bloom, F.E., 1986. The laminar and regional distribution of neocortical somatostatin and neuritic plaques: implications for Alzheimer's disease as a global neocortical disconnection syndrome. In: Scheibel, A.B., Weschler, A.F. (Eds.), The Biological Substrates of Alzheimer's Disease. Academic-Press, New York, NY, pp. 115–131.

Mountcastle, V.B., 2007. Perceptual Neuroscience: The Cerebral Cortex. Harvard University Press, Cambridge, MA.

Newman, M.E.J., Park, J., 2003. Why social networks are different from other types of networks. Phys. Rev., E 68 (036122).

Onnela, J.P., Saramaki, J., Kertesz, J., Kaski, K., 2005. Intensity and coherence of motifs in weighted complex networks. Phys. Rev., E Stat. Nonlinear Soft Matter Phys. 71 (065103).

Parker, G.J., Wheeler-Kingshott, C.A., Barker, G.J., 2002. Estimating distributed anatomical connectivity using fast marching methods and diffusion tensor imaging. IEEE Trans. Med. Imag. 21, 505–512.

Pearson, R.C.A., Esiri, M.M., Hiorns, R.W., Wilcock, G.K., Powell, T.P.S., 1985. Anatomical correlates of the distribution of the pathological changes in the neocortex in Alzheimer's disease. Proc. Natl. Acad. Sci. U.S.A. 82, 4531–4534.

Salvador, R., Suckling, J., Coleman, M.R., Pickard, J.D., Menon, D., Bullmore, E., 2005. Neurophysiological architecture of functional magnetic resonance images of human brain. Cereb. Cortex 15, 1332–1342.

Sporns, O., Kotter, R., 2004. Motifs in brain networks. PLoS. Biol. 2, e369.

Sporns, O., Zwi, J., 2004. The small world of the cerebral cortex. Neuroinformatics 2, 145–162.

Sporns, O., Tononi, G., Kotter, R., 2005. The human connectome: a structural description of the human brain. PLoS. Comput. Biol. 1, e42.

Stam, C.J., 2004. Functional connectivity patterns of human magnetoencephalographic recordings: a 'small-world' network? Neurosci. Lett. 355, 25–28.

Standring, S., 2004. Gray′s Anatomy: The Anatomical Basis of Medicine and Surgery, 39th edition. Churchill Livingstone.

Strogatz, S.H., 2001. Exploring complex networks. Nature 410 (6825), 268–276 (Mar 8).

Studholme, Hill, Hawkes, 1998. A normalized entropy measure of 3-D medical alignment. Proc. Medical Imaging, vol. 3338. SPIEPress, San Diego, CA, pp. 132–143.

Toga, A., Thompson, P., Susumu, M., Amunts, K., Zilles, K., 2006. Towards multi modal atlases of the human brain. Nat. Rev., Neurosci. 7 (12), 952–966.

Tuch, D.S., 2002. MRI of complex tissues tructure. PhD Thesis.

Tuch, D.S., 2004. Q-ballimaging. Magn. Reson. Med. 52, 1358–1372.

Tzourio-Mazoyer, N., Papathanassiou, D., Crivello, F., Etard, O., Delcroix, N., Mayozer, B., Joliot, M., 2002. Automated Anatomical Labeling of Activations in SPM Using a Macroscopic Anatomical Parcellation of the MNI MRI Single-Subject Brain, pp. 273–289 (15ed).

Watts, D.J., 1999. Small Worlds: The Dynamics of Networks between Order and Randomness. Princeton University Press, Princeton, NJ.

Watts, D.J., Strogatz, S.H., 1998. Collective Dynamics of Small-World Networks, pp. 440–442.

Wedeen, V.J., Hagmann, P., Tseng, W.Y., Reese, T.G., Weisskoff, R.M., 2005. Mapping complex tissue architecture with diffusion spectrum-magnetic resonance imaging. Magn. Reson. Med. 54, 1377–1386.

Witelson, S.F., 1989. Hand and sex differences in the isthmus and genu of the human corpuscallosum. A post mortem morphological study. Brain 112 (Pt3), 799–835.

Worsley, K.J., Chen, J.I., Lerch, J., Evans, A.C., 2005. Comparing functional connectivity via thresholding correlations and singular value decomposition. Philos. Trans. R. Soc. Lond., BBiol. Sci. 360, 913–920.

Young, M.P., 1993. The organization of neural systems in the primate cerebral cortex. Proc. Biol. Sci. 252, 13–18.

3.3. ARTÍCULO 3

Yasser Iturria-Medina, Alejandro Pérez Fernández, David M. Morris, Erick J. Canales-Rodríguez, Hamied A. Haroon, Lorna García Pentón, Mark Augath, Lídice Galán García, Nikos Logothetis, Geoffrey J.M. Parker and Lester Melie-García. Brain Hemispheric Structural Efficiency and Interconnectivity Rightward Asymmetry in Human and Non-Human Primates. Cerebral Cortex, January 2011; 21:56-67.

Cerebral Cortex January 2011;21:56-67
doi:10.1093/cercor/bhq058
Advance Access publication April 9, 2010

Brain Hemispheric Structural Efficiency and Interconnectivity Rightward Asymmetry in Human and Nonhuman Primates

Yasser Iturria-Medina[1], Alejandro Pérez Fernández[2,3], David M. Morris[4,5], Erick J. Canales-Rodríguez[6,7], Hamied A. Haroon[4,5], Lorna García Pentón[2], Mark Augath[8], Lídice Galán García[1], Nikos Logothetis[4,8], Geoffrey J. M. Parker[4,5] and Lester Melie-García[1]

[1]Neuroimaging Department, Cuban Neuroscience Center, CP 10 600, La Habana, Cuba, [2]Laboratory of Cognitive Neuroscience, Universidad Diego Portales, 8370076 Santiago, Chile, [3]Centro de Investigación y Desarrollo del Comercio Interior, CID-CI, CP 10 400, La Habana, Cuba, [4]Imaging Science and Biomedical Engineering Research Group, School of Cancer and Imaging Sciences and, [5]Imaging Science and Biomedical Engineering, Biomedical Imaging Institute, University of Manchester, Manchester, M13 9PT, UK, [6]Centro de Investigación Biomédica en Red de Salud Mental (CIBERSam), 28007, Madrid, Spain, [7]Benito Menni Complex Assistencial en Salut Mental, Barcelona 08830, Spain and [8]Physiology of Cognitive Processes Department, Max Planck Institute for Biological Cybernetics, 72076 Tübingen, Germany

Address correspondence to Yasser Iturria-Medina, Neuroimaging Department, Cuban Neuroscience Center, Avenida 25, Esquina 158, #15202, Apartado Postal 6648, Cubanacán, Playa, Habana 6 CP 10600, Cuba. Email: iturria.medina@gmail.com.

Evidence for interregional structural asymmetries has been previously reported for brain anatomic regions supporting well-described functional lateralization. Here, we aimed to investigate whether the two brain hemispheres demonstrate dissimilar general structural attributes implying different principles on information flow management. Common left hemisphere/right hemisphere structural network properties are estimated and compared for right-handed healthy human subjects and a nonhuman primate, by means of 3 different diffusion-weighted magnetic resonance imaging fiber tractography algorithms and a graph theory framework. In both the human and the nonhuman primate, the data support the conclusion that, in terms of the graph framework, the right hemisphere is significantly more efficient and interconnected than the left hemisphere, whereas the left hemisphere presents more central or indispensable regions for the whole-brain structural network than the right hemisphere. From our point of view, in terms of functional principles, this pattern could be related with the fact that the left hemisphere has a leading role for highly demanding specific process, such as language and motor actions, which may require dedicated specialized networks, whereas the right hemisphere has a leading role for more general process, such as integration tasks, which may require a more general level of interconnection.

Keywords: brain structural network, diffusion-weighted MRI, efficiency, fiber tractography, hemispheric asymmetries, interconnectivity

Introduction

The interregional structural connectivity asymmetry for left–right brain hemispheres is an important topic in the study of the neural basis of brain functional asymmetries, contributing to our understanding of the factors that modulate cognitive specialization in the brain. The recent development of diffusion–weighted magnetic resonance imaging (DW-MRI), a noninvasive technique that quantifies water diffusion process, has allowed the acquisition of structural information about the intravoxel axon arrangement, making possible the noninvasive study of the brain anatomical circuitry (Mori et al. 1999; Koch et al. 2002; Parker et al. 2002; Behrens, Johansen-Berg, et al. 2003; Tuch et al. 2003; Hagmann, Kurant, et al. 2006; Iturria-Medina et al. 2007). In that context, structural asymmetries have been explored analyzing mainly the fractional anisotropy (FA), a measure of local fiber coherence (Kubicki et al. 2002; Gong et al. 2005; Powell et al. 2006; Clark et al. 2007; Rodrigo et al. 2007) and the number of, or existence of, connecting paths between specific regions (Parker et al. 2005; Hagmann, Cammoun, et al. 2006; Powell et al. 2006; Glasser and Rilling 2008), contributing to our understanding of cognitive lateralized process like language and motor control.

These previous interregional studies were focused on identifying which white matter regions and/or connections, corresponding to reported functional lateralization, are more coherent or stronger in one hemisphere than in the other. In other words, to match well-described functional lateralization with the specific white matter structural asymmetries supporting the function. However, in order to characterize brain structural asymmetry through white matter connections, it is necessary to recognize not only the specific interregional asymmetries in a pairwise manner, which could represent a considerable challenge due to the high number of possible connections, but also the broader structural network asymmetries between the hemispheres, in order to assess differences in how their anatomical substrates may be configured to facilitate the management and integration of information flow in a more general sense.

In this study, we aimed to investigate if, besides the specific regional asymmetries, both hemispheres demonstrate dissimilar general structural attributes implying different principles on the management of the information flow. Our analysis is based on a mathematical network framework (Watts and Strogatz 1998; Latora and Marchiori 2001; Onnela et al. 2005; Boccaletti et al. 2006; Costa et al. 2007), allowing us to explore hemispheric differences in terms of quantitative parameters that can be structurally and, by inference, functionally interpreted. Previous brain structural network analyses have used connectivity information obtained from nonhuman post-mortem studies (Sporns and Zwi 2004; Costa and Sporns 2005; Sporns 2006), statistical concurrent change analysis between brain areas in one or more morphological variables (He et al. 2007; Bassett et al. 2008; Chen et al. 2008; He et al. 2008), or DW-MRI techniques (Hagmann, Kurant, et al. 2006; Hagmann et al. 2008; Iturria-Medina et al. 2008; Gong et al. 2009) to investigate large-scale connection patterns of the brain, such as small-world attributes, efficiency, degree distribution, motif composition, and structural core properties. Here, using 3 different tractography algorithms and a graph theory framework, we attempt to estimate white matter interregional

axonal pathways and to infer left and right common anatomical network properties, obtaining global and local measures that allow us to evaluate for the first time structural network (dis)similarities between hemispheres. In particular, we focus on graph measures of efficiency and interconnectivity, for 11 right-handed healthy human subjects and a single macaque monkey. Additional analyses include the identification of those anatomic regions that are significantly more central or indispensable (in terms of their connections) for the whole-brain structural network than their homolog regions in the opposite hemisphere. Finally, some comments are made concerning the relationship between the obtained anatomical findings and some previously reported functional asymmetries, such as visual attention neglect.

Materials and Methods

Data Acquisition and Preprocessing

Dataset 1

High–angular resolution DW-MRI datasets were acquired in 11 right-handed healthy subjects (age range: 23–38 years). All subjects provided informed consent, and the procedures were approved by the Local Research Ethics Committee. Handedness was determined by documenting the dominant hand of the participants.

Data were acquired on a 3-T Philips Achieva scanner (Philips Medical Systems) in Manchester, UK, using an 8-element SENSE head coil. Diffusion-weighted imaging was performed using a dual phase encoded pulsed gradient spin echo protocol designed to allow correction of susceptibility-induced and eddy current–induced distortions (Embleton et al. 2006). Acquisition parameters used were time echo (TE) = 54 ms, time repetition (TR) = 11884 ms, $G = 62$ mT/m, half-scan factor = 0.679, 112 × 112 image matrix reconstructed to 128 × 128 using zero padding, reconstructed resolution = 1.875 × 1.875 mm^2, slice thickness = 2.1 mm, 60 contiguous slices, 61 noncollinear diffusion sensitization directions at $b = 1200$ s/mm^2 ($\Delta = 29.8$ ms and $\delta = 13.1$ ms), 1 at $b = 0$, and SENSE acceleration factor = 2.5. For each diffusion gradient direction, 2 separate volumes were obtained with opposite polarity k space traversal in order to enable the distortion correction method.

T_2-weighted images were also acquired and automatically parcellated into 90 gray matter structures (parcellation scheme 1) (Mazziotta et al. 1995) using the IBASPM toolbox (available at http://www.fil.ion.ucl.ac.uk/spm/ext/#IBASPM) (Alemán-Gómez et al. 2006). Additionally, in order to evaluate possible parcellation scheme effects on lateralization of global/local efficiency and interconnectivity network measures, the registered T_2-weighted images were also parcellated into 71 gray matter structures (parcellation scheme 2) corresponding to the Jacob Atlas developed by the Montreal Neurological Institute (http://www.mni.mcgill.ca/). In order to consider the same left and right gray matter regions, the brain stem region was rejected from this parcellation scheme (for details please see Supplementary Table 4).

Dataset 2

A high–angular resolution DW-MRI dataset was acquired in a formalin-fixed postmortem macaque (*Macaca mulatta*) brain using a Bruker BIOSPEC 4.7-T vertical bore scanner. The macaque brain was perfused, removed from the skull, and kept in 4% paraformaldehyde for 5 years prior scanning. A 2D spin echo MRI sequence was implemented with TE = 78 ms, TR = 9 s, $G = 47$ mT/m, 104 × 94 imaging matrix, 58 contiguous slices, isotropic voxel resolution = 0.8 mm, 61 non-collinear diffusion sensitization directions at $b = 4000$ s/mm^2 ($\Delta = 39$ ms and $\delta = 31$ ms), 7 at $b = 0$, and 4 averages. The total imaging time was ca. 64 h. To improve the signal-to-noise ratio in the diffusion-sensitized images, for the purposes of tractography, we applied 5 iterations of 2D anisotropic diffusion smoothing (rsb.info.nih.gov/ij/plugins/anisotropic-diffusion-2d.html) using ImageJ (rsb.info.nih.gov/ij/index.html).

Following the procedure described in Haroon et al. (2008), we took the cortical parcellation scheme LVE00a (Lewis and Van Essen 2000) available as part of the Caret 5.5 software (available at http://www.brainmap.wustl.edu/caret) for the F99UA1 rhesus macaque brain atlas. Then, using the Normalize tool in SPM5 (available at http://www.fil.ion.ucl.ac.uk/spm/software/spm5/), a nonlinear warping was applied to the F99UA1 MRI brain volume to spatially match the brain volume of our dataset. Finally, the nonlinear warping transformation parameters obtained were applied to the LVE00a parcellation scheme (for a list of region labels see Supplementary Table 5). In addition, macaque cortex structural connections information derived by invasive tracer studies was extracted from Cocomac LVE00a database (cocomac.org/home.asp) (for details please see Fig. 3*a*).

Voxel-Region Axonal Connectivity Estimation

For each subject of datasets 1 and 2, 3 axonal connectivity values between each brain voxel and the surface of each considered gray matter region (voxel-region connectivity) were estimated using 3 fully automated fiber tractography algorithms as follows:

1. Probabilistic tractography from the seed regions was carried out according to Behrens, Woolrich, et al. (2003) using the FSL software package (available at http://www.fmrib.ox.ac.uk/fsl/). For each brain voxel, an index of connectivity, representing the number of generated paths that passed through it from the seed region, was assigned. Tracking parameters used were 5000 as number of generated paths from each seed point (suggested in the FSL software package as optimum to reach the convergence of the algorithm), 0.5 mm as step size, 500 mm maximum trace length, and a curvature threshold of ±80°. In the text we refer to this algorithm as "FSL."
2. Second, probabilistic tractography was performed using the PICo algorithm (Parker et al. 2003; Parker and Alexander 2005). Similarly to the FSL method, a connection probability value with each seed region was assigned to the brain voxels. Tracking parameters used were 5000 as number of generated paths from each seed point, 0.5 mm as step size, 500 mm as maximum trace length, and a curvature threshold over voxel of ±90°. Intravoxel probability density functions of fiber orientation were generated using a model-based residual bootstrap Q-ball approach (Haroon et al. 2009). In the text we refer to this algorithm as "PICo."
3. Finally, a graph-based tractography algorithm (Iturria-Medina et al. 2007) was used, assigning to each brain voxel a probability of connection with each considered seed region. A maximum of 500 mm trace length and a curvature threshold of ±90° were imposed as tracking parameters. The intravoxel white matter orientational distribution function maps were estimated using the Q-ball approach (Tuch 2004). In the text we refer to this algorithm as "GM."

Additionally, in order to evaluate the performance of the previous fiber tractography algorithms (FSL, PICo, and GM) in comparison with the more often used deterministic streamline tractography (SLT) algorithm (Mori et al. 1999), we used also the SLT approach to estimate axonal connectivity values between brain voxels and the surface of each considered gray matter region for the macaque monkey subject (dataset 2). Tracking parameters used for SLT algorithm were 0.5 mm as step size, 500 mm as maximum trace length, a curvature threshold over voxel of ±60°, and a FA threshold of 0.2. Seed points were selected as all brain voxels with an FA value greater than 0.2 (the so-called brute-force approach). Following the procedure described in Li et al. (2009), 2 gray matter regions were considered to be connected if the reconstructed fiber trajectories with 2 end points located in these 2 regions, respectively, were present, and a final connection measurement between these regions was defined as the number of connecting fiber trajectories relative to the number of voxels over the surface of both regions (equivalent to arc weight definition in eq. 1).

Network Construction

For each subject, whole-brain undirected weighted networks were created for each tracking algorithm used as follows: 1) A node was defined to represent each considered anatomic region, 2) An

undirected arc a_{ij} between nodes i and j was established if a nonzero connectivity value was found to exist between the boundary voxels of regions i and j, and 3) Arc weight $u(a_{ij})$ was defined as the connection measurement (the output of the tractography algorithm) between regions i and j (Iturria-Medina et al. 2007), estimated by counting the "effective" number of voxels over the surface of both regions and weighting each voxel by its voxel-region connectivity value with the opposite zone, relative to the total number of considered superficial voxels. Mathematically:

$$w(a_{ij}) \equiv w(a_{ji}) = \frac{\sum_{\forall \vec{r}_n \in N_i^s} \zeta_{\vec{r}_n} + \sum_{\forall \vec{r}_m \in N_j^s} \zeta_{\vec{r}_m}}{\left|N_i^s\right| + \left|N_j^s\right|}, \quad (1)$$

where the term $\zeta_{\vec{r}_n}$ denotes the axonal connectivity value of each node $\vec{r}_n \in N_i^s$ (N_i^s being the set of superficial nodes of region i) with the superficial nodes of region j $\left(N_j^s\right)$. Similarly, $\zeta_{\vec{r}_m}$ denotes the connectivity value of any node $\vec{r}_m \in N_j^s$ with superficial nodes of region i. $\left|N_i^s\right|$ and $\left|N_j^s\right|$ are the number of elements (superficial nodes) of regions i and j, respectively. Note that the first term of the numerator quantifies connections of the region i with j, and the second term quantifies connections of the region j with i.

Eliminating interhemispheric connections, each whole-brain network was segmented into left and right hemispheric networks, each one containing the same number of homolog regions. Graphically, each created undirected weighted network is a discrete set of points (nodes) representing anatomic regions and a set of nondirectional lines (arcs) representing connections between them, which the width of each line reflecting the corresponding arc weight.

Graph Analysis

Efficiency

In terms of the information flow, the global efficiency (E_{glob}) of a network G reflects how efficiently information can be exchanged over G, considering a parallel system in which each node sends information concurrently along the network. It is defined as (Latora and Marchiori 2001):

$$E_{glob} = \frac{1}{n(n-1)} \sum_{\substack{i,j \in G \\ i \neq j}} \frac{1}{d_{ij}}, \quad (2)$$

where n is the number of nodes, and d_{ij} is the geodesic length over all pairs of nodes. In the unweighted network context, the shortest path length d_{ij} is defined as the number of arcs along the shortest path connecting nodes i and j. In the case of weighted networks, the path with the minimum number of nodes is not necessarily the optimal d_{ij} and is necessary to define a physical length associated to each arc (this should be a function of the characteristics of the hypothetical link among any nodes i and j). In this work, we assumed that the physical length of an arc connecting nodes i and j is inversely proportional to the strength of the analyzed connection (Iturria-Medina et al. 2008), i.e., $l_{ij} = \frac{1}{w_{ij}}$. Thus, the shortest path length d_{ij} is finally computed as the smallest sum of the arc lengths throughout all the possible paths from node i to node j. Note that for the particular case of unweighted graphs, $l_{ij} = 1$ for all arcs and the geodesic lengths d_{ij} reduces to the minimum number of arcs traversed to get from i to j.

The local efficiency (E_{loc}) of G is defined as the average efficiency of the local subgraphs (Latora and Marchiori 2001):

$$E_{loc} = \frac{1}{n} \sum_{i \in G} E_{glob}(G_i), \quad (3)$$

where G_i is the subgraph of the first neighbors of node i. This measure has been used to reveal how much a system is fault tolerant, showing how efficient the communication is among the first neighbors of i when i is removed.

In a physiological sense, the global efficiency of a structural brain/hemispheric network reflects the potential parallel exchange of neural information between the involved anatomic regions (a high global efficiency value, i.e., $E_{glob} \approx 1$, may indicate highly parallel information transfer in the brain/hemispheric system, in which each element node could efficiently send information concurrently along the network). The local efficiency of a structural brain/hemispheric network reflects its potential tendency to present communities or clusters of anatomically and physiologically different regions that deal with common neural information (where regions connected to a same region tend also to link to each other). In addition, concurrent higher values of global and local efficiencies indicate a system with a high balance between local necessities (fault tolerance) and wide-scope interactions.

Interconnectivity

In order to obtain a measure of the total amount of connectivity in a weighted network G, here we define the interconnectivity (I_{conn}) of G as the sum of its arc weights. It reflects the amount of connectivity between all the considered anatomic regions.

Betweenness Centrality

Betweenness centrality is a widely used measure to identify the most central nodes in a graph, which are associated to those nodes that act as bridges between the others nodes (Freeman 1977; Bassett et al. 2006; Dall'Asta et al. 2006; Honey et al. 2007). It is defined as the fraction of shortest paths between pairs of nodes that passes through a given node. Mathematically, for weighted networks, if σ_{kj}^w is the number of paths from node k to node j, and $\sigma_{kj}^w(i)$ is the number of these paths passing through node i, the weighted betweenness centrality of i is (Dall'Asta et al. 2006)

$$b_i^w = \sum_{\substack{k,j \in G \\ k \neq j \neq i}} \frac{\sigma_{kj}^w(i)}{\sigma_{kj}^w}. \quad (4)$$

Lateralization Index

In order to characterize asymmetry for a given network measure X (global/local efficiency, interconnectivity, or betweenness centrality), a lateralization index (LI) was computed as:

$$\mathrm{LI}(X) = 100 \times \frac{X(\mathrm{Right}) - X(\mathrm{Left})}{X(\mathrm{Right}) + X(\mathrm{Left})}. \quad (5)$$

This procedure allows us to look at differences between the right and left hemispheres, incorporating the relative network value of X over both hemispheres in one value. The index, ranging between 100 and −100, is positive when X is more prominent over the right hemisphere and lower over the left hemisphere $(X(\mathrm{Right}) > X(\mathrm{Left}))$ and negative when the opposite is the case $(X(\mathrm{Right}) < X(\mathrm{Left}))$.

Receiver Operating Characteristic Analysis

Receiver operating characteristic (ROC) curves are useful for visualizing, organizing, and selecting classifiers based on their performance (Fawcett 2006). Here, in order to evaluate the performance of the FSL, PICo, and GM fiber tractography algorithms in comparison with the traditional SLT algorithm, ROC curves for each of these algorithms were constructed, based on the comparison of their connection results for the macaque monkey subject (dataset 2) and the reference connection pattern defined by macaque cortex structural connections information derived by invasive tracer studies (Fig. 3*a*).

First, because in this analysis we are not differencing between left and right hemispheres due to connection information from invasive tracing studies not being hemisphere specific, connectivity matrix representing each fiber tractography algorithm was created assuming, as final connection value between any 2 regions i and j, the mean of the connection values obtained by this algorithm on both hemispheres (eq. 1). Next, the ROC curve corresponding to a specific tractography algorithm was represented as the fraction of "true positives" (TPR) versus the fraction of "false positives" (FPR) of its connectivity matrix with regard the reference connection pattern (Fig. 3*a*) as a discrimination threshold is varied, that is, a set of threshold values, varying from minimum to maximum value, were applied to the analyzed connectivity matrix and resulting binarized matrix versions were compared with

the reference connection pattern (Fig. 3*a*), allowing to calculate corresponding TPR and FPR values as:

$$\mathrm{TPR} = \frac{\mathrm{TP}}{\mathrm{TP} + \mathrm{FN}}, \quad \mathrm{FPR} = \frac{\mathrm{FP}}{\mathrm{FP} + \mathrm{TN}}, \tag{6}$$

where TP, FN, FP, and TN are the number of true positives, false negatives, false positives, and true negatives, respectively. For a valid comparison, only those matrix cells where a direct (dis)connection by invasive tracer studies (values 0 and 1 on Fig. 3*a*, i.e., a total of 462 values) have been reported were considered. One point in ROC space is considered better than another (each point belonging to a different tracking algorithm) if it is to the northwest (TPR is higher, FPR is lower, or both).

Results

Anatomical connections between cortical and subcortical regions for 11 right-handed healthy human subjects (dataset 1) and a single macaque monkey (dataset 2) were estimated using 3 different fiber tractography algorithms (see Materials and Methods). From the obtained voxel-region connectivity maps (Fig. 1*b*), weighted networks were created for the whole brain (Fig. 1*c*), in which each node represents an anatomic brain region (90 for humans or 176 for macaque monkey), arcs connecting nodes correspond to white matter links, and arc weights correspond to the degree of evidence supporting the

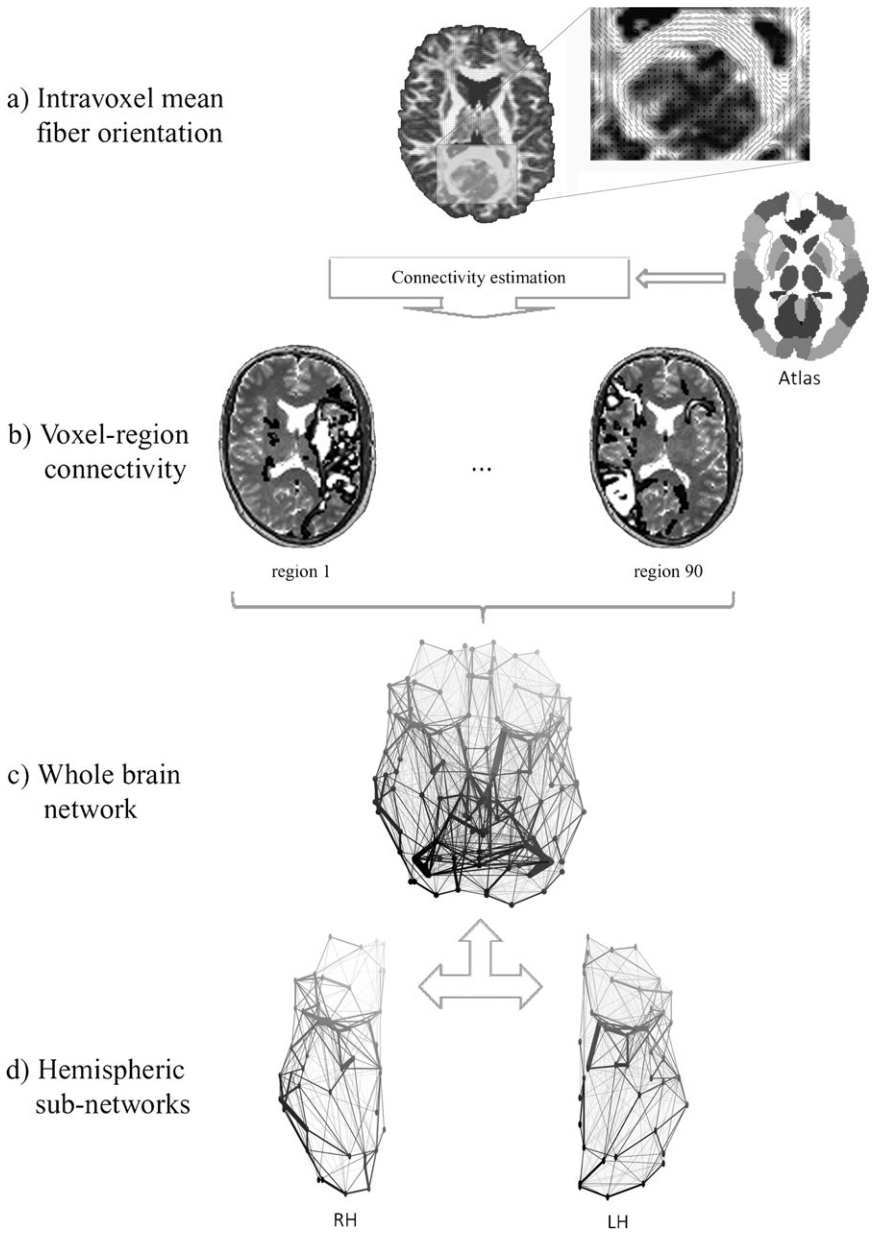

Figure 1. Schematic representation of the connectivity estimation and network construction procedure; for an example, human subject and the first tractography algorithm. (*a*) Axial map representing intravoxel mean fiber orientation (dyadic vectors), overlaid on the FA image; the inset figure provides detail of the high fiber orientation coherence within the splenium of the corpus callosum. (*b*) Axial voxel-region connectivity maps corresponding to region 1 (precentral gyrus) and region 90 (inferior temporal gyrus), overlaid on the registered T_2-weighted image; voxels are color-coded according to whether the connectivity of each voxel is high (white) or low (black). (*c*) Whole-brain structural network derived as described in Materials and Methods. (*d*) Right and left hemispheric networks (RH and LH, respectively), obtained by rejection of callosal connections on the whole-brain structural network (viewed from below). In (*c*) and (*d*), points (nodes) represent anatomic regions, lines without arrow (arcs) correspond to connections between them, and line widths reflect the corresponding arc weights. Lines colors were assigned according to the spatial position of the nodes.

existence of a white matter connection between regions. Eliminating callosal connections, each whole-brain network was segmented into left and right hemispheric networks, each one containing the same number of homolog regions (i.e., 45 regions for humans and 88 regions for macaque monkey; Fig. 1*d*).

In summary, for each subject we obtained a whole-brain network, and corresponding left/right hemispheric networks, each one replicated for each of 3 different fiber tracking algorithms.

Efficiency and Interconnectivity Asymmetries

We evaluated structural asymmetries between left hemisphere and right hemisphere networks according to 3 network properties: global efficiency (E_{glob}, a measure of how efficiently information can be exchanged over a network), local efficiency (E_{loc}, the average global efficiency of the local subnetworks), and interconnectivity (I_{conn}, a measure of the total amount of interconnectivity). These measures were separately computed for each individual's left and right hemispheric networks (see Materials and Methods).

In order to characterize the hemispheric asymmetry for global/local efficiency and interconnectivity, a LI was calculated for each of these 3 network measures, with a positive value meaning a lateralization to the right while negative value indicates a lateralization to the left (see Materials and Methods). Interestingly, the obtained LI results showed a consistent lateralization trend toward the right hemisphere for the 3 efficiency and interconnectivity network measures (Fig. 2).

Before testing for a statistically significant lateralization for human subjects, we compared tracking algorithm effects on the obtained LI values using a Kruskal–Wallis test, testing the null hypothesis that all values for a same network measure (E_{glob}, E_{loc}, or I_{conn}) were drawn from the same distribution independently of the fiber tracking algorithm used. The nonsignificant P values obtained ($P > 0.05$; Table 1) supported that LI values obtained were not statistically dependent on the tracking method used. Right lateralization was then tested using a sign test with the hypothesis that all obtained LI values for a same network measure come from a distribution whose median is zero. The small P values obtained (all $P < 7 \times 10^{-5}$; Table 1) supported the hypothesis of a significant positive lateralization for the 3 measures, indicating that human right hemisphere networks are anatomically more efficient and interconnected than left hemisphere networks for right-handed subjects. The LI values obtained for E_{glob}, E_{loc}, and I_{conn} in the macaque monkey were also positive for the 3 tractography algorithms (Table 1).

Regional Betweenness Centrality Asymmetries

We computed the betweenness centrality associated with each brain region considered in humans (dataset 1) and macaque monkey (dataset 2) with respect to the whole-brain anatomical network. This measure reflects the relative centrality or indispensability of each gray matter region within the entire brain anatomical network in terms of its connections, in which higher betweenness centrality values imply greater importance (see Materials and Methods). Then, in order to characterize centrality asymmetries between left and right homolog regions, a betweenness centrality LI was calculated (a positive value meaning a lateralization to the right while a negative value indicates a lateralization to the left).

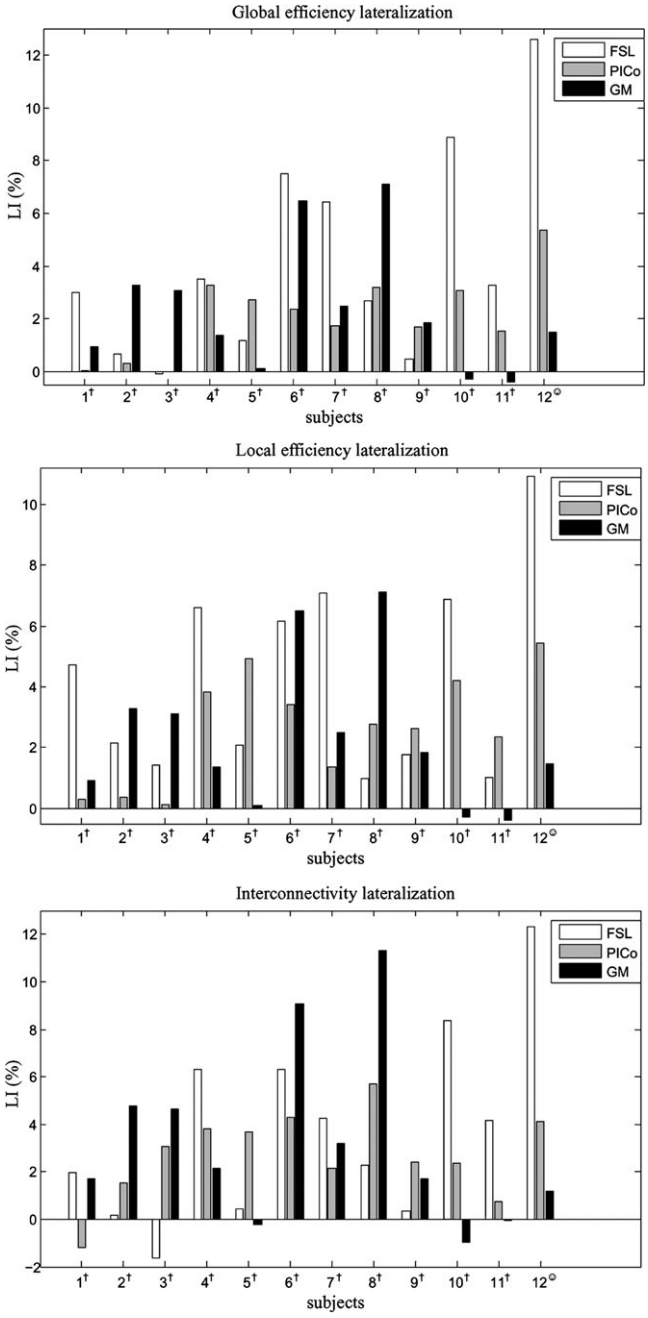

Figure 2. Efficiency and interconnectivity LIs obtained using 3 different fiber tractography algorithms (FSL, PICo, and GM; see Materials and Methods) for 11 right-handed healthy human subjects (dataset 1; denoted by superscript "†") and a nonhuman primate (dataset 2; denoted by superscript "☺"). Each compared left and right hemispheric networks contained the same number of anatomic homolog regions (i.e., 45 for humans or 88 for the nonhuman primate). Note a prevalence of positive bar values, indicating a consistent lateralization to the right hemisphere.

Results in Dataset 1

Before testing for a statistically significant lateralization of the betweenness centrality parameter between human homolog regions, we compared tracking algorithm effects on the measured betweenness centrality LI values using a Kruskal–Wallis test (Table 2). We observed that 9 region pairs had betweenness centrality values that were dependent on method but that the remaining 36 region pairs did not ($P > 0.05$). In a first lateralization analysis, we considered only those 36 pairs

Table 1
Global efficiency, local efficiency, and interconnectivity LIs obtained for the brain anatomical networks of a single macaque monkey (dataset 2) and 11 right-handed healthy subjects (dataset 1)

Brain networks	Measure	Lateralization (mean ± standard error of the mean)			Kruskal–Wallis (*P*)	Sign test (*P*)
		FSL	PICo	GM		
Macaque	E_{glob}	12.67	5.36	1.48	—	—
	E_{loc}	10.97	5.43	1.48	—	—
	I_{conn}	12.35	4.10	1.18	—	—
Human	E_{glob}	3.39 ± 0.90	1.80 ± 0.37	2.35 ± 0.76	0.4903	**1.09×10^{-5}**
	E_{loc}	3.71 ± 0.77	2.39 ± 0.50	2.37 ± 0.76	0.4140	**1.30×10^{-7}**
	I_{conn}	2.98 ± 0.94	2.60 ± 0.56	3.39 ± 1.16	0.9990	**6.61×10^{-5}**

Note: A positive value means a lateralization to the right hemisphere while a negative value indicates a lateralization to the left hemisphere. For human cases, mean values are reported with their corresponding standard errors (i.e., the uncertainty of how the sample mean represents the underlying population mean). The Kruskal–Wallis *P* values corresponds to the null hypothesis that all human LI values for a given measure (E_{glob}, E_{loc}, or I_{conn}) were drawn from the same distribution independently of the used fiber tracking algorithms. The nonsignificant *P* values obtained (all $P > 0.4$) demonstrates that each tracking method yields statistically indistinguishable results. The sign test *P* value corresponds to the null hypothesis that all the human LI values come from a distribution whose median is zero. The small *P* values obtained (all $P < 7 \times 10^{-5}$) supported the hypothesis of a significant positive lateralization for the 3 measures. For an equivalent statistical analysis, in which the same network measures were directly compared without the use of a LI, please see Supplementary Table 1. Significant values are depicted in bold type.

Table 2
Human considered brain regions (dataset 1, parcellation scheme 1) and corresponding statistical results for obtained betweenness centrality LI values

Region		Kruskal–Wallis (*P*)	Sign test (*P*)	Region		Kruskal–Wallis (*P*)	Sign test (*P*)
No.	Name			No.	Name		
1	**Precentral**	0.3753	**−0.0350**	24	Lingual	0.3974	+1
2	Frontal_Sup	0.3281	+1	25	**Occipital_Sup**	**0.1061**	**+0.0350**
3	Frontal_Sup_Orb	0.7893	+0.4582	26	**Occipital_Mid**	0.0031	**+0.0046**
4	Frontal_Mid	0.7311	−0.0614	27	**Occipital_Inf**	0.4269	**−0.0266**
5	**Frontal_Mid_Orb**	0.1131	**−0.0214**	28	Fusiform	0.1493	−0.4868
6	Frontal_Inf_Oper	0.4402	+1	29	Postcentral	0.5276	−0.3770
7	Frontal_Inf_Tri	0.2545	−0.8600	30	Parietal_Sup	0.6837	−0.1496
8	Frontal_Inf_Orb	0.3326	+0.1686	31	**Parietal_Inf**	**5.34×10^{-5}**	**−0.0071**
9	Rolandic_Oper	0.3974	+1	32	**SupraMarginal**	0.8089	**+0.0013**
10	**Supp_Motor_Area**	0.5851	**−0.0427**	33	**Angular**	0.2948	**+6.61×10^{-5}**
11	**Olfactory**	0.2917	**−0.0045**	34	Precuneus	0.4045	+0.0801
12	**Frontal_Sup_Medial**	0.0851	**−0.0059**	35	**Paracentral_Lobule**	0.3069	**−0.0002**
13	Frontal_Mid_Orb	0.0958	+0.2153	36	**Caudate**	0.2482	**−0.0013**
14	Rectus	0.0923	+0.4868	37	Putamen	**0.0059**	+0.2862
15	Insula	0.6338	+0.4868	38	Pallidum	0.2943	+0.5078
16	**Cingulate_Ant**	0.2344	**−1.30×10^{-7}**	39	Thalamus	0.2421	+0.5966
17	**Cingulate_Mid**	0.4021	**−0.0045**	40	Heschl	**8.52×10^{-6}**	−1
18	**Cingulate_Post**	**0.0479**	**−0.0043**	41	**Temporal_Sup**	**0.0069**	**−1.09×10^{-5}**
19	**Hippocampus**	0.5706	**+0.0350**	42	**Temporal_Pole_Sup**	**0.0238**	**−0.0008**
20	ParaHippocampal	0.4523	+0.2004	43	Temporal_Mid	0.2129	+0.8600
21	Amygdala	**0.0030**	+0.1338	44	Temporal_Pole_Mid	**0.0035**	−0.0063
22	Calcarine	0.1609	−1	45	Temporal_Inf	0.0724	−0.8600
23	**Cuneus**	0.4084	**+0.0013**				

Note: The Kruskal–Wallis *P* value corresponds to the null hypothesis that all betweenness centrality LI values for a given region were drawn from the same distribution independently of the used fiber tracking algorithms (a *P* value near to zero, i.e., $P < 0.05$, suggests that at least one sample median is significantly different from the others). The sign test *P* value (preceded by − or + symbols, which indicates a leftward or rightward lateralization, respectively) corresponds to the null hypothesis that the betweenness centrality LI values come from a distribution whose median is zero (a *P* value near to zero, i.e., $P < 0.05$, indicates a significant lateralization). For obtained betweenness centrality LI values corresponding to each region and fiber tracking method, including the complete statistic results of tracking algorithm effects, please see Supplementary Table 2. For an equivalent lateralization statistical analysis, in which the obtained betweenness centrality left/right values were directly compared without the use of a LI, please see Supplementary Table 3. Significant values are depicted in bold type.

of regions whose LI values can be statistically assumed to be drawn from the same distribution for the 3 tracking algorithms. Lateralization was then tested using a sign test, with the hypothesis that all measured LI values of each identified pair of regions came from a distribution whose median is zero.

Significant lateralization of betweenness centrality was found for 15 pairs of homolog regions ($P < 0.05$; Table 2). Leftward asymmetries (negative LI) were observed in 10 pairs of regions: precentral gyrus ($P = 0.0350$), middle orbital frontal ($P = 0.0214$), supplementary motor area ($P = 0.0427$), olfactory bulb ($P = 0.0045$), superior medial frontal gyrus ($P = 0.0059$), anterior cingulate gyrus ($P = 1.30 \times 10^{-7}$), middle cingulate gyrus ($P = 0.0045$), inferior occipital ($P = 0.0266$), paracentral lobule ($P = 0.0002$), and caudate ($P = 0.0013$). Significant rightward asymmetries (positive LI) were observed in 5 pairs of regions: hippocampus ($P = 0.0350$), cuneus ($P = 0.0013$), superior occipital ($P = 0.0350$), supramarginal ($P = 0.0013$), and angular ($P = 6.61 \times 10^{-5}$).

In order to account to a degree for the demonstrated differences in output from different tracking processes, we also assessed those pairs of regions whose LI values can be statistically assumed to be drawn from the same distribution for 2 of the 3 tracking algorithms. Eight additional pairs of homolog regions were included in the lateralization analysis when using this criterion. By means of a sign test, 6 of the additional region pairs were found to demonstrate significant lateralization ($P < 0.05$; Table 2). Leftward (negative LI) asymmetries were observed in posterior cingulate gyrus ($P = 0.0043$), inferior parietal ($P = 0.0071$), superior temporal ($P = 0.0015$), superior temporal pole ($P = 1.09 \times 10^{-5}$), and middle temporal pole (P = 0.0008),

whereas only the middle occipital ($P = 0.0046$) was found to demonstrate rightward asymmetry.

In summary, a total of 21 pairs of human homolog regions were found lateralized in terms of their centrality or indispensability to the whole-brain structural network. In line with a previous cortical thickness study (Luders et al. 2006), we found a more pronounced leftward than rightward asymmetry (15 vs. 6 lateralized regions, respectively).

Results in Dataset 2

Tracking algorithm effects for the macaque monkey data were compared using a Kruskal–Wallis test across all considered region pairs. The high P value obtained ($P = 0.8393$) supported the conclusion that LI values obtained were not statistically dependent on the tracking method used. Lateralization was then tested via a nonparametric permutation test (see Appendix).

Significant lateralization of betweenness centrality was found for 19 pairs of homolog regions ($P < 0.05$). Leftward asymmetry (negative LI) was observed in 11 regions: temporoparietal area ($P = 0.0156$), somatosensory area 2 ($P = 0.0156$), middle temporal area ($P = 0.0313$), ventral sudivisions of the anterior inferotemporal cortex area TE ($P = 0.0156$), dorsal prelunate area ($P = 0.0313$), subdivisions of area 8 ($P = 0.0156$), dorsal cingulate area 24 ($P = 0.0156$), subdivisions of cingulate area 24 ($P = 0.0156$), area 31 ($P = 0.0156$), area 14r ($P = 0.0156$), and medial area 10 ($P = 0.0313$). Significant rightward asymmetry (positive LI) was observed in 8 regions: visual area 3 ($P = 0.0156$), visual area V3A ($P = 0.0156$), area 13m ($P = 0.0156$), ventral visual area ($P = 0.0156$), 11m ($P = 0.0156$), medial intraparietal area ($P = 0.0313$), area 6M ($P = 0.0156$), and area 32 ($P = 0.0156$).

Fiber Tracking Algorithms Performance Evaluation

In order to evaluate the validity of the fiber tractography algorithms used in this paper (FSL, PICo, and GM) in comparison with the more often used deterministic SLT algorithm (Mori et al. 1999), we compared structural networks results obtained for the macaque monkey (dataset 2) with macaque cortex structural connections information derived by invasive tracer studies. Figure 3*a* presents cortical–cortical connection information extracted from Cocomac LVE00a database, corresponding to 63 brain cortical regions (see Materials and Methods, Data Acquisition and Preprocessing), whereas Figure 3*b* presents resultant ROC curves from comparison between previous cortical–cortical connection information and connectivity matrices estimated with FSL, PICo, GM, and SLT algorithms (see Materials and Methods, Receiver Operating Characteristic Analysis).

Although it is not possible to make a statistical comparison between the obtained ROC curves (due to the fact that they correspond to a single dataset), a clear prevalence of the 3 fiber tracking algorithms used in this study (FSL, PICo, and GM) can be seen over the performance of the traditional deterministic SLT algorithm, which is also numerically supported by the corresponding areas under the ROC curves: FSL (AUC = 0.78), PICo (AUC = 0.72), GM (AUC = 0.77), and SLT (AUC = 0.62).

Discussion

We performed a structural network analysis based on DW-MRI techniques and graph theory to identify brain hemispheric anatomical asymmetries. In contrast with previous structural network studies (Hagmann, Kurant, et al. 2006; Hagmann et al. 2008; Iturria-Medina et al. 2008; Gong et al. 2009), here we

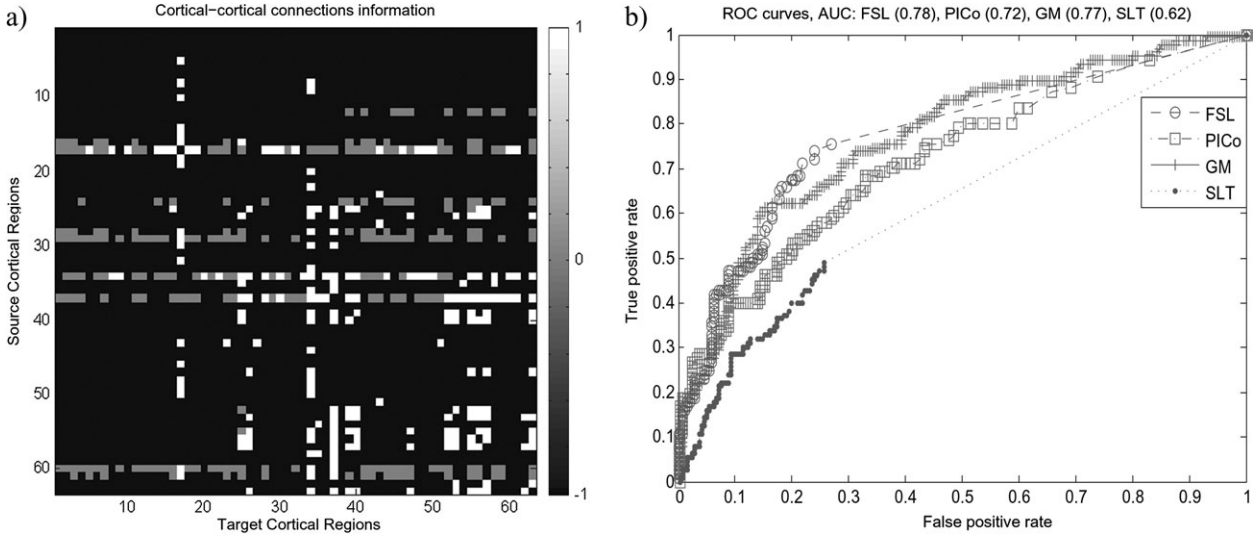

Figure 3. Macaque cortex structural connections derived by invasive tracer studies and ROC curves resulting from a comparison with connections derived by DW-MRI tractography techniques. (*a*) Cortical–cortical connection information extracted from Cocomac LVE00a database (cocomac.org/home.asp). Similarly to methods in Haroon et al. (2008), the source and target cortical regions, numbered 1 to 63 on the matrices, correspond to the subset of cortical areas labeled as follows in the LVE00a scheme: 1, 2, 4, 23, 45, 24d, 3a, 46p, 46v, 4C, 5D, 5V, 6Ds, 6Val, 6Vam, 7a, 7b, 7op, 7t, 8Ac, 8Am, 8As, A1, AIP, DP, FST, G, IPa, LIPd, LIPv, LOP, MDP, MIP, MSTda, MSTdp, MSTm, MT, Pi, PIP, PO, PrCO, Ri, S2, TAa, TE1–3, TEa/m, TF, TPOc, TPOi, TPOr, Tpt, V1, V2, V2v, V3, V3A, V4, V4ta, V4tp, VIPl, VIPm, VOT, and VP, respectively. Values of 1 (or 0) have used to fill in cells where there is (or not) a direct connection, while a value of −1 has been used for connections for which no information is available. (*b*) Resultant ROC curves from comparison between previous cortical–cortical connection information and connectivity matrices estimated with FSL, PICo, GM, and traditional SLT (Mori et al. 1999) algorithms, for a single macaque monkey (dataset 2). For a valid comparison, we considered only those matrix cells where have been reported a direct (dis)connection by invasive tracer studies (values 0 and 1 on panel *a*). Although it is not possible to make a statistical comparison between the obtained ROC curves (due to the fact that they correspond to a single dataset), a clear prevalence of the 3 probabilistic fiber tracking algorithms used in the study (FSL, PICo, and GM) can be seen over the performance of the traditional deterministic SLT algorithm, which is also numerically supported by the corresponding areas under the ROC curves: FSL (AUC = 0.78), PICo (AUC = 0.72), GM (AUC = 0.77), and SLT (AUC = 0.62).

emphasize the use of 3 tractography algorithms, making the results robust to choice of tracking algorithm, which is potentially a significant source of bias, and thus providing a valuable assessment of the relative detail of network information across these methods and, more importantly, providing a robust set of results with which to assess lateralization. We found significant differences between right and left hemispheric networks at a hemispheric level using the metrics E_{glob}, E_{loc}, and I_{conn}, indicating that the right hemisphere is, at the whole-hemisphere level, more efficient and interconnected. However, the subhemisphere regional asymmetries observed using the betweenness centrality measure indicate that the left hemisphere presents more central or indispensable regions for the whole-brain structural network than the right hemisphere. These findings were found to hold true across the human dataset and in the single macaque dataset, indicating that general organizational strategies are broadly similar between these species.

Efficiency and Interconnectivity Hemispheric Asymmetries

We explored general structural differences between both hemispheres via 3 network measures: global efficiency, local efficiency, and interconnectivity (E_{glob}, E_{loc}, and I_{conn}, respectively). A significant rightward asymmetry on both efficiencies and interconnectivity was found (Table 1 and Fig. 2). To our knowledge, this is the first report of brain structural asymmetry of these measures. This whole-hemisphere right-greater-than-left interconnectivity and efficiency are consistent with the reported significant rightward asymmetry in the white matter volume for right-handed healthy subjects (Barrick et al. 2005). Furthermore, the greater efficiency and stronger interconnectivity in the right hemisphere obtained for the macaque monkey suggest that these asymmetry characteristics could be shared among primates, even when caution is applied when considering that a single nonhuman primate case was tested.

Our results raise a number of intriguing questions. For example, what are the functional requirements underlying the fact that one hemisphere is more efficient and interconnected than the other? Interestingly, our leftward regional asymmetry findings, as expressed using the betweenness centrality measure, indicate that left hemisphere presents more central or indispensable regions for the whole-brain structural network than the right hemisphere, which is in line with previous studies (Luders et al. 2006). Since the connectivity of a given region, and thus the measurement of betweenness centrality, is related to its cellular characteristics such as cell packing density, cell size, and number of cortical neurons (Costa 2005; Lerch et al. 2006), connectivity asymmetries of the cortex might be related to hemisphere-specific functional specializations, which based on the high correspondence between our structural results and well-known functional regional asymmetries seems to support the fact that the left hemisphere is "regionally" more specialized than the right hemisphere. When considered in combination with the whole-hemisphere efficiency and interconnectivity results, this induces us to think that a greater left hemisphere functional specialization could lead to its apparently "worse" general structural organization (less efficiency and interconnectivity at the whole-hemisphere scale) in comparison with the right hemisphere. In terms of functional principles, these patterns appear to support the fact that the left hemisphere has a leading role for highly demanding specific process, such as language and motor actions, which may require dedicated specialized networks, whereas the right hemisphere has a leading role for more general process, such as integration tasks, which may require a more general level of interconnection.

Regional Betweenness Centrality Asymmetries, Correspondence with Previous Findings

Previous studies reporting structural differences between homologs areas have been mainly based on specific cytoarchitectonic and morphologic features while our regional asymmetry analysis is based on the fiber connectivity pattern of each region in terms of its relative importance to the whole-brain structural network. Despite the interpretative differences between the measures and procedures employed in different studies, we found a considerable regional correspondence between previous reports, old observations of asymmetric regional specialization (based on the effects of brain lesions), and our asymmetry findings, supporting the hypothesis of a determinant relation between cytoarchitectonic/morphologic characteristics and interregional connectivity (Costa 2005; Lerch et al. 2006; Van Essen 1997).

Dataset 1

In correspondence with previous human studies, leftward asymmetries for the precentral gyrus and supplementary motor area, regions associated with motor control actions as hand preferences, have been well recognized for right-handed subjects (Amunts et al. 1996; Rogers et al. 2004; Dadda et al. 2006; Luders et al. 2006). The paracentral gyrus and cingulate gyrus leftward asymmetries found here are in line with similar cortical thickness results (Luders et al. 2006), although this cingulate gyrus asymmetry is in contrast to rightward asymmetries previously reported using volumetric and voxel-based measures (Paus et al. 1996; Watkins et al. 2001). However, significant left-greater-than-right FA values have previously been reported for the cingulum bundle (i.e., white matter fibers projecting from the cingulate gyrus to the entorhinal cortex), suggesting a more coherent fiber organization in the left hemisphere that is consistent with our findings (Gong et al. 2005; Clark et al. 2007). In addition, our observed leftward asymmetries for superior temporal, superior temporal pole, and middle temporal pole regions agree with many structural reports (Niznikiewicz et al. 2000; Good et al. 2001a; Watkins et al. 2001; Luders et al. 2006) and the documented left hemispheric dominance for language (Price 2000). Nevertheless, we did not find significant localized asymmetries related to the inferior frontal regions, thought to contain Broca's region, which is also associated with dominant language process. Interestingly, a recent study (Keller et al. 2009) concluded that contrary to what has frequently been reported in literature, structural asymmetry of Broca's area has not been reproducibly demonstrated. According to this previous study, if a structural asymmetry of Broca's area does exist, it is variable and may differ from that of the functional asymmetry of language, which is more consistent. Additionally, it is known that the gyral location and extent of Broca's area vary considerably between subjects (Amunts et al. 1999, 2004; Mazziotta et al. 2001; Juch et al. 2005; Lindenberg et al. 2007). Such variation has been demonstrated using cytoarchitectonic and functional imaging methods but cannot be determined

from the purely anatomical parcellation of the cortex used in our study. We must therefore conclude that there is a possibility that a true underlying localized lateralization associated with Broca's area has not been detected using our methodology.

Asymmetries of the caudate nucleus, a region found here with a leftward betweenness centrality asymmetry and thought to be involved in higher order motor control (Graybiel 2005) and learning and memory process (Packard and Knowlton 2002), have been reported for normal children (Filipek et al. 1997; Pueyo et al. 2000; Castellanos et al. 2001) and for children with attention-deficit hyperactivity disorder (Aylward et al. 1996; Sugama et al. 2000; Castellanos et al. 2001; Schrimsher et al. 2002). However, reports on caudate asymmetry have been inconsistent (e.g., in normal subjects a common finding is left-greater-than-right caudate volume although there are also reports of no asymmetry and even of rightward asymmetry; see Schrimsher et al. 2002). Recently, Tremols et al. (2008) argued that these inconsistencies can be explained according to different asymmetric properties of the head and body parts of the caudate, which connect into different fiber pathways. Unfortunately, our study was limited to the whole caudate region without making distinction between its head and body parts due to the nonspecificity of our gray matter parcellation scheme. Further caudate network analysis should focus on more precise parcellations in order to explore how caudate connectivity could be related to head and body volume asymmetries.

In the case of those homotopic regions found with a betweenness centrality rightward asymmetry, the finding of the hippocampus is consistent with the widely reported right-sided asymmetries for this region (Free et al. 1995; Bigler et al. 1997; Bilir et al. 1998; Good et al. 2001b; Pegues et al. 2003). It is striking that all the other right-lateralized regions (i.e., cuneus, superior occipital, supramarginal, angular, and middle occipital) are related to visual processes, and there is evidence that right hemispheric areas play a dominant role in the implementation of visuo-spatial attention (Fink et al. 2000, 2001; Corbetta and Shulman 2002; Halligan et al. 2003). The specific case of a betweenness centrality rightward lateralization for angular and supramarginal gyrus (Brodmann areas 39 and 40, respectively) is an additionally interesting result because evidence exists suggesting that lesions to these regions on the right hemisphere cause visuo-spatial attentional neglect (Vallar 1998; Halligan et al. 2003; Husain and Rorden 2003), a neuropsychological syndrome characterized by an attentional bias. To our knowledge, this is the first structural indication of why the widely investigated phenomenon of visuo-attentional neglect is more commonly a consequence of right hemisphere damage.

Dataset 2

Literature about macaque monkey interhemispheric brain asymmetries is scarce. However, in correspondence with our results, consistent evidence concerning leftward volumetric asymmetry at the cytoarchitectural level of the temporoparietal area (Tpt) has been reported (Gannon et al. 2008). This region, a homologous area of the human planum temporale, is thought to be linked to the participation of the left temporal lobe in auditory and vocalization process, cognitive tasks that have being reported to present a leftward lateralization in the macaque monkey (Heffner HE and Heffner RS 1984; Poremba et al. 2004). In addition, we found a leftward asymmetry to the middle temporal and the ventral subdivisions of the anterior inferotemporal cortex area TE. These results reinforce the view that the macaque could provide a model system for studying the evolutionary development of concepts and language in humans (Gil-Da-Costa et al. 2004).

Interestingly, we also find corresponding interspecies structural asymmetries in the visual system (rightward asymmetry) and cingulate gyrus (leftward asymmetry), which to our knowledge have not been reported before. However, as the parcellation schemes that we used for human and nonhuman primate differed considerably, further analyses are necessary to identify with confidence other possible asymmetry equivalences and differences between species.

Methodological Issues and Future Work

Previous structural and functional studies have provided evidence on how the apparent topological organization of brain networks can be modified by the different parcellation strategies applied (Hagmann, Kurant, et al. 2006; Li et al. 2009; Wang et al. 2009). In principle, our results could be biased by the chosen gray matter parcellation scheme, a key element of the creation of brain anatomical networks due to its influence on the node definition process. Thus, in order to explore possible parcellation effects on our efficiency and interconnectivity findings, we repeated the human structural brain graph asymmetry analysis for another parcellation scheme with a different set of 70 regions, using 1 of the 3 tractography algorithms (GM), and the results indicated a consistent hemispheric rightward asymmetry on these measures (see Supplementary Figure 1 and Supplementary Table 4). However, it is important to consider that although the atlases that we used were carefully created taking into account relevant anatomical and functional details, in the future it might be more meaningful to use advanced integrative atlases based on finer cytoarchitecture, myeloarchitecture, and MRI procedures (Toga et al. 2006).

In contrast to the more often used deterministic tractography approach (Conturo et al. 1999; Mori et al. 1999; Basser et al. 2000), which typically can only progress when there is high certainty of fiber direction limiting their usefulness in defining pathways near gray matter, the 3 different tractography algorithms used in this study include in the tracking procedure the uncertainty of each fiber orientation (based in the high information contained in the acquired high–angular resolution DW-MRI datasets) and attempt to establish the spatially distributed degree of connection confidence across the whole brain to a given start point. However, in spite its advantages over the conventional deterministic tractography (Fig. 3*b*), these methods still present important limitations, like a decrease in probability of connection with distance and the difficulty to separate real from false connections. Thus, in the future it might be more meaningful to use statistical methodologies such as that recently introduced by Morris et al. (2008), which proposed to address the mentioned limitations of current probabilistic tractography algorithms using an objective method for determining significant connections based on statistical comparison with a null pattern of connection, which also has the desirable effect of reducing the effect of distance on extracted patterns of connection.

Another consideration for our study is the relatively small size of the used subject sample, especially with respect to the

macaque brain. Despite this, as previously mentioned, the use of 3 different tractography algorithms allowed us to replicate network measures, making the statistical analysis nonspecific to only one tracking algorithm's results and thus improving the robustness of the study. However, future work should be addressed to analyzing a bigger number of subjects, taking into account also handedness and sex effects, not considered here in spite their evidenced influence on structural and functional asymmetries.

Supplementary Material

Supplementary material can be found at: http://www.cercor.oxfordjournals.org/

Funding

Biotechnology and Biological Sciences Research Council of the United Kingdom (BB/E002226/1).

Notes

We are also grateful to the anonymous reviewers for their useful comments and suggestions. Author contributions: Y.I.-M. and A.P.F. conceived and designed the experiment. G.J.M.P., D.M.M., H.A.H., M.A., and N.L. acquired and preprocessed the MRI datasets. D.M.M., H.A.H., and G.J.M.P. implemented the PICo tractography algorithm used. Y.I.-M. implemented the graph-based tractography algorithm and network analysis tools used. Y.I.-M. and A.P.F. analyzed the data and wrote the paper with input from all other authors. All authors contributed to constructive discussions regarding the interpretation of the results. C*onflict of Interest*: None declared.

Appendix

Permutation Test Used for the Betweenness Centrality Lateralization Analysis of Dataset 2

The analysis consisted of the following steps (Blair and Karniski 1993; Galan et al. 1997):

1. The null hypothesis (H_0) of 0 mean for all the measured LI values is decomposed into the marginal hypotheses H_{0r}: $m_r = 0$, where m_r is the mean of the LI values for a given brain region r.
2. Each marginal hypothesis H_{0r} is tested by:
   a) Computing the t-statistic for the original LI values of the region r (i.e., to compute the t value corresponding to the hypothesis that the data in the vector LI come from a distribution with mean zero).
   b) Obtaining a larger number of permutation resample from the data (without replacement) and constructing the permutation distribution of the t-statistic (in each permutation the sign of at least one of the elements of the original LI vector was changed, being the complete permutation space 2^n, where n is the number of fiber tracking algorithms used).
   c) Finding the P value of H_{0r} by comparing the original t-statistic (obtained in step a) with the t-statistic permutation distribution (obtained in step b), specifically, to perform a 2-sided test (sign test) with the hypothesis that the data in the t-statistic permutation distribution come from a distribution whose median is the original t-statistic.

References

Alemán-Gómez Y, Melie-García L, Valdes-Hernández P. 2006. IBASPM: toolbox for automatic parcellation of brain structures. Neuroimage. 31(1):29–185.

Amunts K, Schlaug G, Schleicher A, Steinmetz H, Dabringhaus A, Roland PE, Zilles K. 1996. Asymmetry in the human motor cortex and handedness. Neuroimage. 4:216–222.

Amunts K, Schleicher A, Burgel U, Mohlberg H, Uylings HBM, Zilles K. 1999. Broca's region revisited: cytoarchitecture and intersubject variability. J Comp Neurol. 412:319–341.

Amunts K, Weiss PH, Mohlberg H, Pieperhoff P, Eickhoff S, Gurd JM, Marshall JC, Shah NJ, Fink GR, Zilles K. 2004. Analysis of neural mechanisms underlying verbal fluency in cytoarchitectonically defined stereotaxic space—the roles of Brodmann areas 44 and 45. Neuroimage. 22:42–56.

Aylward EH, Reiss AL, Reader MJ, Singer HS, Brown JE, Denckla MB. 1996. Basal ganglia volumes in children with attention-deficit hyperactivity disorder. J Child Neurol. 11:112–115.

Barrick TR, Mackay CE, Prima S, Maes F, Vandermeulen D, Crow TJ, Roberts N. 2005. Automatic analysis of cerebral asymmetry: an exploratory study of the relationship between brain torque and planum temporale asymmetry. Neuroimage. 24:678–691.

Basser PJ, Pajevic S, Pierpaoli C, Duda J, Aldroubi A. 2000. In vivo fiber tractography using DT-MRI data. Magn Reson Med. 44:625–632.

Bassett DS, Bullmore E, Verchinski BA, Mattay VS, Weinberger DR, Meyer-Lindenberg A. 2008. Hierarchical organization of human cortical networks in health and schizophrenia. J Neurosci. 28:9239–9248.

Bassett DS, Meyer-Lindenberg A, Achard S, Duke T, Bullmore E. 2006. Adaptive reconfiguration of fractal small-world human brain functional networks. Proc Natl Acad Sci U S A. 103:19518–19523.

Behrens TE, Johansen-Berg H, Woolrich MW, Smith SM, Wheeler-Kingshott CA, Boulby PA, Barker GJ, Sillery EL, Sheehan K, Ciccarelli O, et al. 2003. Non-invasive mapping of connections between human thalamus and cortex using diffusion imaging. Nat Neurosci. 6:750–757.

Behrens TE, Woolrich MW, Jenkinson M, Johansen-Berg H, Nunes RG, Clare S, Matthews PM, Brady JM, Smith SM. 2003. Characterization and propagation of uncertainty in diffusion-weighted MR imaging. Magn Reson Med. 50:1077–1088.

Bigler ED, Blatter DD, Anderson CV, Johnson SC, Gale SD, Hopkins RO, Burnett B. 1997. Hippocampal volume in normal aging and traumatic brain injury. Am J Neuroradiol. 18:11–23.

Bilir E, Craven W, Hugg J, Gilliam F, Martin R, Faught E, Kuzniecky R. 1998. Volumetric MRI of the limbic system: anatomic determinants. Neuroradiology. 40:138–144.

Blair RC, Karniski W. 1993. An alternative method for significance testing of wave-form difference potentials. Psychophysiology. 30:518–524.

Boccaletti S, Latora V, Moreno Y, Chavez M, Hwang D-U. 2006. Complex networks: structure and dynamics. Phys Rep. 424:175–308.

Castellanos FX, Giedd JN, Berquin PC, Walter JM, Sharp W, Tran T, Vaituzis AC, Blumenthal JD, Nelson J, Bastain TM, et al. 2001. Quantitative brain magnetic resonance imaging in girls with attention-deficit/hyperactivity disorder. Arch Gen Psychiatry. 58:289–295.

Chen ZJ, He Y, Rosa P, Germann J, Evans AC. 2008. Revealing modular architecture of human brain structural networks by using cortical thickness from MRI. Cereb Cortex. 18:2374–2381.

Clark C, Ulmer J, Gaggle W, Mark L. 2007. Structural asymmetries of the normal human cingulum. Available at http://www.marquette.edu/engineering/pages/AllYouNeed/Biomedical/Programs/documents/codi_final.pdf. Accessed 1 April 2010.

Conturo TE, Lori NF, Cull TS, Akbudak E, Snyder AZ, Shimony JS, McKinstry RC, Burton H, Raichle ME. 1999. Tracking neuronal fiber pathways in the living human brain. Proc Natl Acad Sci U S A. 96:10422–10427.

Corbetta M, Shulman GL. 2002. Control of goal-directed and stimulus-driven attention in the brain. Nat Rev Neurosci. 3:201–215.

Costa Lda F. 2005. Morphological complex networks: can individual morphology determine the general connectivity and dynamics of networks? Presented at the COSIN final meeting, Salou, Spain, March. arXiv:q-bio/0503041v1 [q-bio.MN]. Available at http://arxiv.org/abs/q-bio/0503041. Accessed 1 April 2010.

Costa Lda F, Rodrigues FA, Travieso G, Villas PR. 2007. Characterization of complex networks: A survey of measurements. Adv. Phys. 56(1):167–242.
Costa Lda F, Sporns O. 2005. Hierarchical features of large-scale cortical connectivity. Eur Phys J B. 48:567–573.
Dadda M, Cantalupo C, Hopkins WD. 2006. Further evidence of an association between handedness and neuroanatomical asymmetries in the primary motor cortex of chimpanzees (Pan troglodytes). Neuropsychologia. 44:2582–2586.
Dall'Asta L, Barrat A, Barthelemy M, Vespignani A. 2006. Vulnerability of weighted networks. J Stat Mech. Published online April 27, doi: 10.1088/1742-5468/2006/04/P04006.
Embleton KV, Lambon Ralph MA, Parker GJ. 2006. A combined distortion corrected protocol for diffusion weighted tractography and fMRI. ISMRM 14th Scientific Meeting & Exhibition; 2006 May 6–12; Seattle, WA. Vol. 14, 1070 p.
Fawcett T. 2006. An introduction to ROC analysis. Pattern Recog Lett. 27:861–874.
Filipek PA, Semrud-Clikeman M, Steingard RJ, Renshaw PF, Kennedy DN, Biederman J. 1997. Volumetric MRI analysis comparing subjects having attention-deficit hyperactivity disorder with normal controls. Neurology. 48:589–601.
Fink GR, Marshall JC, Shah NJ, Weiss PH, Halligan PW, Grosse-Ruyken M, Ziemons K, Zilles K, Freund HJ. 2000. Line bisection judgments implicate right parietal cortex and cerebellum as assessed by fMRI. Neurology. 54:1324–1331.
Fink GR, Marshall JC, Weiss PH, Zilles K. 2001. The neural basis of vertical and horizontal line bisection judgments: an fMRI study of normal volunteers. Neuroimage. 14:S59–S67.
Free SL, Bergin PS, Fish DR, Cook MJ, Shorvon SD, Stevens JM. 1995. Methods for normalization of hippocampal volumes measured with MR. Am J Neuroradiol. 16:637–643.
Freeman L. 1977. A set of measures of centrality based upon betweenness. Sociometry. 40:35–41.
Galan L, Biscay R, Rodriguez JL, PerezAbalo MC, Rodriguez R. 1997. Testing topographic differences between event related brain potentials by using non-parametric combinations of permutation tests. Electroencephalogr Clin Neurophysiol. 102:240–247.
Gannon PJ, Kheck N, Hof PR. 2008. Leftward interhemispheric asymmetry of macaque monkey temporal lobe language area homolog is evident at the cytoarchitectural, but not gross anatomic level. Brain Res. 1199:62–73.
Gil-Da-Costa R, Braun A, Lopes M, Hauser MD, Carson RE, Herscovitch P, Martin A. 2004. Toward an evolutionary perspective on conceptual representation: species-specific calls activate visual and affective processing systems in the macaque. Proc Natl Acad Sci U S A. 101:17516–17521.
Glasser MF, Rilling JK. 2008. DTI tractography of the human brain's language pathways. Cereb Cortex. 18:2471–2482.
Gong GL, He Y, Concha L, Lebel C, Gross DW, Evans AC, Beaulieu C. 2009. Mapping anatomical connectivity patterns of human cerebral cortex using in vivo diffusion tensor imaging tractography. Cereb Cortex. 19:524–536.
Gong GL, Jiang TZ, Zhu CZ, Zang YF, Wang F, Xie S, Xiao JX, Gu XM. 2005. Asymmetry analysis of cingulum based on scale-invariant parameterization by diffusion tensor imaging. Hum Brain Mapp. 24:92–98.
Good CD, Johnsrude I, Ashburner J, Henson RNA, Friston KJ, Frackowiak RSJ. 2001a. Cerebral asymmetry and the effects of sex and handedness on brain structure: a voxel-based morphometric analysis of 465 normal adult human brains. Neuroimage. 14:685–700.
Good CD, Johnsrude IS, Ashburner J, Henson RNA, Friston KJ, Frackowiak RSJ. 2001b. A voxel-based morphometric study of ageing in 465 normal adult human brains. Neuroimage. 14:21–36.
Graybiel AM. 2005. The basal ganglia: learning new tricks and loving it. Curr Opin Neurobiol. 15:638–644.
Hagmann P, Cammoun L, Gigandet X, Meuli R, Honey CJ, Wedeen V, Sporns O. 2008. Mapping the structural core of human cerebral cortex. PLoS Biol. 6:1479–1493.
Hagmann P, Cammoun L, Martuzzi R, Maeder P, Clarke S, Thiran JP, Meuli R. 2006. Hand preference and sex shape the architecture of language networks. Hum Brain Mapp. 27:828–835.
Hagmann P, Kurant M, Gigandet X, Thiran P, Wedeen VJ, Meuli R, Thiran JP. 2006. Imaging the brain neuronal network with diffusion MRI: a way to understand its global architecture. ISMRM 14th Scientific Meeting & Exhibition; 2006 May 6–12; Seattle, WA. Vol. 14, 436 p.
Halligan PW, Fink GR, Marshall JC, Vallar G. 2003. Spatial cognition: evidence from visual neglect. Trends Cogn Sci. 7:125–133.
Haroon HA, Morris DM, Embleton KV, Alexander DC, Parker GJM. 2009. Using the model-based residual bootstrap to quantify uncertainty in fiber orientations from Q-ball analysis. IEEE Trans Med Imaging. 28:535–550.
Haroon HA, Morris DM, Kaiser A, Augath M, Logothetis NK, Parker GJ. 2008. Comparing corticocortical interconnection information from tracer studies and probabilistic tractography in the postmortem macaque brain. ISMRM 16th Scientific Meeting & Exhibition; 2008 May 3–9; Toronto, Ontario, Canada, p. 3369.
He Y, Chen ZJ, Evans AC. 2007. Small-world anatomical networks in the human brain revealed by cortical thickness from MRI. Cereb Cortex. 17:2407–2419.
He Y, Chen Z, Evans AC. 2008. Structural insights into aberrant topological patterns of large-scale cortical networks in Alzheimer's disease. J Neurosci. 28:4756–4766.
Heffner HE, Heffner RS. 1984. Temporal lobe lesions and perception of species-specific vocalizations by macaques. Science. 226: 75–76.
Honey CJ, Kotter R, Breakspear M, Sporns O. 2007. Network structure of cerebral cortex shapes functional connectivity on multiple time scales. Proc Natl Acad Sci U S A. 104:10240–10245.
Husain M, Rorden C. 2003. Non-spatially lateralized mechanisms in hemispatial neglect. Nat Rev Neurosci. 4:26–36.
Iturria-Medina Y, Canales-Rodríguez EJ, Melie-García L, Valdes-Hernández PA, Martínez-Montes E, Alemán-Gómez Y, Sánchez-Bornot JM. 2007. Characterizing brain anatomical connections using diffusion weighted MRI and graph theory. Neuroimage. 36:645–660.
Iturria-Medina Y, Sotero RC, Canales-Rodriguez EJ, Alemán-Gómez Y, Melie-Garcia L. 2008. Studying the human brain anatomical network via diffusion-weighted MRI and Graph Theory. Neuroimage. 40:1064–1076.
Juch H, Zimine I, Seghier ML, Lazeyras F, Fasel JHD. 2005. Anatomical variability of the lateral frontal lobe surface: implication for intersubject variability in language neuroimaging. Neuroimage. 24:504–514.
Keller SS, Crow T, Foundas A, Amunts K, Roberts N. 2009. Broca's area: nomenclature, anatomy, typology and asymmetry. Brain Lang. 109:29–48.
Koch MA, Norris DG, Hund-Georgiadis M. 2002. An investigation of functional and anatomical connectivity using magnetic resonance imaging. Neuroimage. 16:241–250.
Kubicki M, Westin CF, Maier SE, Frumin M, Nestor PG, Salisbury DF, Kikinis R, Jolesz FA, McCarley RW, Shenton ME. 2002. Uncinate fasciculus findings in schizophrenia: a magnetic resonance diffusion tensor imaging study. Am J Psychiatry. 159: 813–820.
Latora V, Marchiori M. 2001. Efficient behavior of small-world networks. Phys Rev Lett. 87:198701.
Lerch JP, Worsley K, Shaw WP, Greenstein DK, Lenroot RK, Giedd J, Evans AC. 2006. Mapping anatomical correlations across cerebral cortex (MACACC) using cortical thickness from MRI. Neuroimage. 31:993–1003.
Lewis JW, Van Essen DC. 2000. Mapping of architectonic subdivisions in the macaque monkey, with emphasis on parieto-occipital cortex. J Comp Neurol. 428:79–111.
Li YH, Liu Y, Li J, Qin W, Li KC, Yu CS, Jiang TZ. 2009. Brain anatomical network and intelligence. PLoS Comput Biol. 5:e1000395.
Lindenberg R, Fangerau H, Seitz RJ. 2007. "Broca's area" as a collective term? Brain Lang. 102:22–29.
Luders E, Narr KL, Thompson PM, Rex DE, Jancke L, Toga AW. 2006. Hemispheric asymmetries in cortical thickness. Cereb Cortex. 16:1232–1238.

Mazziotta J, Toga A, Evans A, Fox P, Lancaster J, Zilles K, Woods R, Paus T, Simpson G, Pike B, et al. 2001. A four-dimensional probabilistic atlas of the human brain. J Am Med Inform Assoc. 8:401–430.
Mazziotta JC, Toga AW, Evans A, Fox P, Lancaster J. 1995. A probabilistic atlas of the human brain: theory and rationale for its development. The International Consortium for Brain Mapping (ICBM). Neuroimage. 2:89–101.
Mori S, Crain BJ, Chacko VP, van Zijl PC. 1999. Three-dimensional tracking of axonal projections in the brain by magnetic resonance imaging. Ann Neurol. 45:265–269.
Morris DM, Embleton KV, Parker GJM. 2008. Probabilistic fibre tracking: differentiation of connections from chance events. Neuroimage. 42:1329–1339.
Niznikiewicz M, Donnino R, McCarley RW, Nestor PG, Iosifescu DV, O'Donnell B, Levitt J, Shenton ME. 2000. Abnormal angular gyrus asymmetry in schizophrenia. Am J Psychiatry. 157: 428–437.
Onnela JP, Saramaki J, Kertesz J, Kaski K. 2005. Intensity and coherence of motifs in weighted complex networks. Phys Rev E. 71:065103.
Packard MG, Knowlton BJ. 2002. Learning and memory functions of the basal ganglia. Annu Rev Neurosci. 25:563–593.
Parker GJM, Alexander DC. 2005. A mechanism for probabilistic fibre tracking using multi-fibre orientation functions. ISMRM Workshop on Methods for Quantitative Diffusion MRI of the brain; 2005 March 13–16; Lake Louise, Alberta, Canada. 74 p.
Parker GJM, Haroon HA, Wheeler-Kingshott CA. 2003. A framework for a streamline-based probabilistic index of connectivity (PICo) using a structural interpretation of MRI diffusion measurements. J Magn Reson Imaging. 18:242–254.
Parker GJM, Wheeler-Kingshott CA, Barker GJ. 2002. Estimating distributed anatomical connectivity using fast marching methods and diffusion tensor imaging. IEEE Trans Med Imaging. 21:505–512.
Parker GJM, Luzzi S, Alexander DC, Wheeler-Kingshott CAM, Clecarelli O, Ralph MAL. 2005. Lateralization of ventral and dorsal auditory-language pathways in the human brain. Neuroimage. 24: 656–666.
Paus T, Otaky N, Caramanos Z, MacDonald D, Zijdenbos A, DAvirro D, Gutmans D, Holmes C, Tomaiuolo F, Evans AC. 1996. In vivo morphometry of the intrasulcal gray matter in the human cingulate, paracingulate, and superior-rostral sulci: hemispheric asymmetries, gender differences and probability maps. J Comp Neurol. 376:664–673.
Pegues MP, Rogers LJ, Amend D, Vinogradov S, Deicken RF. 2003. Anterior hippocampal volume reduction in male patients with schizophrenia. Schizophr Res. 60:105–115.
Poremba A, Malloy M, Saunders RC, Carson RE, Herscovitch P, Mishkin M. 2004. Species-specific calls evoke asymmetric activity in the monkey's temporal poles. Nature. 427:448–451.
Powell HWR, Parker GJM, Alexander DC, Symms MR, Boulby PA, Wheeler-Kingshott CAM, Barker GJ, Noppeney U, Koepp MJ, Duncan JS. 2006. Hemispheric asymmetries in language-related pathways: a combined functional MPI and tractography study. Neuroimage. 32:388–399.
Price CJ. 2000. The anatomy of language: contributions from functional neuroimaging. J Anat. 197:335–359.
Pueyo R, Maneru C, Vendrell P, Mataro N, Estevez-Gonzalez A, Garcia-Sanchez C, Junque C. 2000. Attention deficit hyperactivity disorder. Cerebral asymmetry observed on magnetic resonance. Rev Neurol. 30:920–925.
Rodrigo S, Naggara O, Oppenheirn C, Golestani N, Poupon C, Cointepas Y, Mangin JF, Le Bihan D, Meder JF. 2007. Human subinsular asymmetry studied by diffusion tensor Imaging and fiber tracking. Am J Neuroradiol. 28:1526–1531.
Rogers BP, Carew JD, Meyerand ME. 2004. Hemispheric asymmetry in supplementary motor area connectivity during unilateral finger movements. Neuroimage. 22:855–859.
Schrimsher GW, Billingsley RL, Jackson EF, Moore BD. 2002. Caudate nucleus volume asymmetry predicts attention-deficit hyperactivity disorder (ADHD) symptomatology in children. J Child Neurol. 17:877–884.
Sporns O. 2006. Small-world connectivity, motif composition, and complexity of fractal neuronal connections. Biosystems. 85:55–64.
Sporns O, Zwi JD. 2004. The small world of the cerebral cortex. Neuroinformatics. 2:145–162.
Sugama S, Bingham PM, Wang PP, Moss EM, Kobayashi H, Eto Y. 2000. Morphometry of the head of the caudate nucleus in patients with velocardiofacial syndrome (del 22q11.2). Acta Paediatr. 89:546–549.
Toga A, Thompson P, Susumu M, Amunts K, Zilles K. 2006. Towards multimodal atlases of the human brain. Nat Rev Neurosci. 7(12):952–966.
Tremols V, Bielsa A, Soliva JC, Raheb C, Carmona S, Tomas J, Gispert JD, Rovira M, Fauquet J, Tobena A, et al. 2008. Differential abnormalities of the head and body of the caudate nucleus in attention deficit-hyperactivity disorder. Psychiat Res Neuroimaging. 163:270–278.
Tuch DS. 2004. Q-ball imaging. Magn Reson Med. 52:1358–1372.
Tuch DS, Reese TG, Wiegell MR, Wedeen VJ. 2003. Diffusion MRI of complex neural architecture. Neuron. 40:885–895.
Vallar G. 1998. Spatial hemineglect in humans. Trends Cogn Sci. 2:87–97.
Van Essen DC. 1997. A tension-based theory of morphogenesis and compact wiring in the central nervous system. Nature. 385:313–318.
Wang JH, Wang L, Zang YF, Yang H, Tang HH, Gong QY, Chen Z, Zhu CZ, He Y. 2009. Parcellation-dependent small-world brain functional networks: a resting-state fMRI study. Hum Brain Mapp. 30:1511–1523.
Watkins KE, Paus T, Lerch JP, Zijdenbos A, Collins DL, Neelin P, Taylor J, Worsley KJ, Evans AC. 2001. Structural asymmetries in the human brain: a voxel-based statistical analysis of 142 MRI scans. Cereb Cortex. 11:868–877.
Watts DJ, Strogatz SH. 1998. Collective dynamics of small-world networks. Nature. 393(6684):440–442.

Supplementary material

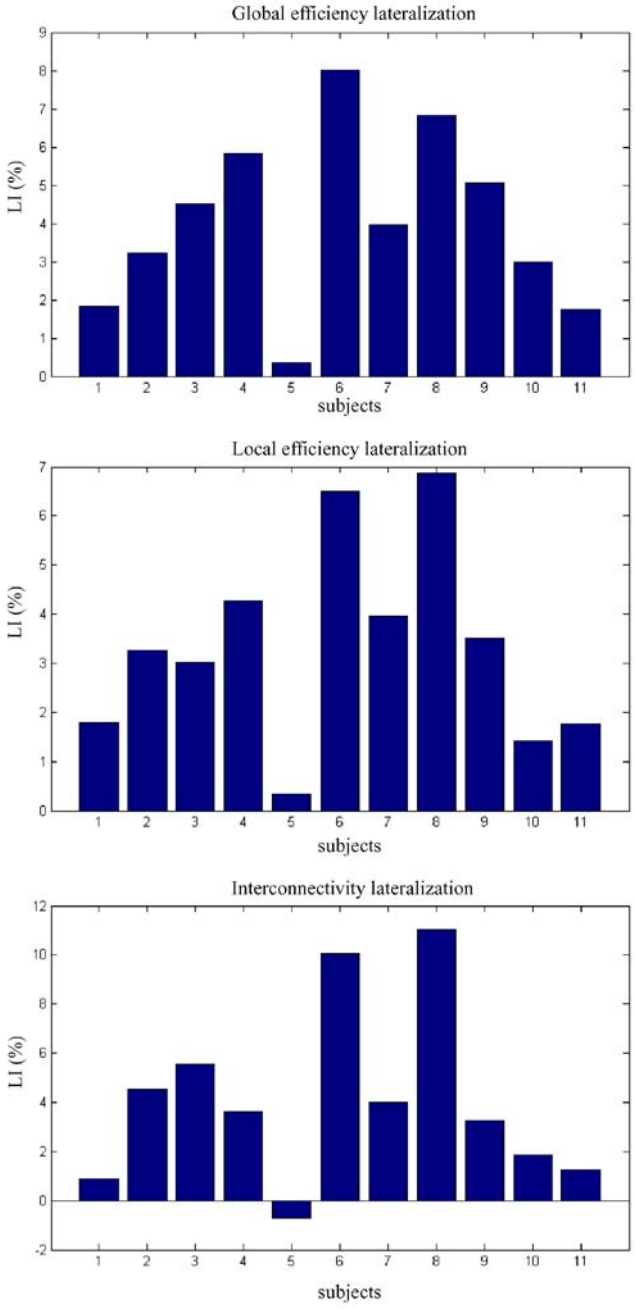

Supplementary Figure 1. Human efficiency and interconnectivity lateralization indexes obtained using one tractography algorithm (GM, see *Materials and Methods*) for 11 right-handed healthy human subjects (dataset 1, parcellation scheme 2). Each compared left and right hemispheric networks contained the same number of anatomic homologue regions (i.e. 35 gray matter regions). Note a prevalence of positive bar values, indicating a consistent lateralization to the right hemisphere.

Supplementary Table 1. Global efficiency, local efficiency and interconnectivity statistical left/right direct comparison results for the hemispheric anatomical networks of 11 right-handed healthy subjects (dataset 1). For each measure, the Friedman P-value (preceded by – or + symbols, which indicates a leftward or rightward lateralization respectively) corresponds to the null hypothesis that medians of obtained left and right hemispheric values are equal, after adjusting for possible subjects and fiber tracking algorithms effects (a P-value near to zero, i.e. P < 0.05, indicates a significant lateralization). Significant values are depicted in bold type. Note the high correspondence with the results obtained using a lateralization index (Table 1 of the main manuscript).

Brain Networks	**Measure**	Friedman test (P)
Human	E_{glob}	**+1.34e-05**
	E_{loc}	**+4.45e-07**
	I_{conn}	**+6.23e-05**

Supplementary Table 2. Human considered brain regions (dataset 1, parcellation scheme 1) and obtained betweenness centrality lateralization indices (mean values and standard errors). The First Kruskal-Wallis P-value corresponds to the null hypothesis that all betweenness centrality LI values for a given region were drawn from the same distribution independently of the used fiber tracking algorithms (same results reported on Table 2; a P-value near to zero, i.e. P < 0.05, suggests that at least one sample median is significantly different from the others). The second Kruskal-Wallis P-value (reported only when the null hypothesis of First Kruskal-Wallis test was rejected), corresponds to the null hypothesis that LI values can be statistically assumed to be drawn from the same distribution for two of the three tracking algorithms. The superscript text indicates the two methods with higher second Kruskal-Wallis P-value, to which corresponds the reported value. Significant values are depicted in bold type.

Region		**BC Lateralization Index (Mean ± SEM)**			**First Kruskal-Wallis (P)**	**Second Kruskal-Wallis (P)**
No.	**Name**	FSL	PICo	GM		
1	Precentral	-4.51 ± 17.43	-21.97 ± 6.00	-28.34 ± 14.82	0.3753	-

2	Frontal_Sup	4.76 ± 2.81	-8.39 ± 7.89	40.00 ± 18.97	0.3281	-
3	Frontal_Sup_Orb	8.47 ± 20.06	12.49 ± 5.96	1.09 ± 17.11	0.7893	-
4	Frontal_Mid	-0.13 ± 14.35	-16.58 ± 7.11	-21.21 ± 26.31	0.7311	-
5	Frontal_Mid_Orb	-31.51 ± 19.36	-36.36 ± 15.21	0 ± 0	0.1131	-
6	Frontal_Inf_Oper	22.88 ± 17.93	1.60 ± 7.69	2.26 ± 18.73	0.4402	-
7	Frontal_Inf_Tri	11.43 ± 16.54	1.87 ± 9.53	-25.49 ± 18.78	0.2545	-
8	Frontal_Inf_Orb	15.95 ± 23.58	19.70 ± 9.21	-4.93 ± 19.69	0.3326	-
9	Rolandic_Oper	19.50 ± 20.18	-4.61 ± 9.50	-4.97 ± 13.30	0.3974	-
10	Supp_Motor_Area	-30.10 ± 20.25	-14.14 ± 10.74	-36.38 ± 15.87	0.5851	-
11	Olfactory	-7.18 ± 17.11	-14.91 ± 5.85	-29.09 ± 15.82	0.2917	-
12	Frontal_Sup_Medial	-45.88 ± 14.51	-19.56 ± 14.06	-60.83 ± 14.79	0.0851	-
13	Frontal_Mid_Orb	-16.18 ± 18.83	-5.36 ± 8.97	23.64 ± 13.79	0.0958	-
14	Rectus	11.57 ± 17.88	-4.75 ± 3.29	13.37 ± 3.83	0.0923	-
15	Insula	13.55 ± 7.96	-1.84 ± 2.97	10.76 ± 13.36	0.6338	-
16	Cingulate_Ant	-55.67 ±	-40.54 ±	-47.95 ±	0.2344	-

		15.65	8.54	7.27		
17	Cingulate_Mid	-43.04 ± 16.61	-20.32 ± 8.59	-30.21 ± 8.25	0.4021	-
18	Cingulate_Post	-73.27 ± 17.76	-16.66 ± 13.12	-29.54 ± 21.23	**0.0479**	$0.8952^{(PICo,GM)}$
19	Hippocampus	22.86 ± 10.23	8.13 ± 3.72	19.64 ± 8.11	0.5706	-
20	ParaHippocampal	21.48 ± 11.94	13.55 ± 6.82	-1.05 ± 16.14	0.4523	-
21	Amygdala	13.85 ± 14.01	7.42 ± 4.82	-38.83 ± 9.83	**0.0030**	$0.5327^{(FSL,PICo)}$
22	Calcarine	2.62 ± 13.88	4.18 ± 3.37	-18.59 ± 9.00	0.1609	-
23	Cuneus	10.14 ± 15.34	33.97 ± 6.49	16.48 ± 12.05	0.4084	-
24	Lingual	6.89 ± 9.28	-4.20 ± 2.81	3.96 ± 8.30	0.3974	-
25	Occipital_Sup	18.08 ± 16.20	33.42 ± 7.74	-9.09 ± 13.60	0.1061	-
26	Occipital_Mid	37.10 ± 14.73	33.01 ± 7.43	-23.85 ± 11.03	**0.0031**	$0.8182^{(FSL,PICo)}$
27	Occipital_Inf	-9.09 ± 21.12	-7.50 ± 16.69	-49.69 ± 15.19	0.4269	-
28	Fusiform	7.46 ± 4.97	-7.81 ± 5.06	-4.17 ± 5.31	0.1493	-
29	Postcentral	-10.62 ± 18.54	-1.71 ± 10.66	-23.89 ± 22.58	0.5276	-
30	Parietal_Sup	-17.72 ± 23.06	-10.18 ± 11.98	-30.94 ± 17.46	0.6837	-

31	Parietal_Inf	-8.46 ± 14.48	0.20 ± 5.57	-85.70 ± 5.66	**5.34e-5**	0.5327$^{(FSL,PICo)}$
32	SupraMarginal	30.21 ± 18.59	52.35 ± 10.50	28.07 ± 20.55	0.8089	-
33	Angular	25.63 ± 17.53	45.47 ± 8.33	53.74 ± 16.71	0.2948	-
34	Precuneus	0.32 ± 10.53	7.84 ± 6.42	24.49 ± 10.74	0.4045	-
35	Paracentral_Lobule	-45.45 ± 15.74	-62.51 ± 14.96	-21.76 ± 17.42	0.3069	-
36	Caudate	-51.11 ± 16.77	-39.97 ± 13.19	-13.51 ± 17.89	0.2482	-
37	Putamen	2.406 ± 3.6395	-14.70 ± 6.14	11.55 ± 4.50	**0.0059**	0.2244$^{(FSL,GM)}$
38	Pallidum	18.18 ± 12.19	24.90 ± 14.72	-11.56 ± 9.37	0.2943	-
39	Thalamus	-2.60 ± 7.27	7.23 ± 4.81	-3.98 ± 2.60	0.2421	-
40	Heschl	0 ± 0	0 ± 0	-74.11 ± 11.65	**8.52e-6**	**0**
41	Temporal_Sup	-11.35 ± 7.73	-14.49 ± 7.73	-46.71 ± 7.58	**0.0069**	0.8695$^{(FSL,PICo)}$
42	Temporal_Pole_Sup	-55.20 ± 19.23	-15.88 ± 7.47	-59.93 ± 18.32	**0.0238**	0.5904$^{(FSL,GM)}$
43	Temporal_Mid	20.31 ± 10.57	-3.05 ± 3.95	0.41 ± 8.27	0.2129	-
44	Temporal_Pole_Mid	-29.09 ± 13.84	-30.54 ± 13.31	50.89 ± 18.90	**0.0035**	0.7299$^{(FSL,PICo)}$
45	Temporal_Inf	15.63 ±	-7.60 ±	-13.49 ±	0.0724	-

		7.81	4.26	11.80		

Supplementary Table 3. Human considered brain regions (dataset 1, parcellation scheme 1) and corresponding statistical left/right comparison results for obtained betweenness centrality values. For each pair of homologue regions, the Friedman P-value (preceded by – or + symbols, which indicates a leftward or rightward lateralization respectively) corresponds to the null hypothesis that medians of obtained left and right betweenness centrality values are equal, after adjusting for possible subjects and fiber tracking algorithms effects (a P-value near to zero, i.e. $P < 0.05$, indicates a significant lateralization). Significant values are depicted in bold type. Note the high correspondence with the results obtained using a lateralization index (Table 2 of the main manuscript).

Region		Friedman (P)	**Region**		Friedman (P)
No.	**Name**		**No.**	**Name**	
1	**Precentral**	**-0.0236**	24	Lingual	+0.8618
2	Frontal_Sup	-0.8574	25	**Occipital_Sup**	**+0.0236**
3	Frontal_Sup_Orb	+0.3531	26	**Occipital_Mid**	**+0.0028**
4	**Frontal_Mid**	**-0.0410**	27	**Occipital_Inf**	**-0.0163**
5	**Frontal_Mid_Orb**	**-0.0114**	28	Fusiform	+0.3840
6	Frontal_Inf_Oper	+0.8618	29	Postcentral	-0.2888
7	Frontal_Inf_Tri	+0.7236	30	Parietal_Sup	-0.1059
8	Frontal_Inf_Orb	+0.1166	31	**Parietal_Inf**	**-0.0045**
9	Rolandic_Oper	+1	32	**SupraMarginal**	**+0.0009**
10	**Supp_Motor_Area**	**-0.0284**	33	**Angular**	**+6.23e-05**
11	**Olfactory**	**-0.0030**	34	Precuneus	+0.0555
12	**Frontal_Sup_Medial**	**-0.0038**	35	**Paracentral_Lobule**	**-0.0002**
13	Frontal_Mid_Orb	-0.1572	36	**Caudate**	**-0.0009**
14	Rectus	+0.3840	37	Putamen	0

15	Insula	+0.3840	38	Pallidum	+0.3173
16	**Cingulate_Ant**	**-4.45e-07**	39	Thalamus	-0.4795
17	**Cingulate_Mid**	**-0.0030**	40	Heschl	0
18	**Cingulate_Post**	**-0.0028**	41	**Temporal_Sup**	**-2.00e-05**
19	**Hippocampus**	**+0.0236**	42	**Temporal_Pole_Sup**	**-6.46e-04**
20	ParaHippocampal	+0.1441	43	Temporal_Mid	+0.7236
21	Amygdala	0	44	**Temporal_Pole_Mid**	**-0.0038**
22	Calcarine	-0.8618	45	Temporal_Inf	+0.7236
23	**Cuneus**	**+0.0009**			

Supplementary Table 4. 70 cortical and sub-cortical gray matter regions (parcellation scheme 2) defined in the Jacob Atlas developed by the Montreal Neurological Institute (MNI, http://www.mni.mcgill.ca/; the brain stem region was rejected from the original Jacob Atlas in order to consider the same left and right gray matter regions).

Region		**Region**	
No.	**Name**	**No.**	**Name**
1	medial front-orbital gyrus right	36	inferior occipital gyrus left
2	medial front-orbital gyrus left	37	superior occipital gyrus right
3	middle frontal gyrus right	38	superior occipital gyrus left
4	middle frontal gyrus left	39	caudate nucleus right
5	insula right	40	caudate nucleus left
6	insula left	41	supramarginal gyrus right
7	precentral gyrus right	42	supramarginal gyrus left
8	precentral gyrus left	43	superior parietal lobule right

9	lateral front-orbital gyrus right	44	superior parietal lobule left
10	lateral front-orbital gyrus left	45	cuneus right
11	cingulate region right	46	cuneus left
12	cingulate region left	47	superior temporal gyrus left
13	medial frontal gyrus right	48	superior temporal gyrus right
14	medial frontal gyrus left	49	middle occipital gyrus right
15	superior frontal gyrus right	50	middle occipital gyrus left
16	superior frontal gyrus left	51	middle temporal gyrus right
17	globus pallidus right	52	middle temporal gyrus left
18	globus pallidus left	53	cerebellum right
19	putamen right	54	cerebellum left
20	putamen left	55	lingual gyrus right
21	parahippocampal gyrus right	56	lingual gyrus left
22	parahippocampal gyrus left	57	postcentral gyrus right
23	angular gyrus right	58	postcentral gyrus left
24	angular gyrus left	59	inferior frontal gyrus right
25	subthalamic nucleus right	60	inferior frontal gyrus left
26	subthalamic nucleus left	61	lateral occipitotemporal gyrus right
27	nucleus accumbens right	62	lateral occipitotemporal gyrus left
28	nucleus accumbens left	63	thalamus right
29	uncus right	64	thalamus left
30	uncus left	65	medial occipitotemporal gyrus right
31	precuneus right	66	medial occipitotemporal gyrus left

32	precuneus left	67	occipital pole right
33	hippocampal formation right	68	occipital pole left
34	hippocampal formation left	69	inferior temporal gyrus right
35	inferior occipital gyrus right	70	inferior temporal gyrus left

Supplementary Table 5. Considered 88 cortical and sub-cortical gray matter regions in the macaque monkey brain (dataset 2, parcellation scheme LVE00a) and obtained betweenness centrality lateralization indices.

Region		**Betweenness centrality lateralization index**		
No.	**Name**	FSL	PICo	GM
1	Ventral occipitotemporal area (VOT)	-3.7634	55.1282	-39.1304
2	Visual area 4 (V4)	9.4736	32.1904	25.9259
3	Subdivisions of the anterior inferotemporal cortex area TE (Tea/m)	-8.8716	-20.9424	-52.8138
4	Visual area 4 transitional area, anterior (V4ta)	3.9244	-15.8283	-41.8938
5	Superior temporal area (Ts)	-0.7812	10.1449	-31.4285
6	Temporoparietal area (Tpt)	-33.3333	-37.2197	-94.5945
7	Primary auditory cortex (A1)	-19.0298	-63.8483	-17.8743
8	Subdivisions of the anterior inferotemporal cortex area TE (TE1-3)	18.8235	-3.4055	-77.7777
9	Dorsal subdivisions of the anterior inferotemporal cortex area TE (TE1-3d)	-15.0602	-12.5714	-33.3333

10	Temporal area TAa (TAa)	9.7472	20.1612	-24.2424
11	Second somatosensory area (S2)	-14.5137	0.2247	-24.4399
12	Precentral opercular cortex (PrCO)	100	100	8.7719
13	Visual area 2, ventral (V2v)	-0.7360	-69.2682	10.3825
14	Visual area 1 (V1)	8.7443	-10.4519	-57.1428
15	Ventral posterior area (VP)	0	-63.3136	100
16	Somatosensory area 2 (2)	0	-86.6666	-33.3333
17	Area 6Vb (6vb)	30.1062	-1.8390	-4.8865
18	Postcentral area PA (PA)	51.8413	-3.4883	47.8260
19	Visual area 2, dorsal (V2d)	6.3965	82.5862	-48.3146
20	Temporal parietal occipital, caudal (TPOc)	49.1803	-23.8805	100
21	Visual area 4 transitional area, posterior (V4tp)	-100	-42.0289	-100
22	Middle temporal area (MT)	-100	7.7809	-100
23	Somatosensory area 7b (7b)	100	-71.7948	100
24	Somatosensory area 3b (3b)	14.6666	34.4961	23.1884
25	Somatosensory area 1 (1)	0	50	0
26	Floor of superior temporal area (FST)	0	-3.3033	100
27	Temporal parietal occipital, intermediate (TPOi)	-55.1401	-12.8630	65.2941
28	Temporal parietal occipital, rostral (TPOr)	40.1746	1.6746	51.6528

29	12	98.0198	-21.7073	-70.5882
30	Opercular area 7 (7op)	-2.1022	-3.2069	-1.3377
31	Intraparietal sulcus associated area in the STS (IPa)	100	-23.7842	98.2300
32	Area 6Va, lateral (6Val)	0	100	0
33	Subdivision of area 7 near tip of intraparietal sulcus (7t)	0	0	0
34	Visual area 3 (V3)	19.0857	24.3902	23.0769
35	Ventral sudivisions of the anterior inferotemporal cortex area TE (TE1-3v)	-45.6066	-42.0765	-100
36	Gustatory cortex (G)	-99.1935	-30.9305	-80.9523
37	Visual area 7a (7a)	-41.8978	58.2952	86.3636
38	Medial superior temporal area, dorsal, anterior (MSTda)	42.7792	-19.7959	-50.0671
39	Somatosensory area 3a (3a)	100	72.4550	-4.4871
40	Retroinsula (Ri)	-15.5873	3.7608	34.0782
41	Dysgranular insular cortex (Iq Id)	-4.4871	-27.0358	40.3470
42	Temporal area F (TF)	-34.6938	-36.8916	-44.4897
43	Area 6Va, medial (6Vam)	75.1801	12.0028	-70.5989
44	Walker area 45 (45)	-100	-100	-98.3606
45	Medial superior temporal, medial (MSTm)	44.1265	-96.5665	-28.7197
46	Lateral intraparietal, dorsal (LIPd)	-100	-48.6666	100
47	Parainsular area (Pi)	-56.7157	-71.7472	-77.5206

48	Visual area 46, posterior (46p)	-100	100	0
49	Medial superior temporal area, dorsal, posterior (MSTdp)	-50.7042	56.7099	33.3333
50	Anterior intraparietal area (AIP)	-99.1525	-25.0836	-100
51	Area 5, ventral (5V)	-57.8102	-11.2016	65.6184
52	4C	91.7525	-21.0526	-33.3333
53	Lateral intraparietal, ventral (LIPv)	84.9350	12.1387	100
54	Primary motor cortex (4)	12	52.7607	100
55	13l	-21.4876	-37.7171	-51.3761
56	Dorsal prelunate area (DP)	-84.6153	0	-100
57	Perirhinal area 36 (36)	0	-100	0
58	Subdivisions of area 8 (8AC)	-100	-10.0204	-99.3827
59	11l	100	100	100
60	Visual area V3A (V3A)	0	75.18037	68.4210
61	13m	-34.3283	100	56
62	Visual area, ventral (46v)	17.2858	13.1824	44.0078
63	Ventral intraparietal, medial (VIPm)	25.0823	-31.8526	30.1932
64	Entorhinal cortex (ER)	23.6442	98.4375	-82.2222
65	Area 5, dorsal (5D)	-66.6666	-94.5126	71.4285
66	Ventral intraparietal, lateral (VIPl)	100	-36.7447	-100
67	Perirhinal area 35 (35)	0	0	0
68	11m	100	-30.5555	100
69	Subdivisions of area 6D (6Ds)	44.1130	42.4390	-19.3347
70	13a_b	3.5161	-32.0872	-51.5021

71	Subdivisions of area 8 (8As)	-100	-3.1141	0
72	Subdivisions of area 6D (6DC)	0	9.7770	0
73	Subdivisions of area 6D (6DR)	0	87.7777	0
74	Lateral occipital parietal (LOP)	29.4755	77.0024	74.3396
75	Subdivisions of area 8 (8Am)	-3.4653	-100	80
76	Posterior intraparietal area (PIP)	44.2815	-100	71.4285
77	9	-53.7399	29.4117	47.8260
78	Medial intraparietal area (MIP)	11.2322	78.2846	22.2222
79	6M	100	0	11.1111
80	Parietal-occipital area (PO)	24.3697	71.7825	-5.2083
81	Medial dorsal parietal area (MDP)	-36.3357	70.5322	-100
82	Cingulate area 23 (23)	11.8279	-67.6660	-84.7328
83	Cingulate area 24 (24d)	-29.0064	-18.2038	-28.7569
84	31	-100	-98.8750	0
85	Subdivisions of cingulate area 24 (24ab)	-77.9555	-93.6603	-83.4170
86	14r	9.6234	-100	-87.8048
87	Medial area 10 (10m)	-100	-8.2352	-100
88	32	2.2727	11.5020	-18.2926

3.4. ARTÍCULO 4

Yasser Iturria-Medina, Alejandro Pérez Fernández, Pedro Valdés Hernández, Lorna García Pentón, Erick J. Canales-Rodríguez, Lester Melie-Garcia, Agustin Lage Castellanos and Marlis Ontivero Ortega, 2011. Automated Discrimination of Brain Pathological State Attending to Complex Structural Brain Network Properties: the Shiverer Mutant Mouse Case. PLOS One, 6(5): e19071.

OPEN ACCESS Freely available online

PLoS one

Automated Discrimination of Brain Pathological State Attending to Complex Structural Brain Network Properties: The Shiverer Mutant Mouse Case

Yasser Iturria-Medina[1]*, Alejandro Pérez Fernández[2,3], Pedro Valdés Hernández[1], Lorna García Pentón[3], Erick J. Canales-Rodríguez[5,6], Lester Melie-Garcia[1], Agustin Lage Castellanos[4], Marlis Ontivero Ortega[7]

1 Neuroimaging Department, Cuban Neuroscience Center, La Habana, Cuba, **2** Basque Center on Cognition Brain and Language, Donostia-San Sebastián, Basque Country, Spain, **3** Laboratory of Cognitive Neuroscience, Universidad Diego Portales, Santiago, Chile, **4** Neurostatistic Department, Cuban Neuroscience Center, La Habana, Cuba, **5** Centro de Investigacion Biomedica en Red de Salud Mental (CIBERSam), Madrid, Spain, **6** Benito Menni Complex Assistencial en Salut Mental, Barcelona, Spain, **7** Neuroengineering Department, Cuban Neuroscience Center, La Habana, Cuba

Abstract

Neuroimaging classification procedures between normal and pathological subjects are sparse and highly dependent of an expert's clinical criterion. Here, we aimed to investigate whether possible brain structural network differences in the shiverer mouse mutant, a relevant animal model of myelin related diseases, can reflect intrinsic individual brain properties that allow the automatic discrimination between the shiverer and normal subjects. Common structural networks properties between shiverer (C3Fe.SWV Mbp^{shi}/Mbp^{shi}, n = 6) and background control (C3HeB.FeJ, n = 6) mice are estimated and compared by means of three diffusion weighted MRI (DW-MRI) fiber tractography algorithms and a graph framework. Firstly, we found that brain networks of control group are significantly more clustered, modularized, efficient and optimized than those of the shiverer group, which presented significantly increased characteristic path length. These results are in line with previous structural/functional complex brain networks analysis that have revealed topologic differences and brain network randomization associated to specific states of human brain pathology. In addition, by means of *network measures spatial representations* and discrimination analysis, we show that it is possible to classify with high accuracy to which group each subject belongs, providing also a probability value of being a normal or shiverer subject as an individual anatomical classifier. The obtained correct predictions (e.g., around 91.6–100%) and clear *spatial* subdivisions between control and shiverer mice, suggest that there might exist specific network *subspaces* corresponding to specific brain disorders, supporting also the point of view that complex brain network analyses constitutes promising tools in the future creation of interpretable imaging biomarkers.

Citation: Iturria-Medina Y, Pérez Fernández A, Valdés Hernández P, García Pentón L, Canales-Rodríguez EJ, et al. (2011) Automated Discrimination of Brain Pathological State Attending to Complex Structural Brain Network Properties: The Shiverer Mutant Mouse Case. PLoS ONE 6(5): e19071. doi:10.1371/journal.pone.0019071

Editor: Yong He, Beijing Normal University, China

Received January 12, 2011; **Accepted** March 21, 2011; **Published** May 27, 2011

Funding: Data used for this study were downloaded from the Mouse BIRN Data Repository, supported by grants to the Mouse BIRN (U24-RR021760) Testbed funded by the National Center for Research Resources at the National Institutes of Health, United States of America. The funders and sponsors of the Mouse BIRN Data Repository, from which the authors downloaded the data, had no role in the study design, data collection and analysis, decision to publish, or preparation of the manuscript.

Competing Interests: The authors have declared that no competing interests exist.

* E-mail: iturria.medina@gmail.com

Introduction

Complex brain network analysis, in which the brain is modeled as a graph whose nodes (or vertices) represent structural/functional regions and the links (or edges) between them represent anatomical or functional connections, provide us with topological measurements that could be interpreted in terms of the management and integration of the nervous information flow and physiological brain dynamics. Initial analyses of brain networks in the graph framework were devoted to describe the key organizational principles of the normal brain, reporting certain brain topological features such as high clustering, small-worldness, the presence of highly connected hubs, assortativity, modularity or hierarchy, properties that are not typical of random graph and regular lattices (for a review see [1]). However, current trends in brain networks analyses are more focused to detect differences in particular topologic measures associated to specific human states of pathology, such as Multiple Sclerosis (MS) [2], tumors [3], Alzheimer's disease [4,5], Schizophrenia [6,7] and Stroke [8,9], contributing to the understanding of pathophysiological mechanisms, and supporting in general the hypothesis that network randomization and subsequent loss of optimal organization could be a common final result of the brain's reaction to lesions or neurodegenerative processes [8].

Among the diversity of techniques from which brain networks could be extracted [10–21], DW-MRI techniques are promising in particular to evaluate topological differences in those brain disorders where the white matter is severely affected, like Multiple Sclerosis [22,23] and Acute Disseminated Encephalomyelitis [24,25]. Based in the non-invasive acquisition of structural information about the intravoxel axons arrangement, DW-MRI techniques allows the *in vivo* approximate mapping of the brain

nervous fiber circuitry [17,26–31]. However, despite of the demonstrated usefulness of DW-MRI techniques to detect anomalies [32–38], to date, brain network analyses based on DW-MRI tractography techniques have been more devoted to describe the brain organizational principles described above [15,17,18,39–42] than to the study of specific brain pathologies [5,9,43], limiting its potential applications to the quantitative description and understanding of specific brain disorders, something with a possible practical outcome for clinical diagnosing.

Here, in line with previous pathophysiological brain studies in a graph framework, we propose to search for altered topological properties using fiber tractography DW-MRI applied to a brain disease where the white matter is severely affected. We have the further purpose of investigating whether possible brain structural network differences reflect intrinsic individual brain properties that allow the automatic discrimination between pathological and normal subjects. More specifically, we search for altered topological properties in six different basic parameters (i.e. clustering, characteristic path length, modularity, global/local efficiency and small-worldness) in the shiverer mouse, a mutant model relevant to the study of myelin related diseases since it is characterized by a deletion of the gene encoding myelin basic protein (MBP), resembling white matter dysmyelinating and demyelinating process that takes place in humans due to an inflammatory process, for example, in those patients affected by MS [22,23,44]. In addition, because a specific focus of clinical diagnostic investigation is the anatomic discrimination between normal and pathological states, we perform an automatic discrimination between shiverer and control subjects based on these complex network characteristics. In order to perform the automatic subject classification, the concept of *network measure spatial representation* is introduced. In this, for each network measure, each subject is spatially represented and determined by a unique point whose coordinates are assigned according to individual network metrics. Then using classification techniques the original *space* is subdivided into two *subspaces*, separating subjects that present similar topological characteristics, and obtaining also an individual probability value of being from one or the other group as an anatomical classifier.

Finally, some comments are made concerning the relationship between the obtained findings and some previously reported human pathological state studies (e.g. MS reports), as well as the possible implications that these complex networks analyses and representations might have on clinical diagnostic investigation, for either, the anatomic classification between normal and pathological states, and the creation of interpretable brain dynamical imaging biomarkers.

Results

Anatomical connections between cortical and subcortical regions for shiverer (C3Fe.SWV Mbp^{shi}/Mbp^{shi}, n = 6) and background control (C3HeB.FeJ, n = 6) mice were estimated using three different fiber tractography algorithms applied to data from high resolution DW-MRI (see *Materials and Methods*). From the obtained whole brain axonal trajectories (Figure 1b), weighted networks were created for the whole brain (Figure 1c), in which each node represents an anatomic brain region (150 gray matter regions in total), arcs connecting nodes correspond to white matter links, and arc weights correspond to the degree of evidence supporting the existence of a effective white matter connection between regions. In summary, for each subject we obtained a whole brain network, each one replicated for each of three different fiber tracking algorithms.

Normal/Shiverer network measures deviation

For these whole brain networks, six different topological properties were evaluated: clustering (C, a measure of the inherent tendency to cluster nodes into strictly connected neighbourhoods), characteristic path length (L, the average number of region-region direct connections that must be traversed to go from one region to another), modularity (Q, the degree to which a network may be subdivided into subnetwork modules with a maximum number of internal links and a minimum number of external links), global efficiency (E_{glob}, a measure of how much parallel information can be potentially exchanged over a network), local efficiency (E_{loc}, the average global efficiency of the local subnetworks) and small-worldness (σ, a measure of how optimally is organized a network) (see Table 1).

In order to evaluate significant (dis)similarities between the control and shiverer group, for each network measure a multivariate permutation test was performed, testing the null hypothesis of equal means between groups (see *Statistical Analysis* on *Materials and Methods*). We found significant differences for C ($P = 0.0015$), L ($P = 0.0495$), Q ($P = 0.0324$), E_{glob} ($P = 0.0045$), E_{loc} ($P = 0.0005$) and σ ($P < 0.0004$). For C, Q, E_{glob}, E_{loc} and σ the mean values of shiverer subjects were lowers than the corresponding mean values of control subjects. This indicates a significant reduction of these structural network attributes in the pathological subjects, which in conjunction with the observed significant increase of corresponding L values, might be interpreted as a considerable decline in the amount of possible nervous information that can be exchanged over the shiverer's brain, and how deficiently and no optimally it can be managed.

Subjects classification

Figure 2 shows locations of controls and shiverer subjects in the 3-dimensional Euclidian spaces corresponding to the *network measure representation spaces* of C, L, Q, E_{glob}, E_{loc} and σmetrics. In each *representation space*, subjects are represented and determined by a unique spatial point, with "length", "width" and "depth" coordinates assigned according to values obtained from three different fiber tracking algorithms (see *Network Measures Spatial representations* on *Materials and Methods*). To assess the competences of these network topological features to discriminate between groups, linear discriminator analysis (LDA) was used [45](see *Subjects Classification* on *Materials and Methods*). Then for each considered network measure we obtained the mean boundary hyperplane that separated the original *representation space* into two *subspaces*, to which belongs respectively the subjects that presented similar spatial positions (topological properties; see Figure 2). In addition, for each network measure and the combination of all of them we obtained the conditional probabilities of belonging to the identified groups (see Table 2).

Note the clear *spatial* subdivisions between control and shiverer subjects obtained for C, E_{glob}, E_{loc} and σ, and the corresponding high values of correct predictions (i.e. 100, 91.66, 100 and 100 percent respectively; Table 2), which supports the hypothesis of a possible discrimination between control and pathological (shiverer) subjects based on their brain structural network descriptors. The *representation space* of the L and Q measures were keep it only for illustrative purposes because, although we previously found a significant difference for these measures, they were not practical to predict between normal and pathological subjects (i.e. providing a low prediction accuracy value of 66.67%, equivalent to predict correctly only 8 of the 12 subjects); as figure 2b and 2c shows the corresponding mean hyperplanes were not able to correctly separate the two groups.

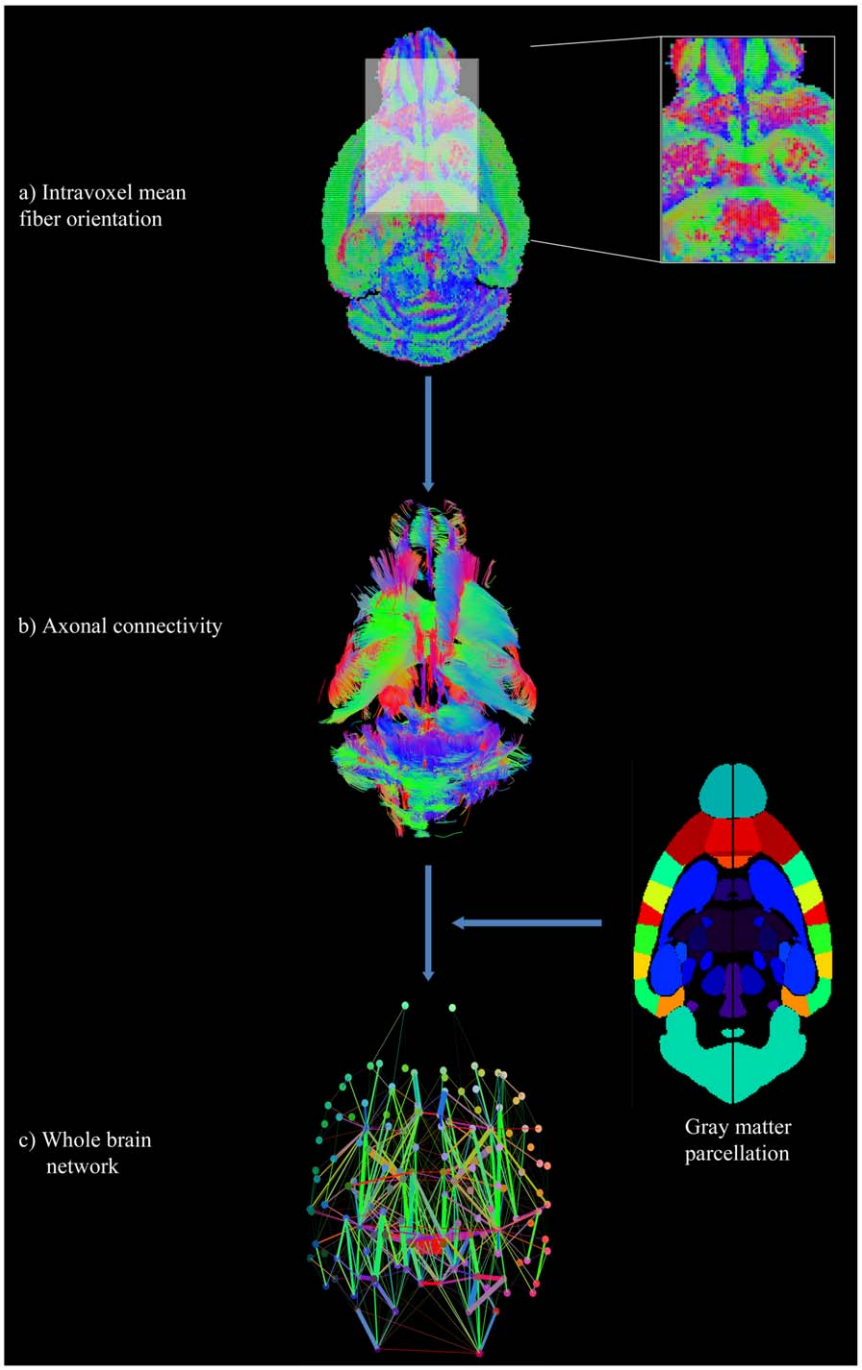

Figure 1. Schematic representation of the connectivity estimation and network construction procedure. Depicted example corresponds to one control subject and FACT tractography algorithm. a) Axial map representing intravoxel mean fiber orientation (dyadic vectors). Inset figure provides detail of the high fiber orientation coherence around the corpus callosum and olfactory areas. b) Obtained whole brain axonal trajectories. c) Whole brain structural network derived as described in *Materials and Methods*; points (nodes) represent anatomic regions, lines (arcs) correspond to connections between them and line widths reflect the corresponding arc weights. In a), b) and c) voxels, fiber trajectories and lines colors were assigned according to the RGB code (i.e. red, green and blue colors indicates rostrocaudal, mediolateral and dorsoventral orientations respectively).
doi:10.1371/journal.pone.0019071.g001

It should be noted also that subject classification based on the combination of the six considered network measures, by means of a forward sequential feature selection in a wrapper fashion (see *Subjects Classification* on *Materials and Methods*), provided 100% prediction accuracy (Table 2). This result it is not surprising when is considered the previously obtained perfect predictions without the combination of all network measures (i.e. aforementioned 100% prediction accuracies for C, E_{loc} and σ individual measures). However, should be noted that in this case (classification based on the combination of the six considered network measures) the contrast between the obtained individual conditioned probability values of control and shiverer subjects is considerably more

Table 1. Clustering (C), characteristic path length (L), modularity (Q), global efficiency (E_{glob}), local efficiency (E_{loc}) and small-worldness (σ) parameters obtained for the brain anatomical networks of control and shiverer mice groups.

Group		Brain network measures (Mean ± SEM)					
		C	L	Q	E_{glob}	E_{loc}	σ
Control	FACT	45.50±1.73	0.06±0.01	0.61±0.00	39.17±0.62	83.49±3.67	5.56±0.23
	TL	46.33±1.28	0.07±0.00	0.65±0.00	37.73±0.37	84.69±2.52	6.31±0.27
	TEND	60.27±2.04	0.06±0.00	0.62±0.00	36.69±0.64	124.22±5.05	5.92±0.22
Shiverer	FACT	32.23±1.92	0.07±0.01	0.59±0.01	29.58±1.52	58.78±4.35	5.47±0.38
	TL	32.71±1.64	0.09±0.01	0.65±0.01	30.01±1.08	62.77±3.85	3.99±0.30
	TEND	47.27±1.41	0.08±0.00	0.60±0.01	29.46±1.14	93.44±2.91	5.07±0.31
P-value		**0.0025**	**0.0455**	**0.0324**	**0.0025**	**0.0015**	**0.0005**

For each measure and fiber tracking algorithm, mean values are reported with their corresponding standard errors (i.e. the uncertainty of how the sample mean represents the underlying population mean). For each measure, the multivariate permutation P-value corresponds to the null hypothesis that means of obtained group values are equal (a P-value near to zero, i.e. $P<0.05$, indicates a significant difference between groups). The small P-values obtained for measures C, Q, E_{glob}, E_{loc} and σ (all $P<0.0324$) indicates a significant decreases on the shiverer subjects of these structural network attributes, which in conjunction with the significant increase of measure L ($P<0.05$) reflects a considerable reduction in the amount of possible nervous information that can be exchanged over the brain and how deficiently and no optimally it can be managed. For obtained gamma (γ) and lambda (λ) parameters, and their influence on the σ index, please see Table S2. Significant P values are depicted in bold type.

doi:10.1371/journal.pone.0019071.t001

accentuated (in the sense of the correct prediction) than when is used only any of the previous measures as a single predictor (Table 2). Thus, the selection of most prominent features [46] allows us to reduce redundant network features information (see Table S6, where is evidenced the characteristic high correlations among almost all the studied network metrics) in order to obtain a final quantitative subject discrimination based on different complementary aspects of the structural brain network.

Discussion

We performed a structural network analysis based on high resolution DW-MRI techniques and graph theory, to search for altered topological properties in the shiverer mouse using matched healthy mice as controls. We found significant differences for specific network measures such as C, L, Q, E_{glob}, E_{loc} and σ, indicating that these metrics (mainly related to the potential amount of nervous information that can be exchanged over the brain, and how efficiently and optimally it could be managed) are significantly altered in the shiverer subjects. In addition, we showed that control and shiverer subjects can be automatically classified by means of *network measures representation spaces* and discriminant analysis (LDA).

Structural network alterations, correspondence with human pathological studies

The significant reduction on small-worldness parameter that we found here for shiverer subjects is in line with similar reductions reported for human patients of Multiple Sclerosis (MS) [2], which tend to have a smaller number of significant regional cortical thickness correlations and a more randomized structural cortical network organization as the white matter lesion load increases. These results are also in line with changes found in graph theoretical studies of other brain disorders such as tumors [3], Alzheimer's disease [4], Schizophrenia [6,7] and Stroke [8], which together reinforce the point of view that network randomization and subsequent loss of optimal organization could be a common final result of the brain's reaction to lesions or neurodegenerative processes [8]. In addition, observed significant decreases for global/local structural efficiencies and modularity in the shiverer subjects suggest a lower brain capacity to establish parallel interactions between distant regions as well as a lower tendency to have communities of different anatomical regions that deal with common neural information. As the network extraction methodology used in this study was based on DW-MRI techniques, we can consider that in general these structural differences are directly reflecting variations in the white matter integrity that in the specific case of the shiverer mutant mouse are provoked by dysmyelinating and demyelinating process.

Subject's classification

The results indicate that is possible to discriminate with high reliability between control and shiverer mice using complex brain structural network properties, providing also a probability of belong to one or the other group as an individual anatomical classifier. Our approach is based on the quantitative differences between network measures (e.g. C, E_{glob}, E_{loc} and σ) that could be interpreted as reflecting the absence of compact myelin in the central nervous system of shiverer mice. This approach should therefore provide useful information on human brain disorders characterized by dysmyelinating and demyelinating process, like MS.

In the specific case of the MS, in which structural affectations are frequently located in the periventricular and juxtacortical white matter regions, the corpus callosum and infratentorial areas [22,23], many of traditional diagnostic approaches, as the McDonald criteria [47], needs an expert's intervention as well as subjective tuning parameters, as the required number of T2 lesions (i.e., nine lesions), which makes the diagnostic more difficult and unspecific. However, recent advantages of non conventional MRI techniques such as magnetization transfer, DW-MRI, proton MRI spectroscopy, and functional MRI, have been contributing to overcome the limitations of conventional MRI and associated diagnostic criteria (for a review see [23]). In this sense, possible advantages of novel network analyses as the here proposed is that theoretically allows a deeper understanding of the alterations provoked to the physiological brain dynamics in terms of the management and integration of the nervous information flow. The introduced *network measures representation spaces* concept constitutes an

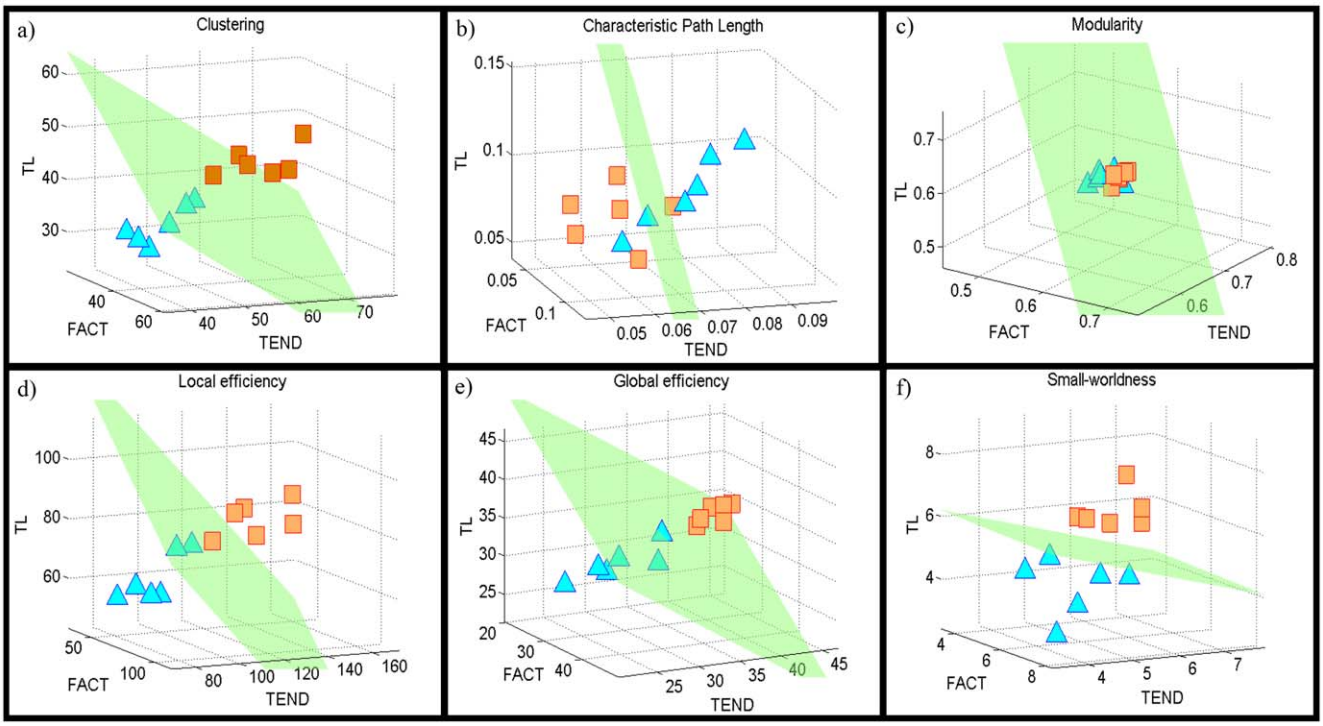

Figure 2. Three-dimensional brain *network measure representation space* for: (a) clustering, (b) characteristic path length, (c) modularity, (d) local efficiency, (e) global efficiency, and (f) small-worldness indices. Control and shiverer subjects are represented by the symbols □and Δ, respectively. For each measure *space*, the green surface constitutes the mean boundary plane between groups obtained by means of a LDA cross-validation approach (see *Subjects Classification* on *Material and Methods* section). Note the correct predictions and clear *spatial subdivisions* between control and shiverer mice for some of the evaluated network measures (panels a, d, e and f), which suggest that might exist specific network *subspaces* corresponding to specific brain disorders.
doi:10.1371/journal.pone.0019071.g002

alternative to combine and summarize network topological properties estimated by different modalities (e.g. different fiber tracking algorithms or even different network extraction modalities, like DW-MRI, electroencelography, magnetoencelography and functional MRI). In addition, and although not performed in this study, it is possible to analyze specific nodal properties as an alternative to evaluate problems in specific brain regions and their influence on the whole brain network. Thus, in general the presented approach has potential clinical applications, which in combination with existing criteria might contribute to the future creation of specific brain dynamical imaging biomarkers.

Methodological issues and future work

Previous methodological studies have provided evidence about how deterministic fiber tracking algorithms can fail on those regions where fibers cross, merge or diverge [48–50]. However, our selection of deterministic fiber tracking algorithms was motivated mainly on the fact that the use of high resolution DW-MRI images (80 μm isotropic voxel size) allows a more detailed characterization of the intravoxel anisotropy as well as a considerable reduction of partial volume effects, decreased significantly compared with the high characteristic levels of DW-MRI images acquired at the typical resolutions for which deterministic methods have been traditionally evaluated, e.g. around $2\times2\times2$ mm^3 (15625 times bigger than the voxel size used here), which even using deterministic tractography algorithms can be translated into a more accurate description of the brain structure. Nevertheless, beyond the statistical nature of the used methods, we emphasize the use of three different tractography algorithms, making the results robust to choice of tracking algorithm, which is potentially a significant source of bias. In addition, the use of *network measures representation spaces* in which results from the different tractography algorithms are represented in the N-dimensional Euclidean space (with an axis corresponding to each tractography algorithm) instead that in a 1-dimensional space (where all tractography algorithms' results are inevitable mixed), allows to apply the discrimination procedure in a way that algorithm interaction effects are reduced, and thus providing a valuable assessment of the relative detail of network information across these methods and a robust set of results with which to assess brain network alterations. Finally, in order to explore quantitatively the performance of the different fiber tracking algorithms with regard the presented discrimination approach, we repeated the subject's classification analysis for each fiber tracking algorithm (see Table S7). As expected, the results confirmed that combination of various fiber tracking algorithms contributed considerably to the stabilization and consistency of the classification results.

A special analysis requires the performed network comparison on a standard brain template. Although individual subjects transformation to the standard template space could introduce propagation of error from normalization procedures, it could be considered that results obtained in a standard space should corresponds mainly to variations on fiber structure and integrity, diminishing possible intersubject fiber tracking variability effects due to technical tracking algorithm limitations, such as the undesired decrease in probability of connection with distance, caused by the progressive dispersion of fiber pathways from voxel

Table 2. Individual conditioned probabilities of being a control subject with regard to clustering (C), characteristic path length (L), modularity (Q), global efficiency (E_{glob}), local efficiency (E_{loc}) or small-worldness (σ) measures obtained for the brain anatomical networks of control and shiverer mice subjects (preceded by the prefixes Wt and Shi, respectively).

Subjects	P(Cs|C)	P(Cs|L)	P(Cs|Q)	P(Cs|E_{glob})	P(Cs|E_{loc})	P(Cs|σ)	P(Cs|$C,L,Q,E_{glob},E_{loc},\sigma$)
Wt 1	0.9999	0.0093	0.8056	0.9999	0.9999	0.9999	0.9999
Wt 2	0.9999	0.6524	0.4438	0.9999	0.9998	0.9560	0.9999
Wt 3	0.9999	0.9724	0.5079	0.9999	0.9999	0.9990	1
Wt 4	0.9999	0.9725	0.9162	0.9999	0.9998	0.9724	0.9999
Wt 5	0.9838	0.7499	0.8080	0.9999	0.8183	0.9722	0.9963
Wt 6	0.9999	0.4841	0.8383	0.9999	0.9999	0.9928	1.0000
Shi 1	0.0179	0.9710	0.7829	0.9889	0.3150	0.0891	0.0083
Shi 2	7.58e-10	0.0163	0.3956	1.97e-10	6.07e-7	2.00e-06	4.44e-16
Shi 3	0.0075	0.1708	0.1862	0.0019	0.1116	0.0327	0.0009
Shi 4	2.30e-10	0.6477	3.2287	2.30e-07	3.31e-06	0.1507	6.66e-16
Shi 5	2.97e-12	0.0339	0.6757	0	7.10e-11	6.93e-05	0
Shi 6	4.46e-07	0.1015	0.6455	5.15e-11	4.19e-06	0.0063	1.87e-12
Predicted (%)	100	66.67	66.67	91.66	100	100	100

For each subject, a P(Cs|I_i) value near to one, e.g. P>0.95, indicates a high probability of belonging to the control group according to the structural network measure I_i; whereas a P(Cs|I_i) value near to zero, e.g. P<0.05, indicates a high probability of belonging to the shiverer group. For comparison, corresponding conditioned probability of being a shiverer subject according to I_i can be obtained similarly as 1-P(Cs|I_i). For each measure, or the combination of all them, the Correct Prediction value indicates the % of subjects that were correctly classified. Note the perfect predictions, i.e. 100 %, obtained from the clustering, local efficiency and small-worldness measures, as well as from the unification of the six considered network measures.

doi:10.1371/journal.pone.0019071.t002

to voxel as a consequence of the intrinsic noise and artifacts in the diffusion data. However, in order to explore for differences in subjects classification accuracy with and without transformation to a standard template, we repeated the structural networks construction and subjects classification analysis in the native space (see Table S3). The results indicated a considerable decrease in the prediction accuracy of each network measure and the unification of all them in comparison with previous results obtained on the standard space (Table 2), supporting the point of view that in the case of DW-MRI techniques, subjects transformation to a standard space might allows the improvement of statistical brain network comparisons by reducing variability on networks estimations resultant from technical limitations.

Another consideration for our study is the selection of the mean diffusivity (MD) measure as an indirect measure of changes in potential fiber pathway efficacy in the mouse brain. Other studies have selected with this purpose the *fractional anisotropy* (FA) measure, the number of connecting fiber paths, the MD measure or/and the tensor's three eigenvalues [5,19,40,43]. Our selection was motivated on the fact that MD is a measure of the local average molecular motion, independent of any tissue directionality, which is expected to reflect cellular size and thus fiber integrity [51–53]. In that sense, significant decreases of MD (or the diffusion tensor's three eigenvalues) has being reported for many regions of pathological brains characterized by myelin-deficit, at the same time that only a small variation (practically no informative) of other diffusion tensor invariant scalars like FA has being found [44,54]. However, in order to explore more the arc weight definition used here in comparison to other alternatives, we repeated the structural networks construction and subjects classification analysis firstly using mean FA as a measure of fiber integrity and latter taking arc weight only as the number of fiber connecting paths between any two regions (see Tables S4 and S5, respectively). As expected, the results indicated lower classification accuracies in both cases when compared it to those obtained with the use of MD, although in fact predictions based on mean FA values can be considered as high, particularly for the combination of the 6 considered network measures (i.e. 91.66% of prediction accuracy), supporting the usefulness of define arc weights not only taking into account the basic white matter structure but also the potential efficacy/integrity of each nervous fiber pathway.

Finally, before a potential clinical application can be consider, further studies need to explore mainly two major points: 1) competence of the classification procedure to reflect different levels of lesion profiles and disease states (the pathological subjects that we analyzed here were theoretically at the same brain disorder state, genetically equivalent, and had a mean age at fixation of 6.9 ± 0.2 weeks. This makes it impossible to analyze other factors like temporal progressions or different white matter lesion affectations). Also, 2) reproducibility in human data, which presents different properties referring to images resolution and contrast due to the lower magnetic field strengths that are usually employed in human protocols, i.e. around 1.5–3 Tesla.

Materials and Methods

Data acquisition

High-resolution (80 μm isotropic) contrast-enhanced diffusion tensor data was acquired from six background control (C3HeB) and six dysmyelinating shiverer (C3Fe.SWV shi/shi) mouse brains. The data consists of nominally unweighted and diffusion weighted images with optimized icosahedral sampling. This dataset is available as part of the Biomedical Informatics Research Network (BIRN) initiative, accession number TBD, and was downloaded from URL http://www.birncommunity.org/data-catalog/mouse-shiverer-dti-high-resolution-contrast-enhanced-data/(for a related publication see [44]). All experiments were performed in accordance with protocols approved by the Institutional Animal

Care and Use Committee of the California Institute of Technology.

Animal protocol. The brains of congenic male homozygous shiverer mutants (C3Fe.SWV Mbp^{shi}/Mbp^{shi}, Jackson Laboratories, mean age at fixation $=6.0\pm0.2$ weeks, $n=6$) and control males with the same background as the shiverers (C3HeB/FeJ, Jackson Laboratories, mean age at fixation 6.9 ± 0.2 weeks, $n=6$) were studied using diffusion tensor imaging. Mice were anesthetized deeply using 2.5% Avertin (0.017 ml/g body weight). The mouse was then fixed by transcardiac perfusion using 30 ml of room temperature heparinized phosphate buffered saline followed by 30 ml of room temperature 4% paraformaldehyde (PFA). After death, the head was removed and rocked in 4% PFA overnight at 4C. The skin, lower jaw, ears and cartilaginous nose tip were removed and the head rocked in 50 ml 0.01% sodium azide in PBS for 7.0 ± 0.1 days (mean $\pm$ sd) at 4C. The head was then transferred to a 5 mM solution of gadoteridol (Prohance, Bracco Diagnostics Inc, Princeton NJ) and 0.01% sodium azide in PBS and rocked for 13.5 ± 1.9 days at 4C prior to MR imaging. All brains were brought to room temperature for 8.5 ± 3.0 hours immediately prior to imaging at 20C. In four control and four shiverer brains, DTI acquisitions were repeated to address B1 homogeneity concerns and the second dataset used in the results analysis. The additional time spent by these brains in 5 mM gadoteridol is included in the quoted time intervals above. The repeated brains also spent an additional 6.8 ± 0.1 hours equilibrating to room temperature prior to imaging.

Image acquisition. All images were acquired using a vertical bore 11.7 Tesla Bruker Avance DRX500 system (Bruker Biospin, Germany) equipped with a Micro2.5 imaging gradient set capable of a peak gradient strength of 1 T/m and a maximum slew rate of 12.5 kT/m/s. The intact head was secured in a Teflon holder and submerged in a perfluoropolyether (Fomblin, Solvay Solexis, Inc, Thorofare, NJ) within a 50 ml vial and imaged using a 35 mm birdcage transmit/receive volume resonator. The ambient bore temperature was maintained at 20C by thermostatically controlled airflow. Optimized second order shimming was achieved across the whole sample using the Bruker implementation of Fastmap 1. Diffusion weighted images were acquired using a conventional pulsed-gradient spin echo (PGSE) sequence (TR/TE $=150$ ms/11.6 ms, $256\times150\times130$ matrix, 19.2 mm $\times15$ mm $\times12$ mm FOV, 80 μm isotropic voxel size, 1 average, $\delta=3$ ms, $\Delta=5$ ms, $Gd=750$ mT/m, nominal b-factor $=1450$ s/mm^2). An optimized six point icosahedral encoding scheme [55] was used for diffusion weighted acquisitions with a single un-weighted reference image for a total imaging time of 6 hours.

Image preprocessing. Individual diffusion tensors maps were estimated [52]. Then, using the Segmentation tools in SPMMOUSE (available at http://www.wbic.cam.ac.uk/~sjs80/spmmouse.html) and SPM5 (available at http://www.fil.ion.ucl.ac.uk/spm/software/spm5/), individual b0 images were non-linearly segmentated into white/gray matter and cerebral spinal fluid probabilistic tissue maps and individual non-linear warping transformation parameters obtained were applied to the corresponding individual diffusion tensors maps [56] in order to transforms them finally into the standard template space of the SPMMOUSE toolbox (a representative atlas of 90 brains scanned at 70 μm isotropic). The previous transformation to the template space was done with the purpose of reduce possible intersubject fiber tracking variability effects on posterior networks estimation and comparison due to technical algorithm limitations, such as the undesired decrease in probability of connection with distance (i.e. the progressive dispersion of fiber pathways with distance that reflects the propagation of uncertainty from voxel to voxel, mainly caused by noise and artifacts in the diffusion data). We comment more about this point in the *Discussion* section.

In addition, we took the image volumes representing the canonical Waxholm Space (WHS) mouse brain [57], which include T1-, T2*-, and T2-Weighted MR volumes, Nissl-stained optical histology, and a label volume describing 37 structures (all volumes are represented at 21.5μ isotropic resolution and are available at http://software.incf.org/software/waxholm-space). From the defined 37 structures we selected 26 gray matter regions. We separated left and right hemispheres, and because in this parcellation scheme the cerebral cortex is originally denoted as only one region, we reparcellated both hemispheric cerebral cortex into 50 small regions of approximately the same volume (1.66 ± 0.23 mm^3). The previous number of new small cortical regions (i.e., 50 for each hemispheric cortex) was defined trying to ensure on these regions a volume size around the mean volume size of the other considered non-cortical gray matter regions, keeping consequently a minimum volume variation across all considered brain gray matter regions. Then, in order to carry out the hemispheric cerebral cortex parcellation into 50 coherent regions (i.e. non-overlapped regions with a coherent and continue structure), we used the spatial *kmeans* clusterization algorithm, which allows to minimizes the sum, over all clusters (small regions), of the within-cluster sums of point-to-cluster-centroid Euclidean distances. In fact, we selected this relative simple clusterization algorithm motivated on the fact that the mouse cerebral cortex presents a clear smoothed convexity (without the presence of pronounced sulcus and gyrus structures like for the brain of other species), which allows to reach a smooth parcellation over each hemispheric cerebral cortex's surface. Finally, the parcellation procedure resulted on a modified WHS parcellation scheme of 75 cortical and subcortical gray matter regions for each hemisphere (for a list of region labels see Table S1). Then, the WHS T2-Weighted MR image was segmentated using SPMMOUSE and SPM5 toolboxes, and resulting non-linear warping transformation parameters obtained were applied to the modified WHS parcellation scheme in order to transforms it into the standard template space of the SPMMOUSE toolbox, similarly as done with the individual background control and shiverer diffusion tensor maps as mentioned above.

Axonal connectivity estimation

For each subject, axonal trajectories between each pair of gray matter regions (defined by the normalized modified WHS parcellation scheme) were estimated using 3 fully automated fiber tractography algorithms: 1) traditional streamline [26], 2) tensor-line [58] and 3) tensor deflection [59]. In the text we refer to these algorithms as: "FACT", "TL" and "TEND", respectively. Tracking parameters used were: 25 μm as step size, 200 mm as maximum trace length, $\pm80^\circ$ as curvature threshold over voxel, and 0.12 as FA threshold. Seed points were selected as all white matter brain voxels with an FA value greater than 0.12 (the so-called brute-force approach). The previous selection of a relative low FA threshold was carried out with the purpose of do not impose in the experiment an initial difference between the two groups with the selection of a higher FA threshold value (e.g. 0.2), which had provoked an early groups difference on the number of seed points, and subsequently on connectivity density and brain network properties. In this sense, we verified a non-significant groups difference ($P=0.9712$) between the number of seed points that satisfied the here imposed condition ($FA>0.12$), while on the contrary a significant difference ($P=0.0068$) was found for the more typically used FA threshold value of 0.2.

Network construction

For each subject, whole brain undirected weighted networks were created for each of the tracking algorithms as follows: 1) a node was defined to represent each considered anatomic region, 2) an undirected arc a_{ij} between any nodes i and j was established with a corresponding arc weight $w(a_{ij})$, defined as the effective number of connecting fiber trajectories relative to the number of voxels over the surface of regions i and j, where each fiber path was quantified according to the arithmetic mean of the inverse of its mean diffusivity values. Mathematically:

$$w(a_{ij}) \equiv w(a_{ji}) = \frac{1}{|N_i^s| + |N_j^s|} \sum_{\forall f \in F_{ij}} \frac{1}{N_f} \sum_{step=1}^{N_f} \frac{1}{MD(step)}, \quad (1)$$

where $|N_i^s|$ and $|N_j^s|$ are the number of elements (superficial nodes) of regions i and j respectively, F_{ij} is the set of fiber trajectories connecting regions i an j, N_f is the number of steps of fiber trajectory $f \in F_{ij}$, and $MD(step)$ the local mean diffusivity of fiber trajectory f in each *step*. Note that region-region connection arc weights are defined not only taking into account the basic white matter structure but also an indirect measure of the potential efficacy of each nervous fiber pathway (for similar arc weight definitions see [60], where the mean of the inverse of the ADC measure was used for a brain maturation analysis, as well as [5], where the FA measure was used to define arc weight in an Alzheimer's Disease study). In the *Discussion* section (*Methodological Issues and Future Work* subsection) we comment more about this point.

Finally, for each created brain structural network its connectivity backbone was estimated [19]: first, a maximum spanning tree, which connects all nodes of the network such that the sum of its weights is maximal, was extracted; then, additional edges were added in order of their weight until the average node degree was 4. All posterior network analysis and visual representations were based on the resultant networks (connectivity backbones).

Graph analysis

Each structural whole brain network obtained was characterized attending to six basic metrics:

Clustering index (C). A measure of the inherent tendency to cluster nodes into strictly connected neighborhoods. In a weighted graph G, the clustering around a node i can be calculated as the geometric average of subgraph node weights [61]:

$$C_i = \frac{1}{k_i(k_i-1)} \sum_{\substack{j,k \in G \\ j,k \neq i}} \left(\tilde{w}_{ij} \cdot \tilde{w}_{jk} \cdot \tilde{w}_{ki}\right)^{\frac{1}{3}}, \quad (2)$$

where k_i is the number of arcs connecting node i and the weights are scaled by the largest weight in the network, $\tilde{w}_{ij} = \frac{w_{ij}}{\max(w_{ij})}$. The clustering coefficient for the whole graph G is defined as the average of clustering around each one of the n nodes:

$$C = \frac{1}{n} \sum_{i \in G} C_i \quad (3)$$

Characteristic path length (L). A measure of the typical separation between any two nodes i and j, and it is defined as the mean of geodesic lengths d_{ij} over all pairs of nodes:

$$L = \frac{1}{n(n-1)} \sum_{\substack{i,j \in G \\ i \neq j}} d_{ij} \quad (4)$$

In the unweighted network context $(w_{ij} = [0,1])$, the geodesic length d_{ij} is defined as the number of arcs along the shortest path connecting nodes i and j. In the case of weighted networks $(w_{ij} \in \Re)$, the path with the minimum number of nodes is not necessarily the optimal d_{ij} and in some cases it is necessary to define a physical length associated to each arc (this should be a function of the characteristics of the hypothetical link among any nodes i and j). In this work, we assumed that the physical length of an arc connecting nodes i and j is inversely proportional to the strength of the analyzed connection [18], i.e. $l_{ij} = \frac{1}{w_{ij}}$. Thus, the shortest path length d_{ij} is finally computed as the smallest sum of the arc lengths throughout all the possible paths from node i to node j. Note that for the particular case of unweighted graphs, $l_{ij} = 1$ for all arcs and the geodesic lengths d_{ij} reduces to the minimum number of arcs traversed to get from i to j.

Modularity (Q). A measure of the degree to which a network may be subdivided into modules or communities, reflecting the inherent tendency to the appearance of densely connected groups of vertices with sparser connections between groups [62,63]. The modularity for a given partition of a network G is defined as [63]:

$$Q = \sum_{i \in N_{\mathrm{mod}}} \left[e_{ii} - a_i^2\right] \quad (5)$$

where N_{mod} is the number of modules, e_{ii} is the fraction of edges in the network that connect vertices within the community i, and a_i represents the fraction of edges that connect vertices of community i with other communities (i.e., $a_i = \sum_{i \in N_{\mathrm{mod}}} e_{ij}$). This quantity measures the fraction of the edges in the network that connect vertices of the same type (i.e., within community edges) minus the expected value of the same quantity in a network with the same community divisions but random connections between the vertices. If the number of within-community edges is no better than random, we will get $Q = 0$. Values approaching $Q = 1$, which is the maximum, indicate networks with strong community structure [63].

In order to identify the modulus of the created structural brain networks that optimize the previous modularity measure (equation 5), we used Newman's spectral optimization method [62] that is implemented as part of the Brain Connectivity Toolbox [64] (available at http://www.brain-connectivity-toolbox.net).

Efficiency parameters (E_{glob}, E_{loc}). In terms of the information flow, the *global efficiency* (E_{glob}) of a network G reflects how efficiently information can be exchanged over G, considering a parallel system in which each node sends information concurrently along the network. It is defined as [65]:

$$E_{glob} = \frac{1}{n(n-1)} \sum_{\substack{i,j \in G \\ i \neq j}} \frac{1}{d_{ij}} \quad (6)$$

The *local efficiency* (E_{loc}) of G is defined as the average efficiency of the local subgraphs [65]:

$$E_{loc} = \frac{1}{n}\sum_{i \in G} E_{glob}(G_i), \quad (7)$$

where G_i is the subgraph of the first neighbors of node *i*. This measure has been used to reveal how much a system is fault tolerant, indicating how efficient the communication is among the first neighbors of *i* when *i* is removed.

In a physiological sense, the global efficiency of a structural brain network reflects the potential parallel exchange of neural information between the involved anatomic regions (a high global efficiency value, i.e. $E_{glob} \approx 1$, may indicate highly parallel information transfer in the brain system, in which each element node could efficiently send information concurrently along the network). The local efficiency of a structural brain network reflects its potential tendency to have communities or clusters of anatomically and physiologically different regions that deal with common neural information (where regions connected to a same region tend also to link to each other). In addition, concurrent higher values of global and local efficiency indicate a system with a high balance between local necessities (fault tolerance) and wide-scope interactions.

Small-world parameter (σ). Small-world networks are defined as those having small mean shortest path length, like random networks ($\lambda \equiv \frac{L^{real}}{L^{rand}} \approx 1$), and high clustering coefficient, much larger than random networks ($\gamma \equiv \frac{C^{real}}{C^{rand}} >> 1$) [66]. Additionally, the small-worldness condition lies in satisfying that $\sigma \equiv \frac{\gamma}{\lambda} > 1$ [67]. A network is said to shifts toward a random network if is small-worldness parameter decreases due to gamma (γ) decreases and/or lambda (λ) increases.

Network measures spatial representations

For each network measure we define here its characteristic *representation space*, in which each subject is spatially represented and determined by a unique point attending to its topological properties. Formally, for a given network measure X, we define the N available values of X obtained for each subject *i* as the coordinates of the point that represents subject *i* in the N-dimensional Euclidean space of measure X. Specifically, because here we used three different fiber tracking algorithms, the three values of any measure X obtained for each subject *i* are assumed as the ''length'', ''width'' and ''depth'' respectively of a point determining uniquely the position of subject *i* on the 3-dimensional space of X. In summary, for each considered brain network measure we obtained a 3-dimensional space in which subjects are represented for unique points whose coordinates corresponds to the obtained values for this measure (see for example Figure 2).

Similarly, the *representation space* of a set of M network measures can be created assuming a point for each subject but, as we have N different values per network measure, now the resulting spatial representation will be on the M*N-dimensional Euclidean space (i.e. an abstract 18-dimensional Euclidean space representing the 6 network measures considered in this study, where to each measure corresponds three coordinates).

Subjects classification

The potential prediction of structural network measures was assessed using linear discriminant analysis (LDA) [45]. This is an extended classification procedure that assumes a multivariate normal distribution of classes around their means and a common covariance matrix, resulting in a linear classification boundary.

In the context of the *network measure spatial representations*, for each network measure the LDA procedure was employed according to a cross-validation approach, in which all but one mouse (a control or a shiverer) were used for training, and the left-out mouse was used for testing. Then the train/test partition was rotated until all subjects have been tested without being included in the training sample. In summary, for each subject the LDA returned the posterior probability of this subject to belong to each of the two training subgroups (integrated by the rest of the control or shiverer subjects respectively; see for example Table 2), as well as the coefficients of the boundary curves between the groups (i.e. the equations of the hyperplane that best separated the groups in the corresponding 3-dimensional *representation space*).

Finally, for subjects classification based on the combination of the considered 6 network measures, the LDA procedure was similar employed according to a cross-validation approach but in this case the number of features (dimensionality = 6) was previously reduced by means of a forward sequential feature selection in a wrapper fashion [46]. In general, the forward sequential feature selection in a wrapper fashion selects a subset of features by sequentially adding a new feature (forward search) until certain stopping conditions are satisfied. More specifically, the feature selection procedure starts prediction using only the network measure that resulted the best single predictor (usually the clustering index or the small-worldness parameter), after this initial prediction, the procedure adds as a new predictor (feature) to the network measure that resulted the second best single predictor, and continues in a similar way (the order of the network measures inclusion can be easily deduced from Table 2, on *Results* section) until the inclusion of a new network measure do not implies an improvement in prediction. According to this procedure, final discrimination results were based on the interaction of the most relevant features, where redundant information is considerable reduced.

Statistical analysis

In order to evaluate differences between two groups of subjects for a same network measure we used a permutation test. This has the following advantages: the test is distribution free, no assumptions of an underlying correlation structure are required, and provides exact p-values for any number of subjects and estimation algorithms. Specifically, for each network the statistics t and *max t* were calculated, where *max t* represent the maximum of statistic t in each fiber tracking algorithm result. The distribution estimated by permutation techniques for *max t* was then used to set significance levels that control the experiment wise error for the simultaneous univariate comparisons [68,69].

Supporting Information

Table S1 Mouse considered regions for each brain hemisphere (modified WHS parcellation scheme).
(DOC)

Table S2 Gamma (γ) and lambda (λ) parameters obtained for the brain anatomical networks of control and shiverer mice groups. For each measure and fiber tracking algorithm, mean values are reported with their corresponding standard errors (i.e. the uncertainty of how the sample mean represents the underlying population mean). For each measure, the multivariate permutation P-value corresponds to the null hypothesis that medians of

obtained group values are equal (a P-value near to zero, i.e. $P < 0.05$, indicates a significant difference between groups). The small P-value obtained for λ indicates a significant increase on the shiverer subjects of this structural network attribute, whereas the γ parameter doesn't show significant differences (although a non significant decrease can be noted). This result, together with the reported significant decrease for the σ parameter, supports the hypothesis of a structural brain network randomization in the shiverer mutant mouse.
(DOC)

Table S3 Individual conditioned probabilities of being a control subject with regard clustering (C), characteristic path length (L), modularity (Q), global efficiency (E_{glob}), local efficiency (E_{loc}) or small-worldness (σ) measures obtained for the brain anatomical networks (estimated in individual native spaces) of control and shiverer mice subjects (preceded by the prefixes Wt and Shi, respectively). For each subject, a $P(Cs|I_i)$ value near to one, e.g. $P > 0.95$, indicates a high probability of belonging to the control group according to the structural network measure I_i; whereas a $P(Cs|I_i)$ value near to zero, e.g. $P < 0.05$, indicates a high probability of belonging to the shiverer group. For comparison, corresponding conditioned probability of being a shiverer subject according to I_i can be obtained similarly as 1-$P(Cs|I_i)$. For each measure, or the combination of all them, the Correct Prediction value indicates the % of subjects that were correctly classified. Note how predictions accuracy, for each considered network measure or the combination of all them, decreases considerably with regard the corresponding results obtained in the standard template space (Table 2 on *Results* section), which supports the point of view that in the case of DW-MRI techniques, subjects transformation to a standard space allows the improvement of statistical brain network comparisons by reducing variability on networks estimations resultant from technical limitations.
(DOC)

Table S4 Individual conditioned probabilities of being a control subject with regard clustering (C), characteristic path length (L), modularity (Q), global efficiency (E_{glob}), local efficiency (E_{loc}) or small-worldness (σ) measures obtained for the brain anatomical networks (using mean FA as an indicator of each fiber path's integrity) of control and shiverer mice subjects (preceded by the prefixes Wt and Shi, respectively). For each subject, a $P(Cs|I_i)$ value near to one, e.g. $P > 0.95$, indicates a high probability of belonging to the control group according to the structural network measure I_i; whereas a $P(Cs|I_i)$ value near to zero, e.g. $P < 0.05$, indicates a high probability of belonging to the shiverer group. For comparison, corresponding conditioned probability of being a shiverer subject according to I_i can be obtained similarly as 1-$P(Cs|I_i)$. For each measure, or the combination of all them, the Correct Prediction value indicates the % of subjects that were correctly classified. Note that although in general prediction accuracies are considerable high, particularly for C, E_{glob}, E_{loc} and the combination of the 6 considered network measures (i.e. 91.66 % of prediction accuracy), the obtained values are lower than those obtained when the mean value of the inverse of MD was used to define arcs weights (Table 2 on *Results* section).
(DOC)

Table S5 Individual conditioned probabilities of being a control subject with regard clustering (C), characteristic path length (L), modularity (Q), global efficiency (E_{glob}), local efficiency (E_{loc}) or small-worldness (σ) measures obtained for the brain anatomical networks (with arc weights between nodes [regions] defined only as the number of connecting fiber paths, i.e., without any indicator of fiber integrity) of control and shiverer mice subjects (preceded by the prefixes Wt and Shi, respectively). For each subject, a $P(Cs|I_i)$ value near to one, e.g. $P > 0.95$, indicates a high probability of belonging to the control group according to the structural network measure I_i; whereas a $P(Cs|I_i)$ value near to zero, e.g. $P < 0.05$, indicates a high probability of belonging to the shiverer group. For comparison, corresponding conditioned probability of being a shiverer subject according to I_i can be obtained similarly as 1-$P(Cs|I_i)$. For each measure, or the combination of all them, the Correct Prediction value indicates the % of subjects that were correctly classified. Note how predictions accuracy, for each considered network measure or the combination of all them, decreases considerably with regard the corresponding results obtained when the mean value of the inverse of MD or the mean FA value were used as measures of fiber integrity (see Table 2 and Table S5, respectively).
(DOC)

Table S6 Pearson correlations values between the six topological measures obtained for brain anatomical networks of mice subjects: clustering (C), characteristic path length (L), modularity (Q), global efficiency (E_{glob}), local efficiency (E_{loc}) and small-worldness (σ). For the sake of simplicity, here we present correlations only trough measures (i.e. without taking into account differences between groups or fiber tracking algorithms). Asterisks indicate significant correlations (i.e. whit a corresponding $P<0.05$). Note that almost all pairs of measures are significantly correlated (except pairs *C-L, L-Q, L-*E_{loc}*, Q-* E_{glob} and *Q-*σ), illustrating the need of reduce redundant network features information when two o more measures are combined with the purpose of obtain a final quantitative subject discrimination.
(DOC)

Table S7 Prediction accuracies (%) obtained for control and shiverer mice subjects according to results of each fiber tracking algorithm and the combination of all them, with regard clustering (C), characteristic path length (L), modularity (Q), global efficiency (E_{glob}), local efficiency (E_{loc}) or/and small-worldness (σ) brain anatomical network measures. For each network measure and fiber tracking, or the combination of all them, the Prediction accuracy indicates the % of subjects that were correctly classified. Note that the combination of various fiber tracking algorithms contributes to the stabilization and consistency of the classification results, in other words, a high prediction for a given network measure usually coincides with a high prediction for the other measures, which do not happens always for the results corresponding to only a given fiber tracking algorithm. For example, in the case of the TL algorithm, although a high prediction accuracy (around 91.66~100%) was obtained for C, E_{glob}, σ and the combination of the six network measures, the prediction accuracy obtained for E_{loc} (i.e. 83.33%) was considerable lower than the obtained for the others algorithms and the combination of the three algorithms (around 91.66~100%); similarly happened with predictions obtained from FACT and TEND algorithms for σ and the combination of the six network measures. These results support the point of view that the use of different tractography algorithms makes the results robust to choice of tracking algorithm, which is potentially a significant source of bias.
(DOC)

Acknowledgments

We are grateful also to Doug Davidson for his comments on the earlier version of the manuscript.

Author Contributions

Conceived and designed the experiments: YIM APF. Performed the experiments: YIM APF. Analyzed the data: YIM APF MOO ALC. Contributed reagents/materials/analysis tools: YIM APF MOO ALC PVH LGP LMG ECR. Wrote the paper: YIM APF.

References

1. Bullmore E, Sporns O (2009) Complex brain networks: graph theoretical analysis of structural and functional systems. Nature Reviews Neuroscience 10: 186–198.
2. He Y, Dagher A, Chen Z, Charil A, Zijdenbos A, et al. (2009) Impaired small-world efficiency in structural cortical networks in multiple sclerosis associated with white matter lesion load. Brain 132: 3366–3379.
3. Bartolomei F, Bosma I, Klein M, Baayen JC, Reijneveld JC, et al. (2006) Disturbed functional connectivity in brain tumour patients: Evaluation by graph analysis of synchronization matrices. Clinical Neurophysiology 117: 2039–2049.
4. Stam CJ, Jones BF, Nolte G, Breakspear M, Scheltens P (2007) Small-world networks and functional connectivity in Alzheimer's disease. Cerebral Cortex 17: 92–99.
5. Chun-Yi Lo, Pei-Nung Wang, Kun-Hsien Chou, Jinhui Wang, Yong He, et al. (2010) Diffusion tensor tractography reveals abnormal topological organizational in structural cortical networks in Alzheimer's disease. 30(50): 16876–16885.
6. Micheloyannis S, Pachou E, Stam CJ, Breakspear M, Bitsios P, et al. (2006) Small-world networks and disturbed functional connectivity in schizophrenia. Schizophrenia Research 87: 60–66.
7. Rubinov M, Knock SA, Stam CJ, Micheloyannis S, Harris AWF, et al. (2009) Small-World Properties of Nonlinear Brain Activity in Schizophrenia. Human Brain Mapping 30: 403–416.
8. Wang L, Yu CS, Chen H, Qin W, He Y, et al. (2010) Dynamic functional reorganization of the motor execution network after stroke. Brain 133: 1224–1238.
9. Crofts JJ, Higham DJ (2009) A weighted communicability measure applied to complex brain networks. The Journal of the Royal Society 6: 411–414.
10. L.da F.Costa, Sporns O (2005) Hierarchical features of large-scale cortical connectivity. European Physical Journal B 48: 567–573.
11. Sporns O (2006) Small-world connectivity, motif composition, and complexity of fractal neuronal connections. Biosystems 85: 55–64.
12. Sporns O, Zwi JD (2004) The small world of the cerebral cortex. Neuroinformatics 2: 145–162.
13. Chen ZJ, He Y, Rosa P, Germann J, Evans AC (2008) Revealing modular architecture of human brain structural networks by using cortical thickness from MRI. Cerebral Cortex 18: 2374–2381.
14. He Y, Chen ZJ, Evans AC (2007) Small-world anatomical networks in the human brain revealed by cortical thickness from MRI. Cerebral Cortex 17: 2407–2419.
15. Gong GL, He Y, Concha L, Lebel C, Gross DW, et al. (2009) Mapping Anatomical Connectivity Patterns of Human Cerebral Cortex Using In Vivo Diffusion Tensor Imaging Tractography. Cerebral Cortex 19: 524–536.
16. Wang JH, Wang L, Zang YF, Yang H, Tang HH, et al. (2009) Parcellation-Dependent Small-World Brain Functional Networks: A Resting-State fMRI Study. Human Brain Mapping 30: 1511–1523.
17. Hagmann P, Kurant M, Gigandet X, Thiran P, Wedeen VJ, et al. (2006) Imaging the brain neuronal network with diffusion MRI: a way to understand its global architecture. Proc. ISMRM. pp 436.
18. Iturria-Medina Y, Sotero RC, Canales-Rodriguez EJ, Alemán-Gómez Y, Melie-Garcia L (2008) Studying the human brain anatomical network via diffusion-weighted MRI and Graph Theory. Neuroimage 40: 1064–1076.
19. Hagmann P, Cammoun L, Gigandet X, Meuli R, Honey CJ, et al. (2008) Mapping the structural core of human cerebral cortex. Plos Biology 6: 1479–1493.
20. Bassettt DS, Meyer-Lindenberg A, Achard S, Duke T, Bullmore E (2006) Adaptive reconfiguration of fractal small-world human brain functional networks. Proceedings of the National Academy of Sciences of the United States of America 103: 19518–19523.
21. Sanabria-Diaz G, Melie-Garcia L, Iturria-Medina Y, Alemán-Gómez Y, Hernandez-Gonzalez G, et al. (2010) Surface area and cortical thickness descriptors reveal different attributes of the structural human brain networks. Neuroimage 50: 1497–1510.
22. Ormerod IEC, Miller DH, McDonald WI, Duboulay EPGH, Rudge P, et al. (1987) The Role of Nmr Imaging in the Assessment of Multiple-Sclerosis and Isolated Neurological Lesions - A Quantitative Study. Brain 110: 1579–1616.
23. Filippi M, Agosta F (2010) Imaging Biomarkers in Multiple Sclerosis. Journal of Magnetic Resonance Imaging 31: 770–788.
24. Jones CT (2003) Childhood autoimmune neurologic diseases of the central nervous system. Neurologic Clinics 21: 745–764.
25. Almendinger S, Lovato L, Fukaura H, Hafler D, O'Connor K (2010) Characterization of the Myelin Specific Autoantibodies in Acute Disseminated Encephalomyelitis. Clinical Immunology 135: S81.
26. Mori S, Crain BJ, Chacko VP, van Zijl PC (1999) Three-dimensional tracking of axonal projections in the brain by magnetic resonance imaging. Ann Neurol 45: 265–269.
27. Conturo TE, Lori NF, Cull TS, Akbudak E, Snyder AZ, et al. (1999) Tracking neuronal fiber pathways in the living human brain. Proc Natl Acad Sci U S A 96: 10422–10427.
28. Tuch DS (2002) MRI of complex tissue structure. PhD Thesis.
29. Koch MA, Norris DG, Hund-Georgiadis M (2002) An investigation of functional and anatomical connectivity using magnetic resonance imaging. Neuroimage 16: 241–250.
30. Parker GJ, Wheeler-Kingshott CA, Barker GJ (2002) Estimating distributed anatomical connectivity using fast marching methods and diffusion tensor imaging. IEEE Trans Med Imaging 21: 505–512.
31. Behrens TE, Johansen-Berg H, Woolrich MW, Smith SM, Wheeler-Kingshott CA, et al. (2003) Non-invasive mapping of connections between human thalamus and cortex using diffusion imaging. Nat Neurosci 6: 750–757.
32. Commowick O, Fillard P, Clatz O, Warfield SK (2008) Detection of DTI white matter abnormalities in multiple sclerosis patients. Med Image Comput Comput Assist Interv 11(Pt 1): 975–982.
33. Pomarol-Clotet E, Canales-Rodriguez EJ, Salvador R, Sarro S, Gomar JJ, et al. (2010) Medial prefrontal cortex pathology in schizophrenia as revealed by convergent findings from multimodal imaging. Molecular Psychiatry 15: 823–830.
34. Assaf Y, Chapman J, Ben-Bashat D, Hendler T, Segev Y, et al. (2005) White matter changes in multiple sclerosis: correlation of q-space diffusion MRI and H-1 MRS. Magnetic Resonance Imaging 23: 703–710.
35. Concha L, Beaulieu C, Collins DL, Gross DW (2009) White-matter diffusion abnormalities in temporal-lobe epilepsy with and without mesial temporal sclerosis. Journal of Neurology Neurosurgery and Psychiatry 80: 312–319.
36. Gross DW, Concha L, Beaulieu C (2005) Diffusion tensor white matter abnormalities in temporal lobe epilepsy with mesial temporal sclerosis. Epilepsia 46: 332.
37. Chua TC, Wen W, Slavin MJ, Sachdev PS (2008) Diffusion tensor imaging in mild cognitive impairment and Alzheimer's disease: a review. Current Opinion in Neurology 21: 83–92.
38. Stebbins GT, Murphy CM (2009) Diffusion tensor imaging in Alzheimer's disease and mild cognitive impairment. Behavioural Neurology 21: 39–49.
39. Hagmann P, Cammoun L, Gigandet X, Meuli R, Honey CJ, et al. (2008) Mapping the structural core of human cerebral cortex. Plos Biology 6: 1479–1493.
40. Li YH, Liu Y, Li J, Qin W, Li KC, et al. (2009) Brain Anatomical Network and Intelligence. Plos Computational Biology 5.
41. Iturria-Medina Y, Pérez Fernández A, Morris DM, Canales-Rodríguez EJ, Haroon HA, et al. (2010) Brain Hemispheric Structural Efficiency and Interconnectivity Rightward Asymmetry in Human and Non-Human Primates. Cerebral Cortex 21: 56–67.
42. Robinson EC, Hammers A, Ericsson A, Edwards AD, Rueckert D (2010) Identifying population differences in whole-brain structural networks: a machine learning approach. Neuroimage 50: 910–919.
43. Wee CY, Yap PT, Li W, Denny K, Browndyke JN, et al. (2011) Enriched white matter connectivity networks for accurate identification of MCI patients. Neuroimage 54: 1812–1822.
44. Tyszka JM, Readhead C, Bearer EL, Pautler RG, Jacobs RE (2006) Statistical diffusion tensor histology reveals regional dysmyelination effects in the shiverer mouse mutant. Neuroimage 29: 1058–1065.
45. Bishop CM (2006) Pattern Recognition and Machine Learning. Springer.
46. Kohavi RJG (1997) Wrappers for feature subset selection. Artificial Intelligence 97: 272–324.
47. McDonald WI, Compston A, Edan G, Goodkin D, Hartung HP, et al. (2001) Recommended diagnostic criteria for multiple sclerosis: Guidelines from the International Panel on the Diagnosis of Multiple Sclerosis. Annals of Neurology 50: 121–127.
48. Basser PJ, Pajevic S (2000) Statistical artifacts in diffusion tensor MRI (DT-MRI) caused by background noise. Magn Reson Med 44: 41–50.
49. Lori NF, Akbudak E, Shimony JS, Cull TS, Snyder AZ, et al. (2002) Diffusion tensor fiber tracking of human brain connectivity: aquisition methods, reliability analysis and biological results. NMR Biomed 15: 494–515.
50. Savadjiev P, Campbell JSW, Descoteaux M, Deriche R, Pike GB, et al. (2008) Labeling of ambiguous subvoxel fibre bundle configurations in high angular resolution diffusion MRI. Neuroimage 41: 58–68.
51. Cercignani M, Inlgese M, Pagani E, Comi G, Filippi M (2001) Mean Diffusivity and Fractional Anisotropy Histograms of Patients with Multiple Sclerosis. American Journal of Neuroradiology 22: 952–958.
52. Basser PJ, Mattiello J, LeBihan D (1994) Estimation of the effective self-diffusion tensor from the NMR spin echo. J Magn Reson B 103: 247–254.
53. Pierpaoli C, Jezzard P, Basser PJ, Barnett A, Di CG (1996) Diffusion tensor MR imaging of the human brain. Radiology 201: 637–648.

54. Bar-Shir A, Duncan ID, Cohen Y (2009) QSI and DTI of excised brains of the myelin-deficient rat. Neuroimage 48(1): 109–116.
55. Hasan KM, Parker DL, Alexander AL (2001) Comparison of gradient encoding schemes for diffusion-tensor MRI. Journal of Magnetic Resonance Imaging 13: 769–780.
56. Alexander DC, Pierpaoli C, Basser PJ, Gee JC (2001) Spatial transformations of diffusion tensor magnetic resonance images. IEEE Trans Med Imaging 20: 1131–1139.
57. Johnson G, Badea A, Brandenburg J, Cofer G, Fubara B, et al. (2010) Waxholm space: an image-based reference for coordinating mouse brain research. Neuroimage, in press.
58. Weinstein D, Kindlmann G, Lundberg E (1999) Tensorlines: advection-diffusion based propagation through diffusion tensor fields. Proceedings In Visualization. pp 249–253.
59. Lazar M, Weinstein DM, Tsuruda JS, Hasan KM, Arfanakis K, et al. (2003) White matter tractography using diffusion tensor deflection. Hum Brain Mapp 18: 306–321.
60. Hagmann P, Sporns O, Madan N, Cammoun L, Pienaar R, et al. (2010) White matter maturation reshapes structural connectivity in the late developing human brain. PNAS 107(44): 19067–72-1.
61. Onnela JP, Saramaki J, Kertesz J, Kaski K (2005) Intensity and coherence of motifs in weighted complex networks. Phys Rev E Stat Nonlin Soft Matter Phys 71: 065103.
62. Newman MEJ (2006) Finding community structure in networks using the eigenvectors of matrices. Physical Review E 74: 036104.
63. Newman MEJ, Girvan M (2004) Finding and evaluating community structure in networks. Physical Review E 69: 026113.
64. Rubinov M, Sporns O (2010) Complex network measures of brain connectivity: Uses and interpretations. Neuroimage 52: 1059–1069.
65. Latora V, Marchiori M (2001) Efficient behavior of small-world networks. Phys Rev Lett 87: 198701.
66. Watts DJ, Strogatz SH (1998) Collective dynamics of small-world networks. Nature. pp 440–442.
67. Humphries MD, Gurney K (2008) Network 'Small-World-Ness': A Quantitative Method for Determining Canonical Network Equivalence. Plos One 3.
68. Galan L, Biscay R, Rodriguez JL, Perez Abalo MC, Rodriguez R (1997) Testing topographic differences between event related brain potentials by using non-parametric combinations of permutation tests. Electroencephalography and Clinical Neurophysiology 102: 240–247.
69. Blair RC, Karniski W (1993) An Alternative Method for Significance Testing of Wave-Form Difference Potentials. Psychophysiology 30: 518–524.

Supplementary material

Supplementary Table 1. Mouse considered regions for each brain hemisphere (modified WHS parcellation scheme).

No.	Label
1	Thalamus
2	Superior Colliculus
3	Inferior Colliculus
4	Lateral lemniscus
5	Periaqueductal gray
6	Septal nuclei complex lateral
7	Ventral nuclei of the thalamus
8	Pontine gray
9	Substantia nigra
10	Interpeduncular nucleus
11	Globus pallidus
12	Deep mesencephalic nuclei
13	Lateral dorsal nucleus of thalamus
14	Medial Geniculate
15	Anterior pretectal nucleus
16	Striatum
17	Hippocampus
18	Lateral Geniculate

19	Pineal Gland
20	Amygdala
21	Hypothalamus
22	Nucleus accumbens
23	Olfactory areas
24	Cochlear nuclei
25	Cerebellum
26-75	Small cortical regions of approximately the same volume (1.66±0.23 mm^3)

Supplementary Table 2. Gamma (γ) and lambda (λ) parameters obtained for the brain anatomical networks of control and shiverer mice groups. For each measure and fiber tracking algorithm, mean values are reported with their corresponding standard errors (i.e. the uncertainty of how the sample mean represents the underlying population mean). For each measure, the multivariate permutation P-value corresponds to the null hypothesis that medians of obtained group values are equal (a P-value near to zero, i.e. $P < 0.05$, indicates a significant difference between groups). The small P-value obtained for λ indicates a significant increase on the shiverer subjects of this structural network attribute, whereas the γ parameter doesn't show significant differences (although a non significant decrease can be noted). This result, together with the reported significant decrease for the σ parameter, supports the hypothesis of a structural brain network randomization in the shiverer mutant mouse.

Group		**Brain network measures (Mean ± SEM)**	
		γ	λ
Control	FACT	7.6285±0.1863	1.3985±0.0382
	TL	8.1151±0.2790	1.3112±0.0347
	TEND	9.2655±0.1940	1.5791±0.0462
Shiverer	FACT	7.5311±0.1813	1.4210±0.0923

	TL	7.5458±0.3092	1.9842±0.2001
	TEND	8.9363±0.2368	1.8108±0.1318
P-value		0.3621	**0.0084**

Supplementary Table 3. Individual conditioned probabilities of being a control subject with regard clustering (*C*), characteristic path length (*L*), modularity (*Q*), global efficiency (E_{glob}), local efficiency (E_{loc}) or small-worldness (σ) measures obtained for the brain anatomical networks (estimated in individual native spaces) of control and shiverer mice subjects (preceded by the prefixes Wt and Shi, respectively). For each subject, a $P(Cs|I_i)$ value near to one, e.g. $P > 0.95$, indicates a high probability of belonging to the control group according to the structural network measure I_i; whereas a $P(Cs|I_i)$ value near to zero, e.g. $P < 0.05$, indicates a high probability of belonging to the shiverer group. For comparison, corresponding conditioned probability of being a shiverer subject according to I_i can be obtained similarly as $1\text{-}P(Cs|I_i)$. For each measure, or the combination of all them, the Correct Prediction value indicates the % of subjects that were correctly classified. Note how predictions accuracy, for each considered network measure or the combination of all them, decreases considerably with regard the corresponding results obtained in the standard template space (Table 2 on *Results* section), which supports the point of view that in the case of DW-MRI techniques, subjects transformation to a standard space allows the improvement of statistical brain network comparisons by reducing variability on networks estimations resultant from technical limitations.

Subjects	$P(Cs\|C)$	$P(Cs\|L)$	$P(Cs\|Q)$	$P(Cs\|E_{glob})$	$P(Cs\|E_{loc})$	$P(Cs\|\sigma)$	$P(Cs\|C,L,A,E_{glob},E_{loc},\sigma)$
Wt 1	0.9999	0.4526	0.2851	0.9998	0.9961	0.3433	0.9999
Wt 2	0.9635	0.6170	0.0370	0.9805	0.0285	0.0808	0.4369
Wt 3	0.9991	0.3430	0.5124	0.7836	0.9999	0.4146	0.9999
Wt 4	0.9819	0.6063	0.0611	0.0001	0.9951	0.6604	0.9999
Wt 5	0.9995	0.6189	0.7637	0.9988	0.9000	0.6040	0.9999
Wt 6	0.9994	0.7850	0.6607	0.9996	0.9578	0.5502	0.9999
Shi 1	0.9896	0.9985	0.3554	0.9999	0.4954	0.8943	0.9894
Shi 2	0.0010	0.2471	0.4636	0.0013	0.4969	0.3560	0.0010
Shi 3	1.53e-05	0.1950	0.5402	0.0069	0.0050	0.7937	7.75e-08

Shi 4	0.0054	0.4962	0.7487	0.0187	0.0741	0.3480	0.0004
Shi 5	1.90e-09	0.9995	0.3931	0.0002	0.0007	0.6360	1.46e-12
Shi 6	0.0002	0.2670	0.3389	0.0004	0.0033	0.3980	6.77e-07
Predicted (%)	91.67	66.67	58.33	83.33	91.67	50	83.33

Supplementary Table 4. Individual conditioned probabilities of being a control subject with regard clustering (*C*), characteristic path length (*L*), modularity (*Q*), global efficiency (E_{glob}), local efficiency (E_{loc}) or small-worldness (σ) measures obtained for the brain anatomical networks (using mean FA as an indicator of each fiber path´s integrity) of control and shiverer mice subjects (preceded by the prefixes Wt and Shi, respectively). For each subject, a $P(Cs|I_i)$ value near to one, e.g. P > 0.95, indicates a high probability of belonging to the control group according to the structural network measure I_i; whereas a $P(Cs|I_i)$ value near to zero, e.g. P < 0.05, indicates a high probability of belonging to the shiverer group. For comparison, corresponding conditioned probability of being a shiverer subject according to I_i can be obtained similarly as $1-P(Cs|I_i)$. For each measure, or the combination of all them, the Correct Prediction value indicates the % of subjects that were correctly classified. Note that although in general prediction accuracies are considerable high, particularly for *C*, E_{glob}, E_{loc} and the combination of the 6 considered network measures (i.e. 91.66 % of prediction accuracy), the obtained values are lower than those obtained when the mean value of the inverse of MD was used to define arcs weights (Table 2 on *Results* section).

Subjects	P(Cs|*C*)	P(Cs|*L*)	P(Cs|*Q*)	P(Cs|E_{glob})	P(Cs|E_{loc})	P(Cs|σ)	P(Cs|*C,L,A,* E_{glob},E_{loc}, σ)
Wt 1	0.9999	0.0018	0.5500	0.9999	0.9999	0.9999	0.9999
Wt 2	0.3276	0.4898	0.7333	0.4022	0.6888	0.7456	0.5190
Wt 3	0.9997	0.5946	0.7166	0.9753	0.9981	0.3953	0.9999
Wt 4	0.9973	0.6162	0.5500	0.9966	0.9976	0.3820	0.9999
Wt 5	0.9882	0.5048	0.6333	0.9991	0.9874	0.8162	0.9998
Wt 6	0.9790	0.2971	0.6333	0.9992	0.8694	0.8422	0.9967
Shi 1	0.0265	0.8140	0.4500	0.0189	0.0382	0.5327	0.0010
Shi 2	0.0018	0.6770	0.3666	8.27e-05	0.0003	0.0363	7.51-07

Shi 3	0.4383	0.3915	0.4500	0.2727	0.9593	0.0669	0.9485
Shi 4	0.0006	0.5508	0.7333	0.0051	0.0062	0.5059	4.18e-06
Shi 5	5.28e-06	0.5510	0.8166	0.0001	8.20e-08	0.1657	4.34e-13
Shi 6	0.0017	0.4485	0.7166	0.001	0.0064	0.2478	1.15e-05
Predicted (%)	91.66	41.66	41.66	91.66	91.66	66.66	91.66

Supplementary Table 5. Individual conditioned probabilities of being a control subject with regard clustering (*C*), characteristic path length (*L*), modularity (*Q*), global efficiency (E_{glob}), local efficiency (E_{loc}) or small-worldness (σ) measures obtained for the brain anatomical networks (with arc weitghs between nodes [regions] defined only as the number of connecting fiber paths, i.e. without any indicator of fiber integrity) of control and shiverer mice subjects (preceded by the prefixes Wt and Shi, respectively). For each subject, a $P(Cs|I_i)$ value near to one, e.g. P > 0.95, indicates a high probability of belonging to the control group according to the structural network measure I_i; whereas a $P(Cs|I_i)$ value near to zero, e.g. P < 0.05, indicates a high probability of belonging to the shiverer group. For comparison, corresponding conditioned probability of being a shiverer subject according to I_i can be obtained similarly as $1\text{-}P(Cs|I_i)$. For each measure, or the combination of all them, the Correct Prediction value indicates the % of subjects that were correctly classified. Note how predictions accuracy, for each considered network measure or the combination of all them, decreases considerably with regard the corresponding results obtained when the mean value of the inverse of MD or the mean FA value were used as measures of fiber integrity (see Table 2 and Supplementary Table 5, respectively).

Subjects	$P(Cs\|C)$	$P(Cs\|L)$	P(Cs|Q)	$P(Cs\|E_{glob})$	$P(Cs\|E_{loc})$	$P(Cs\|\sigma)$	$P(Cs\|C,L,A,E_{glob},E_{loc},\sigma)$
Wt 1	0.9980	0.0061	0.7333	0.9846	0.8853	0.5924	0.9997
Wt 2	0.0990	0.1493	0.7333	0.4629	0.4961	0.0829	0.0977
Wt 3	0.9982	0.6180	0.6333	0.7243	0.9759	0.0233	0.9999
Wt 4	0.9999	0.6801	0.7333	0.9492	0.9830	0.6131	0.9999
Wt 5	0.2956	0.6240	0.6333	0.7690	0.2538	0.3051	0.1249
Wt 6	0.6402	0.4973	0.8333	0.9955	0.9568	0.6537	0.9752
Shi 1	0.1453	0.8307	0.6333	0.2550	0.4085	0.5469	0.1051

Shi 2	0.0015	0.4867	0.3666	0.0015	0.0095	0.2649	1.45e-05
Shi 3	0.5698	0.4241	0.4500	0.9720	0.8674	0.5087	0.8966
Shi 4	0.0116	0.8272	0.2833	0.7496	0.3250	0.9508	0.0056
Shi 5	0.0020	0.3666	0.8166	0.0003	0.0001	0.4297	2.90e-07
Shi 6	0.1719	0.4514	0.6333	0.3222	0.2188	0.5503	0.0549
Predicted (%)	75	58.33	50	75	75	41.66	75

Supplementary Table 6. Pearson correlations values between the six topological measures obtained for brain anatomical networks of mice subjects: clustering (*C*), characteristic path length (*L*), modularity (*Q*), global efficiency (E_{glob}), local efficiency (E_{loc}) and small-worldness (σ). For the sake of simplicity, here we present correlations only trough measures (i.e. without taking into account differences between groups or fiber tracking algorithms). Asterisks indicate significant correlations (i.e. whit a corresponding $P < 0.05$). Note that almost all pairs of measures are significantly correlated (except pairs *C-L, L-Q, L-* E_{loc}, *Q-* E_{glob} and *Q-* σ), illustrating the need of reduce redundant network features information when two o more measures are combined with the purpose of obtain a final quantitative subject discrimination.

Measures	*C*	*L*	*Q*	E_{glob}	E_{loc}	σ
C	-	-0.2932	0.6582*	0.6238*	0.9822*	0.4934*
L		-	0.0744	-0.4674*	-0.2761	-0.3754*
Q			-	0.0630	0.6808*	0.0786
E_{glob}				-	0.5400*	0.5420*
E_{loc}					-	0.4243*
σ						-

Supplementary Table 7. Prediction accuracies (%) obtained for control and shiverer mice subjects according to results of each fiber tracking algorithm and the combination of all them, with regard clustering (*C*), characteristic path length (*L*), modularity (*Q*), global efficiency (E_{glob}), local efficiency (E_{loc}) or/and small-worldness (σ) brain anatomical network measures. For each network measure and fiber tracking, or the combination of all them, the Prediction accuracy indicates the % of subjects that were correctly classified.

Note that the combination of various fiber tracking algorithms contributes to the stabilization and consistency of the classification results, in other words, a high prediction for a given network measure usually coincides with a high prediction for the other measures, which do not happens always for the results corresponding to only a given fiber tracking algorithm. For example, in the case of the TL algorithm, although a high prediction accuracy (around 91.66~100 %) was obtained for C, E_{glob}, σ and the combination of the six network measures, the prediction accuracy obtained for E_{loc} (i.e. 83.33 %) was considerable lower than the obtained for the others algorithms and the combination of the three algorithms (around 91.66~100 %); similarly happened with predictions obtained from FACT and TEND algorithms for σ and the combination of the six network measures. These results support the point of view that the use of different tractography algorithms makes the results robust to choice of tracking algorithm, which is potentially a significant source of bias.

Prediction (%)	C	L	Q	E_{glob}	E_{loc}	σ	$C,L,A,E_{glob},E_{loc},\sigma$
FACT	91.66	58.33	83.33	91.66	91.66	33.33	91.66
TL	100	66.67	58.33	91.66	83.33	100	100
TEND	91.66	83.33	8.333	91.66	91.66	75	91.66
FACT,TL, TEND	100	66.67	66.67	91.66	100	100	100

4. DISCUSIÓN GENERAL

En la presente Tesis se ha propuesto una metodología que permite caracterizar las conexiones anatómicas cerebrales, sobre el marco de las técnicas basadas en neuroimágenes de la difusión y la teoría de grafos. Al diseñar la metodología se tuvo en cuenta: i) que fuera capaz de evaluar la conectividad anatómica entre diferentes regiones cerebrales a partir de la reconstrucción inicial de las trayectorias de fibras nerviosas, ii) que permitiera caracterizar cuantitativamente la topología de la red establecida por las conexiones anatómicas (aportando medidas biológica/físicamente interpretables, como eficiencia y optimización estructural para lidiar con el flujo de información neural), iii) y que contribuyera a la identificación automática de sujetos patológicos según las modificaciones que presenten sus patrones de conectividad cerebral al compararseles con sujetos sanos. Todos los métodos desarrollados se aplicaron a datos simulados y datos reales (humanos y no-humanos), con el propósito de validarles y de profundizar en la descripción de los patrones de conectividad anatómica cerebral presentes en sujetos sanos y patológicos.

Tractografía y cuantificación de la conectividad anatómica cerebral

Las técnicas basadas en neuroimágenes de la difusión han permitido reconstruir la compleja arquitectura del cableado cerebral por primera vez *in vivo*. Los axones viajan de unos grupos neurales a otros llevando información neural básica, y al desempeñar esta función elemental definen en el espacio patrones de conectividad que han sido objeto de examen durante siglos y a los cuales por fin nos acercamos gracias a los métodos recientes de tractografía (Conturo y col., 1999; Hagmann y col., 2003; Hagmann y col., 2004; Iturria-Medina y col., 2005a; Iturria-Medina y col., 2005b; Iturria-Medina and Valdes-Hernández, 2007; Mori y col., 1999; Mori and van Zijl, 2002; Parker y col., 2002; Parker y col., 2003), como si usáramos el lente de una lupa que nos permite “ver” las trayectorias aproximadas de los grupos individuales de fibras.

Existen ya muchos métodos de tractografía basados en las neuroimágenes de la difusión, cada uno presenta características propias diseñadas para lidiar con la incertidumbre de los datos y extraer a la vez la mayor cantidad posible de información anatómica (ver Anexo B). Entonces, ¿por qué tratar, como en nuestro caso, de modelar el cerebro como una red que simula el espacio de sus conexiones para introducir así nuevos elementos al campo de la tractografía y aumentar el número y la complejidad de los métodos ya existentes? Si nos fijamos en ello, existe gran similaridad entre nuestro concepto general de la estructura anatómica cerebral (regiones anatómicas/funcionales ubicadas en sitios específicos del cerebro que se comunican entre sí a través de fibras nerviosas) y la representación típica que nos hacemos de un grafo (puntos en el espacio, con coordenadas únicas, que se conectan entre sí a través de arcos o líneas). Esta similaridad, y la conocida flexibilidad y riqueza de la teoría de grafos para la modelación y caracterización de diferentes fenómenos físicos, nos impulsaron a considerar el cerebro como un grafo en el que los nodos representan voxeles (o regiones anatómicas concretas) y los arcos representan las conexiones de materia blanca entre voxeles; el peso de los arcos, correspondiente a cada conexión, estaría reflejando la probabilidad o fuerza de la conexión, ya sea como una medida de la posibilidad real de su existencia o del número de fibras nerviosas involucradas. El acercamiento a la teoría de grafos nos permitiría alcanzar una representación espacial similar a la de la estructura cerebral, pero más importante aún, de emplearse las múltiples herramientas físicas/matemáticas que usualmente son utilizadas en el análisis de cualquier grafo de interés, permitiría caracterizar las propiedades principales de la estructura cerebral de acuerdo a sus patrones intrínsecos, admitiendo no sólo hallar o describir conexiones anatómicas específicas sino también evaluar las relaciones entre estas y sus potencialidades para gestionar e integrar el flujo de información neural.

En esta tesis, para determinar las rutas de conexión entre dos puntos en un grafo cerebral definido, se propone explorar exhaustivamente el conjunto de todos los caminos discretos posibles y seleccionar la ruta que maximice cierta

función de costo definida de acuerdo a criterios fisiológicos. Un procedimiento similar es realizado en las técnicas de propagación de frentes de onda (Parker y col., 2002; Staempfli y col., 2006), en las que la ruta de conexión es aquella que minimiza el “tiempo” necesario para arribar de un voxel a otro. En nuestro caso, la tractografía se expresa en términos del camino más probable sobre el grafo cerebral. Los resultados mostrados en el Artículo 1 han mostrado como el método es capaz de reconstruir correctamente estructuras complejas de fibras: cruce en línea recta, cruce en curva, trayectoria Feuille, tracto bifurcado y cruce ortogonal de tres tractos. Para la última configuración de las anteriores, el modelo fue comparado con algoritmos tradicionales de propagación de líneas y de propagación de frentes, mostrando mejores resultados que ambos tipos de procedimientos (Artículo 1, Figura 9). Además, se presentan las rutas de conexión anatómica obtenidas entre el polo occipital izquierdo y el derecho (Artículo 1, Figura 10a), un plano axial definido a la altura del tallo cerebral (PA) y ambos giros postcentrales (Figura 10d), los tálamos y los giros postcentrales mediales (Figura 10d), y entre ambos giros postcentrales mediales (Figura 10d). Los resultados concuerdan con la información anatómica reportada antes por estudios invasivos (Gómez-Padrón y col., 1985; Standring, 2004; Witelson, 1989).

Para caracterizar las conexiones anatómicas entre K estructuras de materia gris, el grafo cerebral inicialmente definido es tratado como un grafo K+1 partito, para ello se particiona el conjunto de nodos (voxeles) inicial en K subconjuntos no solapados de materia gris (grupos de voxeles) y un subconjunto que reúne a los nodos restantes (aquellos voxeles que pertenecen a la materia blanca o al líquido cefalorraquídeo). Basado en dicho grafo multipartito, se definen tres medidas de conectividad entre regiones: Fuerza de Conexión Anatómica (ACS), Densidad de Conexión Anatómica (ACD) y Probabilidad de Conexión Anatómica (ACP). ACS provee una estimación del flujo potencial de información entre cualquier par de regiones, considerando que dicho flujo es proporcional a la cantidad de fibras nerviosas compartidas por estas. DCA es una medida de la fracción del área externa de las regiones que se encuentra conectada con

respecto al área externa total de ambas, es, por tanto, una medida que intenta corregir por el tamaño de las regiones involucradas en cada conexión. Esta permite, por ejemplo, conocer si un par de regiones determinado está más o menos conectado que otro par de regiones con igual o diferente área superficial. Dos regiones con un valor alto de ACS (comparado con la ACS de otras dos regiones) no necesariamente debe presentar un valor alto de ACD, lo que puede ocurrir cuando el primer par de regiones tiene una elevada área superficial en comparación con el segundo par. Similarmente, un par de regiones puede tener un bajo valor de ACS y un alto valor de ACD, lo que ocurre específicamente cuando estas regiones presentan poca área superficial y la mayoría de su neuronas ubicadas en la superficie externa están conectadas a través de fibras con las de la otra región.

Mientras ACS y ACD cuantifican la fuerza y densidad de la posible conexión entre dos regiones de interés, ACP es una medida de la probabilidad de conexión, al menos por una fibra nerviosa, entre estas regiones. Dicha medida permite inferir si dos regiones se pueden encontrar vinculadas funcionalmente de forma directa, sin tener en cuenta las características de la conexión. Otras medidas de conectividad región-región pueden ser definidas, algunas de ellas podrían ser formuladas incluso como una combinación de las medidas ya presentadas. Además, en el futuro sería útil considerar no sólo los parámetros de las rutas de fibras halladas para cuantificar determinada conexión anatómica, como en este estudio, sino también tener en cuenta información a priori sobre la conexión analizada. Tal información a priori podría obtenerse a través de estudios anatómicos o funcionales basados en métodos histológicos o en otras técnicas de neuroimágenes (por ejemplo fMRI, tomografía EEG/MEG o PET), permitiendo la integración entre diferentes fuentes de investigación de la conectividad anatómica y funcional.

Por último, vale resaltar que la falta de información sobre el sentido direccional de las fibras, considerada una de las limitaciones intrínsecas más importantes de las neuroimágenes de la difusión, imposibilita distinguir entre proyecciones

aferentes o eferentes. Por tanto, en todos los grafos cerebrales definidos en este estudio, la dirección de los arcos es irrelevante y cada medida de conectividad anatómica propuesta es simétrica. Pese a ello, un trabajo previo (Young, 1993) ha reportado una matriz de conectividad entre 73 regiones de la corteza cerebral en primates, reconstruida según trazadores invasivos, y en la misma aproximadamente sólo el 15 % de todas las conexiones posibles no son recíprocas.

Análisis topológico de redes cerebrales

Ya tenemos las redes que representan las conexiones anatómicas cerebrales de varios sujetos, pero ¿qué hacer con ellas?, ¿cómo analizar la información que contienen?, ¿qué conclusiones biológicas pueden extraerse? En los Artículos 2 y 3 presentamos dos aplicaciones al estudio de las redes anatómicas cerebrales, una dedicada a la caracterización de las redes de 20 humanos saludables, y la segunda dedicada a explorar semejanzas y diferencias entre las redes correspondientes a el hemisferio izquierdo y derecho para un grupo de 11 humanos saludables y un primate no-humano. En ambos casos, para cada red calculada se evaluaron un conjunto de medidas topológicas, propias de la teoría de grafos, que buscan caracterizar las propiedades de la red en su forma general (como eficiencia global, índice de “mundo-pequeño”, longitud del camino medio, configuración de motivos estructurales) y las de sus nodos locales (eficiencia local, centralidad, vulnerabilidad), brindando valores cuantitativos que reflejan las facultades intrínsecas para apoyar o soportar el fluyo potencial de actividad neural.

Los análisis anteriores de redes cerebrales en humanos, tanto de redes anatómicas (Hagmann y col., 2006; He y col., 2007) como de redes funcionales (Achard y col., 2006; Bassett y col., 2006; Eguiluz y col., 2005; Salvador y col., 2005b; Stam, 2004), trataron siempre la red analizada en su forma binaria, es decir, como una red en la cual cada posible conexión es considerada verdadera o falsa, sin ningún matiz intermedio. Para ello aplicaron un valor umbral arbitrario

a cada matriz de conectividad estimada, considerándose sólo como válidos aquellos valores de conectividad superiores al umbral (los que después pasaron a valer indistintamente 1) y como no válidos aquellos que no superaron el umbral (que luego pasaron a valer cero y por tanto dejaron de ser considerados en el análisis de la red). Este tipo de procedimiento presenta, además de la selección arbitraria del valor umbral, la limitación de que todas las conexiones son consideradas como iguales, sin diferenciación entre ellas, pese a que en la realidad un par de regiones cualquiera puede estar más o menos fuertemente conectado que otro par, perdiéndose por tanto la información asociada sobre la "intensidad" de las conexiones. Una de las diferencias principales que nuestra metodología, expuesta en los Artículos 2, 3 y 4, presenta con estos estudios anteriores donde se analizaron redes cerebrales, es que precisamente propusimos analizar las redes teniendo en cuenta siempre el peso de cada conexión estimada. Para ello se mantuvieron las redes anatómicas obtenidas a partir del método propuesto en el Artículo 1 (donde cada valor de conexión representa numéricamente la probabilidad, densidad o fuerza de una conexión anatómica) y se sustituyeron las medidas de grafos empleadas en los estudios anteriores, para redes binarias, por medidas ya definidas en la teoría de grafo para el análisis de redes pesadas (Boccaletti y col., 2006; Latora y Marchiori, 2001; Onnela y col., 2005; Watts, 1999; Watts y Strogatz, 1998). Por cuanto el peso de las conexiones refleja semejanzas y diferencias anatómicas intrínsecas entre ellas, el análisis de redes pesadas permitiría sin dudas una descripción más realista de la estructura cerebral.

Sin embargo, pese al empleo de redes pesadas, es necesario mencionar una limitación importante que puede afectar el nivel de realidad con que se analice la estructura cerebral. Y es que, según el método de tractografía introducido, en cada mapa global de conectividad estimado quedan valores de conectividad espurios, es decir, valores diferentes a cero en voxeles del volumen cerebral que no presentan en la realidad una conexión anatómica a través de fibras nerviosas con la región fuente. Esto provoca que los valores de ACS, ACD o ACP definidos entre pares de regiones queden afectados por pequeños valores

espurios cuya acumulación, digamos en el orden de cientos de voxeles, afecte negativamente la confiabilidad de cada red estimada. Pero, ¿por qué es tan difícil discriminar entre conexiones falsas y verdaderas, cómo eliminar estos valores? Hasta el momento no existe un consenso en la manera de eliminar conexiones falsas estimadas a partir de métodos de tractografía. La incertidumbre típica de los datos, donde en cada voxel es necesario tomar una decisión sobre la dirección que presentan las fibras, provoca una acumulación de errores a lo largo de cada trayectoria de fibra estimada, los que serán más o menos pequeños según la calidad de las imágenes y el método de reconstrucción de la anisotropía intravoxel que se use. Esta acumulación de pequeños errores se traduce en una disminución, con la distancia, de la certidumbre que tenemos sobre si una trayectoria de fibra estimada es cercana a la trayectoria real. Mientras más larga es una fibra nerviosa, más difícil nos es saber si la aproximación de la trayectoria correspondiente que calculamos es real o no, lo que se refleja, según el modelo propuesto en el Artículo 1, en un decaimiento de la probabilidad de conexión entre dos voxeles (o regiones) cualesquiera, que no siempre responde a que no exista una fibra nerviosa conectándolos, sino más bien queda en dependencia de la distancia que existe entre estos voxeles (o regiones). Por tanto, ¿cómo diferenciar entre conexiones reales y falsas cuando quedan mezclados otros efectos además que la información sobre la direccionalidad de las fibras que nos ofrecen los datos de las neuroimágenes de la difusión?, en otras palabras, ¿un valor de conexión estimado es bajo porque las dos regiones involucradas están poco conectadas por fibras nerviosas, según las neuroimágenes de la difusión, o porque se encuentran muy distantes entre sí?

Discriminación de patologías

En el Artículo 4 de esta tesis se propuso emplear, por primera vez, parámetros topológicos elementales de la red anatómica cerebral pesada para discriminar una condición cerebral anómala que afecta la integridad de la materia blanca.

Estudios anteriores habían mostrado que algunos parámetros de redes, como el grado de *mundo-pequeño* y la *eficiencia global*, decrecen significativamente, al compararseles con un grupo control, ante patologías como la Esclerosis Múltiple (He y col., 2009), la esquizofrenia (Micheloyannis y col., 2006; Rubinov y col., 2009), el Alzheimer (Chun-Yi Lo y col., 2010; Stam y col., 2007) y el accidente vascular encefálico (Crofts y Higham, 2009; Wang y col., 2010), soportando la hipótesis de una aleatorización cerebral asociada a la pérdida de organización estructural/funcional como resultado ante lesiones o procesos neurodegenerativos (Wang y col., 2010). Sin embargo, el hallazgo de una diferencia significativa entre grupos no implica necesariamente que se pueda predecir o discriminar qué sucederá en una nueva muestra de datos. Aunque históricamente relacionados, los conceptos de diferencia significativa y predicción difieren grandemente en su interpretación, mientras el primero ocurre cuando la probabilidad de observar el efecto estudiado no puede considerarse aleatoria en una muestra específica, el segundo implica una capacidad para distinguir si un sujeto específico pertenece o no a grupos diferentes (digamos grupos de sujetos sanos o patológicos, a los que no se sabe si el sujeto pertenece), siendo un concepto más cercano a nuestra idea de un diagnóstico clínico. Es, por tanto, que nuestro objetivo primario es alcanzar una herramienta predictiva que ayude a discriminar entre sujetos sanos y patológicos, en lugar de sólo realizar una comparación entre dos o más grupos; logrando de esa manera utilizar la información contenida en los parámetros topológicos de las redes cerebrales, reconstruidas con técnicas de tractografía basadas en las neuroimágenes de la difusión, para discriminar automáticamente patologías donde la materia blanca es severamente afectada.

Al estudiar el caso específico del ratón tembloroso (shiverer), un modelo animal relevante para el estudio de enfermedades donde la mielina se afecta, dado que se caracterizan por la ausencia del gen que codifica una proteína básica en la producción de mielina, los resultados mostraron que es posible discriminar con alta confiabilidad entre los sujetos sanos y patológicos (91.6-100 %). La metodología se sustenta en un análisis discriminatorio aplicado a la

representación espacial de parámetros topológicos de redes cerebrales (grado de clusterización, longitud del camino medio, modularidad, eficiencia global/local y grado de mundo-pequeño) que pueden llegar a interpretarse como reflectores de la ausencia de mielina compacta en el sistema nervioso del ratón tembloroso. De las seis medidas topológicas consideradas, dos medidas específicas (longitud del camino medio y modularidad) mostraron, sin embargo, un bajo poder predictivo de apenas un 66.67 %. Ambas habían presentado también diferencias significativas menos acentuadas que las cuatro medidas restantes entre los dos grupos de sujetos. Una posible explicación ha dicho resultado podría considerar el hecho de que aunque el ratón tembloroso presenta una extrema desmielinización en sus axones de materia blanca, este conserva de forma general la estructura de las conexiones de su sistema nervioso. Cualquier medida topológica que refleje más la estructura global de las redes, como es el caso de la longitud del camino medio y la modularidad (indicadoras de la cantidad básica del número de conexiones entre regiones y de los módulos básicos que integran la red global, respectivamente), será menos susceptible a reflejar variaciones en la integridad de las conexiones específicas y revelará por tanto apenas una ligera diferencia cuantitativa acerca de las desigualdades anatómicas reales entre los ratones temblorosos y controles.

Por último, debemos resaltar que la metodología propuesta podría ser particularmente útil en el estudio de patologías humanas que se caractericen por procesos de desmielinización, como la Esclerosis Múltiple (Filippi y Agosta, 2010; Ormerod y col., 1987) y la Encefalomielitis Difusa Aguda (Almendinger y col., 2010; Jones, 2003). Sin embargo, no podemos olvidar que antes de que una aplicación clínica en humanos pueda ser considerada, es necesario explorar, primeramente, la capacidad del método para reflejar diferentes estados de la misma patología (todos los sujetos considerados en este estudio se encontraban en un estado similar, no siendo viable evaluar si se detectaba o no, según las medidas empleadas, que unos estaban más afectados que otros), y luego, la reproducibilidad en sujetos humanos, para los cuales siempre se usan diferentes protocolos de adquisición de imágenes, usualmente con menor fuerza

de campo magnético y resolución, que los utilizados para adquirir los datos de los ratones aquí estudiados.

5. CONCLUSIONES

1. La metodología formulada y evaluada sobre el marco de las técnicas de DW-MRI y la teoría de grafos, permite estimar de forma no invasiva las trayectorias de las fibras nerviosas y cuantificar las conexiones que estas establecen entre las diferentes regiones cerebrales según la fuerza, densidad y probabilidad de cada conexión. Los resultados obtenidos, tanto en datos simulados como en datos reales, presentaron una alta correspondencia con los patrones de conectividad esperados, y mostraron elevada replicabilidad a través de los diferentes sujetos sanos.
2. La metodología propuesta sobre el formalismo de la teoría de grafos, permite caracterizar topológicamente el conjunto de todas las conexiones anatómicas cerebrales en cuanto a sus capacidades globales y locales para controlar e integral el flujo de información neural. Esta permitió corroborar la alta similitud organizativa entre los patrones de conectividad anatómica estimados en humanos sanos con aquellos reportados para redes funcionales también en humanos sanos, así como con los correspondientes a redes anatómicas de otras especies de mamíferos, cuyas conexiones estructurales han sido mapeadas utilizando métodos invasivos.
3. El enfoque propuesto y evaluado para identificar las asimetrías inter-hemisféricas cerebrales teniendo en cuenta las semejanzas y diferencias topológicas entre las correspondientes subredes anatómicas, permite comparar ambos hemisferios según la eficiencia y optimización estructural de estos para lidiar con el flujo de información neural. Tanto en un grupo de humanos sanos y en un primate no-humano, esta estrategia permitió identificar asimetrías locales altamente consistentes con asimetrías anatómicas y funcionales ya reportadas, así como asimetrías globales en correspondencia con los patrones reportados del procesamiento funcional global.

4. La metodología propuesta y evaluada para analizar las propiedades topológicas de las redes anatómicas cerebrales, permite discriminar automáticamente condiciones patológicas relacionadas a afectaciones en la integridad de las conexiones anatómicas. Los resultados obtenidos en la discriminación de animales experimentales con afectaciones en la mielina de sus fibras nerviosas mostraron una alta precisión diagnóstica, así como revelaron el alto grado de aleatorización en los patrones organizativos de las conexiones vinculado a una menor optimización estructural en las redes cerebrales de dichos animales.

6. RECOMENDACIONES

1. Crear una metodología, complementaria al modelo de conectividad presentado, que permita discriminar entre conexiones reales y espurias (resultantes de la incertidumbre intrínseca en los datos de difusión). Ello permitirá lograr una descripción más realista de la estructura cerebral.
2. Al comparar las redes anatómicas del hemisferio cerebral derecho e izquierdo, incluir en el análisis también otros factores como el sexo y la manualidad, además de incrementar el número de sujetos. Deben incluirse además otras especies animales, buscando puntos comunes en las estrategias evolutivas.
3. Aplicar a otras patologías y diferentes estados de las mismas, la metodología propuesta para discriminar automáticamente alguna condición cerebral anómala, lo que permitirá valorar con mayor robustez si existen espacios topológicos correspondientes a patologías específicas.
4. Extender a humanos la metodología propuesta para discriminar automáticamente condiciones cerebrales anómalas.

7. REFERENCIAS BIBLIOGRÁFICAS

Achard, S., Bullmore, E., 2007. Efficiency and cost of economical brain functional networks. PLoS Comput Biol. Feb 2;3(2):e17.

Achard, S., Salvador, R., Whitcher, B., Suckling, J., Bullmore, E., 2006. A resilient, low-frequency, small-world human brain functional network with highly connected association cortical hubs. J.Neurosci. 26, 63-72.

Albert, R., Jeong, H., Barabasi, A.-L., 1999. Diameter of World-Wide Web. pp. 130-131.

Almendinger, S., Lovato, L., Fukaura, H., Hafler, D., O'Connor, K., 2010. Characterization of the Myelin Specific Autoantibodies in Acute Disseminated Encephalomyelitis. Clinical Immunology 135, S81.

Basser P., 1997. *New Histological and Physiological Stains Derived From Diffusion Tensor MR Images*. Ann.New York Acad.Sci, 820.

Basser, P.J., Mattiello, J., LeBihan, D., 1994. Estimation of the effective self-diffusion tensor from the NMR spin echo. J.Magn Reson.B 103, 247-254.

Basser, P.J., Pajevic, S., 2000. Statistical artifacts in diffusion tensor MRI (DT-MRI) caused by background noise. Magn Reson.Med. 44, 41-50.

Basser, P.J., Pajevic, S., Pierpaoli, C., Duda, J., Aldroubi, A., 2000. In vivo fiber tractography using DT-MRI data. Magn Reson.Med. 44, 625-632.

Basser, P.J., Pierpaoli, C., 1996. Microstructural and physiological features of tissues elucidated by quantitative-diffusion-tensor MRI. J.Magn Reson.B 111, 209-219.

Basser, P.J.D.J., 2002. Diffusion-Tensor MRI: theory,eperimental design and data analysis,technical review. , NMR in Biomedicine, 456.

Bassett, D.S., Bullmore, E., 2006a. Small-world brain networks. Neuroscientist. 12, 512-523.

Bassett, D.S., Bullmore, E., 2006b. Small-world brain networks. Neuroscientist. 12, 512-523.

Bassett, D.S., Meyer-Lindenberg, A., Achard, S., Duke, T., Bullmore, E., 2006. Adaptive reconfiguration of fractal small-world human brain functional networks. Proc.Natl.Acad.Sci.U.S.A 103, 19518-19523.

Behrens, T.E., Johansen-Berg, H., Woolrich, M.W., Smith, S.M., Wheeler-Kingshott, C.A., Boulby, P.A., Barker, G.J., Sillery, E.L., Sheehan, K., Ciccarelli, O., Thompson, A.J., Brady, J.M., Matthews, P.M., 2003a. Non-invasive mapping of connections between human thalamus and cortex using diffusion imaging. Nat.Neurosci. 6, 750-757.

Behrens, T.E., Woolrich, M.W., Jenkinson, M., Johansen-Berg, H., Nunes, R.G., Clare, S., Matthews, P.M., Brady, J.M., Smith, S.M., 2003b. Characterization and propagation of uncertainty in diffusion-weighted MR imaging. Magn Reson.Med. 50, 1077-1088.

Behrens, T.E., Woolrich, M.W., Jenkinson, M., Johansen-Berg, H., Nunes, R.G., Clare, S., Matthews, P.M., Brady, J.M., Smith, S.M., 2003c. Characterization and propagation of uncertainty in diffusion-weighted MR imaging. Magn Reson.Med. 50, 1077-1088.

Boccaletti, S., Latora, V., Moreno, Y., Chavez, M., Hwang, D.-U., 2006. Complex networks: Structure and dynamics. pp. 175-308.

Broca, P., 1861. Loss of Speech, Chronic Softening and Partial Destruction of the Anterior Left Lobe of the Brain. Bulletin de la Société Anthropologique, 2, 235-238.

Canales-Rodríguez, E., Melie-García, L., Valdez-Hernández, P., Iturria-Medina, Y., Alemán-Gómez, Y., Bouza-Dominguez, J., 2005. A new method for extracting information from intravoxel white matter structures distribution. Presented at the 11th Annual Meeting of the Organization for Human Brain Mapping, June 12-16, 2005, Toronto, Ontario, Canada. Available on CD-Rom in NeuroImage, Vol. 26, No.1.

Chun-Yi Lo, Pei-Nung Wang, Kun-Hsien Chou, Jinhui Wang, Yong He, Ching-Po Lin, 2010. Diffusion tensor tractography reveals abnormal topological organizational in structural cortical networks in Alzheimer's disease. 30(50) ed, The Journal of Neuroscience, pp. 16876-16885.

Conturo, T.E., Lori, N.F., Cull, T.S., Akbudak, E., Snyder, A.Z., Shimony, J.S., McKinstry, R.C., Burton, H., Raichle, M.E., 1999. Tracking neuronal fiber pathways in the living human brain. Proc.Natl.Acad.Sci.U.S.A 96, 10422-10427.

Crofts, J.J., Higham, D.J., 2009. A weighted communicability measure applied to complex brain networks. 6 ed, Journal of the Royal Society, pp. 411-414.

Eguiluz, V.M., Chialvo, D.R., Cecchi, G.A., Baliki, M., Apkarian, A.V., 2005. Scale-free brain functional networks. Phys.Rev.Lett. 94, 018102.

Filippi, M., Agosta, F., 2010. Imaging Biomarkers in Multiple Sclerosis. Journal of Magnetic Resonance Imaging 31, 770-788.

Gómez-Padrón, I., Silva Loynaz, C., Seuc Chiu, A., 1985. Anatomía II. Folleto complementario. Ministerio de salud pública, Cuba.

Hagmann, P., Kurant, M., Gigandet, X., Thiran, P., Wedeen, V.J., Meuli, R., Thiran, J.P., 2006. Imaging the brain neuronal network with diffusion MRI: a way to understand its global architecture. Proc. ISMRM, p. 436.

Hagmann, P., Reese, T.G., Tseng, W.Y., Meuli, R., Thiran, J.P., Wedeen, V.J., 2004. Diffusion Spectrum Imaging tractography in complex crerebral white matter: an investigation of the centrum semiovale. Proc. ISMRM, p. 623.

Hagmann, P., Thiran, J.P., Jonasson, L., Vandergheynst, P., Clarke, S., Maeder, P., Meuli, R., 2003. DTI mapping of human brain connectivity: statistical fibre tracking and virtual dissection. Neuroimage. 19, 545-554.

He, Y., Dagher, A., Chen, Z., Charil, A., Zijdenbos, A., Worsley, K., Evans, A., 2009. Impaired small-world efficiency in structural cortical networks in multiple sclerosis associated with white matter lesion load. Brain 132, 3366-3379.

He, Y., Chen, Z.J., Evans, A.C., 2007. Small-World Anatomical Networks in the Human Brain Revealed by Cortical Thickness from MRI. Cerebral Cortex, doi: 10.1093/cercor/bhl 149.

Hilgetag, CC., Kaiser, M., 2004. Clustered Organization of Cortical Connectivity. 2 ed, pp. 353-360.

Ito, R., Mori, S., Melhem, E.R., 2002. Diffusion tensor brain imaging and tractography. Neuroimaging Clin.N.Am. 12, 1-19.

Iturria-Medina, Y., 2004. De las neuroimágenes de la difusión a la conectividad anatómica cerebral. Tesis de Diploma.

Iturria-Medina, Y., Canales-Rodríguez, E., Melié-García, L., Valdés-Hernández, P., 2005a. Bayesian formulation for fiber tracking. Available on CD-Rom in NeuroImage, Vol. 26, No.1; Presented at the 11th Annual Meeting of the Organization for Human Brain Mapping, June 12-16, 2005,Toronto, Ontario, Canada.

Iturria-Medina, Y., Valdes-Hernandez, P., Canales-Rodriguez, E., 2005b. Measures of anatomical connectivity obtained from neuro diffusion images. Available on CD-Rom in NeuroImage, Vol. 26, No.1; Presented at the 11th Annual Meeting of the Organization for Human Brain Mapping, June 12-16, 2005,Toronto, Ontario, Canada.

Iturria-Medina, Y., Valdes-Hernández, P.A., 2007. De las neuroimágenes de difusión a la conectividad anatómica cerebral. 37 ed, CENIC Ciencias Biológicas, pp. 307-315.

Jones, C.T., 2003. Childhood autoimmune neurologic diseases of the central nervous system. Neurologic Clinics 21, 745-+.

Jun Zhang, Hao Ji, Ning Kang and Ning Cao, 2005. Fiber Tractography in Diffusion Tensor Magnetic Resonance Imaging: A Survey and Beyond. Technical Report No. 437-05 ed, Department of Computer Science; University of Kentucky; Lexington; KY.

Koch, M.A., Norris, D.G., Hund-Georgiadis, M., 2002. An investigation of functional and anatomical connectivity using magnetic resonance imaging. Neuroimage. 16, 241-250.

Latora, V., Marchiori, M., 2001. Efficient behavior of small-world networks.

Lazar, M., Weinstein, D.M., Tsuruda, J.S., Hasan, K.M., Arfanakis, K., Meyerand, M.E., Badie, B., Rowley, H.A., Haughton, V., Field, A., Alexander, A.L., 2003. White matter tractography using diffusion tensor deflection. Hum.Brain Mapp. 18, 306-321.

LeBihan D., Mangin, J.F., Poupon, C., Clark, C.A., Pappata, S., Molko, N., Chabriat, H., 2001. Diffusion tensor imaging: concepts and applications. J.Magn Reson.Imaging 13, 534-546.

LeBihan, D., 1995. Diffusion and Perfusion Magnetic Resonance Imaging, Applications to Functional MRI.

Lori, N.F., Akbudak, E., Shimony, J.S., Cull, T.S., Snyder, A.Z., Guillory, R.K., Conturo, T.E., 2002. Diffusion tensor fiber tracking of human brain connectivity: aquisition methods, reliability analysis and biological results. NMR Biomed. 15, 494-515.

McDonald, W.I., Compston, A., Edan, G., Goodkin, D., Hartung, H.P., Lublin, F.D., McFarland, H.F., Paty, D.W., Polman, C.H., Reingold, S.C., Sandberg-Wollheim, M., Sibley, W., Thompson, A.J., van den Noort, S., Weinshenker, B.Y., Wolinsky, J.S., 2001. Recommended diagnostic criteria for multiple sclerosis: Guidelines from the International Panel on the Diagnosis of Multiple Sclerosis. Annals of Neurology 50, 121-127.

Micheloyannis, S., Pachou, E., Stam, C.J., Breakspear, M., Bitsios, P., Vourkas, M., Erimaki, S., Zervakis, M., 2006. Small-world networks and disturbed functional connectivity in schizophrenia. Schizophrenia Research 87, 60-66.

Milos, R., Shen-Orr, S., Itzkovitz, S., Kashan, N., Chklovskii, D., Alon, U., 2002. Network motifs: simple building blocks of complex networks. Science 298, pp. 824-827.

Mori, S., Crain, B.J., Chacko, V.P., van Zijl, P.C., 1999. Three-dimensional tracking of axonal projections in the brain by magnetic resonance imaging. Ann.Neurol. 45, 265-269.

Mori, S., van Zijl, P.C., 2002. Fiber tracking: principles and strategies - a technical review. NMR Biomed. 15, 468-480.

Onnela, J.P., Saramaki, J., Kertesz, J., Kaski, K., 2005. Intensity and coherence of motifs in weighted complex networks. Phys.Rev.E.Stat.Nonlin.Soft.Matter Phys. 71, 065103.

Ormerod, I.E.C., Miller, D.H., McDonald, W.I., Duboulay, E.P.G.H., Rudge, P., Kendall, B.E., Moseley, I.F., Johnson, G., Tofts, P.S., Halliday, A.M., Bronstein, A.M., Scaravilli, F., Harding, A.E., Barnes, D., Zilkha, K.J., 1987. The Role of Nmr Imaging in the Assessment of Multiple-Sclerosis and Isolated Neurological Lesions - A Quantitative Study. Brain 110, 1579-1616.

Parker, G.J., Alexander, D.C., 2003. Probabilistic Monte Carlo based mapping of cerebral connections utilising whole-brain crossing fibre information. Inf.Process Med.Imaging 18, 684-695.

Parker, G.J., Haroon, H.A., Wheeler-Kingshott, C.A., 2003. A framework for a streamline-based probabilistic index of connectivity (PICo) using a structural interpretation of MRI diffusion measurements. J.Magn Reson.Imaging 18, 242-254.

Parker, G.J., Wheeler-Kingshott, C.A., Barker, G.J., 2002. Estimating distributed anatomical connectivity using fast marching methods and diffusion tensor imaging. IEEE Trans.Med.Imaging 21, 505-512.

Pierpaoli, C., Basser, P.J., 1996. Toward a quantitative assessment of diffusion anisotropy. Magn Reson.Med. 36, 893-906.

Ramnani, N., Behrens, T.E., Penny, W., Matthews, P.M., 2004. New approaches for exploring anatomical and functional connectivity in the human brain. Biol.Psychiatry 56, 613-619.

Rubinov, M., Knock, S.A., Stam, C.J., Micheloyannis, S., Harris, A.W.F., Williams, L.M., Breakspear, M., 2009. Small-World Properties of Nonlinear Brain Activity in Schizophrenia. Human Brain Mapping 30, 403-416.

Salvador, R., Suckling, J., Coleman, M.R., Pickard, J.D., Menon, D., Bullmore, E., 2005a. Neurophysiological architecture of functional magnetic resonance images of human brain. Cereb.Cortex 15, 1332-1342.

Salvador, R., Suckling, J., Coleman, M.R., Pickard, J.D., Menon, D., Bullmore, E., 2005b. Neurophysiological architecture of functional magnetic resonance images of human brain. Cereb.Cortex 15, 1332-1342.

Sethian, J.A., 1999. Level set Methods and Fast Marching Methods. 2 ed. Cambridge, MA:Cambridge Univ. Press.

Sotero, R.C., Trujillo-Barreto, N.J., Iturria-Medina, Y., Carbonell, F., Jimenez, J.C., 2007. Realistically coupled neural mass models can generate EEG rhythms. Neural Computation, 19 ed, pp. 478-512.

Sporns, O., Tononi, G., Kotter, R., 2005. The human connectome: a structural description of the human brain. PLoS.Comput.Biol. 1, e42.

Sporns, O., Zwi, J., 2004. The small world of the cerebral cortex. **2** ed, pp. 145-162.

Staempfli, P., Jaermann, T., Crelier, G.R., Kollias, S., Valavanis, A., Boesiger, P., 2006. Resolving fiber crossing using advanced fast marching tractography based on diffusion tensor imaging. Neuroimage. 30, 110-120.

Stam, C.J., 2004. Functional connectivity patterns of human magnetoencephalographic recordings: a 'small-world' network? Neurosci.Lett. 355, 25-28.

Stam, C.J., Jones, B.F., Nolte, G., Breakspear, M., Scheltens, P., 2007. Small-world networks and functional connectivity in Alzheimer's disease. Cerebral Cortex 17, 92-99.

Standring, S., 2004. Gray's anatomy: The Anatomical Basis of Medicine and Surgery, 39th edition. Churchill Livingstone.

Stejskal, E.O., Tanner, J.E., 1964. *Spin diffusion measurements: spin echoes in the presence of a time-dependent field gradient*. 42 ed, pp. 288-292. 42 ed, pp. 288-292.

Tench, C.R., Morgan, P.S., Blumhardt, L.D., Constantinescu, C., 2002. Improved white matter fiber tracking using stochastic labeling. Magn Reson.Med. 48, 677-683.

Tournier, J.D., Calamante, F., Gadian, D.G., Connelly, A., 2003. Diffusion-weighted magnetic resonance imaging fibre tracking using a front evolution algorithm. Neuroimage. 20, 276-288.

Tuch D.S, 2002. MRI of complex tissue structure. PhD Thesis.

Tzourio-Mazoyer, N., Papathanassiou, D., Crivello, F., Etard, O., Delcroix, N., Mayozer, B., Joliot, M., 2002. Automated Anatomical Labeling of

Activations in SPM Using a Macroscopic Anatomical Parcellation of the MNI MRI Single-Subject Brain. 15 ed, pp. 273-289.

Wang, L., Yu, C.S., Chen, H., Qin, W., He, Y., Fan, F.M., Zhang, Y.J., Wang, M.L., Li, K.C., Zang, Y.F., Woodward, T.S., Zhu, C.Z., 2010. Dynamic functional reorganization of the motor execution network after stroke. Brain 133, 1224-1238.

Watts, D.J., 1999. Small Worlds: The Dynamics of Networks between Order and Randomness. Princeton University Press, Princeton, NJ.

Watts, D.J., Strogatz, S.H., 1998. Collective dynamics of small-world networks. pp. 440-442.

Wedeen, V.J., Reese, T.G., Tuch, D.S., Weigel, M.R., Dou, J.G., Weisskoff, R.M., Chessler, D., 2000. Mapping fiber orientation spectra in cerebral white matter with Fourier transform diffusion MRI. In Proc. Int. Soc. Magn. Reson. Med., vol. 8, pag. 82, Denver, Colorado.

Weinstein, D., Kindlmann, G., Lundberg, E., 1999. Tensorlines: advection-diffusion based propagation through diffusion tensor fields. Proceedings of IEEE Visualization, pp. 249-253.

Wernicke, C., 1874. Der aphasische Symptomencomplex : eine psychologische Studie auf anatomischer Basis. Breslau : Max Cohn und Weigert 72 p. ill.

Witelson, S.F., 1989. Hand and sex differences in the isthmus and genu of the human corpus callosum. A postmortem morphological study. Brain 112 (Pt 3), 799-835.

Young, M.P., 1993. The organization of neural systems in the primate cerebral cortex. Proc.Biol.Sci. 252, 13-18.

8. ANEXOS

8.1. ANEXO A. CARACTERIZACIÓN DE LA ANISOTROPÍA INTRAVOXEL Y SU RELACIÓN CON LA DISTRIBUCIÓN DE FIBRAS NERVIOSAS A PARTIR DE LAS NEUROIMÁGENES DE LA DIFUSIÓN

A1 NEUROIMÁGENES DE LA DIFUSIÓN

Las imágenes de RMN y los procesos intrínsecos que se relacionan a estas, constituyen la base técnica de los estudios de neuroimágenes de la difusión. La mayoría de dichos estudios emplean la serie de Stejskal y Tanner (Stejskal y Tanner, 1964), que constituyen la esencia de todas las series de impulsos que pretenden lograr imágenes cuyo contraste quede definido por la cantidad de difusión de agua en cada voxel de la muestra. Según dicho estudio, al someter una muestra a un campo magnético externo en un equipo de RMN, la señal de resonancia magnética ponderada en difusión que se recibe $S(\vec{r})$, perteneciente al voxel con posición $\vec{r}$, puede ser expresada como una función monoexponencial de la forma:

$$S(\vec{r}) = S_0(\vec{r}) \exp\left[-b\hat{g}^T D(\vec{r})\hat{g}\right], \qquad \text{(A1.1)}$$

donde el termino b depende de la forma del gradiente de difusión de campo magnético aplicado $G(t)$:

$$b = \gamma^2 \int_0^t \left[\int_0^{t'} G(t'')dt''\right] dt', \qquad \text{(A1.2)}$$

siendo γ la razón giromagnética del núcleo en estudio, en este caso el núcleo de hidrógeno; $\hat{g}$ es el vector unitario en la dirección del gradiente $G(t)$. Para el caso

específico en que se apliquen pulsos de gradiente rectangular con amplitud G, duración δ e intervalo entre los pulsos Δ, el valor b puede computarse como:

$$b = (\gamma G \delta)^2 \left(\Delta - \frac{1}{3}\delta \right). \qquad \text{(A1.3)}$$

De forma general, se establece que el término b contiene los parámetros del experimento, mientras $\hat{g}^T D \hat{g}$ es el ADC (o coeficiente de difusión aparente) en la dirección $\hat{g}$, siendo $D(\vec{r})$ el tensor de difusión en el voxel con posición espacial $\vec{r}$.

Si se toman imágenes con altos gradientes de difusión, y se divide la magnitud de la señal espacial obtenida por el valor de la señal de una imagen obtenida en ausencia de gradiente de difusión, S_0, se obtienen las imágenes ponderadas en difusión, las cuales reflejan en cada voxel, según los niveles de intensidad, los niveles de difusión del agua para una dirección dada de gradiente $\hat{g}$. La Figura A1.1 muestra una imagen ponderada en difusión. La señal obtenida es hipointensa (baja intensidad) en zonas de alta difusión (a excepción de las regiones donde hay ausencia de tejido cerebral): aquellos lugares donde abunda líquido cefalorraquídeo o donde existen fibras nerviosas de materia blanca orientadas de forma paralela al gradiente utilizado, en estas zonas el movimiento de las moléculas de agua encuentra barreras sólo en las direcciones perpendiculares a las direcciones de las fibras nerviosas, por lo que en las direcciones restantes suele existir alta difusión. De manera contraria, en las regiones donde abunda materia gris o existen fibras nerviosas orientadas perpendicularmente al gradiente de difusión aplicado, la señal es hiperintensa (alta intensidad), reflejando que en tales zonas la difusión es baja.

Figura A1.1. Imagen ponderada en difusión. Las zonas hipointensas de la imagen, a excepción de las regiones donde hay ausencia de tejido cerebral, reflejan que en ellas existe una difusión alta en la dirección paralela a la dirección del gradiente aplicado.

A2 ESTIMACIÓN DEL TENSOR DE DIFUSIÓN A PARTIR DE LAS NEUROIMÁGENES DE LA DIFUSIÓN. MEDIDAS ESCALARES

En Basser y col., 1994, fue presentado un método para estimar el Tensor de Difusión del agua en cada voxel del cerebro. Dado que el tensor de difusión posee seis elementos diferentes, hallarlo se reduce a determinar estos seis elementos. Del apéndice anterior, conocemos que a cada voxel le corresponde una señal de RMN, y en el caso de las imágenes ponderadas en difusión, esta señal se encuentra relacionada con el tensor de difusión según la expresión (A1.1), que puede ser rescrita de la siguiente forma:

$$\begin{aligned} S &= S_0 \exp\left[-\mathrm{Tr}(bD)\right] \\ &= S_0 \exp\left[-\sum_{i=1}^{3}\sum_{j=1}^{3} b_{ij} d_{ij}\right]. \end{aligned} \qquad \text{(A2.1)}$$

Los coeficientes b_{ij} de la expresión anterior se determinan para cada gradiente de difusión aplicado. Si se mide la señal para n direcciones de gradientes de difusión de campo magnético y se repite este experimento m veces se obtienen $n \cdot m$ valores de la señal. Entonces (A2.2) puede ser reformulada según:

$$\vec{X} = B\vec{d} + \vec{e}\,, \tag{A2.3}$$

donde:

$$B = \begin{pmatrix} b_{xx}^{1} & b_{yy}^{1} & b_{zz}^{1} & 2b_{xy}^{1} & 2b_{xz}^{1} & 2b_{yz}^{1} & 1 \\ \vdots & & & & & & \vdots \\ b_{xx}^{n\cdot m} & b_{yy}^{n\cdot m} & b_{zz}^{n\cdot m} & 2b_{xy}^{n\cdot m} & 2b_{xz}^{n\cdot m} & 2b_{yz}^{n\cdot m} & 1 \end{pmatrix}, \tag{A2.4}$$

el vector columna $\vec{X}$, de longitud $n \cdot m$, reúne los logaritmos de las señales medidas mientras el vector $\vec{d}$ está formado por los seis elementos independientes del tensor y el logaritmo de la señal en ausencia de gradiente de difusión, es decir:

$$\vec{d} = \left\{ d_{xx} \;\; d_{yy} \;\; d_{zz} \;\; d_{xy} \;\; d_{xz} \;\; d_{yz} \;\; \ln(S_0) \right\}^{T}. \tag{A2.5}$$

El vector $\vec{e}$ representa el error asociado a cada medición. Generalmente $\vec{e}$ se asume proveniente de un ruido blanco, es decir, gaussiano y con media cero.

Mediante una regresión multilineal, basada en la expresión (A2.1), se obtiene un predictor de $\vec{d}$:

$$\hat{\vec{d}} = (B^{T} \Sigma^{-1} B)^{-1} (B^{T} \Sigma^{-1}) X\,, \tag{A2.6}$$

donde Σ es la matriz de covarianza del error asociado a las mediciones.

Finalmente se puede construir el estimador del tensor:

$$\hat{D} = \begin{pmatrix} \hat{d}_{xx} & \hat{d}_{xy} & \hat{d}_{xz} \\ \hat{d}_{yx} & \hat{d}_{yy} & \hat{d}_{yz} \\ \hat{d}_{zx} & \hat{d}_{zy} & \hat{d}_{zz} \end{pmatrix}, \tag{A2.7}$$

y el estimador de la señal en ausencia de gradiente: $\hat{S}_0 = \exp\left(\widehat{\ln}(S_0)\right)$.

Es necesario obtener un mínimo de siete adquisiciones de imágenes de RMN ponderadas en difusión para estimar de forma única la magnitud de la señal en ausencia de gradiente y los seis elementos únicos de la matriz del tensor. En este caso, cada ecuación lineal en el sistema (A2.1) debe ser independiente, lo

cual implica que la matriz B debe ser de rango completo, es decir, los gradientes de difusión deben aplicarse en direcciones diferentes.

Asociadas a cada tensor de difusión se pueden definir medidas escalares (Basser P., 1997; Basser y Pierpaoli, 1996; Pierpaoli y Basser, 1996). Aquellas definidas como función de los autovalores del tensor son conocidas como *índices invariantes* y son intrínsecas del medio ya que son independientes de la orientación de la estructura de los tejidos y de la orientación relativa de la muestra en el equipo de resonancia magnética, así como de la dirección del campo magnético y de los gradientes de difusión aplicados, y de la elección del sistema de coordenadas de laboratorio.

Tres de los índices invariantes fundamentales son:

$$\begin{aligned} I_1 &= \lambda_1 + \lambda_2 + \lambda_3 = \mathrm{Tr}(D), \\ I_2 &= \lambda_1\lambda_2 + \lambda_2\lambda_3 + \lambda_1\lambda_3, \\ I_2 &= \lambda_1\lambda_2\lambda_3 \end{aligned} \qquad \text{(A2.8)}$$

I_1 es proporcional a la suma de los cuadrados de los semiejes del elipsoide de difusión, I_2 es proporcional a la suma de los cuadrados de las áreas de las proyecciones del elipsoide de difusión en los planos xy, yz y xz, mientras que I_3 es proporcional al cuadrado del volumen de este elipsoide.

Mediante éstos índices se pueden obtener otras medidas invariantes con sus interpretaciones geométricas y físicas, como por ejemplo la difusividad media:

$$\langle D \rangle = \frac{I_1}{3}, \qquad \text{(A2.9)}$$

que caracteriza la difusión del agua en el voxel.

Sin embargo, ninguno de los tres índices definidos anteriormente provee información sobre la anisotropía del medio, por lo que se define para ello la anisotropía fraccional (FA, del inglés *fractional anisotropy*) (Pierpaoli y Basser, 1996):

$$FA = \sqrt{\frac{3}{2}\frac{\sum_{i=1}^{3}\left(\lambda_i - \langle D\rangle\right)^2}{\sum_{i=1}^{3}\lambda_i{}^2}}\,. \qquad \text{(A2.10)}$$

La anisotropía fraccional cuantifica la anisotropía del voxel en un rango de 0 a 1. Si su valor es cercano a 1, existe alta orientación estructural, como sucede cuando por el voxel sólo pasan fibras nerviosas paralelas. Si FA es cercano a 0, es muy posible que en el voxel exista cruce de fibras o que haya presencia mayoritaria de líquido cefalorraquídeo o de materia gris.

A3 MODELO DEL MULTITENSOR

Ante la presencia en un voxel de cruce, abanicamiento o doblez de fibras nerviosas el tensor de difusión no es válido para inferir la dirección de las fibras involucradas. En el cruce de dos conjuntos de fibras perpendiculares el elipsoide que representa geométricamente al tensor es muy parecido a un disco achatado. En ocasiones donde ocurre abanicamiento y dispersión es posible observar tensores muy parecidos a una esfera. En ambos casos es imposible definir la dirección principal del tensor por lo que la dirección o direcciones de la fibras dentro del voxel queda indeterminada.

Con la intención de resolver la distribución de las direcciones de las fibras dentro de un voxel, es introducido el modelo del MultiTensor (Tuch D.S, 2002). En este se considera que el voxel puede ser dividido en varios subvoxeles independientes cuyo comportamiento es bien descrito por un tensor de difusión, es decir, donde sólo existe una dirección preferencial para las fibras nerviosas. La independencia entre los subvoxeles se traduce en bajo intercambio de partículas entre sí. Considerando que los distintos compartimentos tienen igual índices de relajación y densidad de agua, por el principio de superposición para las señales de resonancia la señal en el voxel se puede expresar como:

$$S = S_0 \sum_{i=1}^{n} f_i \exp(-Tr(bD_i))\,, \qquad \text{(A3.1)}$$

donde f_i es la fracción de volumen que ocupa el subvoxel i en el voxel, nótese que $\sum_{i=1}^{n} f_i = 1$; D_i es el tensor de difusión correspondiente y n la cantidad de subvoxeles, que a su vez representa la cantidad de fibras presentes si se asume que la causa de la heterogeneidad direccional es debido a cruces de fibras.

El objetivo es encontrar el grupo de n tensores D_i y sus correspondientes fracciones de volumen f_i que mejor se ajusten a la señal de difusión proveniente del voxel. Se necesitan para ello al menos $7n-1$ imágenes de difusión adquiridas con diferentes gradientes.

En el modelo del MultiTensor se fijan los autovalores del tensor de difusión ($\lambda_1, \lambda_2, \lambda_3$), y se minimiza a través de todo el volumen de la imagen la función de error:

$$\chi = \sum_{k} \left(\sum_{i=1}^{n} f_i \hat{S}_i(k) - S(k) \right)^2, \qquad \text{(A3.2)}$$

donde $\hat{S}_i(k)$ es el predictor de la señal de difusión para el subvoxel i del voxel k.

A4 FUNCIÓN DE DISTRIBUCIÓN ORIENTACIONAL DE LA MATERIA BLANCA

Una alternativa ampliamente utilizada en la caracterización de la anisotropía intravoxel y su relación con la orientación de las fibras nerviosas lo constituye la Función de Distribución Orientacional de la materia blanca (ODF, del inglés *Orientational distribution fuction*) $\psi(\hat{u})$, la cual también es desarrollada sobre el esquema de registro de Alta Resolución Angular (Tuch D.S, 2002), y se define como la proyección radial de la función de densidad de probabilidad (PDF) $P(\vec{R})$:

$$\psi(\hat{u}) = \int_{0}^{+\infty} P(\hat{u}R) R^2 dR, \qquad \text{(A4.1)}$$

siendo $\hat{u}$ un vector unitario y $\vec{R} = \hat{u}R$ el desplazamiento relativo de los espines.

En múltiples estudios se han propuesto diferentes modelos para integrar la expresión anterior (Canales-Rodríguez y col., 2005; Tuch D.S, 2002; Wedeen y col., 2000). Una ventaja de esta formulación (A4.1) es que no necesariamente se necesitan hacer restricciones sobre el tipo de proceso de difusión que existe (recordemos, por ejemplo, que tanto en el modelo del tensor de difusión como en el modelo del multitensor se considera que la difusión es gaussiana). La ODF expresa la probabilidad de desplazamiento de un espín en un diferencial de ángulo sólido alrededor de una dirección de fibra $\hat{u}$ (como se deduce de la expresión A4.1, es sacrificada la información radial, pero se mantiene la información direccional relevante).

La ODF puede ser representada entonces como una superficie en 3D, donde la distancia desde un punto cualquiera de dicha superficie hasta el punto de origen denota la magnitud de la difusión en la dirección que forman ambos puntos. En el marco de los trabajos de difusión por resonancia magnética nuclear, se asume generalmente que la superficie en 3D, correspondiente a la ODF en un voxel, representa la orientación de las fibras nerviosas en este voxel (ver Figura A4.1).

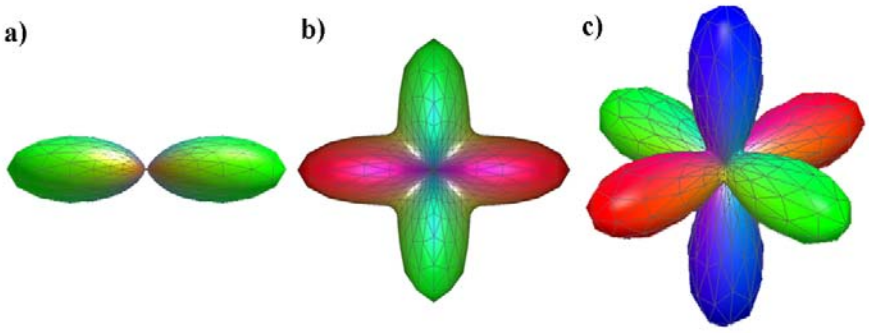

Figura A4.1. Representación en 3D de las ODFs obtenidas (según Canales-Rodríguez y col., 2005) para cuando en el voxel hay: a) una fibra, b) dos fibras en cruce perpendicular, o c) tres fibras en cruce perpendicular.

A5 FUNCIÓN DE DENSIDAD DE PROBABILIDAD DE LAS ORIENTACIONES DE LAS FIBRAS

En Behrens y col., 2003b, fue propuesto un marco bayesiano para caracterizar estadísticamente la anisotropía intravoxel y ofrecer una distribución de probabilidad sobre las orientaciones de las fibras en cada voxel. En dicho estudio se asume que existe una incertidumbre asociada a la orientación de las fibras, y esta es causada tanto por la posible presencia de fibras con distintas direcciones dentro del voxel, como por los ruidos intrínsecos en las imágenes ponderadas en difusión. La incertidumbre entonces se representa en forma de función de densidad de probabilidad, $P(\theta,\varphi|Y)$, donde (θ,φ) representa la dirección de la fibra en coordenadas polares y Y corresponde a los datos de difusión.

Para la estimación de la distribución $P(\theta,\varphi|Y)$ se emplea un modelo de volumen parcial, en el cual se asume que la señal de resonancia magnética es la suma de una señal que refleja la difusión alrededor de un tracto homogéneo de materia blanca (que constituye una difusión altamente anisotrópica) y una señal que refleja la difusión libre isotrópica. Luego, para el i-ésimo gradiente de difusión, aplicado en la dirección del vector unitario $\hat{g}_i$ con el parámetro de adquisición b_i, la señal predecida en cada voxel es:

$$\mu_i = S_0\left((1-f)\exp\left[-b_i d\right] + f\ \exp\left[-b_i d\ \hat{g}_i^T R A R^T \hat{g}_i\right]\right), \qquad \text{(A5.1)}$$

donde S_0 es la señal de resonancia magnética sin gradiente de difusión, d es la difusividad, f es la fracción de volumen de difusión anisotrópica en el voxel, y RAR^T es el tensor de difusión anisotrópico en la dirección principal de difusión (θ,φ), donde A queda definido como:

$$A = \begin{bmatrix} 1 & 0 & 0 \\ 0 & 0 & 0 \\ 0 & 0 & 0 \end{bmatrix}, \qquad \text{(A5.2)}$$

siendo R es una matriz de rotación que modifica a la matriz A de forma tal que su autovector principal quede en la dirección de (θ,φ).

El modelo de la señal (A5.1) tiene parámetros $(\theta, \varphi, d, S_0, f)$ que deben ser estimados de los datos, y parámetros $\hat{g}_i$ y b_i, que son definidos en la adquisición de los datos.

El ruido es modelado de forma separada para cada voxel, será idénticamente distribuido según una distribución gaussiana con media cero y desviación estándar σ. La probabilidad de encontrar en cada voxel el dato, Y, dado el modelo, M, y una selección aleatoria de los parámetros del modelo, $\Omega = (\theta, \varphi, d, S_0, f)$, se escribe:

$$P(Y \mid \Omega, M) = \prod_{i=1}^{n} P(y_i \mid \Omega, M), \tag{A5.3}$$

donde $P(y_i \mid \Omega, M) \sim N(\mu_i, \sigma)$.

Utilizando la regla de Bayes:

$$P(\Omega \mid Y, M) = \frac{P(Y \mid \Omega, M) P(\Omega \mid M)}{\int_{\Omega} P(Y \mid \Omega, M) P(\Omega \mid M) d\Omega}, \tag{A5.4}$$

siendo $P(\Omega \mid Y, M)$ la distribución posterior conjunta de los parámetros, Ω. El término $P(\Omega \mid M)$ es la distribución a priori de los parámetros de cada modelo, que es escogida de forma no informativa.

La incertidumbre en los parámetros de orientación (θ, φ) es contenida entonces en la distribución marginal posterior $P(\theta, \varphi \mid Y, M)$, que es formulada:

$$P(\theta, \varphi \mid Y, M) = \int_{\overline{\Omega}} P(\Omega \mid Y, M) d\overline{\Omega}, \tag{A5.5}$$

donde $\overline{\Omega}$ es el conjunto de parámetros Ω, excluyendo a (θ, φ).

Aunque las integrales (A5.4) y (A5.5) no pueden ser resueltas analíticamente, en Behrens y col., 2003b, se propone emplear Cadenas de Markov-Monte Carlo (MCMC) para resolver numéricamente dichas expresiones.

8.2. ANEXO B. DESCRIPCIÓN DE MÉTODOS MÁS EMPLEADOS EN EL TRAZADO DE LA TRAYECTORIA DE LAS FIBRAS NERVIOSAS

En este Anexo son brevemente descritos algunos métodos utilizados en el trazado de la trayectoria de las fibras nerviosas. Con ese fin se clasifican los métodos de tractografía en dos tipos fundamentales: 1) Métodos de propagación de líneas (deterministas y estocásticos) y 2) Métodos de propagación de frentes.

Antes de pasar a la descripción específica, de forma general se establecerá que cada camino 'ρ' (representando, en un sistema de referencia ortogonal, la trayectoria hipotética de una fibra nerviosa) es caracterizado por un conjunto de puntos ordenados $\{\vec{r}_i,\ i = 1,\ldots,L\}$, de coordenadas (x_i, y_i, z_i), siendo $\vec{r}_1$ el punto inicial y L-1 el número de pasos de este camino.

B1 MÉTODOS DE PROPAGACIÓN DE LÍNEAS

En este tipo de métodos se reconstruye la trayectoria aproximada de las fibras de materia blanca a partir de un punto inicial de interés (conocido como punto semilla) y avanzando discretamente desde el interior de un voxel hacia el interior del otro, según un estimado de la orientación local de las fibras nerviosas. Generalmente, la formación del camino se detiene cuando este alcanza los límites del volumen, llega a una región donde la anisotropía fraccional o algún índice de coherencia intervoxel es menor que ciertos valores umbrales para los cuales se considera alta la incertidumbre al tomar una dirección a seguir, o se arriba a alguna región de interés previamente seleccionada.

Empleo de la dirección del autovector principal del tensor de difusión local

Inicialmente, fue propuesto utilizar sólo la información local del tensor de difusión en cada paso de la expansión (Basser y col., 2000; Conturo y col., 1999; Mori y col., 1999), de forma tal que en cada punto $\vec{r}_i$ es seguida la dirección del autovector principal ($\vec{\varepsilon}_1$) del voxel en cuyo interior se encuentra ese punto para hallar el nuevo punto $\vec{r}_{i+1}$ del camino, empleando un paso de avance $0 < \mu \leq 1$, tal que:

$$\vec{r}_{i+1} = \vec{r}_i + \mu \cdot \vec{\varepsilon}_1 . \qquad \text{(B1.1)}$$

Dicho procedimiento determinista de propagación de líneas (al que nos referiremos como SLT, del inglés *Streamline Tractography*), aporta mejores resultados cuando se emplean algoritmos para aproximar o interpolar el campo del tensor de difusión. Sin embargo, al utilizarse el modelo del tensor de difusión para obtener la configuración de direcciones en cada voxel, cuando existe cruce, doblez o abanicamiento de fibras, los caminos calculados son poco fiables debido a la incompleta información que brinda el tensor de difusión en tales casos. La técnica entonces puede ser generalizada fácilmente para utilizar el modelo del multitensor. Pero de forma general este tipo de algoritmo, aunque sigue siendo ampliamente utilizado (debido, sobre todo, al bajo costo computacional que requiere), continúa siendo muy sensible a la influencia del ruido proveniente de la señal de resonancia magnética, otra de las causas que provoca que los caminos trazados se desvíen de la trayectoria real de las fibras nerviosas (Basser y Pajevic, 2000; Lori y col., 2002).

Considerando la incertidumbre asociada al autovector principal del tensor de difusión

El método anterior es clasificado como determinista pues pese a la incertidumbre presente en los datos de difusión de cada punto de partida es obtenida una y sólo una trayectoria posible de conexión hasta otro punto. Con el fin de lidiar con la incertidumbre presente en los datos, surgen entonces un conjunto de métodos que le confieren un carácter probabilístico a los caminos

calculados (Behrens y col., 2003a; Hagmann y col., 2003; Iturria-Medina, 2004; Iturria-Medina y col., 2005a; Parker y col., 2003; Tench y col., 2002), y en los cuales desde cada punto semilla son iniciados una alta cantidad de caminos a las cuales suele asignárseles un índice de validez para expresar qué tan cerca se encuentran de representar la trayectoria real de fibras nerviosas. En tales métodos, la dirección de propagación en un punto del camino es escogida según una función de probabilidad que puede depender del tensor de difusión, de tensores en el caso del modelo de multitensor, de la ODF o de alguna otra función que permita tener un estimado de la distribución intravoxel de las fibras nerviosas. A estas técnicas nos referiremos como mSLT (del inglés *modified Streamline Tractography)*.

Como ejemplo ilustrativo, en Parker y col., 2003, es propuesto un algoritmo probabilístico conocido como PICo (del inglés *Probabilistic Index of Connectivity*), que se basa en técnicas de Monte-Carlo para mapear las conexiones anatómicas cerebrales cuantificando los resultados obtenidos con la técnica tradicional SLT (Basser y col., 2000; Conturo y col., 1999; Mori y col., 1999). En dicho estudio, al trazar los caminos se considera como dirección de propagación una perturbación de la dirección del autovector principal del tensor de difusión, la cual se obtiene teniendo en cuenta la incertidumbre sobre la orientación correcta que debe presentar este autovector.

En cada punto $\vec{r}_i$ del camino, luego de interpretar la forma del tensor de difusión local, el autovector principal $\vec{\varepsilon}_1$ es modificado a un nuevo autovector $\vec{\varepsilon}_1^{\,\mathrm{mod}} = \vec{\varepsilon}_1 + \delta\vec{\varepsilon}_1$, cuyas diferencias con el anterior ($\delta\vec{\varepsilon}_1$) dependerán de la incertidumbre que se tiene sobre si $\vec{\varepsilon}_1$ refleja en ese punto o no la orientación correcta de fibras nerviosas. Dos funciones diferentes de distribución de probabilidad, una conocida como función de orden 0 y la otra como función de 1er orden, son definidas para evaluar esa incertidumbre. La función de orden 0 se diseña teniendo en cuenta la anisotropía fraccional del tensor (FA) con el fin de evaluar el grado de coherencia de los tractos de materia blanca en la

dirección de $\vec{\varepsilon}_1$. Esta función es escogida de forma tal que a medida que el valor local de FA es cercano a cero, lo que podría corresponder a la existencia de fibras orientadas en otras direcciones, mayor es la perturbación $\delta\vec{\varepsilon}_1$ que puede ser aplicada al autovector $\vec{\varepsilon}_1$. En el caso de la función de 1er orden, se considera que la FA no provee información específica sobre posibles dobleces o abanicamientos de las fibras, y para lidiar con ello se propone adicionalmente cuantificar las contribuciones relativas a la FA del segundo y el tercer autovalor del tensor de difusión. El proceso anterior, en el que en cada paso del camino se modifica el autovector principal del tensor de difusión del voxel correspondiente, se repite N veces al partir de cada punto semilla, computándose por tanto igual número de caminos. Luego, a cada voxel de interés en el volumen de la imagen cerebral es asignado un índice probabilístico de conectividad anatómica con respecto a cada voxel semilla. Este índice se define como la relación entre el número de caminos que pasan por el punto de interés y el número total de caminos generados a partir del punto semilla.

Empleo de la información direccional contenida en los voxeles vecinos más cercanos

A diferencia de la metodología anterior, en Iturria-Medina, 2004, se propone un algoritmo de tractografía en el que no sólo se tiene en cuenta la incertidumbre sobre la orientación de fibras de acuerdo al tensor de difusión local, sino que, para elegir una dirección probabilista de propagación en cada punto del camino, también se tiene en cuenta la información direccional de los tensores de difusión de los voxeles vecinos más cercanos. El procedimiento es descrito a continuación.

Para continuar trazando el camino a partir de un punto $\vec{r}_i$, se escogen aleatoriamente L_j vectores unitarios $\vec{q}_{ij}$ que formen con el vector $\vec{v}_i = \vec{r}_i - \vec{r}_{i-1}$, (el cual indica la última dirección de avance del camino) un ángulo menor que cierto valor crítico θ establecido, lo que constituye una restricción de curvatura. Para

cada uno de estos vectores aleatorios, se define la probabilidad de que el camino siga su dirección según:

$$P_{ij} = \frac{1}{Z_i} \frac{e^{\left(\frac{1}{M_i}\sum_{k=1}^{M_i}\left|\vec{\varepsilon}_{1,k}\cdot\vec{q}_{ij}\right|\right)} - 1}{e-1} \quad , \tag{B1.2}$$

donde M_i es la cantidad de voxeles vecinos que aportarán información sobre la dirección a seguir, dichos voxeles deben estar incluidos en el interior de un cono definido por el ángulo sólido β con eje en la dirección $\vec{v}_i$ (ver Figura B1.1). El término $\vec{\varepsilon}_{1,k}$ es el autovector principal del tensor de difusión en el voxel vecino k y $\vec{\varepsilon}_{1,k}\cdot\vec{q}_{ij}$ representa el coseno del ángulo que forman ambos vectores. El término Z_i es una constante de normalización. De esta forma las direcciones más probables son aquellas que tengan una mayor colinealidad con los autovectores principales de los voxeles vecinos.

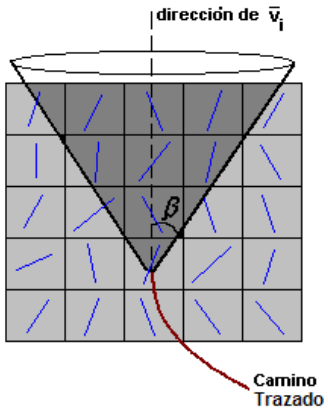

Figura B1.1. Los M_i voxeles vecinos a tener en cuenta para crear la función de probabilidad direccional están contenidos en un cono definido por el ángulo sólido β con eje en la última dirección $\vec{v}_i$ en la que avanzó el camino. Los segmentos azules representan a los autovectores principales del tensor de difusión en cada voxel.

Del conjunto de vectores unitarios $\vec{q}_{ij}$, es escogido el vector de avance $\vec{q}_{ij}^{*}$ al que corresponde la probabilidad P_{ij}^{*} obtenida de muestrear aleatoriamente en el conjunto de probabilidades P_{ij}. Cuando existen dos o más direcciones con altas probabilidades para seguir el camino, lo cual es típico en el caso de cruce de fibras o al dividirse una fibra en otras, la elección entre estas direcciones predominantes ocurre al azar y no de forma determinista, lo cual se realiza con el objetivo de que al efectuar varias repeticiones los caminos trazados representen a la mayor cantidad de trayectorias posibles a pesar de la incertidumbre implícita en los datos.

Luego, la nueva posición se calcula combinando la dirección más probable $\vec{q}_{ij}^{*}$ con el tensor de difusión D_i en este punto y empleando un tamaño de paso de avance μ:

$$\vec{r}_{i+1} = \vec{r}_i + \mu \cdot D_i \cdot \vec{q}_{ij}^{*}. \tag{B1.3}$$

Cada camino comienza en un voxel de la zona de partida escogida y en el primer paso las direcciones escogidas no tienen restricción de curvatura. Para el camino ρ con número de puntos *L*, el índice de validez IV se define:

$$IV = \left(\prod_{i=1}^{L-1} \frac{\vec{\Omega}_i^T D_i \vec{\Omega}_i}{\vec{\varepsilon}_{1,i}^T D_i \vec{\varepsilon}_{1,i}} \right)^{\frac{1}{L-1}} = \left(\prod_{i=1}^{L} \frac{\vec{\Omega}_i^T D_i \vec{\Omega}_i}{\lambda_{1,i}} \right)^{\frac{1}{L-1}}, \tag{B1.4}$$

donde $\vec{\Omega}_i$ es la dirección en que avanzó el camino al dar el paso i, D_i es el tensor de difusión en esa posición y $\vec{\varepsilon}_{1,i}$ es su autovector principal. La magnitud de $\vec{\Omega}_i^T D_i \vec{\Omega}_i$ equivale al coeficiente de difusión aparente en la dirección $\vec{\Omega}_i$ del voxel correspondiente al punto i, por lo que la expresión:

$$\frac{\vec{\Omega}_i^T D_i \vec{\Omega}_i}{\vec{\varepsilon}_{1,i}^T D_i \vec{\varepsilon}_{1,i}}, \tag{B1.5}$$

representa la relación entre el coeficiente de difusión aparente en la dirección del desplazamiento $\vec{\Omega}_i$ y la difusividad máxima $\lambda_{1,i}$. En un medio fuertemente

anisotrópico, donde, según la información que brinda el tensor de difusión, es baja la incertidumbre sobre la dirección que presentan las fibras reales, el coeficiente dado por la ecuación (B1.5) refleja cuan similar es la dirección del camino a la dirección media de las fibras en el punto i, resultando en caso de coincidencia su valor igual a uno, y en el caso que sean perpendiculares entre sí un valor cercano a cero. Al aplicar la media geométrica de tales valores a lo largo de todo el camino, el índice de validez describe en el intervalo $\left[\left(\prod_{i=1}^{L-1}\frac{\lambda_{3,i}}{\lambda_{1,i}}\right)^{\frac{1}{L-1}},1\right]$ el grado de correspondencia entre las direcciones seguidas en cada punto de la trayectoria y las propiedades locales de la difusión. Mientras menor sea el índice de validez IV, más alejado debe estar el camino de la trayectoria real que presentan las fibras nerviosas. Este índice puede ser utilizado, estableciendo un valor umbral, para eliminar aquellos caminos poco representativos de las trayectorias de las fibras. Adicionalmente, en dicho estudio se considera la conectividad anatómica entre dos voxeles cualesquiera como una función dependiente de los índices de validez de los caminos que unen a estos puntos. Específicamente, se toma como valor representativo de conectividad entre dos voxeles el mayor índice de validez de los caminos compartidos.

En las Figuras B1.2 y B1.3 se ilustra la reconstrucción de caminos de fibras nerviosas entre diversas zonas cerebrales de un sujeto normal mediante el empleo de este algoritmo de tractografía.

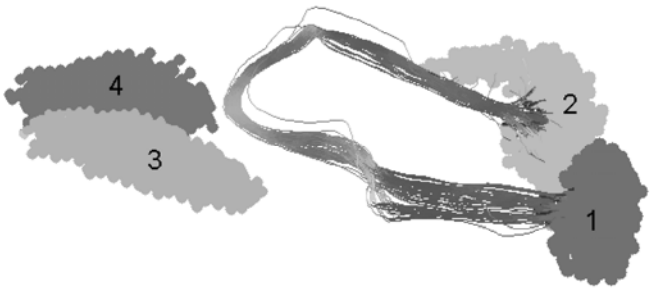

Figura B1.2. Caminos calculados entre: Polo occipital izquierdo (1)– Polo occipital derecho (2). Los tálamos (3 y 4) se representan en virtud de establecer una referencia anatómica que ayude a entender la posición en el cerebro de los caminos trazados.

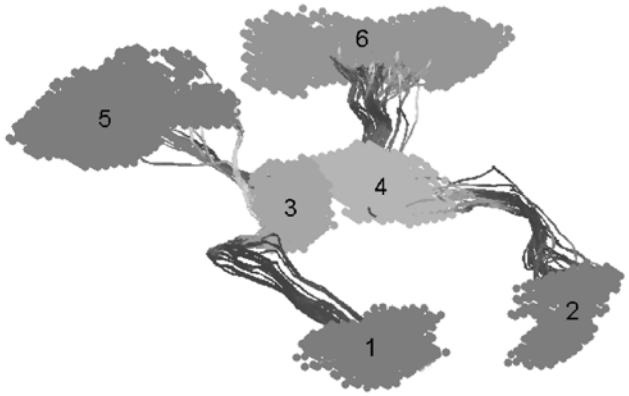

Figura B1.3. Caminos calculados entre: Tálamo izquierdo (3)– Polo occipital izquierdo (1), Tálamo derecho (4)–Polo occipital derecho (2), Giro frontal medio izquierdo (5)–Tálamo izquierdo (3), Giro frontal medio derecho (6)–Tálamo derecho (4).

Empleo de la función de densidad de probabilidad de las orientaciones de las fibras

Los métodos descritos anteriormente, aunque de manera diferente, emplean el modelo de tensor de difusión para obtener un aproximado de las trayectorias de las fibras nerviosas en cada punto. Veamos por último un ejemplo de mSLT (Behrens y col., 2003a) en el que la tractografía se realiza a partir de la distribución de probabilidad de las orientaciones de las fibras (Behrens y col., 2003c), y en el cual se propone un marco bayesiano para estimar la probabilidad de conexión anatómica entre diferentes voxeles.

Behrens y colaboradores evalúan de forma aproximada la incertidumbre de encontrar una fibra nerviosa en una orientación dada. Recordemos que dicha incertidumbre se representa en forma de función de densidad de probabilidad, $P(\theta,\varphi \mid Y)$, donde (θ,φ) representa la posible dirección de la fibra en

coordenadas polares y Y corresponde a los datos de difusión. Luego, se plantea que de forma general dos voxeles, A y B, pueden conectarse sólo si existe un camino de fibra que los une, formulándose:

$$P\left(\exists A \rightarrow B \mid (\theta,\varphi)_x\right) = \begin{cases} 1, \text{ si existe un camino común} \\ 0, \text{ otros casos} \end{cases}, \qquad \text{(B1.6)}$$

siendo $P\left(\exists A \rightarrow B \mid (\theta,\varphi)_x\right)$ la probabilidad de que exista un camino conector entre A y B dada una configuración particular estimada $(\theta,\varphi)_x$ (el subíndice x hace referencia a todos los voxeles en el cerebro, por tanto $(\theta,\varphi)_x$ es el conjunto completo de las direcciones que presentan las fibras). Pero no se conoce con certeza a $(\theta,\varphi)_x$ (es decir, no se posee una solución única para esta distribución), y la ecuación (B1.6) no debe ser aplicada en tal caso. Entonces cobra interés la función de distribución de probabilidad $P\left(\exists A \rightarrow B \mid Y\right)$, que expresa la probabilidad de conexión entre A y B dados los datos de difusión. Con el fin de calcular esta probabilidad es incorporada, para cada configuración posible de dirección de fibras en los voxeles, $(\theta,\varphi)_x$, la probabilidad de conexión según una distribución $(\theta,\varphi)_x$ y además la probabilidad de esta distribución dados los datos Y recolectados, $P\left((\theta,\varphi)_x \mid Y\right)$. El planteamiento anterior queda finalmente formulado:

$$P\left(\exists A \rightarrow B \mid Y\right) = \int_0^{2\pi}\int_0^{\pi}\ldots\int_0^{2\pi}\int_0^{\pi} P\left(\exists A \rightarrow B \mid (\theta,\varphi)_{local}\right) P\left((\theta,\varphi)_{x_1} \mid Y_{x_1}\right)\ldots P\left((\theta,\varphi)_{x_v} \mid Y_{x_v}\right) d\theta_{x_1} d\varphi_{x_1} \ldots d\theta_{x_v} d\varphi_{x_v}, \qquad \text{(B1.7)}$$

donde $x_1,\ldots,x_v$ son los voxeles del volumen cerebral.

B2 MÉTODOS DE PROPAGACIÓN DE FRENTES DE ONDA

En contraste con las técnicas de propagación de líneas, los métodos de propagación de frentes de onda (Parker y col., 2002; Staempfli y col., 2006;

Tournier y col., 2003), también conocidos como técnicas de Fast Marching (FM), expresan la tractografía en términos de un frente de onda que emana de un punto fuente $\vec{r}_0$ y cuya velocidad de expansión depende de los datos de difusión. En dependencia de la velocidad espacial del frente, a cada punto cerebral es asignado un valor de tiempo, que puede interpretarse como el tiempo necesario que demora el frente para llegar desde la fuente hasta ese punto. Luego, el camino de conexión entre el voxel fuente y un voxel de interés queda establecido por aquella ruta que minimice el tiempo de arribo del frente hasta este voxel. Suele considerarse (Jun Zhang y col., 2005) que los métodos de FM presentan dos ventajas fundamentales sobre los métodos de propagación de líneas: 1) mejor comportamiento ante situaciones de cruce, doblez o abanicamiento de fibras, y 2) estimación directa de la probabilidad de conexión a través de la materia blanca entre dos puntos.

Al comenzar la propagación del frente desde el voxel fuente $\vec{r}_0$, que es equivalente al crecimiento de un volumen desde este punto, en cada iteración el conjunto de los voxeles cerebrales es dividido en tres subconjuntos no solapados: 1) *voxeles del frente,* aquellos que pertenecen al frente en expansión; 2) *voxeles en la banda de transición,* aquellos que son contiguos a los voxeles del frente, constituyen los candidatos a ser parte del frente en cada iteración, y 3) *voxeles externos,* en los cuales se agrupan el resto de los voxeles del volumen cerebral (ver Figura 3.4). En cada iteración, el frente se expande desde un voxel con posición $\vec{r}_i$, perteneciente a los *voxeles del frente*, hasta un voxel $\vec{r}_j$, ubicado en la *banda de transición*. Dicho crecimiento del frente, desde $\vec{r}_i$ hasta $\vec{r}_j$, es caracterizado por una función de velocidad ν. Esta función debe ser diseñada de forma tal que sea mayor cuando existan fibras nerviosas orientadas en la dirección que une a los voxeles $\vec{r}_i$ y $\vec{r}_j$, provocando que la expansión del frente sea más rápida en estas direcciones. Inicialmente, ν fue definida por Parker y col., 2002, como una función dependiente del autovector

principal de los tensores de difusión en el voxel origen, $\vec{\varepsilon}_1(\vec{r}_i)$, y en el voxel de destino, $\vec{\varepsilon}_1(\vec{r}_j)$:

$$\nu(\vec{r}_j) = \frac{1}{1 - \min\left(\left(\left|\vec{\varepsilon}_1(\vec{r}_j)\cdot n(\vec{r}_j)\right|\right),\left(\left|\vec{\varepsilon}_1(\vec{r}_i)\cdot n(\vec{r}_j)\right|\right),\left(\left|\vec{\varepsilon}_1(\vec{r}_j)\cdot \vec{\varepsilon}_1(\vec{r}_i)\right|\right)\right)}. \quad \text{(B2.1)}$$

El vector unitario $n(\vec{r}_j)$ describe la dirección de dispersión del frente en $\vec{r}_j$, siendo siempre ortogonal al frente. Esta expresión asegura que la expansión del frente sea más rápida mientras $\vec{\varepsilon}_1(\vec{r}_i)$ y $\vec{\varepsilon}_1(\vec{r}_j)$ sean más colineales con $n(\vec{r}_j)$, es decir, cuando ambos se acerquen a estar mutuamente orientados.

Para asignar el tiempo de arribo T, desde el voxel fuente a cualquier otro voxel del volumen, se considera que ν y T están relacionados por la ecuación de Eikonal (Sethian, 1999):

$$|\nabla T|\cdot \nu = 1. \quad \text{(B2.2)}$$

Para asignar un valor a $T\left(\vec{r}_j\right)$ se aproxima la expresión anterior a:

$$T\left(\vec{r}_j\right) = T\left(\vec{r}_i\right) + \frac{\left|\vec{r}_j - \vec{r}_i\right|}{\nu}. \quad \text{(B2.3)}$$

En cada paso de iteración, es seleccionado entre los *voxeles de la banda de transición* aquel que presenta menor tiempo de arribo para ser incluido entre los *voxeles del frente*. Al finalizar las iteraciones, todos los voxeles del volumen cerebral pertenecen al conjunto de los *voxeles del frente*.

Siguiendo la dirección del gradiente descendiente se estima entonces la ruta ρ de conexión anatómica entre el voxel fuente $\vec{r}_0$ y un nodo cualquiera $\vec{r}_j$, de forma tal que se cumpla:

$$T\left(\vec{r}_j\right) = \min_{\tau} \int_{\vec{r}_0}^{\vec{r}_j} \left|\nabla T\left(\rho(\tau)\right)\right| d\tau, \quad \text{(B2.4)}$$

indicando τ en este caso la posición en el camino ρ.

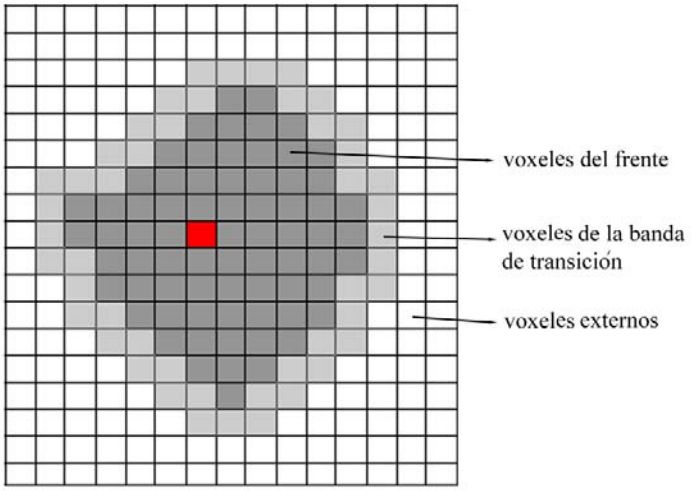

Figura B2.1. Representación en 2D de la propagación de un frente hipotético a partir del voxel fuente (mostrado en rojo). El conjunto de los voxeles del volumen cerebral es dividido en tres subconjuntos: 1) *voxeles del frente,* aquellos que pertenecen al frente en expansión (mostrados en gris oscuro); 2) *voxeles en la banda de transición,* aquellos que son contiguos a los voxeles del frente y constituyen los candidatos a formar parte del frente en la próxima iteración (mostrados en gris claro), y 3) *voxeles externos,* en los cuales se agrupan el resto de los voxeles del volumen cerebral (mostrados en blanco).

La probabilidad de que el camino obtenido represente la trayectoria real de fibras nerviosas es estimada estableciendo una métrica heurística de conectividad entre $\vec{r}_0$ y $\vec{r}_j$, la cual permite emplear un valor umbral para seleccionar las trayectorias más probables además de ofrecer directamente una medida de conectividad anatómica, o posibilidad de conectividad anatómica, entre ambos voxeles. Un forma frecuente de definir esta medida es:

$$\phi\left(\vec{r}_j\right) = \min_{\tau} \nu\left(\rho(\tau)\right). \qquad \text{(B2.1)}$$

Expresión según la cual se evalúa la validez de un camino para representar la trayectoria de fibras nerviosas de acuerdo al peor caso de coherencia entre la dirección local que sigue el camino y la distribución direccional que presentan los datos de difusión. Basta para que un camino avance en una dirección en la cual la expansión del frente presentó baja velocidad, lo que debe concordar con que

no existan fibras orientadas en esa dirección, para que este camino sea considerado poco representativo de una conexión anatómica a través de la materia blanca.

Dos factores prácticos a tener en cuenta para la implementación de los métodos de FM son: 1) el diseño de la función de velocidad de expansión del frente, y 2) el carácter de avance discreto del frente de onda, que suele ser de voxel en voxel, implicando la acumulación de errores por discretización. En ambos factores se ha continuado trabajando. Posterior a Parker y col., 2002, donde ν depende solamente del autovector principal del tensor de difusión, otras funciones de velocidad de propagación han sido propuestas (Staempfli y col., 2006; Tournier y col., 2003) con el objetivo de lograr una evaluación más realista ante estructuras complejas de fibras, como son los cruces, dobleces y abanicamientos. En el primer caso citado, se utiliza en lugar del autovector principal del tensor de difusión una ODF heurística obtenida a partir del mismo tensor, mientras que en el segundo caso se realiza la clasificación del tensor de difusión (según tres coeficientes que caracterizan su componente linear, planar y esférica) con el fin de emplear diferentes funciones locales de velocidad creadas de acuerdo a cada clasificación (sobre este procedimiento nos referiremos más adelante como aFM, del inglés *advanced Fast Marching*). En dichos trabajos, los errores de discretización han sido disminuidos al aumentar el número de direcciones en las que se considera la expansión del frente, o estableciendo puntos intermedios entre los voxeles a los que puede arribar el frente (ver como ejemplo la interesante propuesta de expansión introducida en Tournier y col., 2003). Otra alternativa es el empleo de métodos de interpolación para reducir la dimensión de los voxeles, obteniendo así un medio de expansión más continuo. Sin embargo, tal procedimiento presenta el inconveniente de disminuir la relación señal ruido (SNR, del inglés *signal to noise ratio*) de las imágenes de difusión, a la vez que implica un mayor costo computacional.

9. GLOSARIO

Materia gris: en esta se encuentran las neuronas, unidades básicas del sistema nervioso, que se comunican entre sí mediante prolongaciones muy pequeñas llamadas dendritas, la cuales recogen la información proveniente de otras neuronas u órganos del cuerpo, y mediante prolongaciones más largas, parecidas a cables eléctricos, a los que se les llama axones o fibras nerviosas, que conducen los mensajes codificados en forma de impulsos nerviosos que unas neuronas envían a las otras. Aunque a menudo poco mencionadas, las células Glías (también en la materia gris) representan un soporte indispensable para el buen funcionamiento de las neuronas, cumpliendo para estas labores de sostén y nutrición, actúan como guías en las migraciones neuronales y contribuyen a formar las vainas de mielina que protegen y aíslan los axones.

Materia blanca: La materia blanca está compuesta enteramente por los axones que parten de la materia gris, los cuales van desde un grupo de neuronas a otro organizados en arreglos paralelos de entre 50 y 100 axones, a los que se les llama tractos de fibras nerviosas. El color blanco de las vainas de mielina, sustancia grasosa que cubre partes de las superficies de los axones y que actúa como aislante electroquímico, es lo que da nombre de materia blanca al conjunto de todas las fibras nerviosas mielinizadas.

Neuroimágenes de la difusión (*diffusion-weigthed magnetic resonance images*, en inglés): reflejan cómo ocurre el movimiento caótico de las moléculas de agua alrededor de diferentes tejidos. En una imagen típica de difusión, cuando el valor de intensidad de un pixel es bajo (pixel oscuro en la imagen), esto indica que en el pequeño volumen cúbico de volumen al cual representa este pixel hay mucha difusión en una dirección dada, y cuando por el contrario el valor de intensidad del pixel es alto (pixel brillante en la imagen), se considera entonces que ocurre poca difusión en la dirección observada.

Tensor de difusión (*diffusion tensor*, en inglés): matriz de 3 x 3 elementos, donde cada elemento refleja el grado de difusión molecular que ocurre en alguna

dirección espacial. El tensor de difusión suele ser representado geométricamente como un elipsoide. En el marco de las neuroimágenes de la difusión, los tensores de difusión se utilizan para reconstruir o poner de manifiesto la trayectoria que presentan las fibras nerviosas al conectar diferentes regiones cerebrales.

Función orientacional de las fibras nerviosas (*Orientational Distribuction Function*, en inglés): función de distribución de probabilidad que, en cada pequeño volumen cúbico del volumen cerebral, expresa la probabilidad de encontrar una fibra nerviosa en cualquier dirección del espacio. Se estima a partir de las neuroimágenes de la difusión.

Tractografía (*fiber tractography*, en inglés): procedimiento de reconstruir o poner de manifiesto la trayectoria que presentan las fibras nerviosas a partir de la información que brindan las neuroimágenes de la difusión.

Teoría de grafos (*graph theory*, en inglés): rama de las matemáticas que se dedica a la codificación y caracterización de redes.

Red: estructura matemática utilizada para modelar las relaciones entre objetos de una naturaleza dada. Una red queda definida por un conjunto de nodos (los objetos que se estudian), arcos que unen a los nodos (las relaciones que existen entre los pares de objetos) y pesos de los arcos (las magnitudes que caracterizan las relaciones entre los pares de objetos considerados). Al definirse una red, cuando los pesos de los arcos entre todos los pares de nodos son intrascendentes y no se consideran, se dice que la red es no-pesada. Mientras que, por el contrario, cuando al definir la red se consideran los pesos de los arcos se dice que esta red es pesada.

Topología de una red: patrones intrínsecos de conexiones entre los nodos de una red dada. Suele analizarse a través de medidas matemáticas que poseen una interpretación física, entre las que destacan:

Eficiencia global: refleja qué tanta información puede ser intercambiada de forma paralela (o al unísono) a través de toda una red.

Eficiencia Nodal: refleja la eficiencia global media que poseen todas las subredes locales contenidas en una red.

Grado de clusterización (*clustering index*, en inglés): refleja la tendencia inherente de los nodos de una red a agruparse en vecindarios estrictamente interconectados.

Longitud del camino medio (*characteristic path length*, en inglés): corresponde al número promedio de conexiones nodo-nodo que deben considerarse para llegar de un nodo dado a otro cualesquiera en la red.

Mundo pequeño (*small-world index*, en inglés): refleja que tan optimizada para el intercambio de información se encuentra estructurada una red.

Centralidad nodal (*betweenness centrality*, en inglés): refleja la importancia específica que posee cada nodo en una red dada, teniendo en cuenta qué tan es indispensable es este para que se mantenga el flujo de información entre nodos distantes en la red.

Modularidad: refleja el grado en el cual una red puede ser subdividida en módulos que contienen un máximo de conexiones internas y un mínimo de conexiones con nodos pertenecientes a otros módulos.

Vulnerabilidad: refleja qué tan vulnerable es una red dada ante la afectación hipotética de cada uno de sus nodos. La vulnerabilidad de cada nodo se evalúa como el decaimiento que ocurre en la eficiencia global de la red cuando este nodo es eliminado. La vulnerabilidad de toda la red suele considerarse como el valor máximo de vulnerabilidad de todos sus nodos.

Composición de motivos estructurales (*structural motif composition*, en inglés): identificación de los subgrafos que aparecen de forma más frecuente en una red dada de lo que pudiera esperarse estadísticamente en redes aleatorias con igual número de nodos y conexiones.

Representación espacial de una medida de red (*Network Measure Spatial Representation*, en inglés): corresponde a la representación espacial de una medida topológica específica, donde cada sujeto de una muestra considerada es

representado y determinado por un punto único en el espacio cuyas coordenadas son dadas de acuerdo a los valores obtenidos para la medida estudiada según diferentes métodos de estimación. Facilita la interpretación del resultado obtenido por diferentes vías, así como la clasificación en subgrupos característicos de los sujetos considerados.